THE UNIVERSITY OF HULL

Applications of Radiation in Photodiagnosis and Photodynamic Therapy

being a Thesis submitted for the Degree of

Doctor of Philosophy in the University of Hull

by

Guy Entract, MChem (Hons)

February 2020

Abstract

The application of radiation to porphyrin-based photosensitisers for the purposes of photodiagnosis and photodynamic therapy have been described in an effort to explore combined therapies, which seek to extend the use of photodynamic therapy beyond its traditional applications.

A fluorine-18 radiolabelled photosensitiser has been developed to combine photodynamic therapy with positron emission tomography (PET) into a single "theranostic agent". Synthesis of this novel theranostic agent was carried out through the conjugation of a cationic water-soluble porphyrin bearing an azide moiety to a fluorine-18 radiolabelled PEG chain bearing an alkyne moiety *via* a copper-catalysed azide-alkyne cycloaddition (CuAAC). A biological evaluation of the theranostic agent was undertaken *in vitro*, exhibiting good uptake into the HT-29 human cancer cell line. It was the first time a porphyrin labelled with fluorine-18 had been shown to have retained photocytotoxicity following radiolabelling. *In vivo* evaluation confirmed uptake into neoplastic tissue and demonstrated potential as a radiotracer for (PET).

Several suitable nanoparticles were synthesised for the potential to generate visible light under the irradiation of hard X-rays by scintillation pathways. Many of the nanoparticles developed were synthesised for the first-time using microwave-assisted syntheses, which was found to optimise their characteristics and had not previously been tested for their potential as scintillators. An entirely new $EuWO_4$ scheelite morphology was discovered in nanoparticle form, which has not previously been achieved and was found to be a scintillator with good potential.

A range of scintillating-nanoparticle photosensitiser conjugates (ScNP-PS) were developed by the functionalisation of scintillating nanoparticles and conjugation to a

porphyrin photosensitiser. Preliminary evaluation of conjugates was tested by irradiation using energy of 160 keV, whilst singlet oxygen generation was measured spectrophotometrically using a singlet oxygen probe. All the peptide coupled conjugates displayed $^{1}O_{2}$ generation, with the rare earth fluorides $La_{1-x}Eu_{x}F_{3}$ and $Lu_{1-x}Eu_{x}F_{3}$ exhibiting the best results.

Acknowledgements

I would like to thank my supervisors Ross Boyle and Grazia Francesconi for their support throughout my PhD. I would also like to thank the many technicians who have assisted me throughout this work and my co-authors on published work.

I dedicate this to Αιμιλία and Ιωάννα.

Abbreviations

$^1O_2$	Singlet oxygen
3D CFRT	3-Dimensional conformal radiotherapy
$^3O_2$	Triplet oxygen
ABDA	9,10-anthracenediyl-bis(methylene) dimalonic acid
ALA	5-Aminolaevulinic acid
APTES	3-Aminopropyl)triethoxysilicate
ATP	Adenosine triphosphate
ATR-IR	Attenuated total reflectance infra-red spectroscopy
CIS	Carcinoma *in situ*
CT	Computed tomography
CuAAC	Copper (I) catalysed alkyne-azide cycloaddition reaction
DAMP	Damage associated molecular patterns
DCFH-DA	2',7'-dichlorofluorescein diacetate
DI	Deionised water
DNA	Deoxyribonucleic acid
DPBF	1,3-Diphenylisobenzofuran
DSB	Double-strand breakages
EDX	Energy dispersive X-ray analysis
EPR	Enhanced permeability retention
EG	Ethylene glycol
eV	Electron volt
FDG	Fluorodeoxyglucose
FRET	Forster resonance energy transfer

HAL	Hexyl aminolevulinate
HOMO	Highest occupied molecular orbital
Hp	Haematoporphyrin
HPD	Haematoporphyrin derivative
HPLC	High performance liquid chromatography
ICD	Immunogenic cell death
ICP-MS	Inductively coupled plasma mass spectroscopy
IGRT	Image guided radiotherapy
IMRT	Intensity-modulated radiotherapy
LDL	Low-density lipoproteins
LUMO	Lowest occupied molecular orbital
MC540	Merocyanine 540
MLC	Multi-leaf collimators
MPCA	Metalloporphyrin contrast agents
MRI	Magnetic resonance imaging
MS	Mass spectrometry
MSN	Mesoporous silica nanoparticles
MVP	Methoxyvinylpyrene
NMR	Nuclear magnetic resonance
NP	Nanoparticle
OAR	Organs at risk
PDT	Photodynamic therapy
PEG	Polyethylene glycol
PET	Positron emission tomography
PPIX	Protoporphyrin nine

PS	Photosensitiser
PTV	Planning target volume
PVP	Polyvinylpyrrolidine
PXRD	Powder X-ray diffraction
QD	Quantum dot
RB	Rose Bengal
RE	Rare-earth
ROS	Reactive oxygen species
SAO	$SrAl_2O_4$
SBRT	Stereotactic body radiotherapy
SCNP	Scintillating nanoparticle
ScNP-PS	Scintillating nanoparticle photosensitiser conjugate
SEM	Scanning electron microscopy
SI	International system of units
SLPDT	Self-lighting photodynamic therapy
SOSG	Singlet oxygen sensor green
SPECT	Single-photon emission computed tomography
SSB	Single strand breakages
SUV	Standardised uptake value
TBAF	Tetrabutylammonium fluoride
TEG	Triethylene glycol
TEM	Transmission elelctron microscopy
TEOS	Tetraethoxysilane
TLC	Thin-layer chromatography
UCNP	Upconverting nanoparticles

UV-Vis	Ultraviolet-visible
VP	Verteporfin
XRIL	X-ray induced luminescence

COSHH statement

All of the experiments carried out had a full COSHH and risk assessment signed by the student, supervisor and safety officer and were in accordance with the University of Hull's Health and Safety guidelines.

Table of contents

Table of Figures

Table of Tables

Table of Schemes

Table of Equations

1. Literature review

1.1. Photodynamic therapy

Porphyrins are a naturally occurring group of macrocycles of intense colour, found in biological systems for processes such as oxygen transport, enzyme functioning and photosynthesis. Both naturally occurring and synthetic porphyrins have been used for the applications of imaging and therapeutic medicine known as photodynamic therapy (PDT).[1]

PDT is a clinical treatment of cancerous or unwanted tissues that employs a photosensitiser in combination with light of an activating wavelength (typically 400 - 700 nm) to bring about a cytotoxic effect within the targeted tissue by the generation of reactive oxygen species (ROS), most notably singlet oxygen ($^1O_2$) from ground state molecular oxygen ($^3O_2$).[2] The photosensitiser is typically introduced into the body by intravenous or topical application and will accumulate preferentially within rapidly proliferating tissue. When the drug has accumulated within the target tissue to a favourable ratio of target to non-target tissues, a light dose is employed (**Figure 1**). This bestows a dual-selective mode of action as the drug has a favourable localisation within neoplastic tissues, combined with a light dose delivered only to that region. Dark toxicity tends to be negligible, making this treatment far more selective than other chemotherapies, and with significantly reduced side effects.

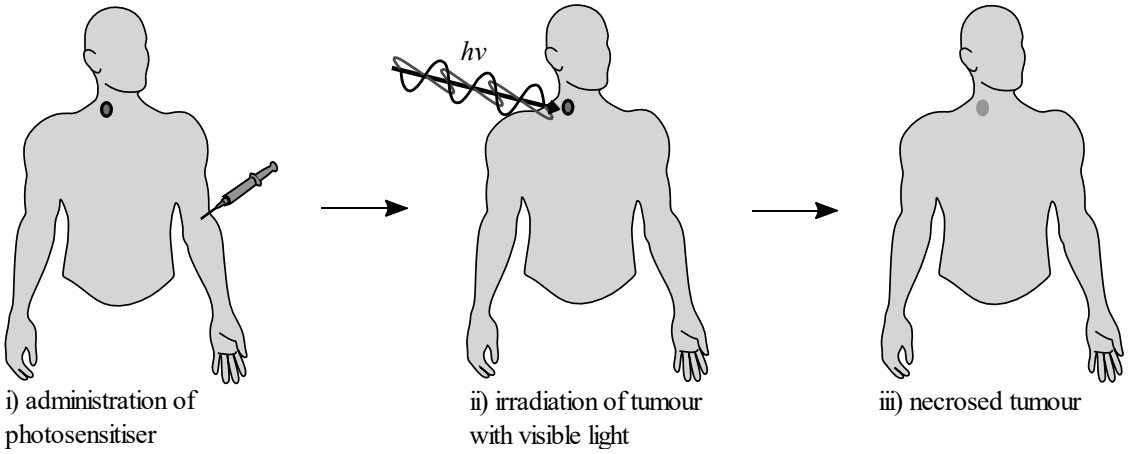

Figure 1 Clinical procedure for photodynamic therapy.

PDT is generally used to treat skin cancers and some cancers on the lining of internal organs or within cavities. It is not yet considered a viable treatment against deeper seated tumours as compared with more conventional cancer treatments such as radiotherapy, chemotherapy and surgery.[3] One of the main issues keeping PDT from more mainstream uptake is that the visible light used to activate the photosensitisers has limited tissue penetration depth, due to its absorption in the visible light region which restricts its efficacy to superficial tumours. However, it does have the potential to offer advantages over the conventional treatments. It is a non-invasive treatment with few side effects that are arguably of lesser severity than that experienced with the alternatives. There has been some advancement toward the treatment of deeper tumours which involve the introduction of fibre optics, however an incision must be made to introduce the fibre optic to the tumour location, somewhat negating the advantage of its original non-invasive nature.

1.1.1. Photophysical reactions

For the generation of ROS to occur within the target tissue, the photosensitiser is irradiated with visible or near infra-red light. The photosensitiser (PS) initially exists in the ground state (S_0) with electrons paired in the highest occupied molecular orbital (HOMO). Irradiation of the PS with visible/NIR light promotes one of the paired electrons in the HOMO to the lowest unoccupied molecular orbital (LUMO) (**Figure 2**), giving an excited singlet state (S_n) made up of a number of vibrational sub levels (**Figure 3**). The S_n is a short-lived transition state (10^{-9} - 10^{-6} seconds) and decays through the *vibrational* sub levels through internal conversion (IC) or by a return to the ground state with an (S_n-S_0) emission of a photon known as fluorescence.

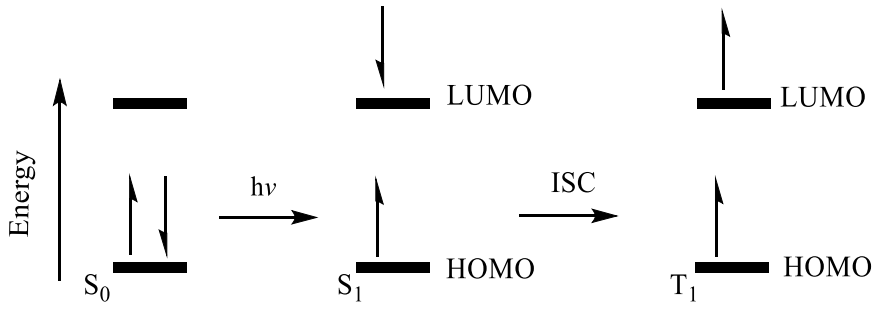

Figure 2 Electronic orbitals of a PS in the ground state (S_0), the first excited singlet state ($S_{1)}$ and first excited triplet state (T_1).

Alternatively, the S_1 state can undergo a process known as intersystem crossing (ISC) to the excited triplet state (T_1), (a spin inversion). The T_1 transition state is a longer-lived state (10^{-3} - 1 seconds), enhancing the probability of an electron transfer reaction with proximal cell components (type I reaction) or energy transfer to triplet ground state molecular oxygen ($^3O_2$), (type II reaction). Unreacted T_1 states can also return to the ground state via the formally spin forbidden (T_1-S_0) transition by emission of a photon, a process known as phosphorescence. It is the disallowed nature of triplet to singlet transitions which accounts for the long lived T_1 state.

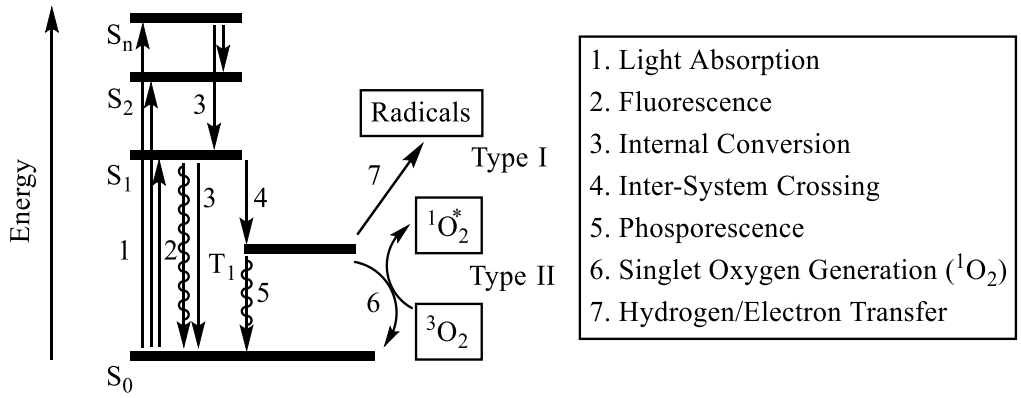

Figure 3 Modified Jablonksi diagram showing the photophysical and photochemical pathways of photosensitisers following irradiation.

1.1.2. Photochemical reactions

Photosensitisers in the excited triplet state (T_1) can undergo both type-I and type-II processes[4] (**Figure 4**), the ratio of which will likely depend on the nature of the photosensitiser used, the concentrations of ground state molecular oxygen available and cell substrates present. The PS in a type-I reaction, reacts directly with cell substrate transferring electrons to form radical anions or cations respectively.[5]

Possible pathways for Type I processes include T_1 transferring of an electron to $^3O_2$ to form a super oxide anion ($^3O_2^{\cdot-}$) and an excited triplet state cation ($T_1^{\cdot+}$). The ($^3O_2^{\cdot-}$) can react with a second superoxide molecule, catalysed by super oxide dismutase (SOD) to give hydrogen peroxide (H_2O_2) and $^3O_2$. The ($^3O_2^{\cdot-}$) can reduce Fe^{3+} to Fe^{2+}, which can then react with H_2O_2 to form a hydroxyl radical ($OH^{\cdot}$) and hydroxide (OH^-). ($OH^{\cdot}$) can react with $^3O_2^{\cdot-}$ to give the potent cytotoxic ROS, singlet oxygen, as produced in the type-II process. Many of the other species shown in **Figure 4** are ROS in their own right however and are capable of inducing cell death.

The type-II process is a direct energy transfer between T_1 and $^3O_2$ undergoing a triplet-triplet annihilation (T_1-S_1 * $^3O_2$-$^1O_2$) in which the antibonding electrons of $^3O_2$ are spin

inverted in two ways to give the two possible forms of singlet oxygen ($^1\Delta_g$ and $^1\Sigma g$) (**Figure 5**).

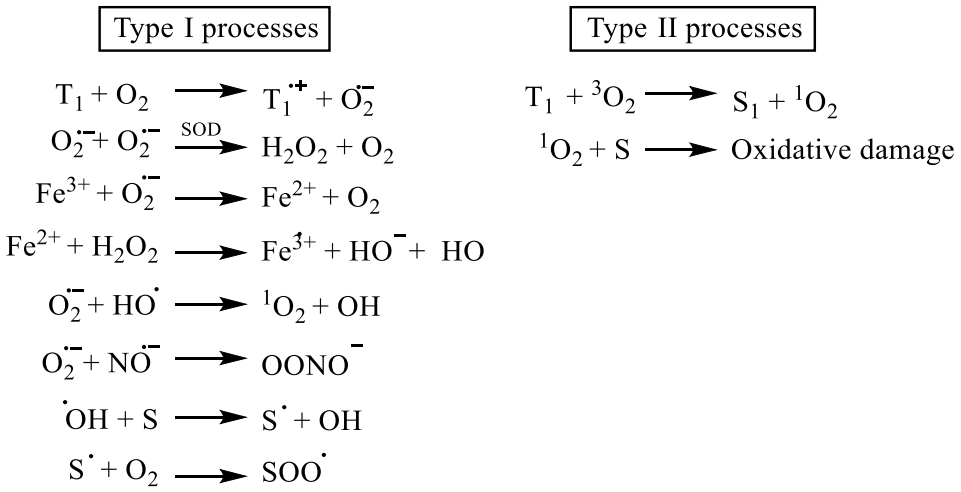

Figure 4 Type-I and type-II processes. Excited state photosensitiser (T_1), singlet state photosensitiser (S_1), cell substrate (S).

1.1.3. Singlet oxygen

Singlet oxygen is considered to be the major cytotoxic agent in PDT,[6] formed by an electronic spin inversion of an outer electron in the anti-bonding electron orbital of molecular oxygen.

In the outer antibonding orbitals of ground state molecular oxygen there are two unpaired electrons of parallel spin (triplet state) in π_y and π_z (**Figure 5**). The electrons occupy separate degenerate orbitals with identical quantum numbers, with three possible configurations; hence it is a triplet state.

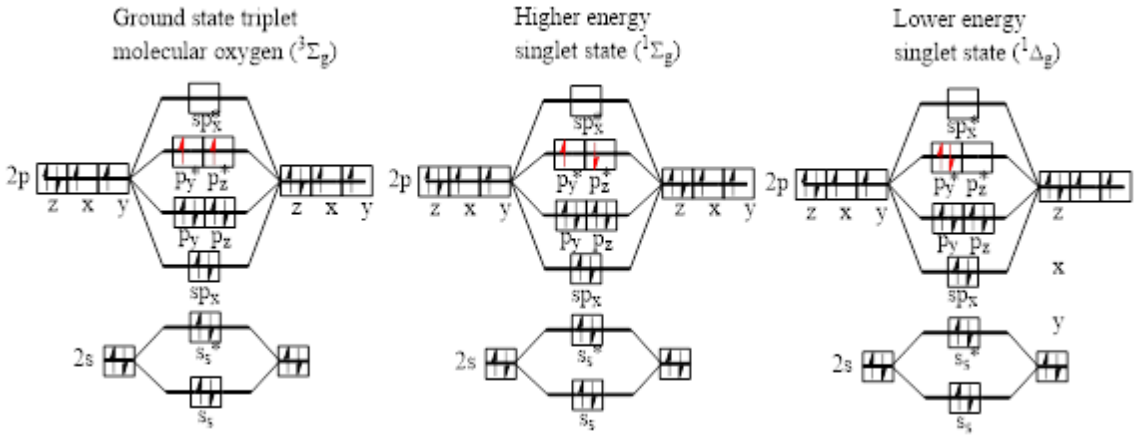

Figure 5 Molecular orbital diagram of molecular oxygen in the triplet ground state, higher energy singlet state, and lower energy singlet state.

Singlet oxygen is a very reactive species in a biological environment undergoing several possible reactions with substrates such as oxidation and cycloadditions, which are highly damaging to biological systems (**Scheme 1**).[2,7]

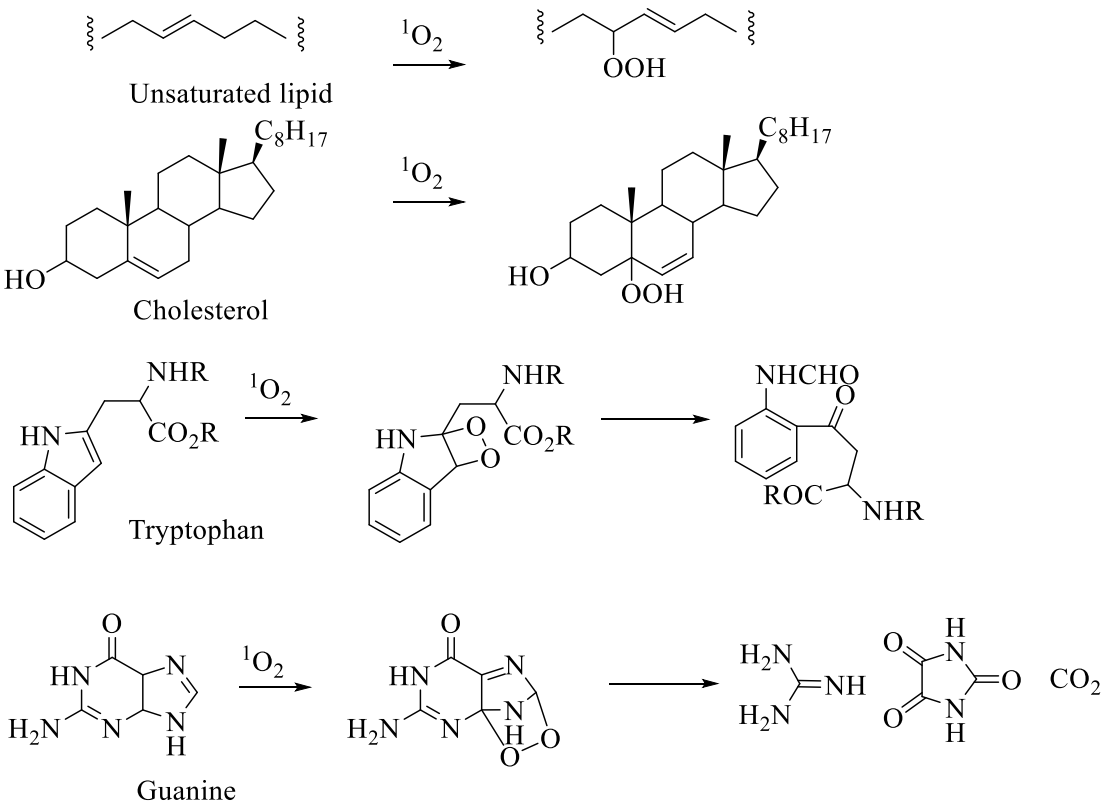

Scheme 1 Possible reactions of Singlet Oxygen with biological substrates.

Two energy states of singlet oxygen can be generated when triplet-triplet annihilation occurs between the PS and $^3O_2$ giving the two singlet states ($^1\Delta_g$ and $^1\Sigma_g$) (**Figure 5**). The higher of the two energy states $^1\Sigma_g$ (157 kJ mol^{-1} > $^3\Sigma_g$) has electrons of opposing spins in different orbitals, and is a very short lived state (130 ns in carbon tetrachloride).[8] This state rapidly relaxes to the longer lived lower energy state $^1\Delta_g$ (94 kJ mol^{-1} > $^3\Sigma_g$), which is the energy state implicated in cell death.[9]

1.1.4. Cell death

During PDT different subcellular components can be attacked, including the cell membrane or organelles such as the mitochondria, lysosomes or nuclei depending on the localisation and biodistribution of the photosensitiser being used. It is this subcellular localisation that can affect the form of cell death to be incurred *via* either necrosis or apoptosis or both.[10]

Apoptosis was first described in 1972,[11] and was later shown to occur in response to PDT in 1991.[12] Apoptosis is believed to have evolved in altruistic, or defensive single celled bacteria, whereby they would feed themselves to starving neighbouring cells or commit "cell suicide" to stop the spread of an infection. These mechanisms might then have been adopted for use in development and homeostasis after the evolution of multi-cellular organisms.[13]

Apoptosis is a mechanism of programmed cell death, that is usually initiated by a process of the genetic apparatus,[14] that results in certain morphological and biochemical changes. These changes include maintenance of adenosine triphosphate (ATP) levels, caspase activation, nuclear DNA fragmentation, membrane blebbing, cell shrinkage and eventual dissociation of the cell into membrane bound particles known as apoptotic bodies.[15] The

apoptotic bodies release signals enabling phagocytes to locate and engulf them (**Figure 5**). This is a programmed cell death that minimises the release of inflammatory products and represents the key difference with cell necrosis.

Necrosis is an uncontrolled form of cell death characterised by a passive non-ATP driven process. Cell necrosis is often characterised by a swelling and breakdown of the plasma membrane, resulting in an inflammatory reaction due to the expulsion of the cells contents. **Figure 6** demonstrates the relationship between these two types of cell death.[13,16,17]

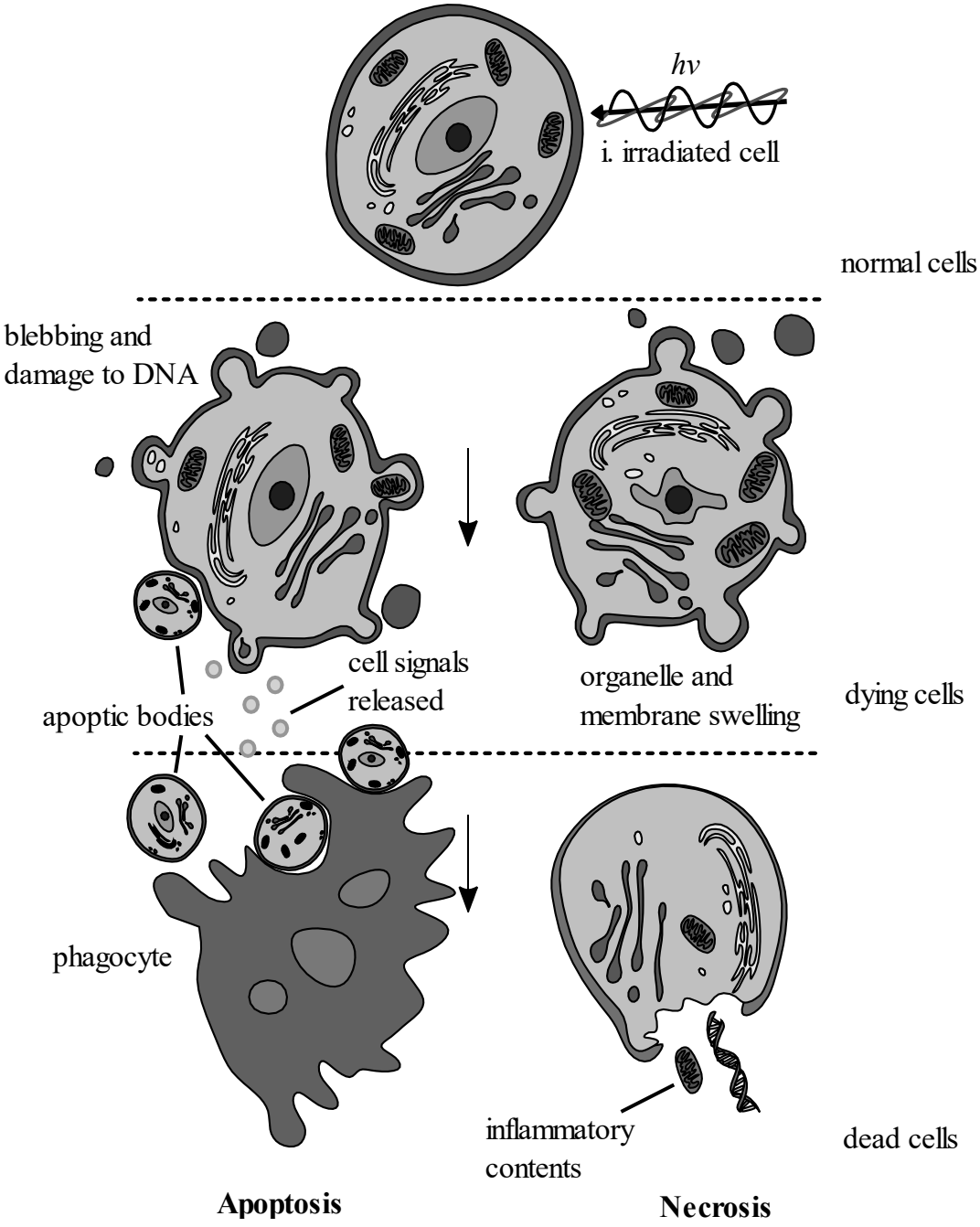

Figure 5 Cell death by necrosis and apoptosis in response to PDT.

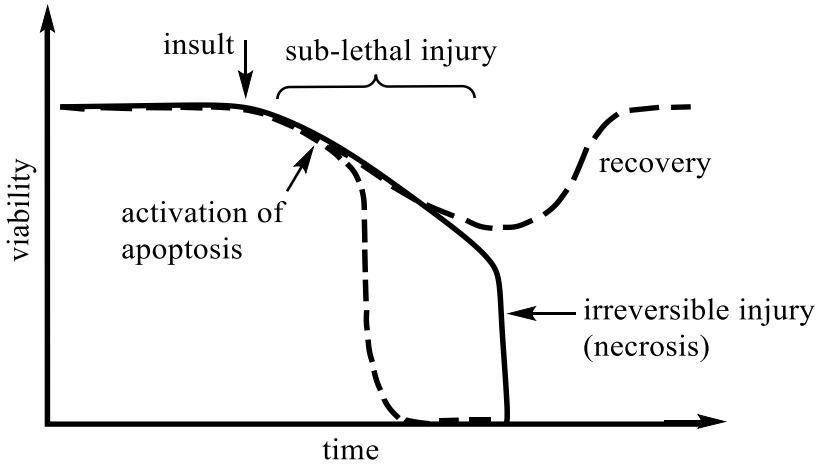

Figure 6 The relationship between necrosis and apoptosis. A cell responding to destructive stimulus by apoptosis (---). A cell undergoing the pathological disordered cell death of necrosis (___).[11]

1.2. Porphyrins as photosensitisers

The word "porphyrin" comes from the ancient Greek *porphura* meaning a deep red or purple. Porphyrins derive from a group of naturally occurring heterocyclic tetrapyrolic macrocycles bearing extensive conjugation, which allow for a structure dependant tunability of light absorption in the visible spectrum. The core structure of the planar macrocycle is known as porphine and consists of four pyrrolic sub-units joined together at the α-positions 1,4,6,9,11,14,16 and 19 by four methine bridges (*meso*- positions) labelled 5,10,15 and 20 (**Figure 7**). It is these meso positions that are often substituted as well as the *β*-positions (2, 3, 7, 8, 12, 13, 17 and 18) to synthesise conjugated or functionalised molecules for a variety of different applications.

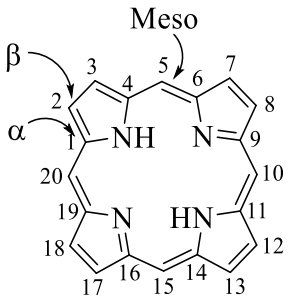

Figure 7 Porphine structure.

Many porphyrins have been evaluated for their potential as photosensitisers. In the general search for new and improved photosensitisers, a design criteria for the ideal photosensitiser has been established, across many sources of literature including Dolphin, Bonnett and Berenbaum and Dougherty:[1,18,19]

i. Single substance - In multi-component photosensitisers such as Photofrin, interpretation of results becomes increasingly complex. A single pure compound of known and constant composition becomes preferable.

ii. Good photophysical credentials - A high triplet quantum yield ($\varphi_t > 0.5$) and a triplet energy > 94 kJ mol^{-1} for an efficient energy transfer to ground state molecular oxygen.[9] For singlet oxygen reactions the most important parameter is a good singlet oxygen quantum yield ($\varphi_\Delta > 0.5$).

iii. No or minimal dark toxicity.

iv. An absorption band with high (> 20,000 - 30,000 $M^{-1}cm^{-1}$)[20] extinction coefficient between 630 - 850 nm. Light within this wavelength has a good tissue penetration and still enough energy for the oxygen triplet to singlet conversion.

v. A good accumulation of the photosensitiser within target tissue over surrounding tissues.

Although there are non-tetrapyrrolic photodynamic sensitisers being developed the

majority are based on modified tetrapyrrolic structures of porphyrins, chlorins, bacteriochlorins and phthalocyanines (**Figure 8**).[21] Apart from phthalocyanines, these structures are based on naturally occurring molecules which have minimal dark toxicity and have been studied and developed extensively over the years.[2,5,10,18,22–24] They lend themselves to modification by metalation of the inner cavity and substitution of the meso and beta positions to alter amphiphilicity as well as photochemical and photophysical properties, (Q- band positions (see **Figure 9**) , singlet oxygen quantum yields etc).

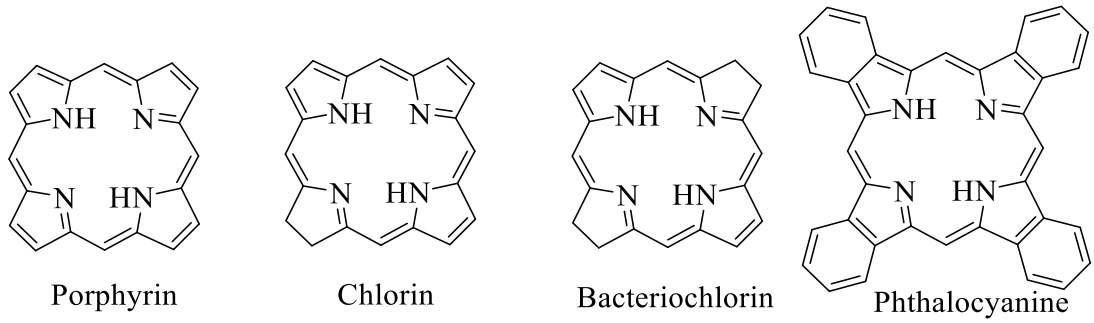

Figure 8 Parent structure of the major photosensitisers used in PDT.

Porphyrins are commonly used photosensitisers as they have a good oxidative stability and can be easily synthesised. They have a strong intensity absorption band at around 400 nm called the Soret band and four weaker (unmetallated) Q-bands at higher wavelengths, typically 500 - 640 nm for naturally occurring porphyrins (**Figure 9**)[20] with the synthetic meso substituted porphyrins being capable of slightly higher wavelengths.[22] Chlorins and bacteriochlorins have increased molar absorptivities for their lowest energy absorptions at approximately 665 nm and 780 nm respectively, offering potentially better tissue penetration if used for PDT, but unless structurally stabilised these compounds will readily oxidise to the more stable porphyrin, raising issues of stability. Phthalocyanines have extended conjugation pathways due to the additional aryl rings fused to the tetrapyrrolic core producing longer Q-band λ_{max} values of around 670 - 700 nm, and with

enhanced extinction coefficients (approx. 200,000 M^{-1} cm^{-1}).[22] This however increases lipophilicity meaning sulphonation or a carrier system is typically required for drug administration.

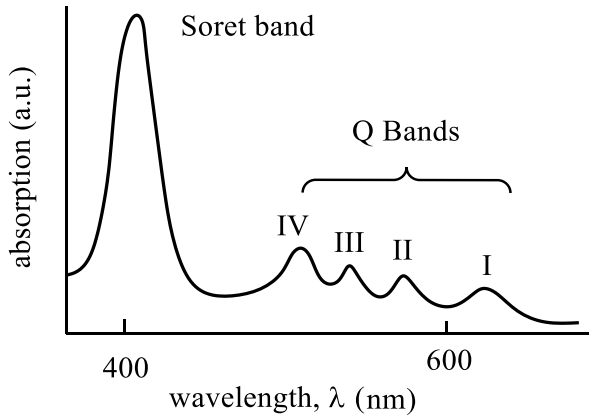

Figure 9 Typical etio type porphyrin absorption spectra.[20]

1.2.1. First-generation photosensitisers

The discovery of photodynamic action was made by an observant student of the German von Tappeiner group named Oscar Raab, in 1898. He was investigating the toxic effects of acridine on paramecia when he noticed a difference in the survival rate at incubation between 1.5 hours and 15 hours for identical experiments. The only difference he noted was that for the experiment with a much shorter survival time, there had been a heavy thunderstorm for the duration. The group attributed this to the combination with light and hence discovered photodynamic action. They also recognised the important role of oxygen in the photodynamic effect and published their findings.[25–27]

The first-generation of photosensitisers were derived from a naturally occurring porphyrin, haematoporphyrin (Hp), which was prepared from dried blood by Scherer in 1841, by removing iron by a treatment with sulphuric acid.[28] Between 1908 and 1913

photobiological experiments demonstrated the sensitisation of paramecia, erythrocytes, mice,[29] guinea pigs,[30] and humans,[31] to light, when injected with haematoporphyrin. The German physician Friedrich Meyer Betz became highly sensitive to light for several months following the self injection of 200 mg of hematoporphyrin, (**Figure 10**).

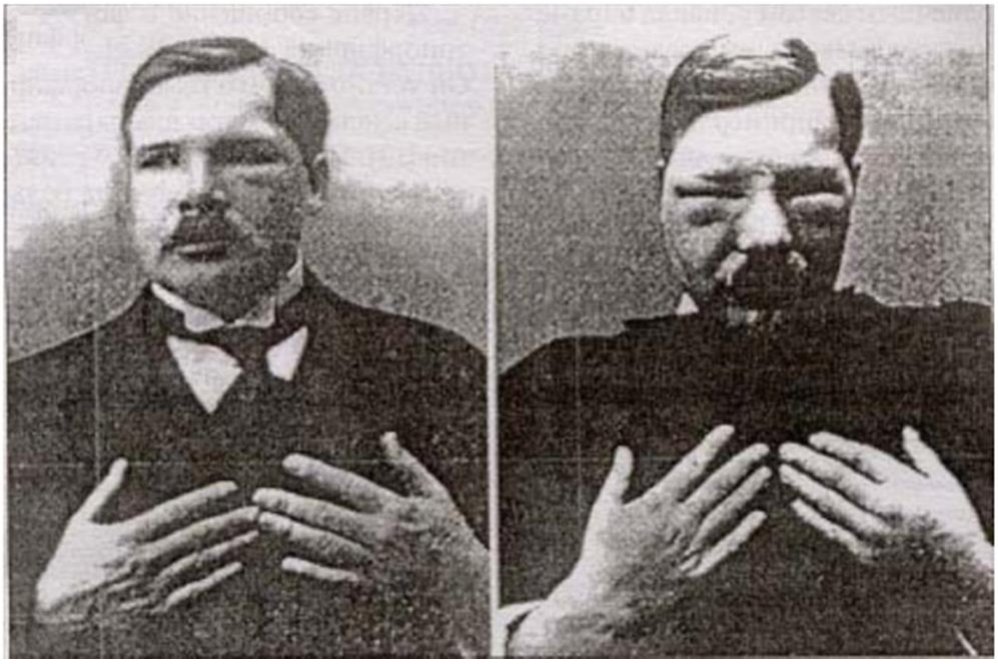

(a) (b)

Figure 10 Photograph of German physician Friedrich Meyer-Betz before and after self-injection with 200 mg of Hp leading to severe photosensitisation of the skin for several months.[31]

Several observations of the accumulation of porphyrins within tumours were made, first from Policard in 1924 who published findings of porphyrin fluorescence for tumours.[32] However, Auler and Banzer were the first to study the accumulation of injected porphyrins into the tumours of animals who were then treated with light.[33]

It was discovered by Schwartz[34] that the treatment of hematoporphyrin with acetic-sulphuric acid gave a mixture of components with superior tumour localising properties,

which came to be known as haematoporphyrin derivative (HPD). This mixture of haematoporphyrin oligomers, was described by Lipson in 1961[35] and was used by Lipson and co-workers for a large number of clinical studies for diagnostic and therapeutic purposes.[36] Dougherty and co-workers then partly purified HpD by removing monomers and lower oligomers, producing Porfimer sodium (tradename Photofrin™) (**Figure 11**) which has become the most widely used sensitiser for PDT,[28] and was granted regulatory approval in 1993. It has subsequently received approval for the clinical treatment of obstructing oesophageal cancer, obstructing lung cancer, microinvasive endobronchial cancer, gastric and papillary bladder cancer and cervical dysplasia and cancer.[37]

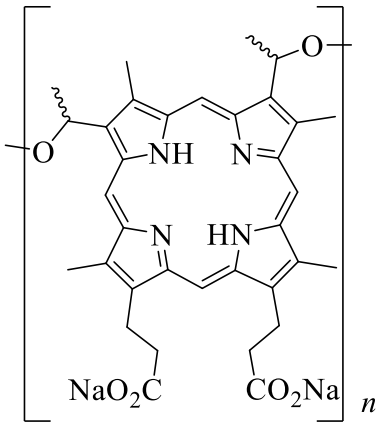

Figure 11 A simplified structure of the porphyrins present in Photofrin™ joined together by ester and ether linkages.

Although HpD and Photofrin™ have been the most successful photosensitisers so far in a clinical setting; these first generation photosensitisers suffer three important disadvantages.[7] Firstly, the longest wavelength Q-band at 630 nm suffers a relatively weak absorption ($\varepsilon_{630} \sim 1170\ M^{-1}\ cm^{-1}$).[19] This limits the size and depth of the tissues that can be effectively treated (**Figure 12**).

Secondly, although both have been partly purified, they are both a complex mixture of compounds from which it has not proved possible to isolate any single active component.

Thirdly, although Porfimer sodium has been shown to have an increased accumulation in neoplastic tissues over HpD and over less purified forms of the photosensitiser; accumulation is only about 3% of the administered dose, with a significant proportion of the remaining dose accumulating in the skin, leading to photosensitivity for the patient.

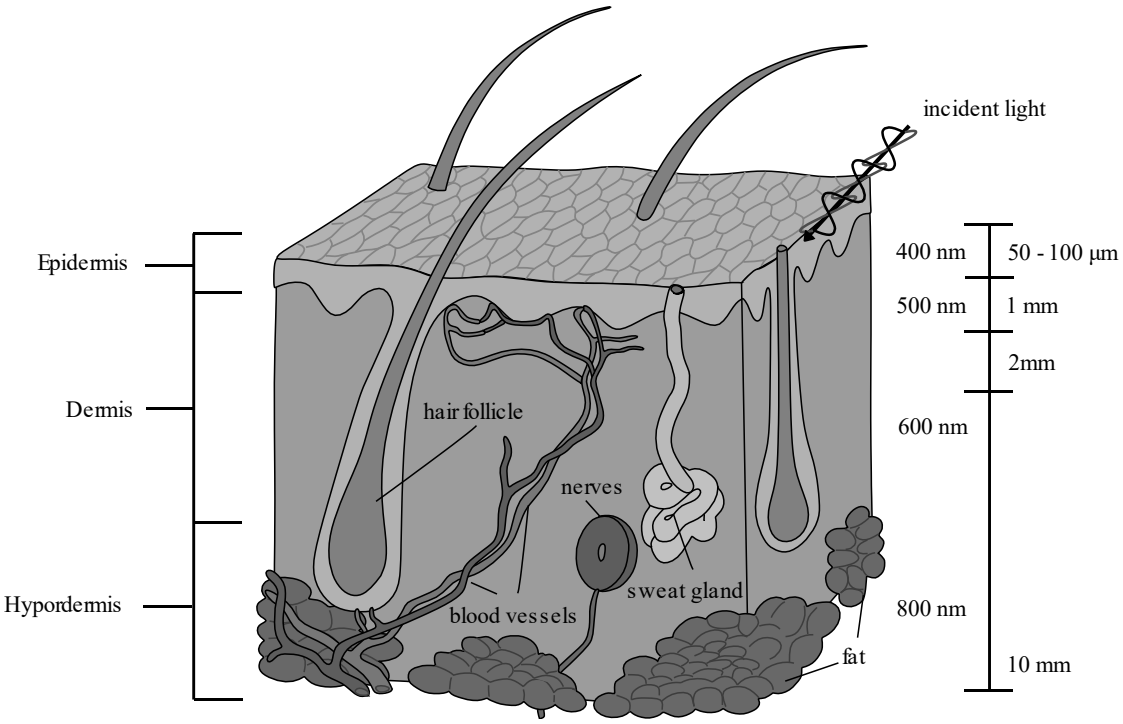

Figure 12 Light propagation through tissues.

1.2.2. Second-generation photosensitisers

It is due to the limitations of the first-generation photosensitisers that second-generation photosensitisers consist of chemically pure compounds, largely based around the tetrapyrollic skeleton. The following list discusses some of the clinically approved second generation photosensitisers:

5-Aminolaevulinic acid (ALA) is a precursor to the endogenous porphyrin, haem (Fe(II) protoporphyrin IX (PPIX)). By overloading the cells with administered ALA, the production of PPIX, the immediate precursor of haem, is made faster than the iron chelating enzyme ferrochelatase can insert iron, which would otherwise deactivate the desired photosensitising action of PPIX. This leads to the production of the free-base photosensitiser *via* the biosynthetic pathway. Together with the ALA derivatives (**Figure 13)** Metvix® (a methyl ester derivative), Benvix® (a benzyl ester derivative) and Hexvix® (a hexyl derivative), this group of precursor photosensitisers have been used in the clinic for imaging and the treatment of basal cell carcinomas, skin, brain, oesophagus gastrointestinal cancers and the diagnosis of bladder cancer.[17,21]

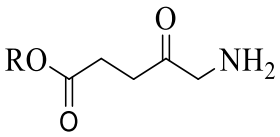

Levulan	R = H
Metvix	R = CH_3
Hexvix	R = C_6H_{13}
Benvix	R = $C_6H_5CH_2$

Figure 13 5-Aminolaevulinic acid (ALA) derivatives - Levula®, Metvix®, Hexvix® and Benvix®.

Benzoporphyrin derivative-monoacid ring A (Verteporfin®) is a second generation PS, (**Figure 14**) sold under the trade names Visudyne® or (Verteporfin® for cancer applications) which has been used to treat millions of patients worldwide for wet age-related macular degeneration (wAMD),[38] and has recently undergone Phase I clinical study in human patients with pancreatic cancer.[38] Verteporfin shows promise as it accumulates within the mitochondria, which has been shown to be a good inducer of apoptosis,[14] as well as having an absorption band at 690 nm, giving a significant tissue penetration increase relative to Photofrin™. Verteporfin® has been clinically applied in

the treatment of ophthalmic, pancreatic and skin cancers.[17]

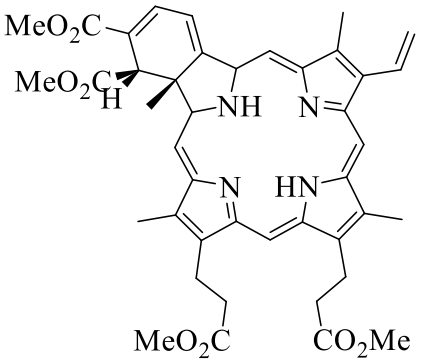

Figure 14 Verteporfin™ - Benzoporphyrin derivative-monoacid ring A (BPD-MA).

Tetra (m-hydroxyphenyl) chlorin, mTHPC (Foscan®) is a chlorin photosensitiser sold under the trade name Foscan® (**Figure 15**). It is one of the most potent of the second-generation photosensitisers, 100 times more photoactive than Photofrin™ when activated at 652 nm and 10 times more photoactive when activated at 514 nm.[39] As a consequence it requires lower drug doses (0.1 mg/kg) and light doses (10 J/cm^2)[14] for efficacy. Head and neck, lung, brain, skin and bile cancers have been clinically treated using Foscan.[17]

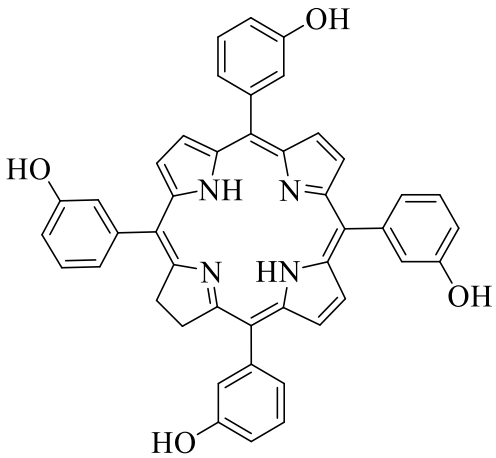

Figure 15 Meta-tetra(hydroxylphenyl)chlorin, mTHPC (Foscan™).

1.2.3. Third-generation photosensitisers

The second-generation photosensitisers have had some clinical success, but none have fulfilled all the criteria outlined previously, for the ideal photosensitiser. An area of particular focus for improvement for the third generation of photosensitisers is accumulation in target tissue. All of the second-generation photosensitisers use passive targeting, taking advantage of the enhanced permeability of tumour blood vessels (**Figure 16**). Porphyrins make use of the enhanced permeability and retention effect, described by Maeda, depending on two factors: (a) capillary endothelium in neoplastic tissue is disordered and permeable to macromolecules, allowing permeation of the photosensitiser. (b) Tumour tissue has a lack of lymphatic drainage in the tumour bed resulting in drug accumulation.[40]

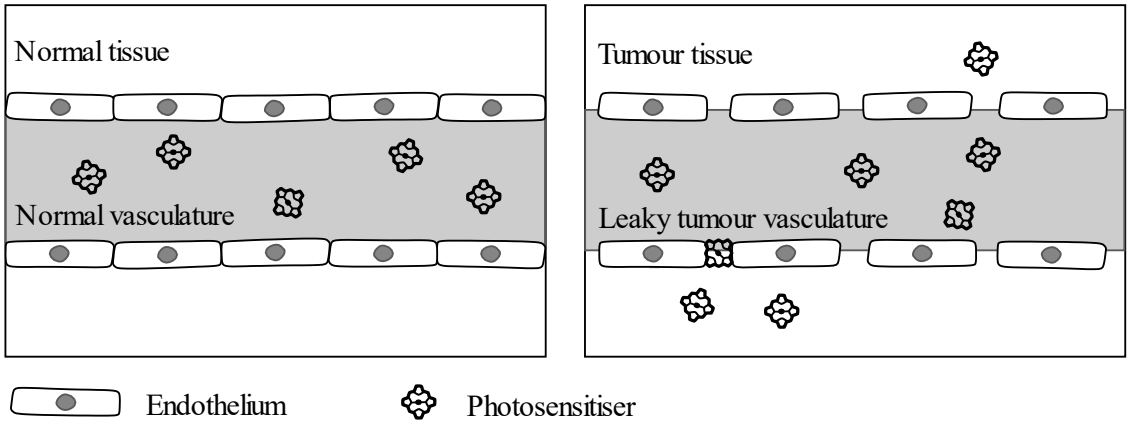

Figure 16 Enhanced permeability and retention effect. Normal tissue vasculature with tight endothelial cells prevents permeability. Tumour tissue vasculature has gaps between the endothelial cells, allowing passage of photosensitiser molecules to be retained in the tissues.

1.3. Photodynamic therapy as a combined treatment

An interesting new avenue of research for third-generation photosensitisers that may finally challenge the predominance of mainstream treatments over PDT is the

combination of photosensitiser action with other modalities for a more intelligent and individual treatment. Combining photosensitiser action with the many potential diagnostic modalities available to porphyrin structures gives an interesting new field of research termed "theranostics". There is also an amounting degree of research investigating the efficacy of PDT used in conjunction with other treatment therapies, such as immunostimulants,[41–43] ionising radiation and/or chemotherapy.[44–46]

1.3.1. Photodynamic therapy in combination with immunotherapy

Direct cell death mechanisms of PDT include apoptosis (programmed cell death), necrosis (uncontrolled cell degradation), macroautophagy and damage to the tumour vasculature. Which effect is predominant is dependent on photosensitiser uptake, light dose and the ROS concentration following PDT.

Photodynamic therapy has also been shown to induce immunogenic cell death (ICD), which is capable of enhancing the effect of PDT beyond that of direct cell death mechanisms,[47] by stimulating both innate and adaptive immune responses. Innate immune response is a highly inflammatory response involving macrophage activation, maturation of dendritic cells, neutrophil activation, and an increase in natural killer cells activity.[47] Adaptive immunity is given by the B and T cells which are antigen-specific. B cells are responsible for eliminating extracellular microorganisms by producing the antigen-specific antibodies known as immunoglobulins. T cells have a number of sub categories and are responsible for the eradication of intercellular pathogens, activation of macrophages, assisting B cells to make antibodies, destroying cancer cells or virally infected cells, and immunosuppression.[47]

An *in vivo* immunogenic response is defined by the triggering of the innate or adaptive immune system, leading to an antitumor effect that is the result of mechanisms that are independent of the immune system, in this case by PDT. Immunogenic cell death is triggered by the release of damage associated molecular patterns (DAMPs) onto the cell surface or released extracellularly in response to stress or damage. These DAMPs initiate a production of tumour antigens which prime the adaptive immune system to create tumour specific antibodies to the corresponding cells.[48]

Several studies have demonstrated the efficacy of PDT generated tumour immunity by the *ex vivo* PDT of tumour cells that are then administered in a state of lysis to confer immunity. These anti-cancer vaccines from PDT-killed tumour cells have proven to be superior to tumour cell lysates generated by UV, ionising radiation or freeze-thawing.[49–52]

Due to the strong anti-tumour immunity response demonstrated by use of PDT, there has been a growing interest in creating an immunologic adjuvant effect by combining the therapy with a number of immunostimulants.[41] Several studies have been carried out on different tumour models including melanoma, squamous cell sarcoma, lung cancer, breast cancer and colon cancer with promising *in vivo* results, demonstrating increased survival rates and tumour volume reduction as well as improving tumour recurrence rates following PDT alone.[51,53–56] The studies demonstrated that the choice of photosensitiser would play an important part in the efficacy of treatment for different combinations of immunostimulants on different cell lines. This demonstrates that different photosensitisers may have specificity for different types of immune stimulation (cytokine, T-cell, macrophage etc.) just like the immunostimulants being investigated.

In the coming years, as our understanding of the pathways that tumours use to evade the immune system's effective response increases, we can expect more efficient and more selective ways to overcome this evasion. PDT offers a great deal of promise in complimenting these adjuvant therapies in creating a better efficacy of treatment.

1.3.2. Photodynamic therapy in combination with chemotherapy

Chemotherapy is one of the most commonly used strategies in the treatment of cancer but comes with well-known and severe side effects. Poor targeting efficiency and the ability of tumours to build up a chemo-resistivity can lead to limited therapeutic outcomes in certain types of malignancies. PDT offers a very promising strategy for a combined therapy that can be utilised to overcome chemo-resistant cancers by offering a different and complimentary cell death mechanism.[57]

Depending on the cell death mechanisms involved with the chemotherapeutic drug being used, there are a number of possible synergistic effects possible for a chemo-PDT adjuvant.[58] The potential for a combined treatment offers improved efficacy but also the potential to reduce the dose required and lead to less severe side effects.[59] For instance, the toxically dose limited chemotherapy agent cisplatin has shown potential *in vitro* and *in vivo* to give a substantially increased antitumour effect in combination with PDT.[60,61]

1.3.3. Photodynamic therapy in combination with diagnostic modalities for a single theranostic agent

Porphyrins offer excellent potential as diagnostic imaging agents as they are biologically compatible, innately fluorescent and have a higher avidity with cancerous tissues. Porphyrins have been shown to selectively accumulate in tumorous tissue with an uptake

two to three times higher than surrounding tissues[62] and with much higher intake observed in some malignant tumours.[63] Specificity was shown to be as high as 10:1 (tumour to skin) based on fluorescence for endogenous porphyrins like PPIX (generated *in situ* by 5-ALA) for topical applications.[64] The mechanisms for preferential uptake are not fully understood but properties of the tumour tissue that seem to be of importance include a leaky vasculature, reduced lymphatic drainage, low interstitial pH, a high number of mlc receptors[65] and large interstitial space with high amounts of collagen.[24]

The term "theranostic" combines both the modalities of therapy and diagnostic imaging into a single unit. Porphyrins are well suited as theranostic agents due to their potential as activatable[66] photosensitisers but also their intrinsic luminescent properties; bearing a central cavity capable of metal chelation for PET[67–73] and MRI[74] as well as established synthetic pathways for conjugation to targeting moieties or functionalisation for increased water solubility.[75,76]

Therapeutic strategies utilised include nucleic acid delivery, chemotherapy, hyperthermia (photothermal ablation), PDT and radiation therapy.[77] These strategies have been combined with imaging strategies including MRI, PET, SPECT and fluorescence.

1.4. Porphyrin fluorescence

Luminescence is the emission of light from a material by the relaxation of electronically excited states. The two subcategories of luminescence are fluorescence and phosphorescence, dependant on the condition of the excited state. During fluorescence one electron is excited from a ground state pair to a higher energy state and maintains its spin, opposite to its partner electron in the ground state orbital. This is an excited singlet state for which the return of the excited electron to the ground state is a spin allowed

transition, by the rapid emission of a photon, typically occurring in 10^8 s^{-1}, with a fluorescence lifetime of 10 ns.

During phosphorescence an electron is excited from a ground state pair to a higher energy state with the same spin as its partner electron in the ground state orbital. This is an excited triplet state, for which the return of the excited electron to the ground state is a spin forbidden transition and consequently emission rates of a photon are typically of 10^3 - 10^0 s^{-1}, with lifetimes between milliseconds and seconds.

Fluorescence can be used to illuminate certain tissues within the body and by developing novel fluorophores, the dependence on purely endogenous chromophores is eliminated leading to an optimised signal to background ratio (SBR) by reducing auto fluorescence, with a large Stokes shift, significantly increasing the contrast between target tissue and healthy tissue.[78]

Utilisation of porphyrins for fluorescence imaging in humans took place in the mid-20th century for the detection of head and neck malignancies. These initial endeavours successfully established that tumour fluorescence intensity increased in proportion to porphyrin dose.[79] This result was promising but progress stalled due to the large doses (1000 mg) required for tumour fluorescence, which would lead to unacceptable photosensitivity for patients exposed to light.[79] Lipson *et al.* further investigated haematoporphyrin derivative for the detection of malignant diseases in the 1960s.[35,80,81]

However, these early studies together with a low cytotoxicity, when patients were not exposed to light, eventually led (2007) to the first clinically approved porphyrin-based compound for photodetection using hexyl aminolevulinate (HAL) for the diagnosis of bladder cancers. HAL was shown to give an overall improved diagnosis over standard methods. In a study with 58 patients with a total of 113 carcinoma *in situ* (CIS) lesions,

104 (92%) were correctly detected by HAL cystoscopy vs. 77 (68%) by standard white light cystoscopy.[82] HAL was also shown to deliver improved detection rates for Ta and T1 papillary tumours of white light cystoscopy by rates of 95 to 83% and 95 and 86% respectively.

The ideal fluorophore should have a high quantum yield of fluorescence, a large Stokes shift and either target affinity or active targeting, as well as minimal photobleaching. Fluorescence is a promising property for a multimodal agent, particularly in combination with other therapies such as PDT, for guidance or surgery.

1.5. Porphyrins for MRI

Magnetic resonance (MR) is a principle based upon the interaction between an applied external magnetic field and a spin possessing nucleus. ^{1}H nuclei consist of a single proton and have a response to an applied magnetic field that is one of the largest found in nature; coupled with their innate prevalence within tissues this makes them the natural choice for imaging the human body.[83]

For a given volume of tissue containing ^{1}H nuclei, each proton will have an equal magnitude of spin vectors all randomly oriented, giving a net magnetisation **M** of zero. When a magnetic field $\mathbf{B_0}$ is applied to the tissue, the protons begin to precess about the magnetic field so that the axis of rotation is parallel to $\mathbf{B_0}$ (**Figure 17**).

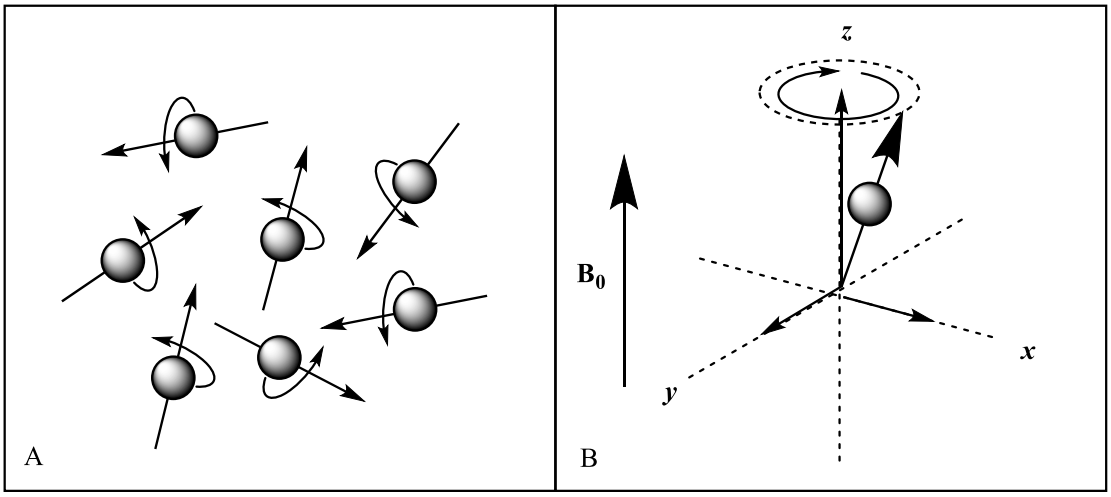

Figure 17 A) randomly oriented spin vectors of ^{1}H nuclei. B) An applied magnetic field causes protons to line up along field lines.

A radio frequency pulse is applied to the protons within the tissue of interest with a delay between pulses. The break between pulses allows the protons to release their absorbed energy and return to a random vector orientation by two relaxation processes, differing in their final disposition of energy. The relaxation time T1 is the time taken for the Z-component of M to return to 63% of their original value. The relaxation time T2 is the time taken for the transverse component of M to decay to 37% of its original value.

Magnetic resonance imaging (MRI) gives an intrinsic contrast in images between different tissues due to different T1 and T2 relaxation times of these tissues under observation. However cancerous tissue may not necessarily have different T1 and T2 relaxation times to the surrounding tissue, and therefore might give negligible detectable difference between healthy and pathogenic tissues. It is for this reason that a contrast agent may be employed.

The development of MRI in the latter half on the 20th century led to the emergence of paramagnetic metalloporphyrins as magnetic resonance contrast agents, due to their tumour localising properties. Metalloporphyrin contrast agents (MPCA's) are synthesised

by the chelation of paramagnetic metals that have electrons in the outer shells of their electron orbitals with unpaired electron spins and long electron-spin relaxations such as the transition metals manganese (Mn^{+2}) and gadolinium (Gd^{+3}). Many of the FDA approved contrast agents used most Magnavist®, Omniscan® and Prohance®, suffer from fast clearance rates of 15 minutes or less; limiting the available time for data acquisition.[84] Tumours offer much slower plasma clearance rates as well as tumour avidity. Many gadolinium porphyrins have been investigated as they offer enhanced tumour localisation, one in particular comprising of porphyrin based photosensitiser conjugated to Gd(III) contrast agents showed improved tumour uptake over Magnevist®, using a tenfold lower dose, whilst maintaining active PDT activity. Such theranostic agents that show the potential of porphyrins as multimodal platforms capable of outperforming commonly used drugs whilst offering a therapeutic modality in a single agent, highlights precisely why this field of study has increasing interest.

1.6. Positron emission tomography and porphyrins

Paul Dirac postulated[85,86] and Carl Anderson[87] experimentally observed the existence of the positron in the early 20th century, for which they both received the Nobel Prize, independently, for Physics. The positron was theorised to be an "anti-electron" with the same mass and opposite charge to the electron, and would mutually annihilate on contact with an electron.[88]

The general equation for positron decay from an atom is:

$$ {}^{A}_{Z}X \rightarrow {}^{A}_{Z-1}Y + {}^{0}_{1}\beta + v + Q\ (+e^{-}) \quad \textit{Equation 1} $$

The proton rich atom (X) self-stabilises by converting a proton into a neutron by the emission of the positive charge in the form of a positron ${}^{0}_{1}\beta$. A neutrino, v and energy, Q are also emitted as well as an electron of the daughter nucleus from an outer orbital, in order to balance the charge.

The positron will have an initial kinetic energy that is lost by inelastic collisions or elastic scattering with atomic electrons or by elastic or inelastic scattering with a nucleus. Eventually the positron will combine with an electron when they are both essentially at rest to form a positronium with a lifetime of approximately 10^{-7} seconds.

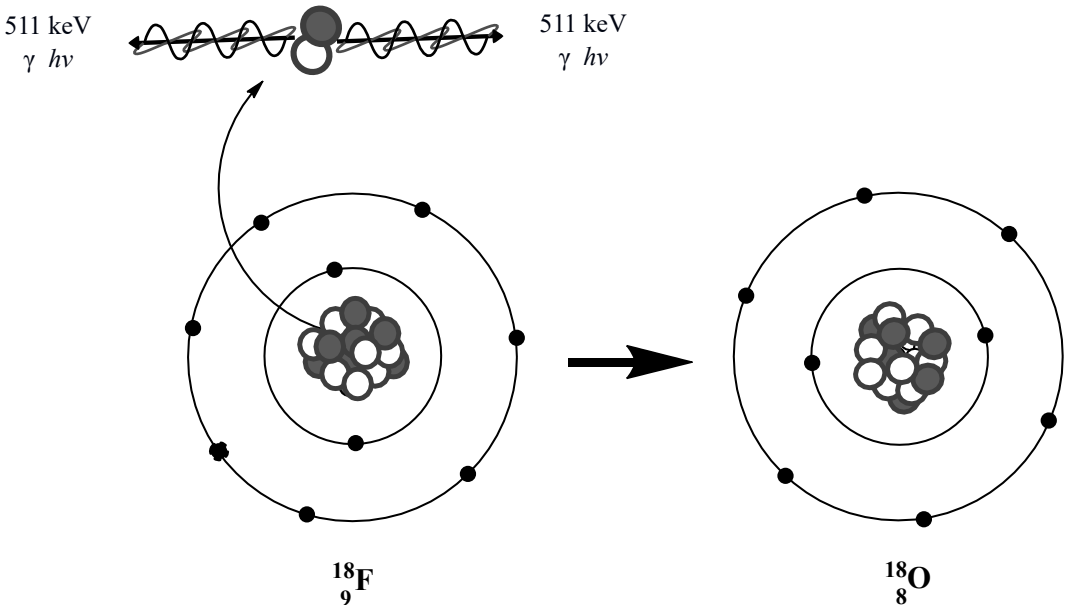

Figure 18 Decay of Fluorine-18 to Oxygen-18 by the emission of a positron.

Annihilation radiation occurs when an electron and its anti-matter equivalent, the positron, meet and convert into *pure energy* in the form of two photons of energy 511 keV. This energy can easily be calculated from the resting mass of an electron and positron using Einstein' s theory of relativity. Both an electron and a positron have a

resting mass (no kinetic energy) of 9.11 x 10^{-31} kg; calculating the equivalent energy uses the well-known equation:

$$E = mc^2$$

$$= 9.11\ x\ 10^{-31}\ kg\ x\ (3\ x\ 10^{8})^2\ ms^{-1} \quad Equation\ 2$$

$$= 8.2\ x\ 10^{-14}\ J$$

Although the joule is a unit of energy in the Systeme International d'Units (SI units), when discussing the energy of electromagnetic radiation, more commonly the electron volt (eV) is used. The electron volt is defined as the energy acquired or lost by an electron accelerating through an electric potential difference of one volt in a vacuum, and is approximately equal to 1.6 x 10^{-19} J.

Therefore, the equivalent energy of an electron's resting mass is equal to:

$$= \frac{8.2\ x\ 10^{-14}\ J}{1.6\ x\ 10^{-19}\ Jev^{-1}} \quad Equation\ 3$$

$$= 511\ keV$$

where both photons produced by an annihilation event will be emitted at 180˚ to one another. It is this property of the emitted photons which is exploited in PET (**Figure 19**), known as the line-of-sight of the event.

PET uses coincidence detection, using a ring of scintillators that pick up two photons (511 keV) upon a line of incidence. The scintillator detectors consist of high-density inorganic scintillator material which attenuates the high energy photons, by scintillation pathways to eventually emit light within the visible spectrum. A photodetector will convert the scintillation photon radiation into a measurable electrical signal and the origin of this signal can then be calculated to build up a picture for imaging.

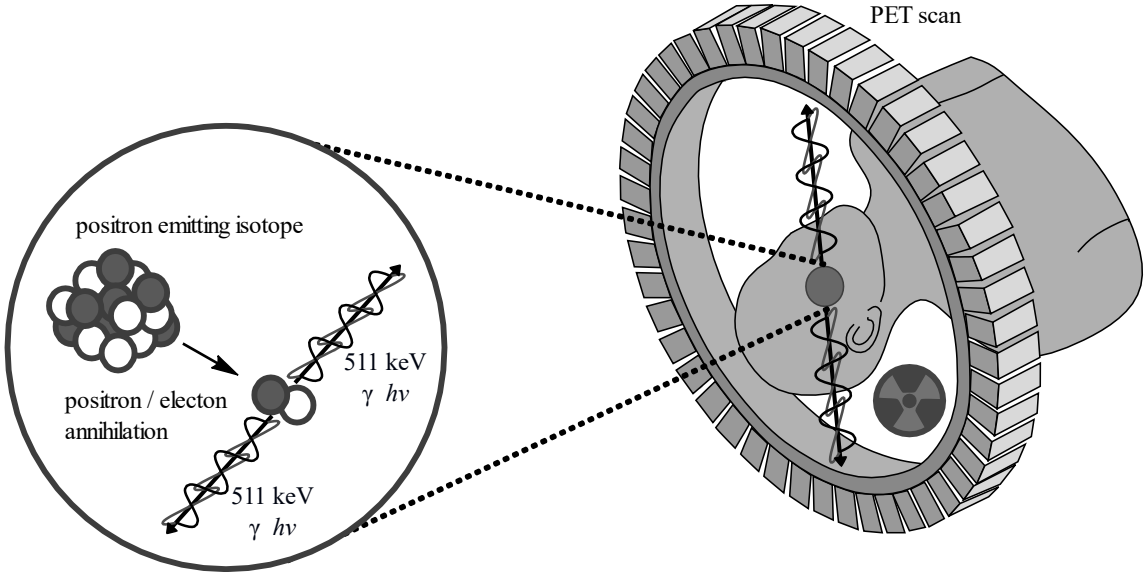

Figure 19 PET scanner for the diagnosis of malign tissues.

Evaluations on the impact of PET for patient management has shown a significant alteration in management of up to 40%, following imaging with PET.[89] Thousands of scans are taking place worldwide on a daily basis and PET is used for studying cancers, brain metabolism and cardiac function; decisions for avoiding inappropriate surgery or enabling curative resection have been made based on the unprecedented level of imaging detail possible using this technique.[90] PET imaging with ^{18}F-fluorodeoxyglucose (FDG) has been developed to show local glucose metabolism quantitatively. Because benign and malignant tumours metabolise glucose very differently, it possible to detect the degree of malignancy and evaluations for the likely effectiveness of following treatments with chemo- or radiotherapy can be assessed.[21]

1.7. Photodynamic therapy in combination with ionising radiation

Ionising radiation causes cell death mainly by direct double strand breakages (DSBs) and single strand breakages (SSBs) of the DNA structure. There are potential synergistic affects with PDT as damage to the cell and DNA from PDT will decrease the cell's ability

to repair damage by the often sub lethal single strand breakages induced from ionising radiation.[91]

Investigation into the order in which PDT and ionising radiation were administered in a combined treatment showed that a potent anti-tumour effect was independent of the order of treatment.[58] Potential strategies for combining PDT and radiotherapy include subsequent treatments, dual purpose photosensitiser/radiosensitisers and self-lighting photodynamic therapy (SLPDT) which makes use of scintillating nanoparticles to attenuate ionising radiation into visible light for a dual treatment.

1.7.1. Radiotherapy

Over 50% of all new cancer patients receive radiotherapy at least once during the course of their illness.[92] The last few decades have seen a marked improvement in precision of applied dose, whilst progressively reducing unwanted dose to surrounding tissues.[93] This has been achieved by improvements in advanced techniques such as intensity modulated radiotherapy (IMRT), image guided radiotherapy (IGRT), and stereotactic body radiation therapy (SBRT) which help to reduce the dose to unwanted tissues and reduce the size of the planning target volume (PTV).[93]

1.7.2. 3-Dimensional conformal radiotherapy (3D CFRT)

3D conformal radiotherapy (3D CFRT) uses 3D computed tomography (CT) to visualise the PTV, linking CT scans to treatment planning software allowing the PTV to be generated in 3D. The oncologist and dosimetrist will use 3D growth algorithm software paying consideration to the homogeneity of the dose distribution and the tumour cell density as well as the organs at risk (OAR) to make a final plan.[94]

1.7.3. Intensity modulated radiotherapy (IMRT)

IMRT is an advanced form of 3DCFT that uses techniques that modulate the beam intensity and geometric shape of the radiation beam, to produce concave shapes that fit around critical structures and avoid irradiation of OAR.

IMRT can be delivered with linear accelerators using static multileaf collimators (MLC) or dynamic MLCs, to modulate the beam intensity independently in different regions of each incident beam, to deliver the desired dose distribution to the PTV.[93] The ability of IMRT to deliver a varying dose to various target volumes within a single PTV, minimises dosimetric uncertainties and allows for the delivery of a higher dose than traditional radiation therapy methods could offer. This development of a more precise delivery of dose does, however, bring new concerns, regarding patient stabilisation, organ movement, tumour tracking, and treatment reproducibility,[95] driving the advancement of other areas of radiation oncology such as image guided radiation therapy (IGRT).

1.7.4. Multi-leaf collimators (MLC)

Typical MLCs have 20 to 80 pairs of leaves arranged to a fixed shape as shown in **Figure 20**. The field is shaped to conform to the shape of the tumour targeted, and reduces time and operational costs, compared with solid beam blocks.[96]

MLCs are made from tungsten alloys because of the high density of pure tungsten (19.3 gcm^{-3}). Due to the brittle nature of pure tungsten and the machinability of tungsten alloys, mixtures of nickel, iron, and copper are incorporated with only slightly decreased densities of up to 18.5 gcm^{-3}.

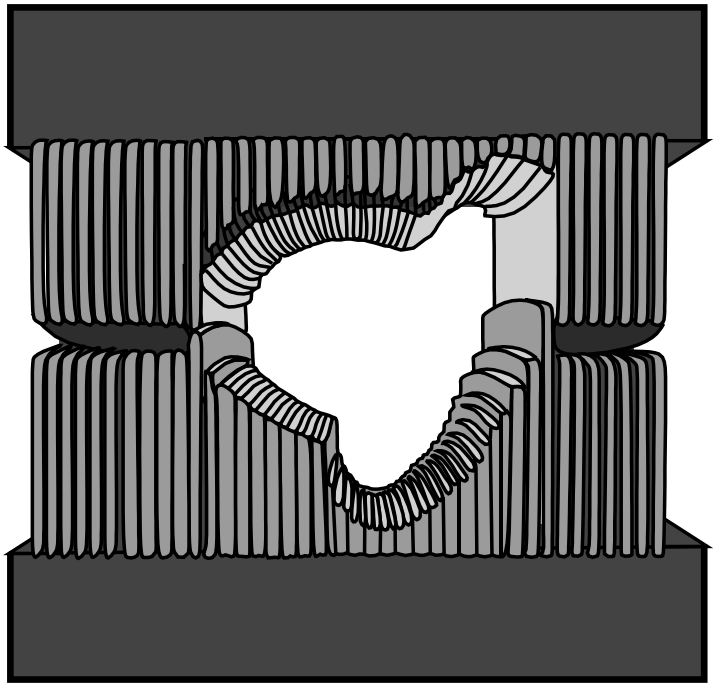

Figure 20 Varian Millenium multileaf collimator.

As well as replacing conventional blocking and field shaping, an important application of MLCs is to achieve beam intensity modulation. The motion of leaves during irradiation can be used to create a dynamic compensating filter for different beams used in IMRC.

1.7.5. Image guided radiotherapy (IGRT)

Tissues move with time, whether by the intratreatment movements of respiratory motion or peristalsis, or the day by day intertreatment changes such as tumour shrinkage. CT scans can be insufficient in showing these changes from a single snapshot. A lung tumour can experience movement due to respiratory motion, atelectasis, pulmonary oedema and tumour shrinkage all in one session. Restricting motion with harnesses and controlled breathing is employed to restrict motion however more dynamic approaches to accurately track motion are being developed to combat this problem.

Electronic portal imaging and digital reconstruction are basic forms of IGRT. More advanced techniques are being introduced in clinical practice to allow for target oriented positioning over patient oriented positioning.[93] Current patient oriented positioning includes techniques employing optical imaging devices with tattoos (markers on the skin). The patient will then employ the activated breathing technique (ABC) and treatment is delivered while the patient holds their breath. Respiratory gating can use CT scans by imaging devices on the linear accelerator, to trigger treatment when the image matches respiration correlated spiral CT planning images. These techniques can reduce dose to OARs but growing evidence suggests respiratory gating may be of limited benefit as the techniques are time consuming and increase treatment time.[94]

IGRT refers to all imaging techniques used to check that the treated volume actually matches the PTV. CT scans, now synonymous X-ray CT are the standard imaging modality; giving a 3D view of tumours and normal tissue as well as electron density data, enabling dose calculations. Magnetic resonance imaging (MRI) gives better detailed resolved images of soft tissues and increasingly CT-MRI is being used where possible. Positron emission tomography (PET) can give a biological imaging of tumours. Studies using 18-F fluoro-deoxy-D-glucose PET (FDG-PET) have been shown to highlight the proliferating areas of tumours.[97]

1.7.6. Stereotactic body radiation therapy (SBRT)

Stereotactic body radiation therapy (SBRT), also called stereotactic ablative radiotherapy (SABR) delivers high ablative doses of radiation in a small, highly pretomography and focused number of fractions.[98] Conventional radiotherapy delivers fractionations of 1.8 - 2.0 Gy compared with fewer fractionations of much higher radiation doses for SBRT.[99]

For lung metastases trials from Omiinaru *et al.* and Norihisa *et al.* gave median dose fractions as high as 48 Gy followed by 60 Gy.[100,101] This difference in dose may give a different mechanism of cell death. Apoptosis has been shown in mouse MCA129 fibrosarcoma and B16 melanoma cells after fraction doses of 15 - 25 Gy with a reaction for cell death, found to be mediated through the acid sphingomyelinase (ASMase) pathway, absent from conventional fractionated radiation.[102]

1.8. Self-lighting photodynamic therapy (SLPDT)

In order that PDT is effective, light of the corresponding wavelength to excite an electron in the highest occupied molecular orbital (HOMO), must be delivered efficiently to the photosensitiser. The limitations of this activation arise due to the optical window of tissue. Wavelengths longer than 800 nm do not provide enough energy to excite oxygen to its singlet state,[103] and wavelengths at and below this, have a maximum tissue penetration of around 10 mm, limiting the effectiveness of PDT to skin lesions, or introducing the requirement for invasive techniques using optical fibres, thereby removing the non-invasive potential that this treatment promises to offer.

To overcome this issue, Chen *et al.* introduced research using X-rays as an energy source for the activation of PDT in 2006.[104] In order for the activation of the photosensitiser from X-ray irradiation to work, a material mediator, capable of attenuating the energies from X-ray to UV and visible light energies is required as no photosensitiser directly activated by X-rays has yet been observed. This concept was coined self-lighting photodynamic therapy (SLPDT) and was proposed to work by coating porphyrins onto scintillating nanoparticles. Upon excitation with ionising radiation, the scintillating material undergoes scintillation mechanisms which culminate in the generation of visible light, which in turn activate the photosensitiser to produce cytotoxic $^1O_2$ for PDT (**Figure 21**).

The advantages outlined by Chen *et al.* in the 2006 paper for SLPDT over radiotherapy and photodynamic therapy alone are as follows:

1) Light delivery to the photosensitiser is not necessary.
2) Radiotherapy and photodynamic therapy are combined and activated by a single energy source.
3) Similar therapeutic results could be achieved by using a lower radiation dose.
4) The system is simpler and less expensive than PDT alone or with both therapies used in conjunction with one another.

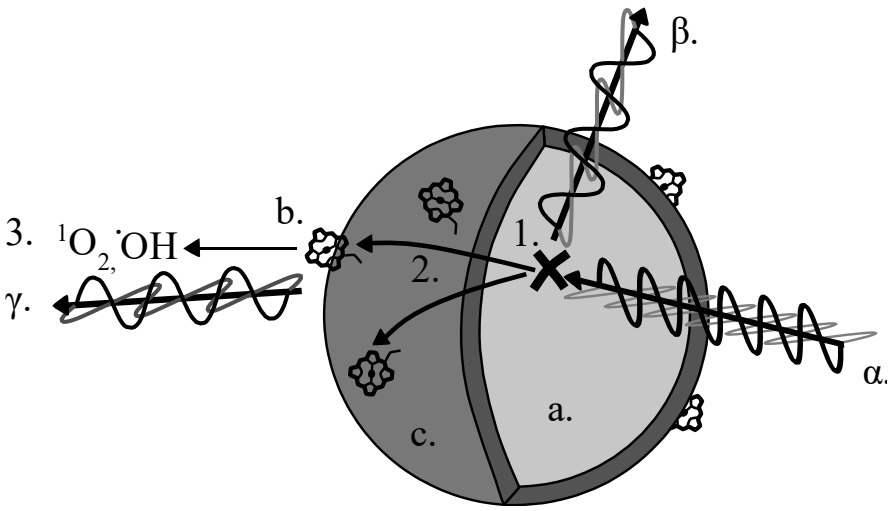

Figure 21 (α) Ionising radiation incident X-rays, interact with the high density, high z-value (a) inorganic nanoparticle. (1) Scintillation occurs here by a number of mechanisms and the incident light is attenuated and luminescence occurs in the visible region (β). This light can interact with a (b) photosensitiser that is conjugated to the (c) linker/shell of the nanoparticle, via (2) radiative transfer or Forster resonance energy transfer. Once activated the porphyrin will either (γ) luminesce or undergo (3) PDT.

1.8.1. Scintillation

Scintillation as a means of detecting radiation has been in use for over a century. In 1895 Rontgen discovered X-rays and a search began for luminescent materials capable of absorbing X-rays and converting the energy into a radiation able to blacken photographic

films, for use in medical radiography. Less than a year later $CaWO_4$ was put forward for use in the X-ray intensifying screens (**Figure 22**), decreasing the exposure times needed by 3 orders of magnitude, it was used for the next 75 years before being replaced by more efficient materials.

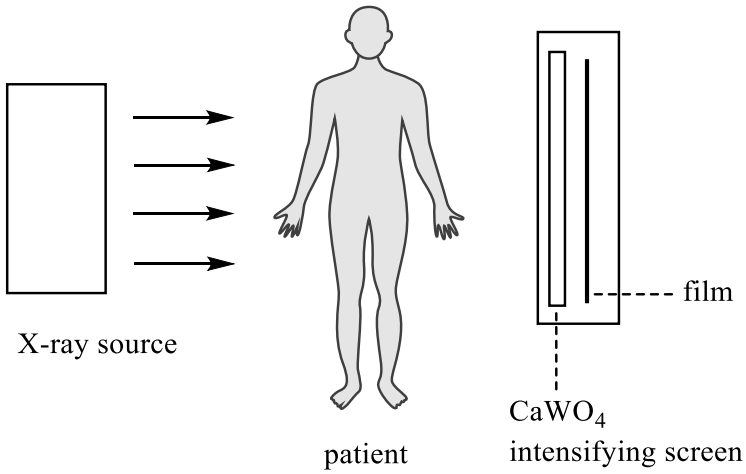

Figure 22 Representation of radiography system based on using an intensifying screen.

Scintillators have been used in cathode ray tubes, solid state lasers as well as medical diagnosis and high energy physics. Scintillation materials grown into large single crystals are capable of detecting α and γ radiation and are used for medical diagnostics in the detectors for positron emission tomography (PET), as well the 1200 crystals of $Bi_4Ge_3O_{12}$ (BGO) used in the detector for electrons and photons in the large electron-positron collider (LEP) machine at CERN[105] and later the compact muon solenoid (CMS) detector at CERN with over 80,000 $PbWO_4$ crystals of 25 cm length.[106]

A history of some of the most significant and important inorganic scintillators is shown in **Figure 23**. The scintillators shown are important either because they became widely used and commercially available or triggered the development of further materials.

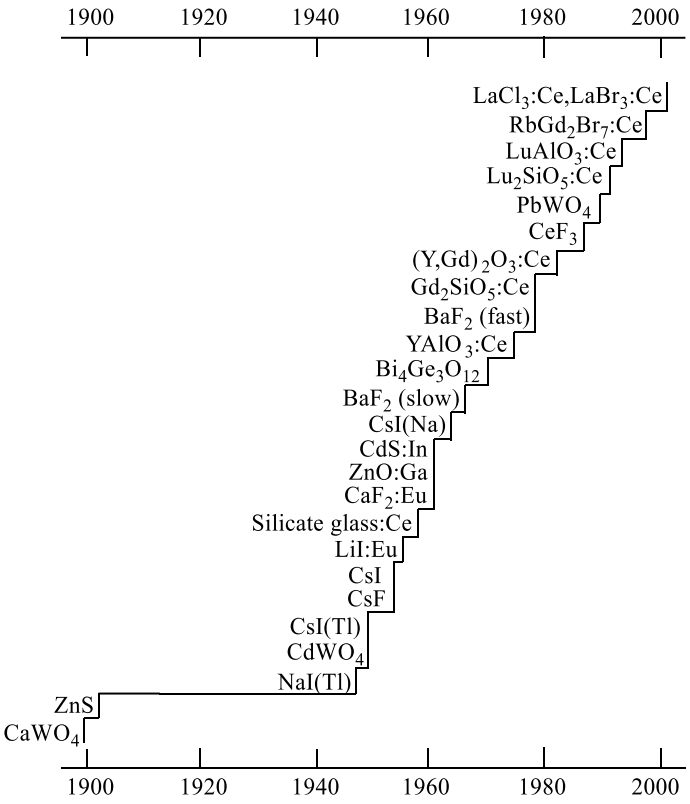

Figure 23 History of discovery of important scintillators of the 20th century.

1.8.2. Scintillation mechanism

It is important to note the difference between scintillation and luminescence, though the end effect may seem very similar, as H. A. Klasens, a pioneer in luminescent materials put it, "ultraviolet excitation compares to striking one key of the piano whereas X-ray excitation compares to throwing the piano down the stairs."[105] The mechanism of luminescence results from radiative relaxation by the emission of light following the direct excitation of an active ion from its electronic ground state to excited states.

Scintillation on the other hand arises from the energy loss of ionising radiation through matter, which occurs in several ways.

Three fundamental mechanisms of electromagnetic interaction occur between ionising radiation and matter (**Figure 24** and **Figure 25**):

(i) Photo-absorption,

(ii) Compton scattering,

(iii) electron-positron pair formation.

The cross section of interaction for these mechanisms is dependent on the energy of the incident photon and on the atomic number of the absorbing ions in the scintillator, as shown in **Figure 24**. Photo-absorption and Compton scattering are dominant at low to medium energies, with electron-positron pair formation beginning at 1.02 MeV, the at rest mass energy of an electron-positron pair.[107]

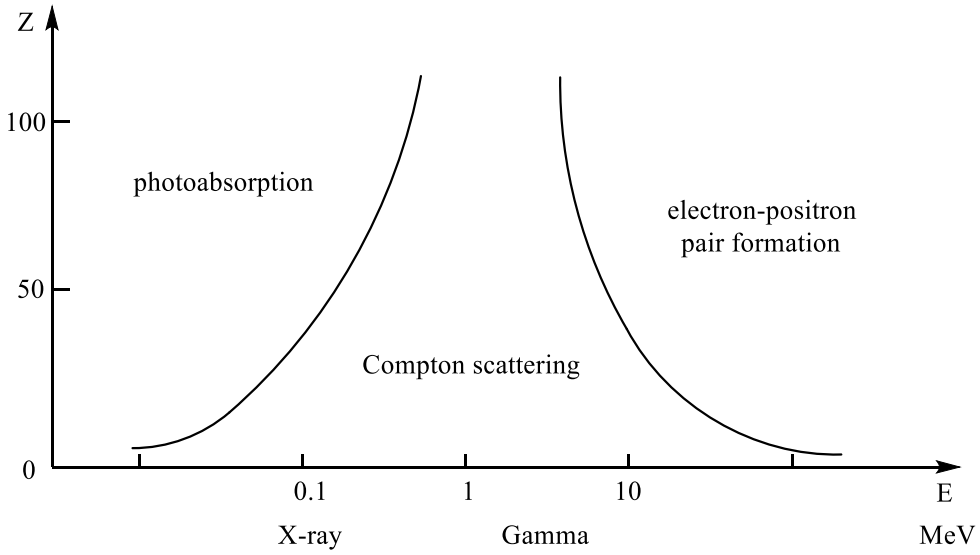

Figure 24 The cross-sectional effect of energy of incident photon (MeV) and the atomic number (Z) of the absorbing ion in the scintillator.

(i) A photon is absorbed by an ion and a subsequent (photo) electron is ejected from an inner core shell. The photoelectron gains the energy E_{pe} equal to the difference between the photon energy hν and the binding energy of the electron E_b. The energy E_b is in the form of, secondary X-rays, or Auger electrons, when the K-shell vacancy is filled. The X-rays are then absorbed in a second photoabsorption, so that all the incident photon's (hν) energy has been absorbed into the scintillator.

(ii) A photon interacts with an electron of an ion, transferring part of its energy to the electron. This results in a Compton scattered photon with energy hν' ($\nu > \nu'$) and a Compton electron of energy E_c. The Compton scattered photon may interact with further electrons, at different sites or may leave the scintillating material. Less scintillation radiation is produced in Compton scattering than photoabsorption due to this escape of energy.

(iii) High energy photons result in electron-positron pair production. The incident photon is absorbed and converted into an electron-positron pair. The positron annihilates on interacting with an electron, resulting in the emission of two photons of 0.511 MeV.

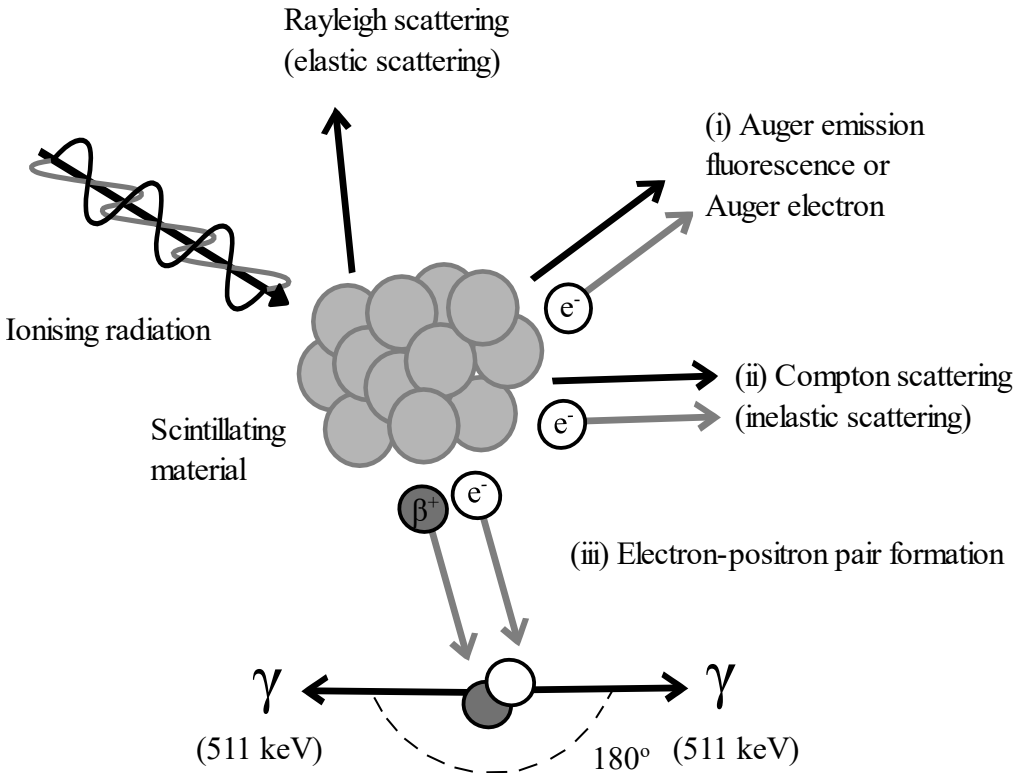

Figure 25 Depiction of the potential mechanisms of interaction of ionising radiation with matter. (i) Auger Emission or Photo-absorption (ii) Compton scattering (inelastic scattering), (iii) Electron-positron pair formation followed by an annihilation reaction.

If the energy of the incident electron is high enough, multiple Compton scattering events and electron-positron pair creations occur as their energy is progressively distributed to secondary particles of lower energy, forming an "electromagnetic shower". Resulting electrons from this shower that have energy in the keV range will couple with the electrons of the atoms in the lattice. These electrons excite the electrons of the occupied electronic states at different levels in the conduction band, forming an electron-hole pair. When the energy of the electron is above the ionisation threshold, free carriers can move freely through the crystal until they recombine on a luminescent centre or are trapped by a defect. If the energy of the electron is below the ionisation threshold, the electron and hole thermalise by intraband transitions and coupling to the lattice vibration modes until the electron relaxes to the bottom of the conductance band and the hole relaxes to the top

of the valence band. The most probable event at this stage is for the electron-holes pairs (e-h) to couple to a luminescent centre by an energy or charge transfer mechanism. There are four processes leading to scintillation in a medium shown in **Figure 26**.

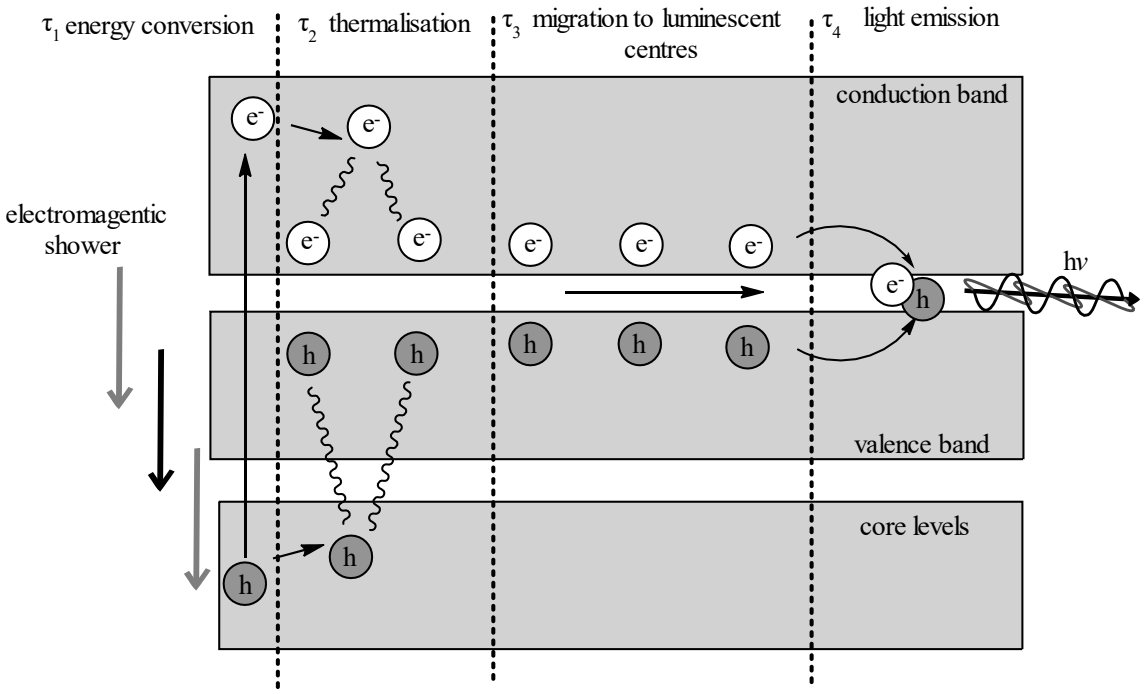

Figure 26 Basic scheme of the sequential stages leading to scintillation in a medium.

Energy conversion: The initial release of energy in a medium, leads to the electromagnetic shower previously discussed which leads to the formation of "hot" electrons and holes over a time $\tau_1 = 10^{-18} - 10^{-9}$.

Thermalisation: The e-h pair undergo inelastic scattering and thermalisation to the bottom of the conductance, and top of the valence bands, respectively over a time $\tau_2 = 10^{-16} - 10^{-12}$.

Migration to luminescent centres: The luminescent centres may become excited by hot electron impact after migration through the host material, transferring their energy to the luminescent centres over a time $\tau_3 = 10^{-12} - 10^{-8}$.

Light emission: Excited luminescent species return to the ground state via the emission of a photon or non-radiative processes. Radiative processes include e-h recombination of free and impurity-bound excitons, self-trapped excitons or core valence transitions[108] over a time $\tau_4 = 10^{-10}$.

1.9. A recent history of self-lighting photodynamic therapy (SLPDT) systems

Since the inception of SLPDT in 2006 there has been an increasing number of publications to further the concept, with a range of approaches attempting to further *in vivo* and clinical applicability in a science that is increasingly gaining momentum. There have been a number of excellent reviews[109–111] summarising the SLPDT conjugate systems of the last decade which are discussed in some detail below.

2006 - Chen *et al.* delivered the paper[104] introducing the concept of "self-lighting photodynamic therapy" utilising scintillating nanoparticles as mediators to deliver a treatment of porphyrin photosensitisers *in vivo*.[104] Nanoparticles including $LaF_3:Ce^{3+}$, $LuF_3:Ce^{3+}$, $CaF_2:Mn^{2+}$ $CaF_2:Eu^{2+}$, $BaFBr:Eu^{2+}$, $BaFBr:Mn^{2+}$, and $CaPO_4:Mn^{2+}$ were reportedly under investigation as potential light sources for a PDT system. The paper reported the use of folic acid as a potential targeting moiety and tetrakis (*o*-aminophenyl) porphyrin (TOAP) to conjugate to nanoparticles through cysteine via a peptide linker. Although limited data has been exhibited, the work has pioneered a new concept and ideas which have been built upon in the decade since this milestone publication.

Two important points were made in this publication:

i) Porphyrins absorb strongly around 420 nm (B or Soret band) with 4 other weak absorption peaks between 500 - 700 nm (Q-bands). Usually the Q-bands are targeted due

to the requirement for enhanced tissue penetration of light for activating the photosensitiser. A potential of these self-lighting nanoparticles means that a FRET between the nanoparticles' luminescence overlapping with the higher extinction coefficient of the Soret band could lead to a more efficient activation of the photosensitiser, not to mention a deeper tissue penetration offered by ionising radiation.

ii) Many of the nanoparticles under study displayed a persistent luminescence for tens of minutes afterwards. With long afterglow phosphors in existence with decay lifetimes ranging up to tens of hours, the potential of such systems could greatly reduce the radiation dose required to activate a PDT response that lasts substantially longer.

2008 - Chen *et al.*[112] followed up the previous publication with a more targeted look at a water soluble LaF_3:Tb^{3+}- meso-tetra(4-Carboxyphenyl) porphine (MTCP) nanoparticle conjugate system, investigating the energy transfer and singlet oxygen generation following X-ray irradiation. Folic acid was again used to target the folate receptors on tumour cells and was shown to have no effect on the quantum yield of singlet oxygen production in the nanoparticle-MTCP conjugate. The energy of X-rays used were 250 keV, with a dose rate of 0.44 G/min, the emission of anthracene dipropionic acid ADPA, (a singlet oxygen probe, the fluorescence of which is quenched upon reacting with singlet oxygen) was entirely quenched after 30 min (13.2 G), positively identifying the production of singlet oxygen. So far neither an *in vitro* nor *in vivo* study of this system has been made.

2011 - In this work an example of an X-ray activated nanoconjugate composed of yttrium oxide (Y_2O_3) nanoscintillator, a fragment of the HIV-1 TAT peptide, and psoralen has

been investigated,[113] in which nanoparticle-tethered psoralen has the potential to cross-link adenine and thymine residues in DNA. In this study, commercially available cubic phase Y_2O_3, a scintillator with an emission at approximately 400 nm due to recombination of self-trapped excitons at defect sites within the crystal lattice[114] was used. 2-chloroethylphosphonic acid ligands were attached to the nanoparticles and formed a thioether linkage to the HIV-1 TAT peptide.

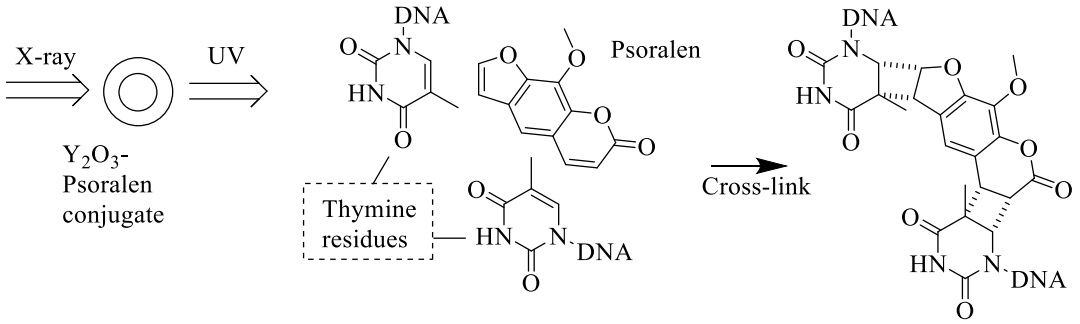

Figure 27 Mechanism of Psoralen cross linking with Thymine residues (recreated).[110]

The peptide has cell penetrating nuclear targeting and was bound to the psoralen. The Y_2O_3 nanoscintillators absorb X-rays and attenuate into UV light which in turn activates the free psoralen to cross link with adenine and thymine residues in DNA (**Figure 27)**, leading to apoptosis *in vitro* and immunogenic response *in vivo*. Results were modest but did show a dose dependant reduction in growth of PC-3 prostate cancer cells compared with controls without psoralen present, under 160 or 320 keV of 2 Gy dose. The potential of this treatment using psoralen to act independently of a ROS mechanism could give unique potential for treating deep seated tumours in hypoxic environments, however no *in vivo* studies have been carried out on this system to date.

2011 - Photofrin II was used in a solution for a co-location strategy, activated by X-ray induced luminescence of 20 micron diameter Terbium doped Gadolinium oxysulfide particles Gd_2O_2S:Tb.[115] Vitamin C absorbance was used to measure the generation of singlet oxygen in this system in which energies between 10 and 160 keV were utilised. No further *in vitro* or *in vivo* studies have been performed with this system.

2013 - In this study a Tb_2O_3 scintillating nanoparticle core (approximately 3 nm) was coated in a polysiloxane layer (Tb_2O_3@SiO_2) and conjugated with a 5-[4-carboxyphenyl]-10,15,20-tri-(4-pyridyl) porphyrin photosensitizer (**Figure 28**).[116]

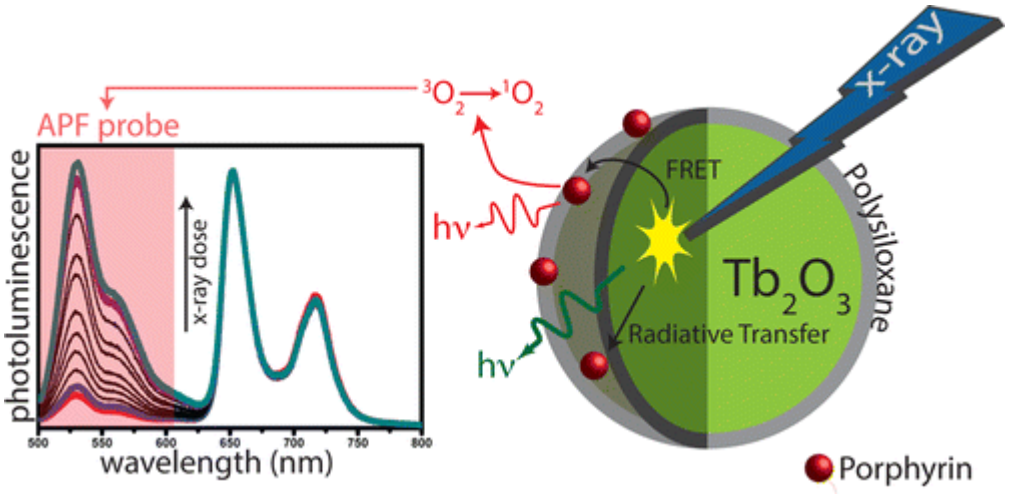

Figure 28 Schematic depicting nanoscintillator photosensitiser conjugate and energy transfer upon X-ray irradiation.[116]

The energy transfer mechanisms were demonstrated by UV excitation of a pulsed laser fixed at 300 nm with time resolved spectra recorded at "short times" t_0 = 0 ns and "long times" t_0 = 500 ns. The fast response corresponded to a direct excitation of the PS with the laser, and the slow component was from Tb^{3+} energy transfer. A study of fluorescence decay measurements of the terbium emission at 545 nm suggested Forster resonance energy transfer (FRET) in the ScNP-PS conjugate. Singlet oxygen ($^1O_2$) generation was observed using two different probes, singlet oxygen sensor green (SOSG) and 3-*p*-

(aminophenyl) fluorescein upon irradiation from a tungsten anode of X-rays 44 keV excitation 5.4 mG/s. No further *in vitro* or *in vivo* experiments have been performed with this system to date.

2014 - In this study cerium doped lanthanum fluoride ($LaF_3:Ce^{3+}$) nanoparticles were encapsulated into poly($_{D,L}$-lactide-*co*- glycolide microspheres (approximately 2 μm diameter),[117] along with protoporphyrin IX (PPIX). The emission band of $LaF_3:Ce^{3+}$ has a strong green emission at around 520 nm, from the metal-to-ligand charge transfer states, and not a d-f transition of the Ce^{3+}.[118] This emission overlaps with one of the weaker absorption bands (Q-bands) within PPIX. Upon irradiating with X-rays of 90 keV, energy transfer from the $LaF_3:Ce^{3+}$/DMSO nanoparticles to PPIX was shown to occur as well as the generation of singlet oxygen. Upon irradiating $LaF_3:Ce^{3+}$/DMSO/PPIX/poly $_{D,L}$ - lactide-*co*-glycolide microspheres (which were shown to have mild cytotoxicity) oxidative stress, mitochondrial damage and DNA fragmentation were shown to occur on PC3 prostate cancer cell lines.

2015 - In an attempt to improve Forster resonance energy transfer (FRET) between scintillator and PS, the authors synthesised mesoporous LaF_3:Tb nanocrystals which have an emission at 544 nm from the Tb^{3+} $^5D_4 \rightarrow {}^7F_5$ transition, with Rose Bengal (RB) photosensitiser which was used due to its good spectral (**Figure 29**) match at 549 nm.[119] Upon preparation of the mesoporous nanoparticles by a facile hydrothermal route, RB was loaded into the nanoparticle pore system (**Figure 29**).

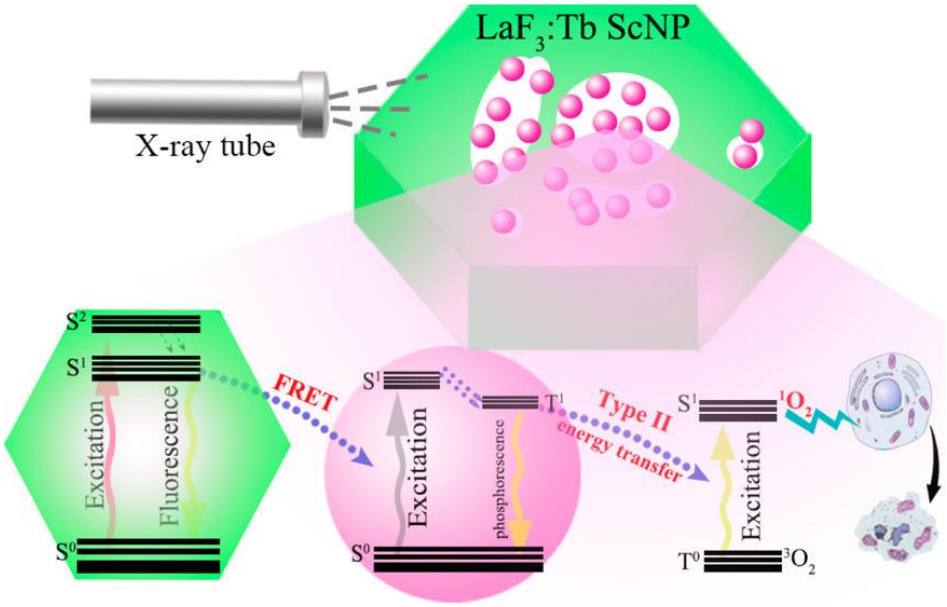

Figure 29 Schematic depiction of mesoporous LaF_3:Tb nano-conjugate loaded with Rose bengal PS and X-ray stimulated deep PDT.[119]

This system is designed to possess advantages including well defined nanostructure, optimised scintillating luminescence, good spectral overlap, simple drug loading approach, high FRET efficiency, good water solubility, and ultra-stable colloidal stability. Steady state spectra and fluorescence delay dynamic analysis was used to demonstrate a high FRET efficiency of this system of up to 85%. Luminescence properties of the nanoparticles' system were obtained under UV and X-ray 75 keV irradiation; however further testing was carried out with use of UV irradiation only. $^1O_2$ oxygen generation was determined by a DPBF probe and compared with RB alone to attribute the increased relative $^1O_2$ generation to the nano-conjugate system, which indicates suitability for X-ray irradiation, though this was not confirmed experimentally.

2015 - In a study by the same group hexagonal phase LaF_3:Tb nanoparticles of approximately 50 nm diameter were synthesised by a simple hydrothermal route.[120] As previously, doping with Tb^{3+} gave the strong green emission 544 nm from the Tb^{3+} $^5D_4$-

$^7F_5$ transition. The positively charged nanoparticles were coated with an adsorbed polyvinylpyrrolidine (PVP) (**Figure 30**) molecule to act as a coupling agent and stabiliser to give higher dispersity and stability in a range of polar and non-polar solvents.[121] Siloxane layers of tetraethyl orthosilicate (TEOS) and (3-aminopropyl)triethoxysilicate (APTES) were deposited onto the surface by hydroxylation reactions using sodium hydroxide (**Figure 30**). A thin silica shell was formed that could be adjusted in thickness from 3 nm to 45 nm by changing the amount of TEOS used during deposition, this is an important factor when considering that FRET typically requires a distance of less than 10 nm between donor and acceptor.

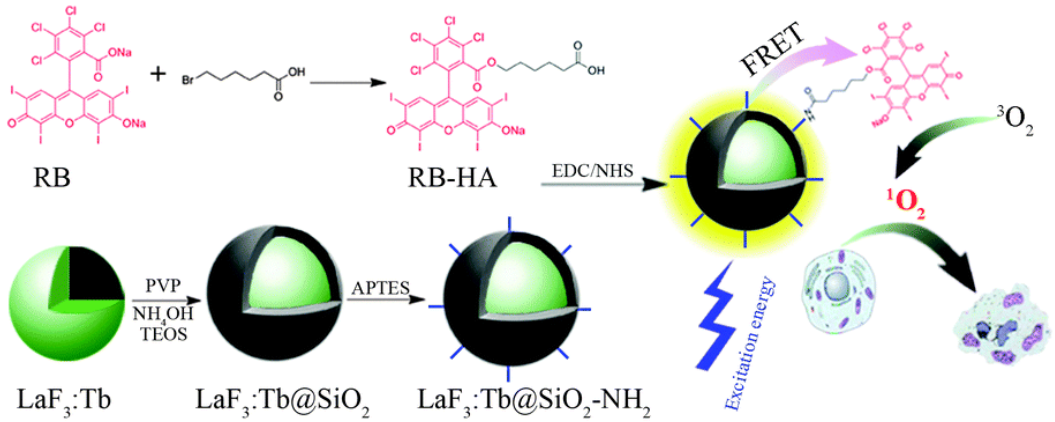

Figure 30 Schematic depiction of LaF_3:Tb@SiO_2-RB nano-conjugate construction and X-ray stimulated deep PDT.[120]

It was observed that there was an unfavourable influence of PVP and silica coating on the luminescence intensity of these nanoparticles, questioning the suitability of this type of conjugation method. However, the X-ray attenuation ability of the conjugate was measured, and *in vivo* X-ray imaging was performed on tumour bearing mice. Following intra-tumoural injection of 50 µL of the LaF_3:Tb scintillating nanoparticles of concentration 20 mg mL^{-1}, the signal intensity in the mouse was found to be greatly

enhanced. The measured CT values of the scintillating nanoparticle (ScNP) dispersion were found to be higher than the commercially available iodine-based clinical CT contrast agent Ultravist 300, which gives the potential of these nanoscintillators to be ideal contrast agents in tumour diagnosis as well as the potential for treatment by X-ray activated PDT. As promising as these results are the LaF_3:TB^{3+}-RB conjugate was again only shown to generate singlet oxygen using UV irradiation and further studies are required to validate this system for PDT effectiveness by X-ray irradiation.

2015 - This work focusses on increasing PS delivery to the cell nucleus by use of GdEuC12 micelles incorporating hypericin (Hyp) photosensitiser within the hydrophobic core (**Figure 31**).[122]

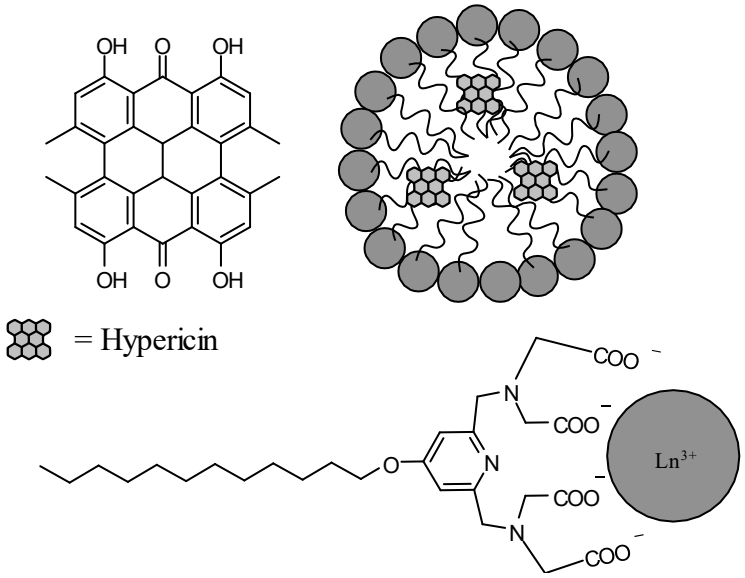

Figure 31 Schematic representation of the Hyp-GdEuC12 micellar particles and respective structures, utilising the hydrophobic loading strategy.[122]

The micelles had an emission peak at 618 nm, corresponding to the Eu emission characteristics, with good spectral overlap for the absorption band of Hyp, implying an efficient energy transfer from NP to PS could be achievable. Using UV luminescence, fluorescence images of HeLa cells treated with Hyp-GdEuC12 micelles under 395 nm

excitation revealed a strong fluorescence located in the nucleus, compared with those treated only with GdEuC12 micelles or Hyp individually. This nuclear localisation of PS is of particular interest as the cell nucleus is very sensitive to $^1O_2$ damage compared with other organelles,[123] which should result in enhanced toxicity and apoptosis. The study also showed the generation of singlet oxygen following irradiation with X-rays with a maximum between 10 and 20 keV, using a methoxyvinylpyrene (MVP) probe which generates 1-pyrenecarboxaldehyde upon interaction with singlet oxygen. A potential benefit to this unique system is the versatility of lanthanides and photosensitisers that could be incorporated. The work also alludes to the potential for an MRI-guided X-ray triggered PDT therapy due to paramagnetism of Gd^{3+} and the ease with which different lanthanides can be included.

2015 - An example of $SrAl_2O_4:Eu^{2+}$ (SAO) nanoparticles coated in mesoporous silica loaded with merocyanine 540 (MC540) photosensitiser has been reported (**Figure 32**).[124] X-ray induced luminescence of the SAO NPs gave an emission peak at 520 nm which overlapped with the excitation wavelength of the photosensitiser MC540, which was loaded through overnight incubation into the mesoporous $SAO@SiO_2$ nanoparticles.

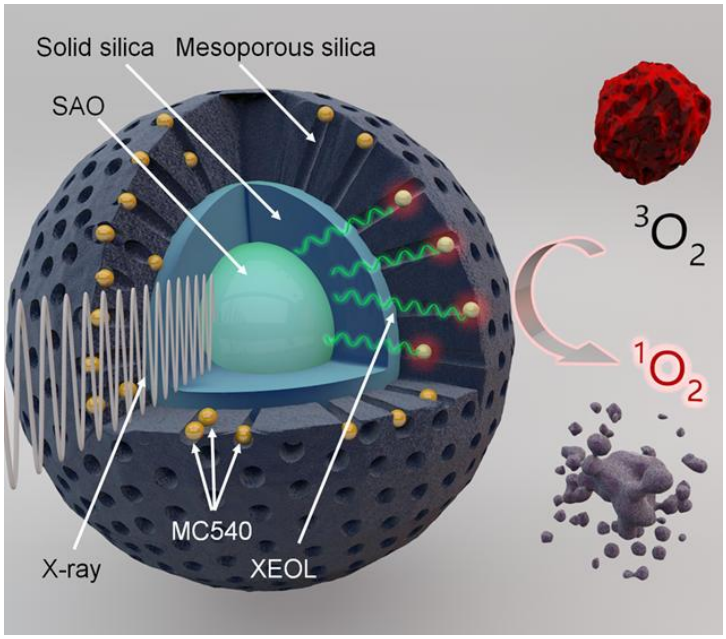

Figure 32 Schematic depiction of nanoconjugate construct of SAO nanoparticles coated with a solid and mesoporous layer of silica into which the MC540 PS is loaded.[124]

Singlet oxygen sensor green (SOSG) was used as a $^1O_2$ probe, a compound which undergoes a structural change in the presence of singlet oxygen and accompanied by an increase of fluorescence (ex/em 504/525 nm). SOSG was used to study $^1O_2$ generation under X-ray irradiation (50 Kev) of both suspensions and then cells (U87MG). Both experiments showed that $^1O_2$ is generated only when all three components MC540, SAO, and X-rays are present. The toxicity of the cells was also investigated correlating with $^1O_2$ generation and further confirmed with an MTT assay, which found a 62.0 ± 9.0% viability drop in cells treated compared with the controls. *In vivo* studies were also performed on 30 U87MG tumour bearing mice randomised to receive the following treatments:

(1) M-SAO@SiO_2 nanoparticles + X-ray,

(2) M-SAO@SiO_2 nanoparticles only,

(3) SAO@SiO_2 nanoparticles + X-ray,

(4) M-SAO@SiO_2 nanoparticles only,

(5) PBS + X-ray, and

(6) PBS only.

Nanoparticles were intratumourally injected and irradiated with 0.5 Gy (50 kV) with a beam diameter of 6 mm. After 12 days the control mice had a relative change in tumour volume (V/V_0) between 700 and 800% for all groups, contrasted with an average tumour reduction of 60.2 ± 6.9% for group (1) M-SAO@SiO_2 nanoparticles + X-ray. All animals were sacrificed on day 16 and organs were evaluated by ICP-MS analysis for remaining Sr contents, which were found to not be above the background due to the hydrolytic nature of the $SrAl_2O_4$:Eu_2+ nanoscintillator, which is reduced to low toxicity ions and cleared from the body within two weeks.

2015 - The combination of a scintillating nanoparticle and semiconductor was devised for ionising radiation activated PDT with a diminished oxygen dependence.[125] PDT typically employs photosensitisers which when activated by light will react with ground state molecular oxygen $^3O_2$, to give cytotoxic singlet state oxygen $^1O_2$, through a type II pathway, causing damage to targeted neoplastic tissues. Unfortunately this makes PDT highly oxygen dependant and drastically decreases the efficacy of treatment of hypoxic tumour tissues,[126] which is also a problem area for radiotherapy. Some semiconductors, for this work ZnO, are capable of reacting with water to give the hydroxyl radical (·OH) reactive oxygen species. Upon light activation a hole (h^+) in the valence band created from an excited electron to the conduction band, becomes a highly oxidising species at the surface of the material, and generating a hydroxyl radical with water.[127]

Octahedral $LiYF_4:Ce^{3+}$ nanoparticles of an average diameter 33 nm were prepared with an X-ray excited emission in the UV at 305 and 325 nm corresponding to a transition from low 5d configuration in the Ce(III) ion to the $^2F_{5/2}$ and $^2F_{7/2}$ levels respectively. Importantly this emission corresponds with the absorbance band of the ZnO semiconductor, which is required for an efficient transfer of energy. The nanoparticles were coated in a silica shell with incorporated thiol groups for direct attachment to the ZnO nanoparticles by strong metal-sulphur bonds. The surface was further modified with polyethylene glycol (PEG) to increase bioavailability and colloidal stability (**Figure 33**).

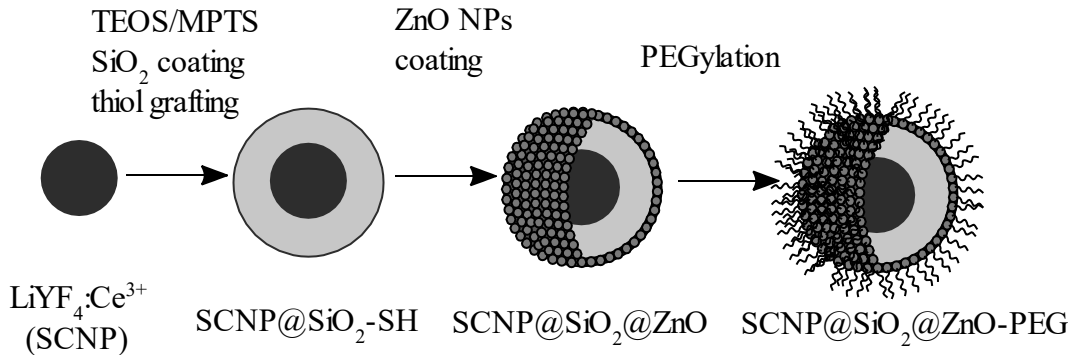

Figure 33 a) Schematic of ScNP@SiO_2@ZnO-PEG nanoconjugate construction.[125]

Bleaching of methylene blue (MB) was used as a ·OH probe[128] to compare the ROS (·OH) yield of the $LiYF_4:Ce^{3+}$@SiO_2-ZnO conjugate under irradiation and control. Upon a positive result, the experiment was repeated in living HeLa cells both normoxic (21% O_2) and hypoxic (2% O_2), this time using the non-fluorescent molecule 2',7'-dichlorofluorescein diacetate (DCFH-DA), which oxidises to a fluorescent product upon interaction with ROS. The cells were irradiated with (3 Gy) and showed significant reductions in cell viability for the conjugate treated and irradiated groups compared with controls, which correlated with the generation of ROS shown in the experiment. Finally,

preliminary *in vivo* experiments were performed with X-ray irradiation (8 Gy) where tumour growth rate was almost completely inhibited after 15 days compared with a 5 times relative tumour increase in the control experiments.

2016 - This work utilised CeF_3 nanoparticles synthesised via co-precipitation reaction, giving an average size of 9 ± 2 nm.[129] Verteporfin (VP), a benzoporphyrin derived clinically available photosensitiser (trade name Visudyne^{TM}), with good spectral overlap with the CeF_3 emission, was attached by electrostatic interaction, relying on the positive charge of CeF_3 nanoparticles and negatively charged VP (**Figure 34**).

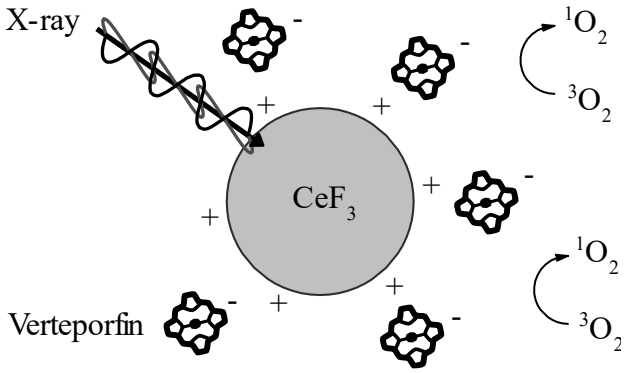

Figure 34 Schematic depicting the electrostatic conjugation of Verteporfin (VP) with CeF_3 nanoparticles.[129]

Singlet oxygen sensor green (SOSG) was used to determine $^1O_2$ generation of a CeF_3-VP conjugate which was estimated to have 31 VP molecules attached, using 8 keV X-ray irradiation. Based on these results the $^1O_2$ yield was determined to be 0.79 ± 0.05. This value was linearly extrapolated to predict the $^1O_2$ generation achievable using clinical doses 6 MeV (high energy) and 30 keV (low energy) to conclude the systems efficiency would be comparable with traditional PDT treatment irradiated at visible wavelengths. The assumptions made in this estimation do not take into account that the stopping power

of 9 nm nanoparticles would likely be nowhere near what would be required to interact with energy of this level. A cell viability test (Panc-1) was reported using 6 MeV radiation, using the same CeF_3-VP conjugate which found most of the cells (> 65%) to still be alive. This is not surprising as only the very lowest energy photons would have been able to interact with a cell culture and the majority of energies would have passed straight through without interaction.

Table 1 Timeline of X-ray scintillators employed for SLPDT.

Year	Nano scintillators	PS	Conjugation	X-ray doses	In vitro	In vivo	ref
2006	$LaF_3:Ce^{3+}$, $LuF_3:Ce^{3+}$, $CaF_2:Mn^{2+}$ $CaF_2:Eu^{2+}$, $BaFBr:Eu^{2+}$, $BaFBr:Mn^{2+}$, $CaPO_4:Mn^{2+}$	TOAP	Covalent	None	None	None	[104]
2008	$LaF_3:Tb^{3+}$	MTCP	Covalent	120 keV	None	None	[112]
2011	Y_2O_3	Psoralen	Covalent	160 and 320 kVp	PC3	None	[113]
2011	$Gd_2O_2S:Tb$	Photofrin II	Colocation	120 keV	Human glioblastoma	None	[115]
2013	Tb_2O_3	Porphyrin	Covalent	UV only	None	None	[116]
2014	$LaF_3:Ce^{3+}$	PPIX	Pore loading	90 keV	PC3	None	[117]
2015	$LaF_{3:}Tb^{3+}$	RB	Pore loading	2-10 keV	None	None	[110]
2015	$LaF_3:Tb^{3+}$	RB	Covalent	None	None	Tumour model	[120]
2015	GdEuC12 micelles	Hyp	Physical loading	10-20 keV	HeLa	None	[122]
2015	$SrAl_2O_4:Eu^{2+}$	MC540	Pore loading	50 keV	U87MG	U87MG mice	[130]
2015	$LiFY_4:Ce^{3+}$	ZnO	Coating	8 Gy	HeLa	Tumour model	[131]
2016	CeF_3	VP	Physical loading	8 keV, 6 MeV	Panc-1	None	[129]

2. Synthesis and biological evaluation of an F^{18} radiolabelled water-soluble porphyrin for a PDT/PET theranostic agent.

Work in the chapter has been published.[132]

2.1. Introduction

2.1.1. Theranostics

The term "theranostic" usually refers to a single compound that combines both the modalities of therapy and diagnostic imaging into a single unit and has been primarily developed for the treatment of neoplastic conditions. It is a concept still in its infancy, the term first attributed to John Funkhouser[133] in 2002, when describing his company's business model. The appeal of developing drugs that are theranostic in nature is highlighted by the fact that they negate the need for multiple agents to be administered individually, which might otherwise be prone to uptake variability. Real-time localisation of the therapeutic agent, pharmaco-kinetic and dynamic behaviour and imaging of the target before, during and after treatment all become possible. This opens the door to the possibility of a more personalised approach to therapy and away from a one-size fits all approach.

2.1.2. Theranostic porphyrins

Therapeutic strategies utilised include nucleic acid delivery, chemotherapy, hyperthermia (photothermal ablation), PDT and radiation therapy.[77] These strategies have been combined with imaging strategies including MRI, PET, SPECT and fluorescence. Porphyrins have a well-documented history of therapeutic action within the field of photodynamic therapy[21,37,74,134] fulfilling the therapeutic modality requirement of a theranostic agent. Additionally, porphyrins have demonstrated efficacy as imaging agents

due to their inherent fluorescence, and their ability to chelate metals suitable for PET, SPECT and MRI.[21,67–74] For this reason porphyrins offer an exciting potential in the emerging field of theranostic agents, especially as they have well established synthetic pathways for conjugation to targeting moieties or functionalisation for increased water solubility.[75,76]

2.1.3. Positron emission tomography

Magnetic resonance imaging (MRI), X-rays and ultrasound, all give structural and anatomical data, but are limited in providing metabolic information, restricting clinical practice to structural abnormalities. PET is an interesting modality for combining with PDT as it is well suited for oncology and whole-body imaging, offering highly resolved images of physiology and pathophysiological activities *in vivo*. Both single-photon emission computed tomography (SPECT) and PET are capable of imaging metabolic processes in patients. Probes can be designed tissue or receptor specific, giving detail for a target structure or biological process.

The majority of strategies for combining PDT with PET have utilised the ability of porphyrins as a chelating agent for radionuclides such as ^{64}Cu, ^{68}Ga, ^{140}Nd and ^{166}Ho.[67–73] This strategy limits the therapeutic modality of the photosensitiser, as proximity to a paramagnetic metal quenches the π^* excited states of the photosensitiser. The phenomenon occurs due to spin-orbit coupling perturbations stemming from orbital overlap between porphyrin excited state orbitals (π^*) and metal dπ orbitals, and can be demonstrated by the comparison of excited singlet and triplet lifetimes of ZnTPP (τ_s = 2.0 ns, τ_T = 1.2 ms) and CuTPP (τ_s = < 10 ps, τ_T = 25 ns).[135]

PET is also capable of utilising positron-emitting radionuclide isotopes of low atomic mass (C, N, O and F) (**Table 2**),[136] which are naturally present in biomolecules and hence strategies can be designed to attach to biomolecules without affecting biological activity.

One important consideration in radiochemistry is the half-life of the radionuclide in question for the purposes of imaging, as the target requires synthesis, purification and analysis before administering. Generally, it is considered that these steps should be achieved within 3 half-lives of the radionuclide being used in order that it remains viable for the purposes of imaging.

Table 2 Common low atomic mass PET radionuclides, half-lives, nuclear reaction, target, product and decay products.

Radionuclide	Half-life, $t_{1/2}$ (min)	Nuclear reaction	Target	Product	Decay product
^{11}C	20.4	$^{14}N(p,\alpha)^{11}C$	$N_2(+O_2)$ $N_2(+H_2)$	$[^{11}C]CO_2$ $[^{11}C]CH_4$	^{11}B
^{13}N	9.97	$^{16}O(p,\alpha)^{13}N$	H_2O H_2O + EtOH	$[^{13}N]NOx$ $[^{13}N]NH_3$	^{13}C
^{15}O	2.07	$^{15}N(d,n)^{15}O$	$N_2(+O_2)$	$[^{15}O]O_2$	^{15}N
^{18}F	110	$^{18}O(p,n)^{18}F$	$[^{18}O]H_2O$	^{18}F	^{18}O

2.1.4. Fluorine-18

Fluorine-18, often referred to as the "radionuclide of choice" for PET imaging agents, offers a compelling potential for investigation. There are very few examples of porphyrin-based photosensitisers radiolabelled with fluorine-18 in the literature. Whilst some methods describing the radiolabelling of a porphyrin[137] and a phthalocyanine[138] do appear, both come with limitations; retention of cytotoxic action of the photosensitiser

after radiolabelling was not investigated. As well both methods required extended reaction times and harsh conditions, limiting the window of activity, while radiochemical yields achieved were less than 25%. For these reasons, bioconjugation utilising the Copper (I) Catalysed Alkyne-Azide cycloaddition reaction (CuAAC)[139–141] to a fluorine-18 radiolabelled chain seems to offer a solution. CuAAC reactions offer a fast and high yielding opportunity to radiolabel water soluble porphyrins with minimal impurities.[75]

2.1.5. Porphyrin synthesis

There are three major synthetic methods for producing *meso*-substituted porphyrins. The Rothemund reaction was first described in 1935 for the synthesis of porphine and tetramethylporphyrin[142] and was also extended to include tetraphenylporphyrin.[143] The Rothemund conditions were based on the premise that the stability of the aromatic porphyrin would allow it to form in greater quantities than other possible products through the cracking of the initially formed adducts of benzaldehyde and pyrrole at high temperatures.[144] The yields were low and the conditions harsh, preventing any but the most robust substituted benzaldehydes from being utilised as starting materials.

Adler and Longo modified the Rothemund method; refluxing pyrrole and benzaldehyde in propionic acid for 30 minutes, at atmospheric pressure and open to the air, allowing oxidation of the intermediate porphyrinogen.[145] The yield was considerably better (20%) and these milder reaction conditions allowed for a much wider range of substituted benzaldehyde starting materials. However, the conditions of this method still prevent the use of sensitive aldehyde starting materials due to the high temperatures and acidic conditions.

The Lindsey method was first described in 1987[144] as a milder synthesis of porphyrins, allowing for a much larger range of sensitive aldehydes to be incorporated. The method is centred around the hypothesis that, prior to oxidation, tetraphenyl porphyrinogen should be the favoured product when benzaldehyde and pyrrole are condensed under the correct conditions, without the need for high temperatures due to the reactivity of benzaldehyde and pyrrole. These milder conditions are compatible with an unprecedented variety of benzaldehydes, with yields of 30 - 40% routinely obtained.

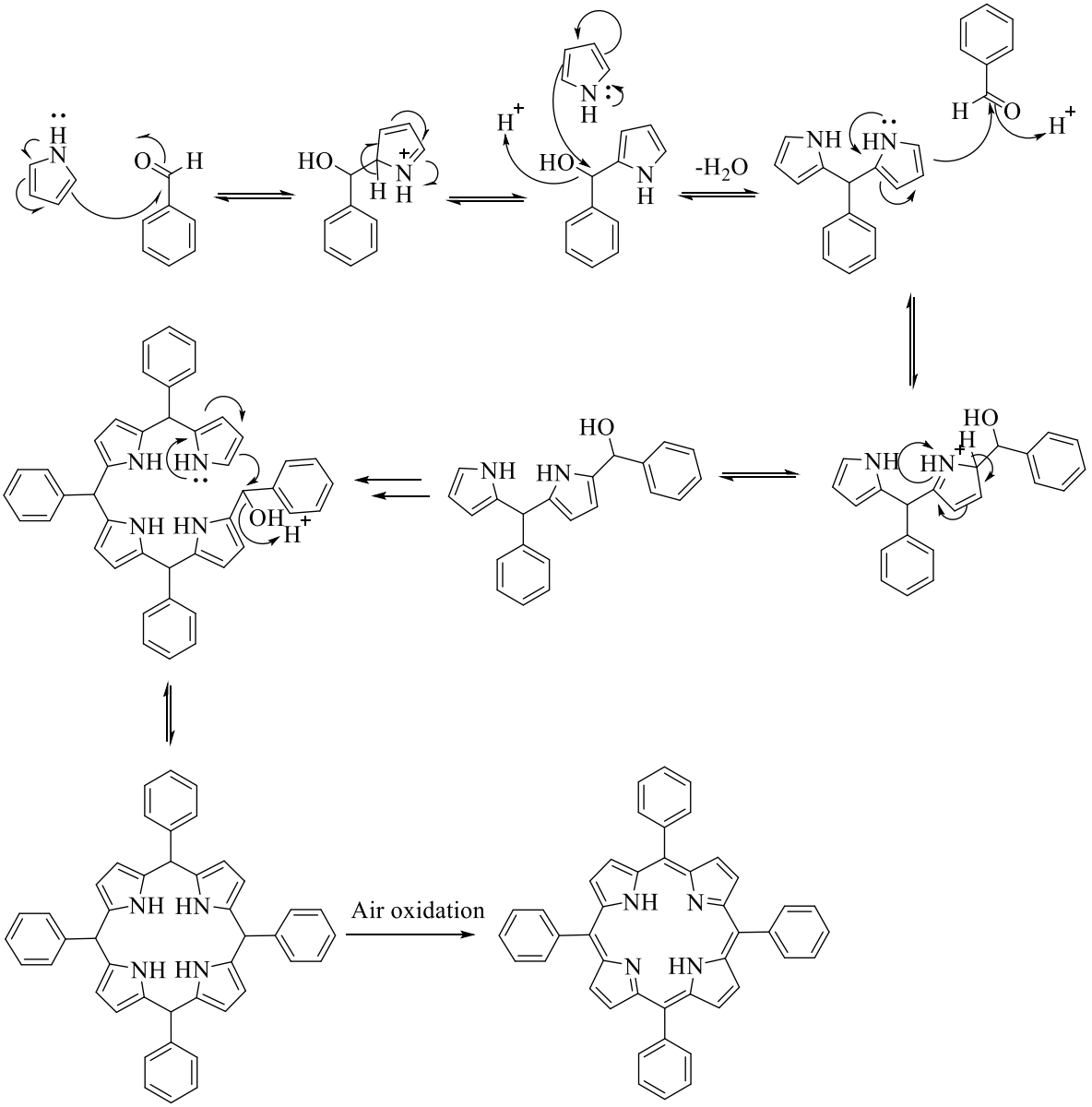

Figure 35 Mechanism of synthesis of tetraphenylporphyrin synthesised by Adler-Longo.

Although the Lindsey method may appear to be the best method for porphyrin synthesis, the low reactant concentrations required, limit the scalability of the method. For this reason, the Adler-Longo synthesis method was used to synthesise porphyrins as it is a more facile and scalable method. Although the harsh reaction conditions of the Adler-Longo method prevent the use of aldehydes bearing unprotected azide functional groups, synthesis using aldehydes bearing robust functional groups followed by subsequent derivatisation can be performed to accomplish the desired porphyrins bearing clickable groups.

The synthesis of the tetra *meso*-substituted porphyrin using the Adler-Longo synthesis occurs *via* a number of oxidation and termination reactions (**Figure 35**) eventually forming the porphyrinogen that is then oxidised to produce the desired porphyrin structure. The porphyrin is therefore only one component of a mixture of linear and cyclic ring structures, hence the relatively poor yields, usually below 10%.

When a condensation of aldehyde and pyrrole is undertaken, a porphyrin with four identical *meso*-substituents is produced. In order to produce porphyrins that are both hydrophilic and contain a click functionality for conjugation, this work utilises a mixed aldehyde condensation reaction (**Figure 36**) to afford an asymmetric porphyrin of 3:1 *meso*-substitution.

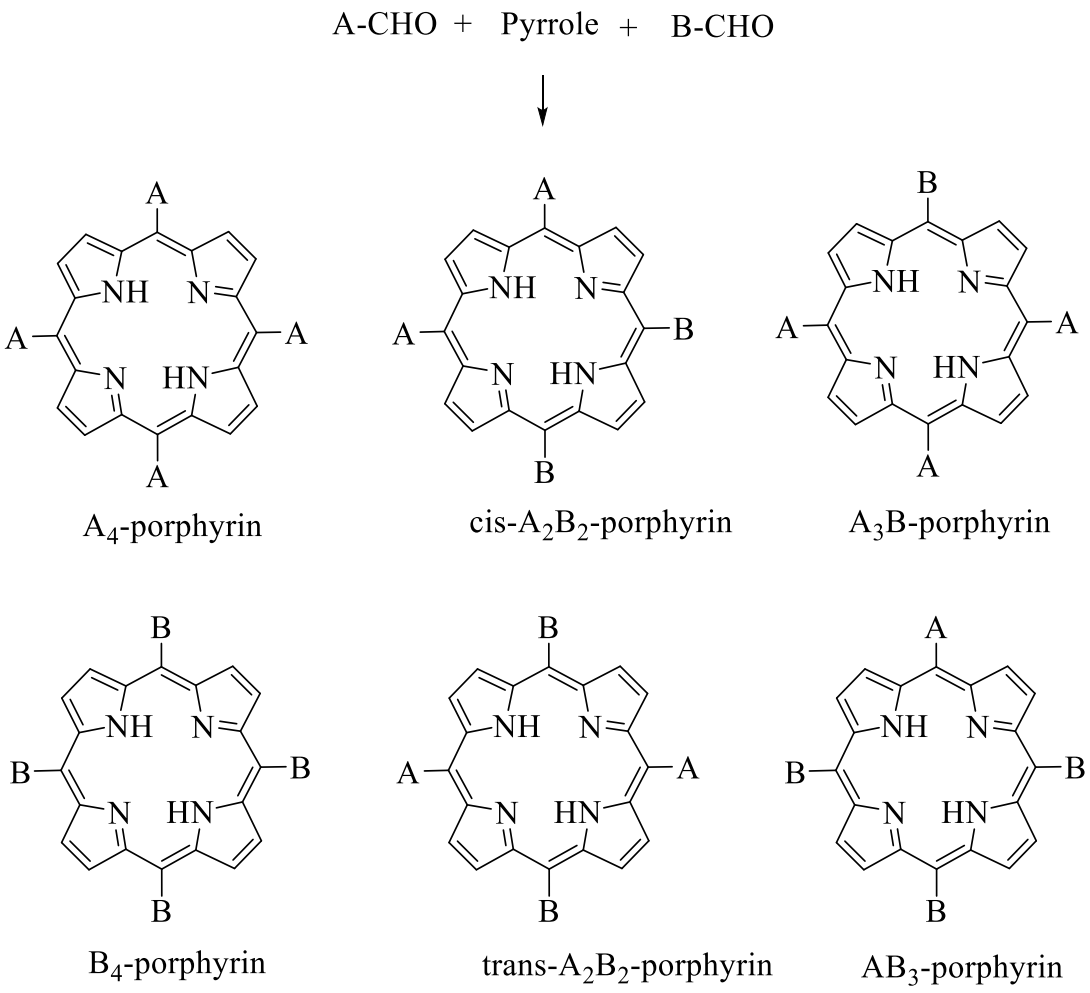

Figure 36 The six porphyrins formed by a mixed-aldehyde condensation using the Adler-Longo synthesis.[146]

The reaction of pyrrole with aldehydes A and B affords a mixture of six products (**Figure 36**), including the 'parent' porphyrins (A_4 and B_4) and four 'hybrid' porphyrins (A_3B, *cis*-A_2B_2, *trans*-A_2B_2 and AB_3)

Assuming equal reactivity of the aldehydes, the ratio of porphyrins in a mixed-aldehyde condensation, with aldehydes with a ratio of 1:1, gives the distribution: A_4, 6.25%; B_4, 6.25%; *cis*-A_2B_2, 25%; *trans*-A_2B_2, 12.5%; AB_3, 25%; A_3B, 25%. The A_3B porphyrin can be maximised by using a ratio of aldehydes 3:1 for A and B, giving the distribution: A_4, 31.64%; A_3B, 42.19%; *cis*-A_2B_2, 14.06%; *trans*-A_2B_2, 7.03%; AB_3, 4.69%; B_4, 0.39%.[147]

The yields obtained of the A_3B-porphyrin in practice are around 5%, which reflects the combination of a 20% yield of porphyrins for an Adler Longo synthesis coupled with the statistical distribution of the mixture of porphyrins.

2.1.6. Copper-catalysed azide-alkyne cycloaddition reaction (CuAAC)

The Cu (I) catalysed variant of the Huisgen 1,3 dipolar cycloaddition to afford a 1,2,3 triazole linkage has become so popular it is often used synonymously with "click reaction". The reaction has many benefits, such as the ease with which the reaction substituents, azides and alkynes, can be introduced into molecules and their stability under a variety of conditions. The reacting substituents are also virtually inert in biological media, including towards highly functionalised biological molecules, molecular oxygen and water.[148] The 1,2,3 triazole linking units also mimic the electronic properties of an amide bond but do not suffer the susceptibility to hydrolytic cleavage.[148]

In the uncatalysed Huisgen concerted cycloaddition, the kinetic stability of azides and alkynes is responsible for their slow cycloaddition, leading to high temperatures and slow reaction times. The products of the thermal 1,3-cycloaddition give a mixture of the 1,4- and 1,5-regioisomers (**Figure 37**).

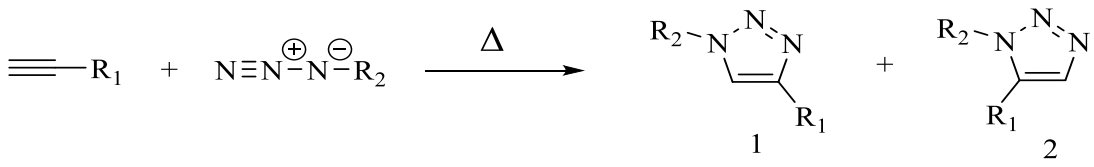

Figure 37 Huisgen 1,3-dipolar cycloaddition producing the 1,5- and 1,4- triazole linkage in 1:1 ratio.

The copper (I) catalysed alkyne-azide coupling, shown by both the Sharpless[149] and Meldal[150] groups independently in 2002, have many benefits. The copper-catalysed method affords increased regioselectivity giving only the 1,4-regioisomer. The other main advantage to this reaction is the increased reaction rate being to 10^7 times faster,[148] offering much milder reaction conditions. The copper-catalysed reaction only works with terminal alkynes, though there is a ruthenium catalysed reaction allowing the reaction between internal alkynes and azides, giving the 1,5-regioisomer.[151]

The Sharpless group proposed a mechanism (**Figure 38**)[149] for the catalytic cycle. The mechanism begins with the formation of the copper (I) acetylide **I,** from the terminal alkyne. The concerted [2+3] cycloaddition (B-direct) is said to be disfavoured[149] and instead the cycle proceeds through the B-1 to B-3 steps ligation via a six membered intermediate **III**.

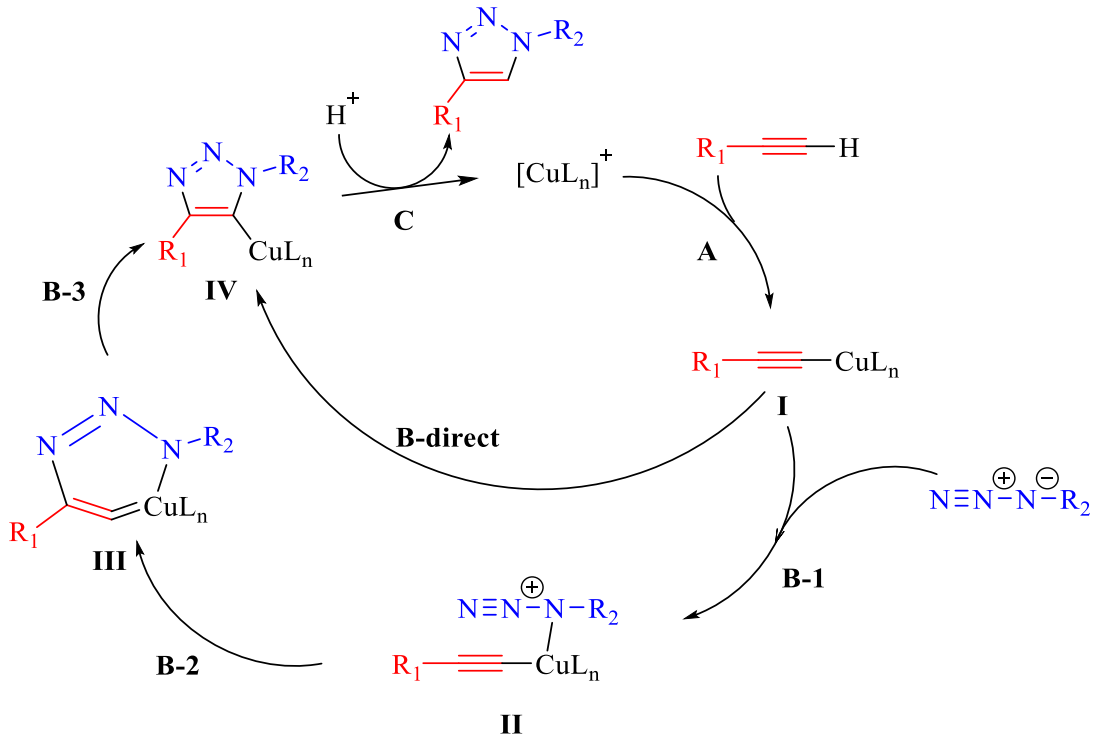

Figure 38 Catalytic cycle for the Cu (I) catalysed ligation proposed by Sharpless group in 2002.

2.1.7. Microwave heating and radiochemistry

Although microwave heating has been used for CuAAC chemistry since 2004[152] but is often underutilised in the field of radiochemistry. It is of great efficacy when reaction times are important, capable of reducing reactions times considerably whilst also increasing yields and minimising side products. When working with PET isotopes such as fluorine-18, with a ~110 min half-life, great importance is placed upon maximizing radiochemical yields (RCY) in order that the product has sufficient amounts of radiotracer remaining for carrying out imaging.

For this reason, microwave reactors are making their way into the lab of radiochemists as an alternative to more conventional heating methods,[153] lending itself to maintaining optimal activity of the radionuclide. It has been demonstrated to improve reaction times of sterically hindered, large macromolecules, such as porphyrins.

Zinc chelation of the porphyrin was required before the CuAAC reaction, to prevent the Cu porphyrin complex being formed. This is due to the quenching of the π^* excited states of the photosensitiser due to the paramagnetic copper.

The absorption spectra for metalloporphyrins are separated into classes of regular, and irregular metalloporphyrins, which are sub-divided into hypso and hyper metalloporphyrins. Hypso spectra are blue shifted due to metal $d\pi$ to porphyrin π^* back donation (**Figure 39**), typically occurring in metal cations with between 6 and 9 d-electrons.[154] The relaxation can be radiationless, phosphorescent or luminescent. Hyper spectra are red shifted and subdivided further into p- and d-type. They are radiationless or very weakly phosphorescent.[154]

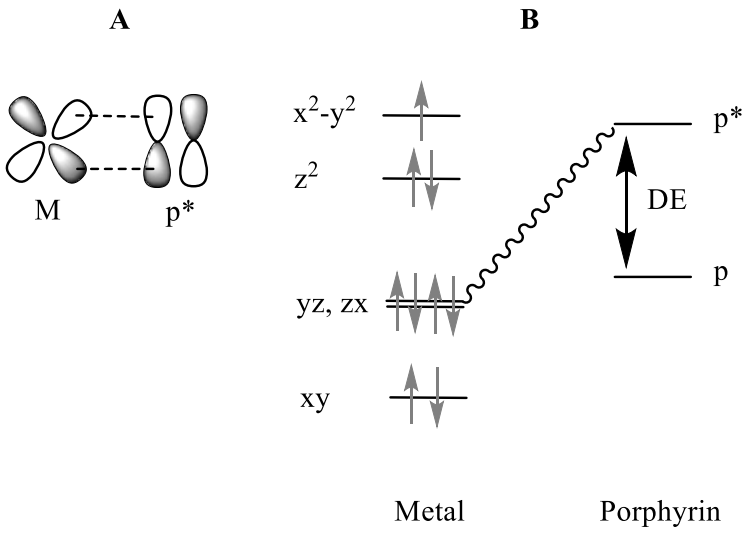

Figure 39 (A) orbital overlap between excited state orbital of porphyrin (π*) and metal dπ orbital. (B) porphyrin to metal back bonding, resulting in a larger π to π* energy gap causing a hypsochromic blue shift.

2.2. Results

2.2.1. Synthesis of a cationic water-soluble 'clickable' porphyrin

Synthesis of a water solubilised porphyrin can be achieved by sulfonation of meso phenyl porphyrins to yield an anionic derivative, or by the methylation of porphyrins bearing a meso pyridyl functionality to yield the cationic quaternary pyridinium salt. A disadvantage of the anionic derivative is a high dark toxicity,[155] which limits their use as therapeutic agents. Although the synthesis of the cationic porphyrin is a bit more involved, a counter ion exchange technique offers a unique strategy for easily maintaining a high level of purity, as impurities can be washed off using the opposing polarity solvent to which the counter ion provides the porphyrin. For these reasons the cationic derivative has arguable advantages over the anionic derivative.

The synthesis of the cationic derivative was achieved by preparation of an AB_3 mixed aldehyde condensation reaction (**Figure 36**), of aldehydes 4-pyridinecarboxaldehyde and

4-acetamidobenzaldehyde in a 3:1 ratio. To synthesise porphyrin **[1]** (**Scheme 2**), the procedure from the literature[75] was carried out, to obtain the 5-[4-acetamidophenyl]-10,15,20-tri-(4-pyridyl)porphyrin in a yield of 5.7%. This yield is comparable with the literature[75] and as previously stated is low due to both the fact that porphyrins make up only approximately 20% of the product in the Adler Longo synthesis; also in part to the asymmetry of the desired porphyrin, as the A_3B porphyrin is only one of six possible configurations for an asymmetric mixed aldehyde condensation reaction and must be separated by column chromatography. The product was confirmed by the characterisation techniques of NMR, MS and UV-Vis.

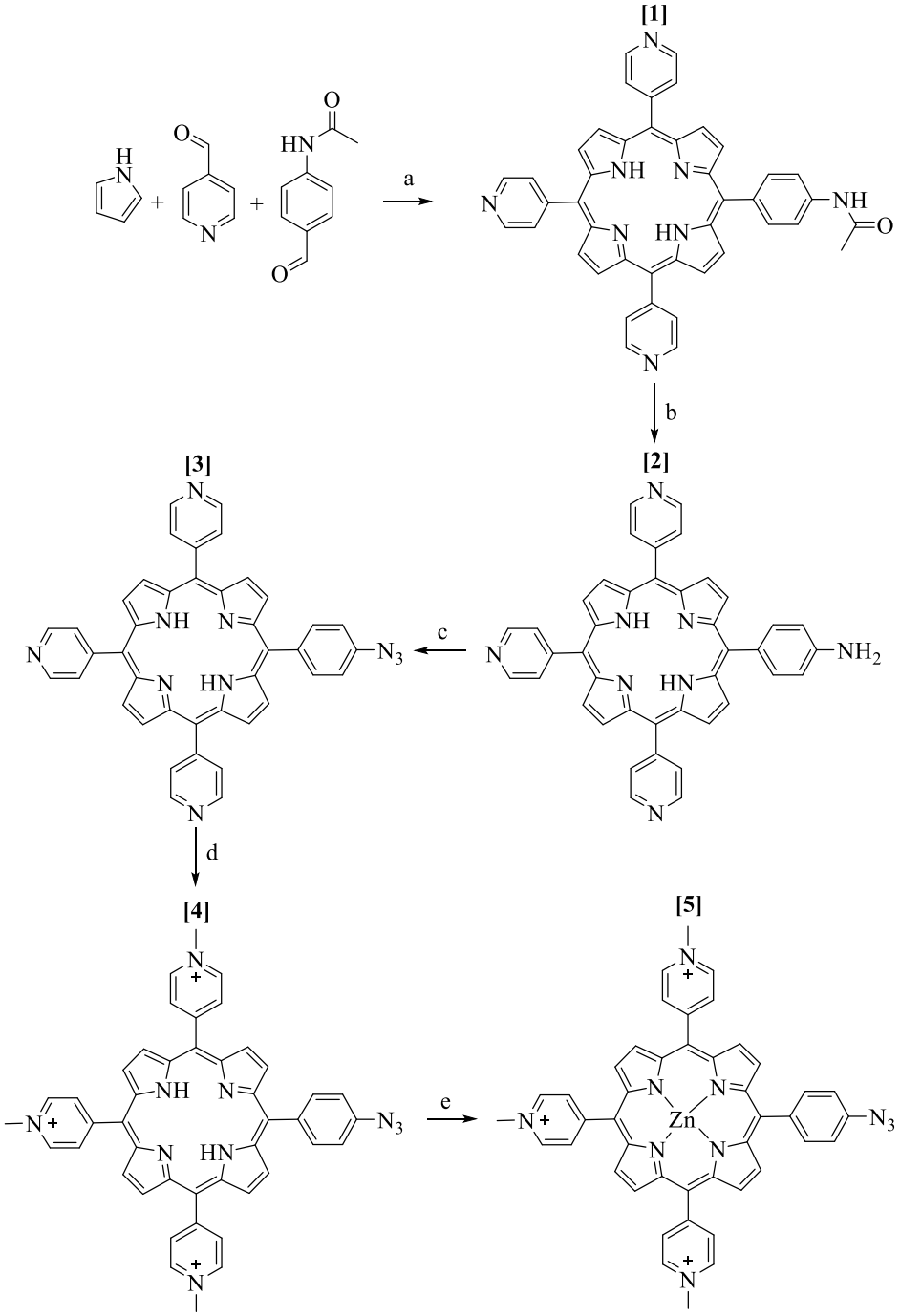

Scheme 2 (a) Pyrrole, 4-pyridinecarboxaldehyde, 4-acetamidobenzaldehyde in propionic acid, 180 °C, 1 h (b) 12 M HCl, 100 °C, 3 h, then DCM/TEA 9:1 10 min (c) (i) $NaNO_2$ (aq) and TFA, 0 °C, 15 min, (ii) NaN_3 (aq), 0 °C, 1 h, (iii) saturated $NaHCO_3$ (aq) (d) (i) CH_3I in DCM, 40 °C, 18 h, (ii) counter ion exchange NH_4PF_6 and TBAC, (e) (i) $Zn(OAc)_2$ (aq), rt, 30 mins, (ii) counter ion exchange NH_4PF_6 and TBAC.

The acetamido group was hydrolysed to an amine porphyrin **[2]** by hydrolysis of porphyrin **[1]**, based on the literature,[75] carried out in refluxing aqueous HCl (12 M) for three hours, affording a 75% conversion to **[2]**. The identity of the product was confirmed NMR, the loss of a carbonyl group was observed in the ^{13}C-NMR for as well the loss of a CH_3 in the ^{1}H-NMR. The product was further characterised by MS and UV-Vis.

The azide bearing porphyrin **[3]** was synthesised by a diazotisation reaction of the amine **[2]** to the azide functionality by reacting with sodium nitrite, forming a diazonium salt which then reacts with sodium azide to give a pentazole intermediate before ultimately yielding the aryl azide and N_2. The synthesis was carried out according to the literature[156] with the desired product obtained in a yield of 96.8%, in keeping with the yields reported, and was confirmed by NMR, MS and UV-Vis.

Porphyrin **[4]** was obtained by methylation reaction to give the cationic pyridiniumyl salt from porphyrin **[3]** following a literature procedure[76] using methyl iodide in DMF, affording a 90% yield. The ^{1}H-NMR clearly showed a CH_3 group was now present that integrated to 9 showing that the methylation reaction had gone to completion. The method also employed an ammonium hexafluorophosphate/tetrabutylammonium chloride workup as described in the literature.[141] This methodology allows removal of both water-soluble and organic impurities, while also exchanging the iodide counter-anions to chloride ions, improving the water solubility of the porphyrin.

The water solubilised porphyrin **[4]** was metallated with zinc to give porphyrin **[5]** with zinc (II) acetate in water, utilising the hexafluorophosphate/tetrabutylammonium chloride workup (**Figure 40**). Conversion was confirmed by TLC, with the reaction giving **[5]** in a yield of 95%. Completion was confirmed by UV-vis spectroscopy showing only two Q-bands in the spectrum of the metallated product. MS also confirmed complete conversion.

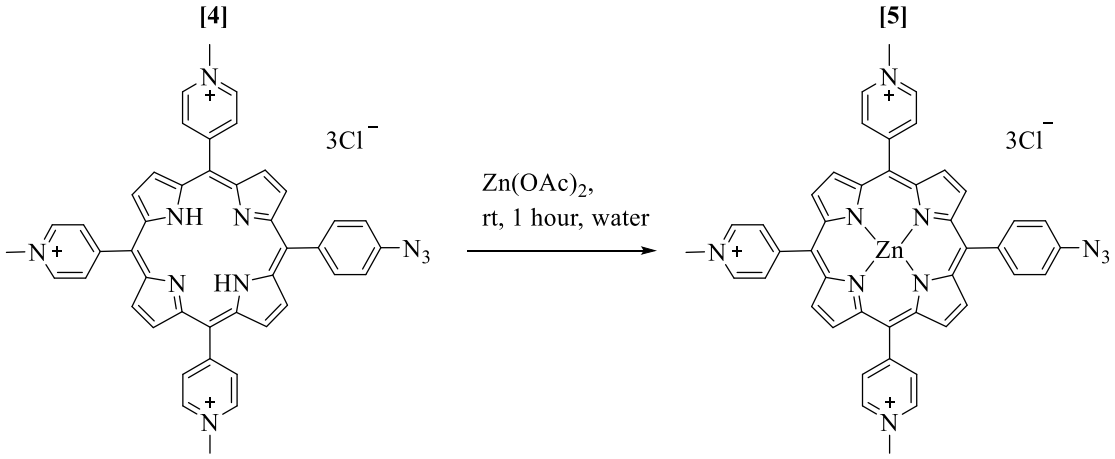

Figure 40 Metallation of porphyrin **[5]** to give the Zn metallated product porphyrin **[6]**.

It was important to metallate the water solubilised porphyrin, rather than metallate first, and then water solubilise. The reason for this comes from the formation of a polymerisation of zinc metallated, meso pyridyl species, leading to an insoluble product. The formation of this polymer has been described in the literature,[157] resulting from the ability of zinc to form a six-coordinate species as well as a four coordinate species. The lone pair of a nitrogen on the pyridyl of an adjacent porphyrin molecule is able to act as a ligand to the chelated zinc of another porphyrin molecule. This can lead to the insoluble porphyrin species (**Figure 41**).

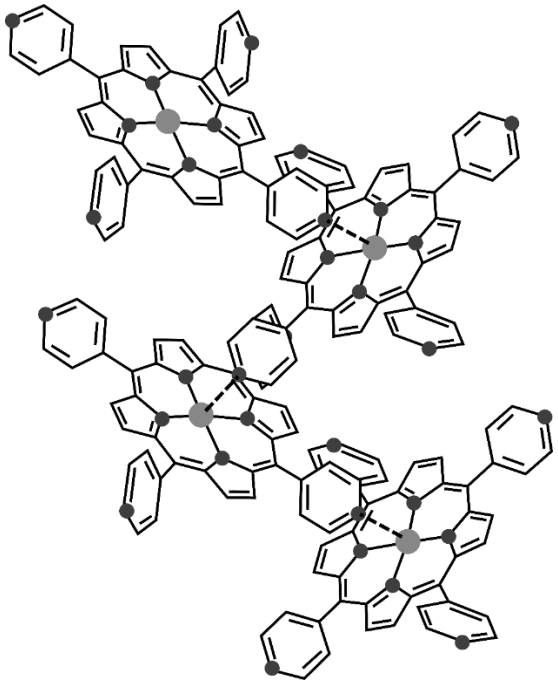

Figure 41 Polymeric structure of zinc metallated meso pyridyl porphyrins, between the pyridyl lone pair and the zinc of an adjacent molecule.

2.2.2. Functionalized PEG chain synthesis and characterisation

A tetraethylene glycol chain was chosen as the carrier for ^{18}F, functionalised with an alkyne group for quick and facile conjugation to the photosensitiser. Offering low volatility and amphiphilicity the tetraethoxy polyethylene glycol (PEG) chain is a highly biocompatible target for radiolabelling. Two PEG chains were synthesised for study (**Scheme 3**), **[7]** was synthesised bearing a tosyl functionality for radiolabelling via a substitution reaction with fluorine-18 whilst **[8]** was investigated for radiolabelling via isotopic substitution as well as for cold cytotoxicity studies *in vitro*.

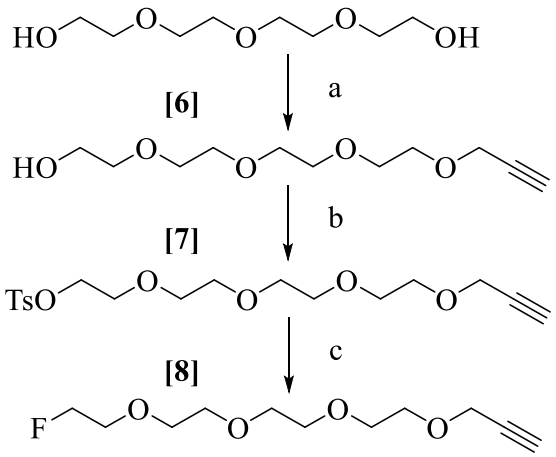

Scheme 3 (a) NaH in THF at −20 °C. Propargyl bromide 18 h under N_2 at rt, (b) TsCl, TEA, DCM 17 h under N_2 at rt (c) anhydrous THF under argon, 80 °C,1 M TBAF in THF.

The synthesis of an alkyne bearing PEG chain on just one side **[6]** was carried out according to the literature,[158] and separated from the difunctionalised chain by column chromatography to yield a pale yellow oil at 68%. Tosylation of this chain was carried out,[159] yielding the product **[7]** in an 80% yield. The synthesis of the cold standard **[8]** using ^{19}F was performed using TBAF; using TLC to monitor the progression of the reaction, it displayed an almost instantaneous generation of **[8]** from **[7]** in a 90% yield in > 5 min. The product structure was confirmed by NMR and MS.

2.2.3. Click conjugation of porphyrin and functionalized PEG chain

Initially it was considered that the click conjugation of PEG chains **[7]** and **[8]** to the water solubilised porphyrin **[5]** might be done first, allowing for a one step radiolabelling process. However, a theoretical and a practical issue prevented this course of action from being suitable. The theoretical issue arises due to the counter ions which imbue the water solubility to the photosensitiser; in the presence of fluoride ions the porphyrin **[5]** was found to undergo a counter ion exchange between chloride and fluoride anions on the pyridiniumyl cationic moieties. This produces a product bearing inferior water solubility,

reducing the applicability for *in vivo* purposes. It also means that when performed with fluorine-18 ions for radiolabelling, a highly labile fluoride would be attached that could easily dissociate *in vivo*.

The other practical challenge to this line of investigation came from the fact the tosylated PEG chain would not undergo click conjugation with the described procedure. It was decided that due to the quick nature of the click reaction that the ^{19}F and ^{18}F chains would be produced before conjugation to the photosensitiser, allowing for a cold optimisation of the click methodology and a cold standard of the porphyrin conjugate **[9]** for analysis and biological evaluation (**Scheme 4**).

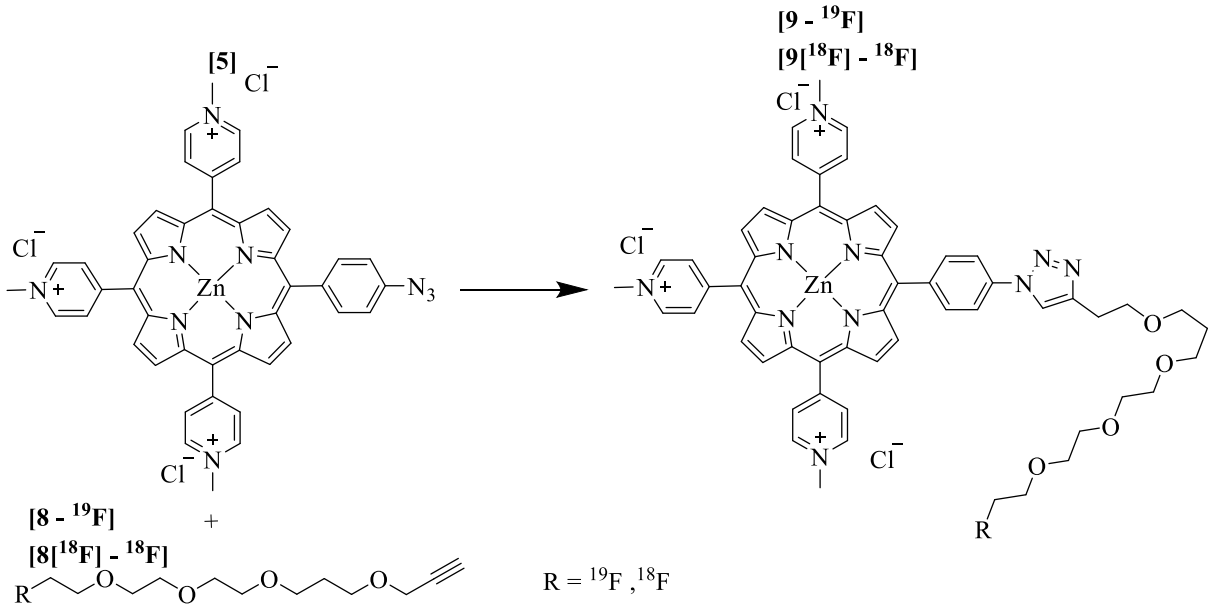

Scheme 4 Copper (II) sulfate, sodium ascorbate and TBTA in 1:3 THF: Water, MW 40 °C, 60W, 15 min.

In contrast to the tosylated chain **[7],** the fluorine bearing chain **[8]** was found to undergo conjugation to yield the conjugate **[9]** in a very rapid and highly yielding manner with a yield of 90%. The reaction progression was monitored using TLC and HPLC. It was found that the HPLC methodology developed to monitor this reaction had excellent

separation between the precursors and the final product, allowing for semi-preparative HPLC purification to isolate the radiolabelled product.

2.2.4. ^{18}F labelling of PEG chain

Two methods for generation of the **[8[^{18}F]]** prosthetic were attempted (**Scheme 5**). The first method employed an isotopic substitution of ^{19}F from **[8]**, the second was nucleophilic substitution of the tosyl group from **[7]**.

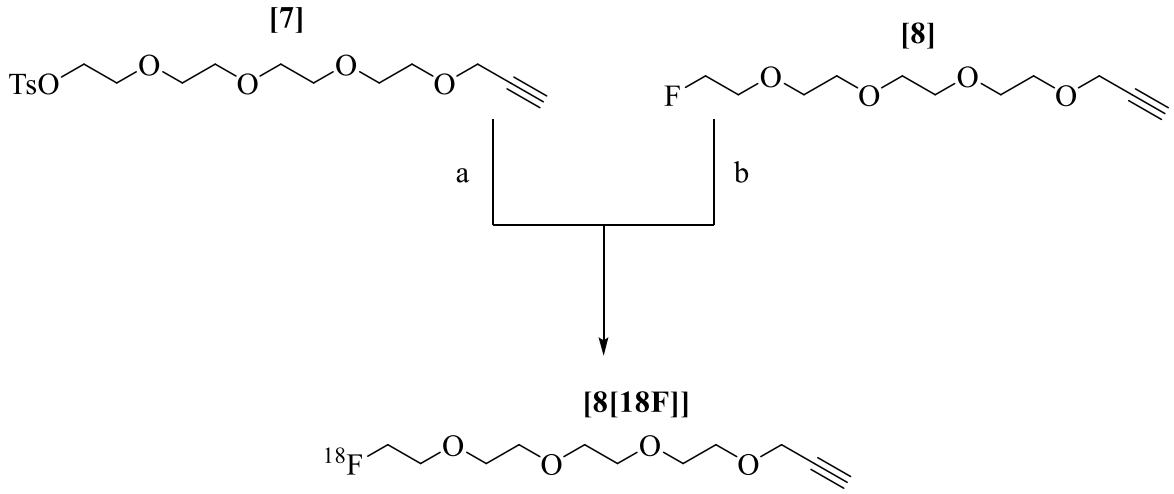

Scheme 5 (a) dried ^{18}F, 140 °C, 10 min. (b) dried ^{18}F, 180 °C, 10 min.

Isotopic substitution of **[8]** was performed with dry ^{18}F at 180 °C for 10 minutes, however, an average incorporation of just 4.48% ± 1.37 (n = 3) ^{18}F was achieved (**Figure 42**), despite forcing reaction conditions utilised. An increased reaction time showed no improvement in yield. However, the method of nucleophilic substitution of **[7]** achieved an excellent ^{18}F incorporation, with heating for just 10 minutes at 140 °C an average incorporation of 93.4% ± 3.34 (n = 3) was attained (**Figure 43**).

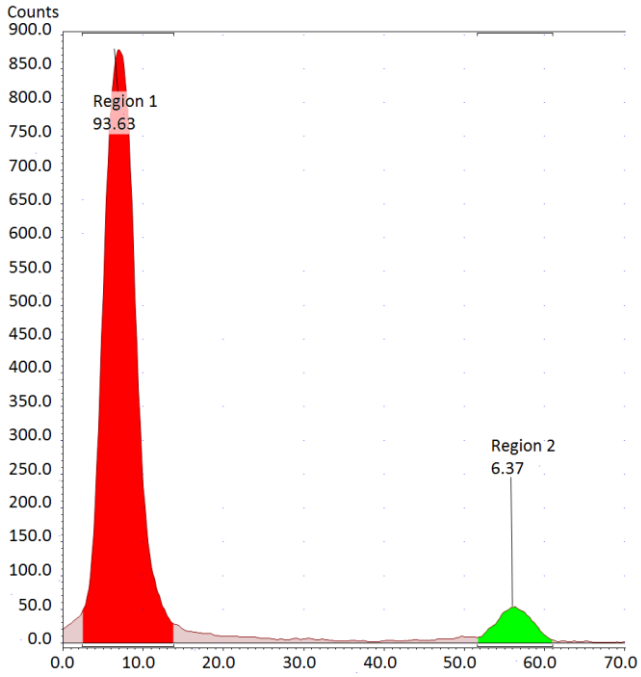

Figure 42 RadioTLC of the isotopic substitution reaction, showing < 5% incorporation. Region 1: free ^{18}F, Region 2: incorporated ^{18}F.

It was found that purification of **[8]** from the precursor **[7]** was not possible by preparative HPLC and instead purification of crude **[8[^{18}F]]** was carried out using Sep-Pak®Light tC18 cartridges, for the removal of the residual ^{18}F. The product was obtained with > 99% radiochemical purity.

An alternative was to generate a carrier-added derivative, with residual [**7]** reacted with TBAF to produce a ^{19}F/^{18}F mixture, giving a single chemical product with no reduction in ^{18}F incorporation observed.

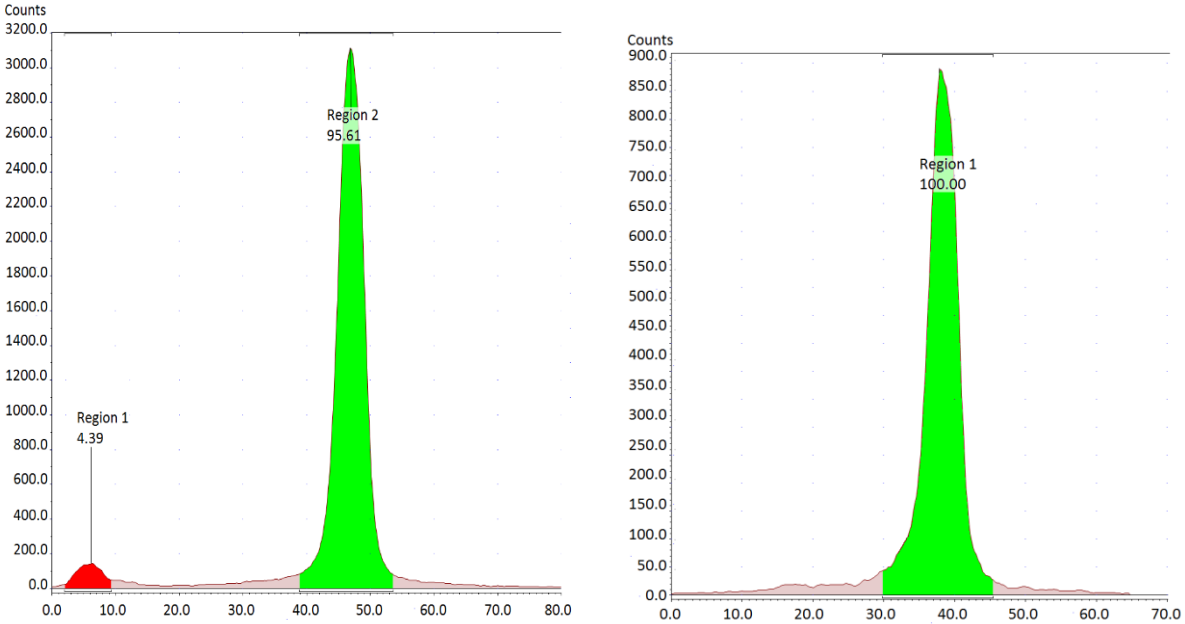

Figure 43 RadioTLC of the substitution reaction, showing > 95% incorporation (Left) and > 99% radiochemical purity following purification (Right).

2.2.5. Radiolabelled porphyrin conjugate synthesis and characterisation

For the purposes of purification of conjugate following CuAAC reaction it is fortuitous that whilst chain **[8]** demonstrated an excellent conjugation yield with porphyrin **[5]**, the precursor **[7]** showed no reaction with the same porphyrin. This meant that click reactions of a mixture of both chains **[7]** and **[8]** with porphyrin **[5]** were found to exclusively yield the conjugate **[9]**, negating any need for purification of the mixture by HPLC.

Microwave reaction was utilised for CuAAC reactions of the porphyrin **[5]** with the radiolabelled chain **[8[^{18}F]]** requiring heating at just 40 °C for 20 minutes as previously described. Purified using a Sep-Pak® Light tC18 cartridge was performed followed by several washes with water. The product was then eluted using ethanol with an incorporation yield of the final product **[9[^{18}F]]** of (34.2% ± 2.46 (n = 3)) (**Figure 44**).

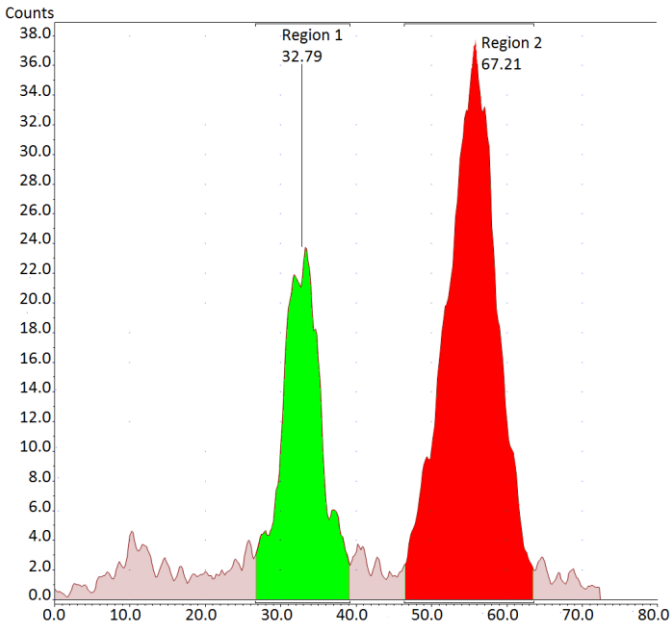

Figure 44 RadioTLC of click reaction; 32.8% incorporation of fluorine-18 within **[9[^{18}F]]** (Region 1).

2.3. Evaluation of cytotoxicity

2.3.1. *In vitro* evaluation

Conjugate **[9]** was confirmed for retention of photodynamic activity of the photosensitiser and hence the application of the conjugate as a therapeutic agent, by evaluation of the phototoxicity *in vitro* using a human adenocarcinoma (HT-29) cell line.

Irradiation of the conjugate **[9]** was carried out using an Oriel light system with a filter to remove light below 550 nm, the results of which were then compared to the non-irradiated control. The decision for the wavelength of the light chosen for irradiation was made to investigate the applicability of the conjugate for both *in vivo* testing and clinical practice. This wavelength excludes the large Soret band intentionally, as it has very limited tissue penetration and would therefore not give indicative results for clinical application. Instead filtering after 550 nm aligns with the two Q-bands of the zinc chelated porphyrin only.

Irradiation was performed upon human colon adenocarcinoma cells (HT-29) incubated for 1 hour with varying concentrations of **[9]**, under irradiation with light (> 550 nm) leading to an LD_{90} of approximately 1 x 10^{-4} M (**Figure 45**). Dark toxicity was minimal with > 75% cell survival for all non-irradiated concentrations.

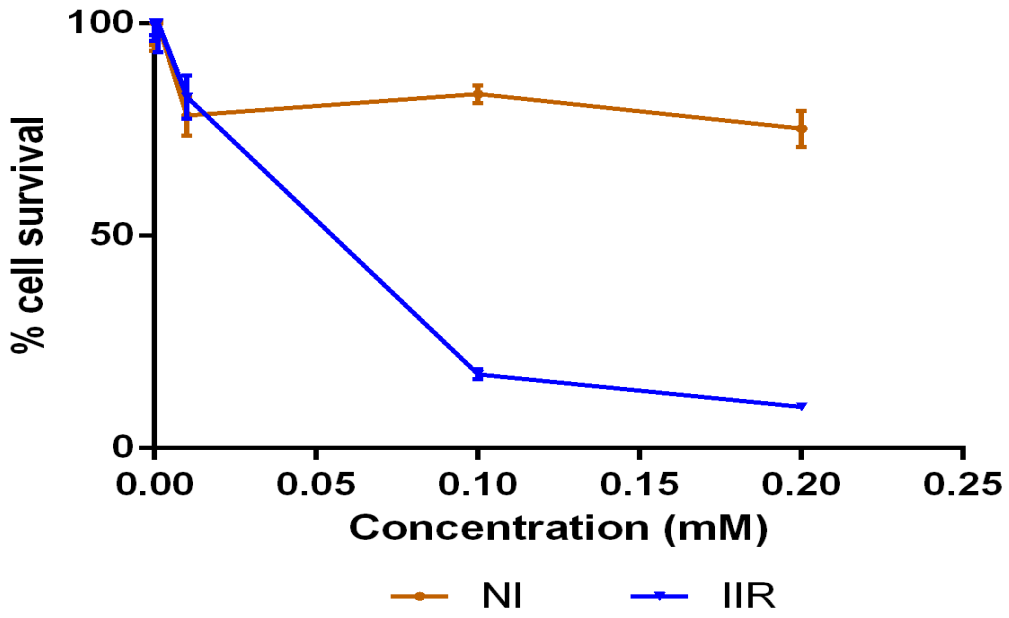

Figure 45 Graph of cytotoxicity assay. Assay was carried out on HT-29 cell lines, with results displayed for conjugate **[9]** following irradiation (IIR) and non-irradiated control (NI).

Cellular uptake of the conjugate within the HT-29 cell line was demonstrated by fluorescence and bright field images. The bright field image clearly exhibits blebbing of the cellular membrane, which is indicative of a rapid onset of apoptosis of the cells by activation of the photosensitiser under excitation of the microscope. This behaviour has previously been observed with cationic porphyrins.[160]

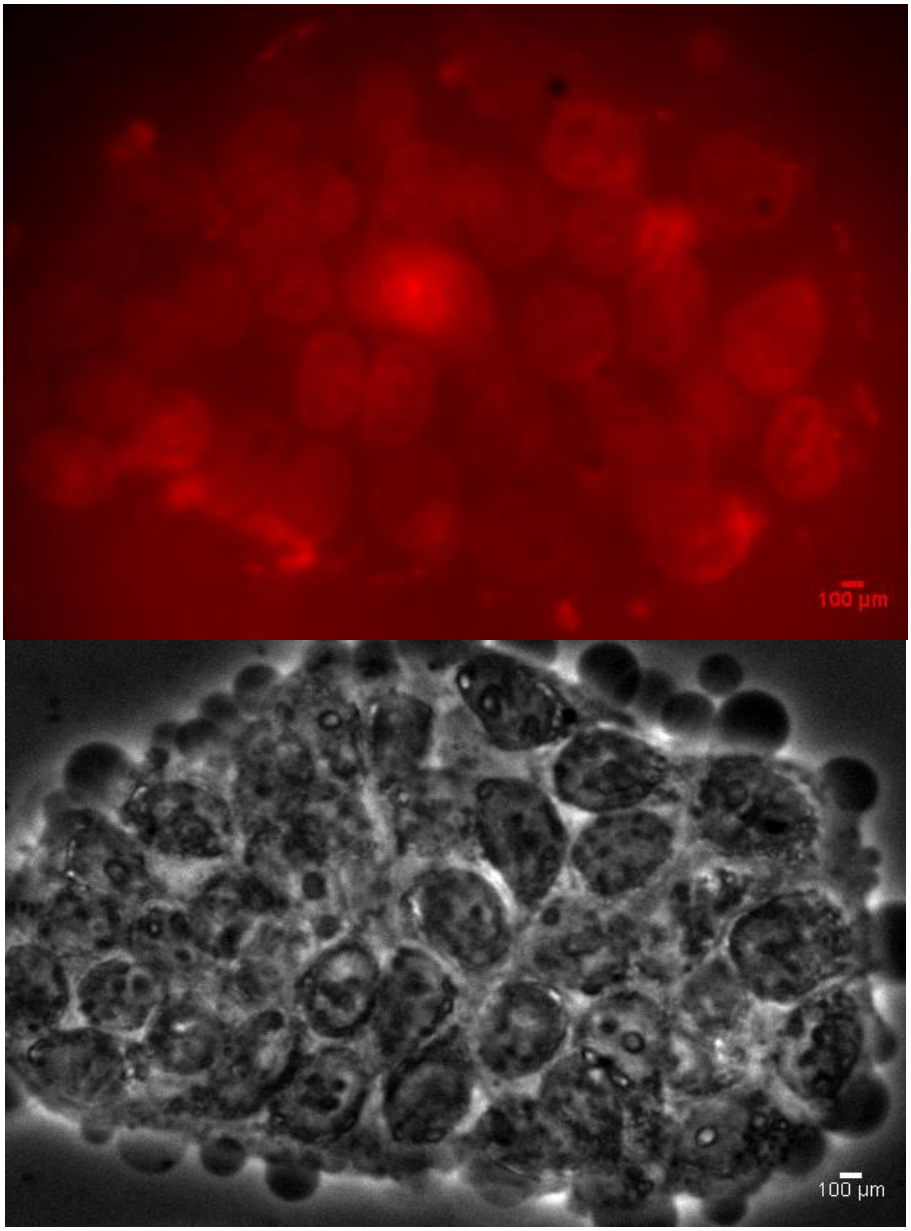

Figure 46 (Top Image) Fluorescence image showing cellular uptake of photosensitizer **[9]** in human adenocarcinoma (HT-29) cells, (bottom Image) Bright field image of HT-29 cells incubated with **[9]**.

2.3.2. *In vivo* evaluation

Tumour uptake of the conjugate **[9[18F]]** was assessed in mice using the HT29 and U87 xenograft models. The conjugate was injected intravenously (iv), and PET imaging was then used to quantify the biodistribution.[69]

[9[18F]] mainly accumulated within the liver (**Figure 47 C,D**), which is consistent with previous investigation of porphyrin biodistribution.[67] Tumour accumulation was also evident in both models used. The average accumulation of tumour to muscle ratios were 1.4 (SUVmean) or 2.3 (SUVmax) at 80 - 90 minutes (**Figure 47 E,F**).

Although this porphyrin conjugate had no active tumour targeting, tumour uptake over other tissues can be explained by a process known as enhanced permeability and retention (EPR) effects and is assumed to be high in preclinical xenograft models.[161] In this study we assessed the uptake of both HT29 and U87 as these models have previously shown to display low and high levels of EPR mediated nanoparticle accumulation, respectively.[162,163] Uptake was observed in all tumours of both models, and therefore exhibits the potential of this conjugate as a theranostic agent for imaging and determining the optimal irradiation time for irradiation and PDT treatment.

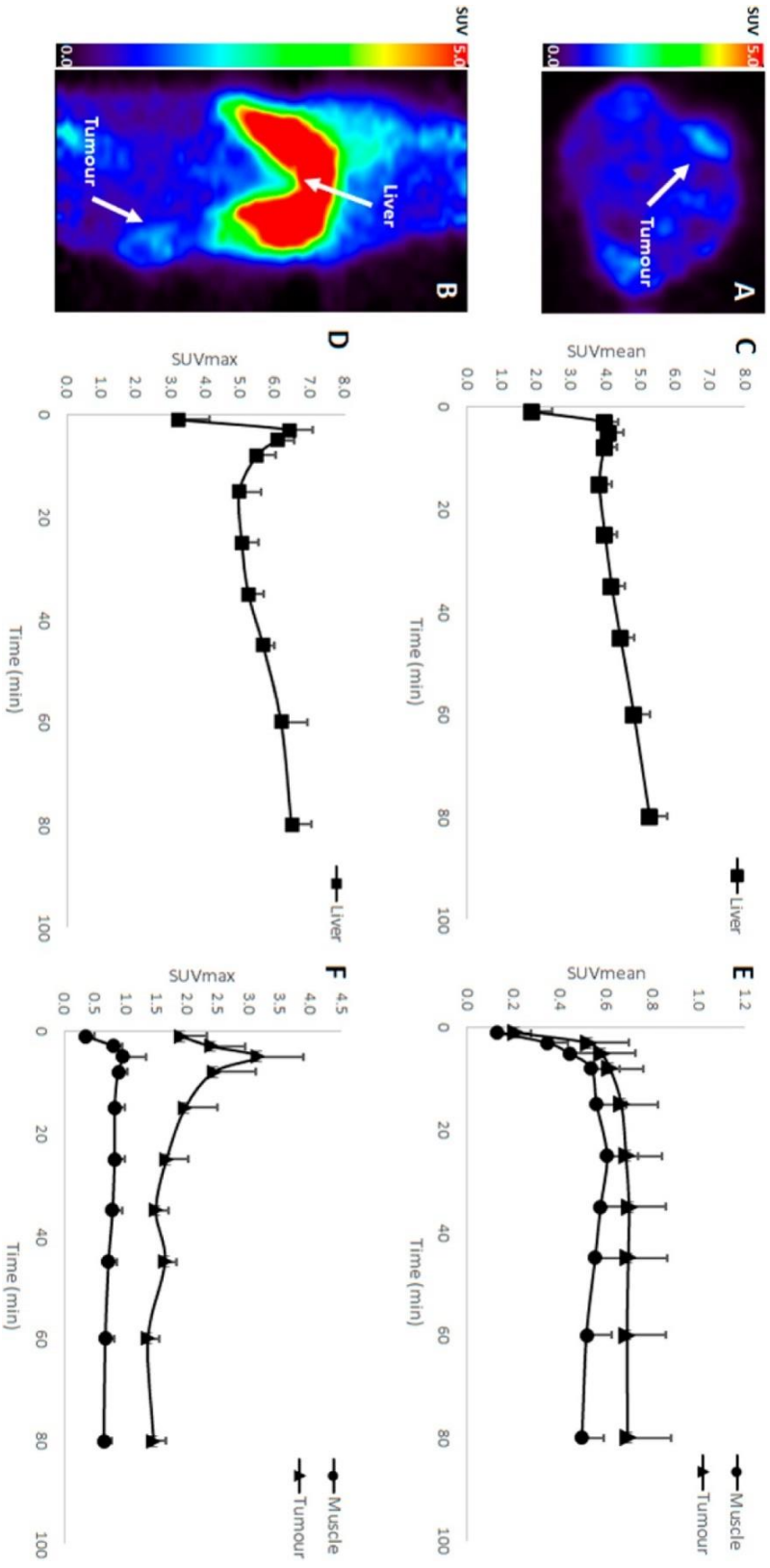

Figure 47 Dynamic **[9[^{18}F]]** uptake in tumour bearing animals. (A, B) Transaxial and coronal image slices centered on the tumour at 80 - 90 min, showing uptake in tumour and liver in representative HT29 tumour (arrows). (C, D) Time activity curves of **[9[^{18}F]]** in liver. (E, F) Time activity curves of **[9[^{18}F]]** in tumour and muscle. All time activity curves represent average data from four tumour-bearing animals ± SEM.

2.4. Conclusions

A novel fluorine-18 radiolabelled, single theranostic agent was synthesised conjugating an azide functionalized, cationic water-soluble porphyrin with an alkyne functionalised ^{18}F PEG chain, *via* CuAAC methodology. This is the first time a porphyrin has been radiolabelled with ^{18}F and demonstrated to retain good photocytotoxicity following radiolabelling, whilst also exhibiting minimal dark toxicity. The compound also demonstrated cellular uptake in relevant human cancer cell lines *in vitro* as well as confirmed uptake into neoplastic tissue *in vivo*, whilst demonstrating potential as a radiotracer. The promising results attained from the biological evaluation performed indicate good potential of the conjugate as a clinically relevant theranostic agent, offering the possibility of a simultaneous imaging and treatment of tumours by PDT.

3. The synthesis of suitable scintillating nanoparticles for use in a PDT assisted radiotherapy

3.1. Introduction

3.1.1. Penetration depths of radiation in inorganic materials

Many important factors are worth consideration for developing applicable nano-scintillating materials for extending the application of PDT for activation by X-rays. The rate at which energy is lost from an incident beam as it passes through a material is described by its stopping power.[164] Stopping power for a scintillator made of inorganic materials under irradiation with ionizing radiation depends on the material density and atomic number of the atoms within the material as well as thickness of the material and the energy of the radiation used.[165] These are important factors that should be considered from designing of the scintillator as they will influence the choice of materials chosen, the size of the nanoparticles synthesized, and the most suitable energy of the ionising radiation.

For radiotherapy a typical daily fractionation is of 2 Gy for an average therapy, with energies from 6 - 20 MeV for an external beam source. Brachytherapy on the other hand uses lower energies from 27 - 35 keV (I-125), 200 - 600 keV (Ir-192), 0.4 - 1 MeV (Au-198) and 0.19 - 2.4 MeV (Ra-226).[166] Higher energies combined with nanoparticulate size massively reduce the effective stopping power of scintillating materials.[167] Taking calcium tungstate ($CaWO_4$) as an example; a 1 cm path length irradiated at 1 MeV will absorb ~ 40% of the radiation passing through it. If that diameter is reduced to 100 nm, that interaction drops to 0.0005% of irradiating energy. If the energy of the radiation is reduced however to 10 keV, a 100 nm diameter particle can be expected to absorb ~ 7% of the ionising radiation. The absorption of X-rays by nanoparticles is substantially

greater at lower X-ray energies, and this holds true for every material.[166] Although it certainly doesn't preclude the potential of working with higher energy (> 1 MeV) radiotherapy techniques, it does suggest that focusing on lower energy X-rays (< 200 keV) has a higher chance of success, and is a good range for investigation in what is still a relatively new technology.[166]

Another important consideration when looking at the best energy window for irradiation is the attenuation length of that energy within human tissue. Although a 10 keV energy will have a better chance of interaction with a nano scintillator material, the penetration depth of those X-rays within tissue will barely exceed 1 mm due to the high value of attenuation coefficient for tissue at this energy. This would offer little to no advantage to current light energies utilized for PDT.

Table 3 Penetration depth of light into tissue from UV to NIR energies.[168]

Wavelength (nm)	Energy (eV)	Colour range	Penetration (mm)
150-380	8.3 – 3.3	Ultra Violet	< 0.1
390-470	3.2 – 2.6	Violet to Blue	~ 0.3
475-545	2.6 – 2.3	Blue-Green	~ 0.3 - 0.5
545-600	2.3 – 2.1	Yellow to Orange	~ 0.5 - 1.0
600-650	2.1 – 1.9	Red	~ 1.0 - 2.0
650-950	1.9 – 1.3	Red to NIR	2 - 3
950-1200	1.3 – 1.0	NIR	1

However, penetration depths dramatically increase between 10 - 50 keV to ~ 5 cm (**Figure 48**), and as much as 7 cm for energies around 150 keV; this may not realise the original vision of this technology to extend the usefulness of PDT to anywhere in the body, but it is still a substantial potential improvement. Crucially these energies will still

interact in significant proportions with nanometre diameter scintillating materials, and in particular many high z-value materials with an absorption edge between 10 - 80 keV. This means that there is a particular energy for a particular material, that optimises both the absorption efficiency of the material whilst maximising the penetrative depth.

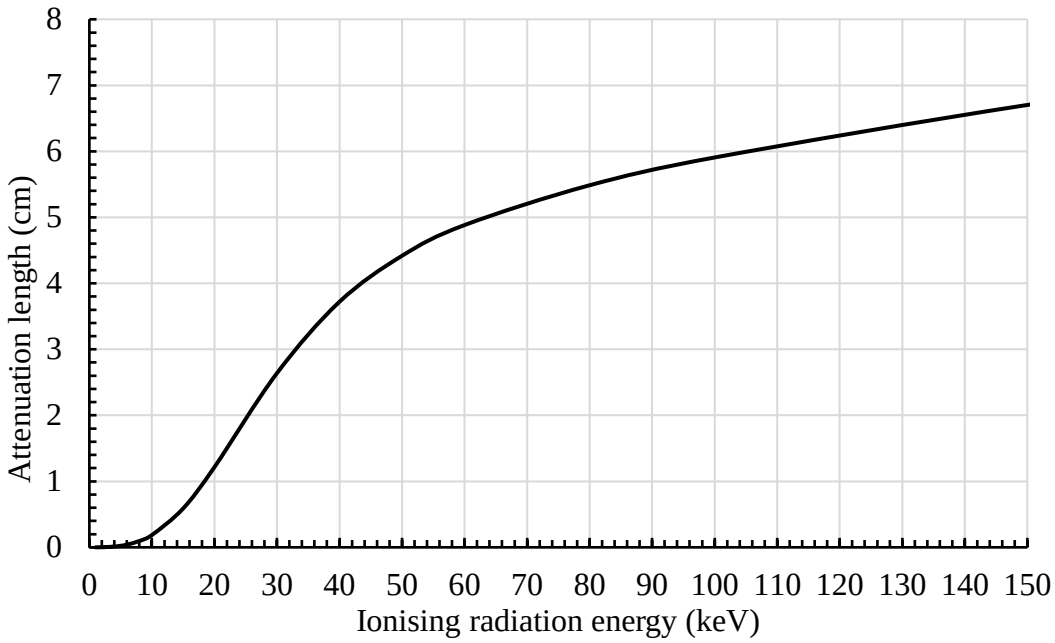

Figure 48 Penetration depth of ionising radiation of increasing energy into human tissue ICRU-44, calculated from absorption coefficient of the NIST database.[169]

3.1.2. Nanoparticle Scintillator materials

For this work, nine materials have been chosen for investigation (**Table 4**), covering a range of densities from ~ 3 - 9.5 gcm^{-3}. These materials also have an interesting range of absorption K-edges changing the order of expected absorptivity between 10 - 80 keV (**Table 4**), before returning to an order that is in ascending order of the calculated effective atomic number Z_{eff} for the material after 80 keV.

Table 4 Nanoparticle materials investigated for their potential as nanoparticle scintillators with density, Z_{eff} and K-edge, in density ascending order.

Material	Density (g/cm^3)	Effective atomic number (Z_{eff})	Absorption K-Edge (keV)
Calcium Fluoride (CaF_2)	3.18	16.07	Ca = 4.03
Yttrium Oxide (Y_2O_3)	5.01	35.59	Y = 17.03
Zinc Oxide (ZnO)	5.61	27.68	Zn = 9.66
Lanthanum Fluoride (LaF_3)	5.9	53.35	La = 38.9
Calcium Tungstate ($CaWO_4$)	6.06	61.87	W = 69.5
Europium Tungstate ($EuWO_4$)	7.56	64.58	Eu = 48.5 W = 69.5
Lutetium Fluoride (LuF_3)	8.33	63.63	Lu = 63.3
Lutetium Oxide (Lu_2O_3)	9.42	67.33	Lu = 63.3

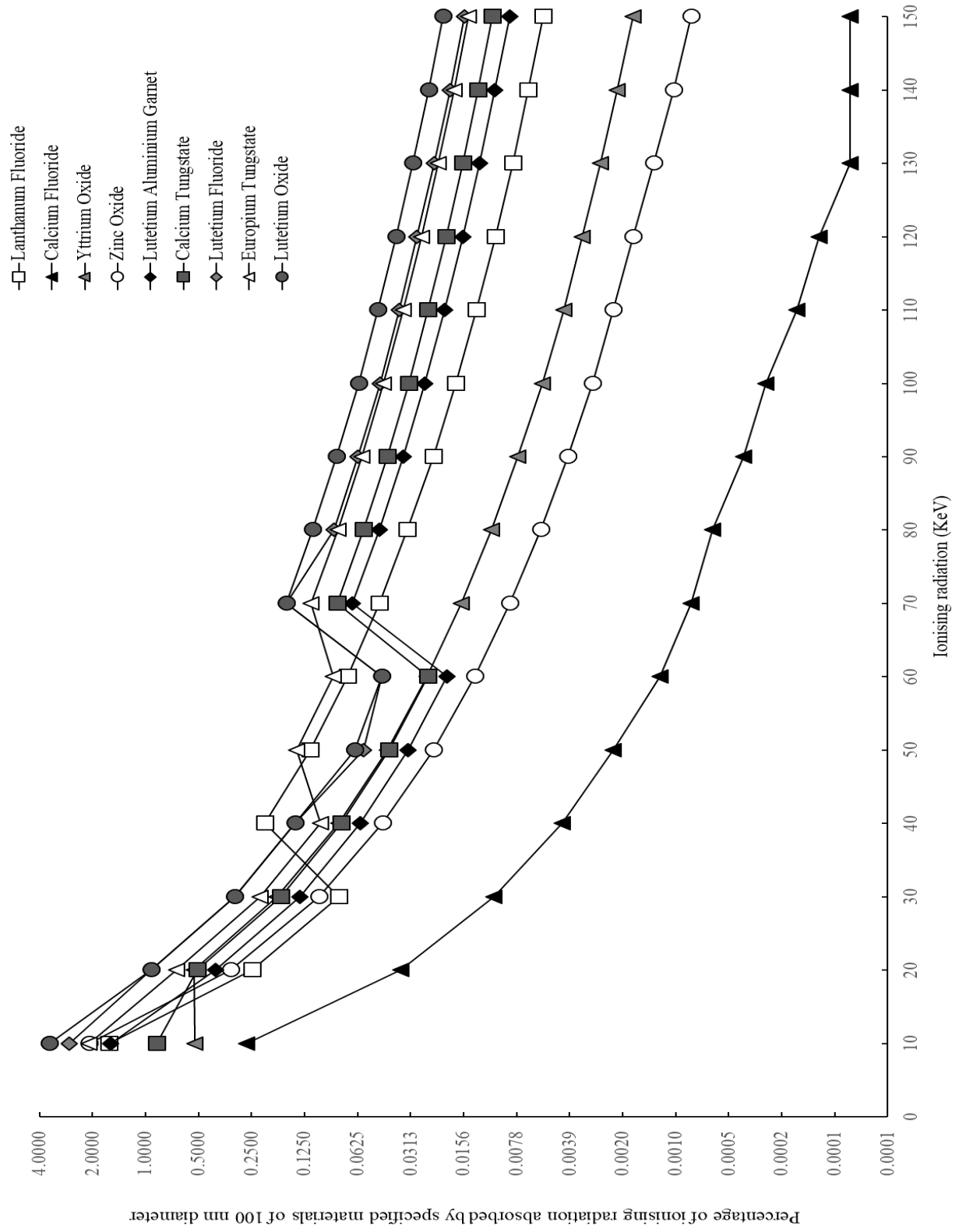

Figure 49 Calculated percentage of ionising radiation absorbed by the nine materials under investigation, for material size 100 nm diameter, at increasing energy of ionising radiation, computed using the Argonne National Laboratories website.[170]

Some interesting things to notice from **Figure 49** is the region of energies from 10 - 80 keV. As previously mentioned, after this point the absorption percentage is highest for materials with the highest calculated Z_{eff} which also roughly correlates with the density of the materials, showing the importance of these properties when choosing a scintillating material. However, the energies below ~ 100 keV, which may be best suited for use with brachytherapy are also strongly influenced by the absorption K-edge of elements present within the compound. For instance, LaF_3 has the highest performance between 30 - 60 keV, which might not have been expected when looking purely at density and Z_{eff} alone. Indeed, it may be possible to sub divide materials into groups most suited to the different types of brachytherapy available.

3.1.3. Absorption relative to soft tissue

Using data published on the NIST database for atomic mass attenuation coefficients, the relative radiation absorbed by nanoparticles to tissue has been calculated.[169] **Figure 50** shows the relative absorptivity (M) of LaF_3 compared with soft tissue and is given by the following formula[166] using LaF_3 as an example:

$$M = \frac{\rho LaF3}{\rho t} \; x \; \frac{(0.709 \; x \; \mu La) + \; (0.291 \; x \; \mu F)}{\mu t} \qquad Equation\ 4$$

where $\rho LaF3$ and ρt are the densities of LaF_3 and ICRU soft tissue respectively. $\mu La,\ \mu F$ and μt are the mass energy absorption coefficients for lanthanum, fluorine and ICRU soft tissue, and were obtained from the NIST database. LaF_3 has a density of 5.93 gcm^{-3} with lanthanum making up 70.9% of the compound by atomic weight, and 29.1% for fluorine.

Possible dopant ions have not been included in this calculation as they are generally of low molar percentage and will make little effect on the stopping power of the material to ionising radiation.

3.1.4. Effective atomic number (Z_{eff})

The approximate Z_{eff} for each material was calculated using the Mayneord:[171,172]

$$Z_{eff} = \sqrt[2.94]{f_1\ x\ (Z_1)^{2.94} + f_2\ x\ (Z_2)^{2.94} + \cdots} \qquad \textit{Equation 5}$$

where f_n is the fraction of the total number of electrons associated with each element and Z_n is the atomic number of each element involved.

Figure 50 compares absorption of the materials relative to soft tissue and will therefore correlate very strongly with the findings of **Figure 49**. It highlights how quickly the difference in relative absorption drops after 100 keV, and why the lower energy, brachytherapy range of energies, are most suited for investigation.

Plotting the calculated relative absorption values, relative to tissue against the calculated effective atomic number at an energy of 100 keV for each material gave the correct order in increasing absorptivity. This did not hold true at lower energies as the K-absorption edge also comes into play but highlights the importance of the Z_{eff} when considering which materials will likely be most effective. The relative atomic number roughly correlates with the density of the material, which was found to be a less accurate predictor.

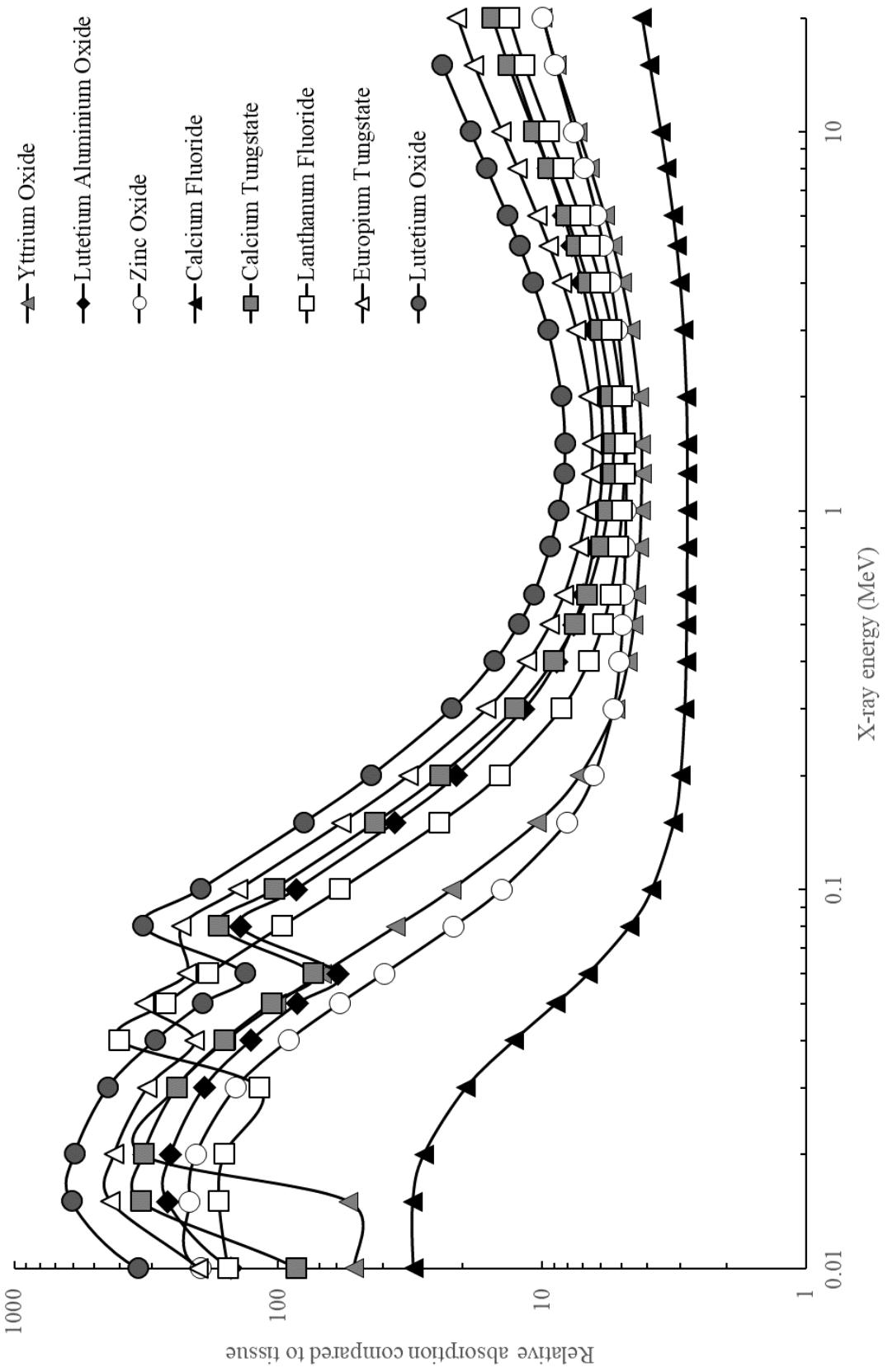

Figure 50 Absorption of different nanoparticle materials relative to soft tissue.

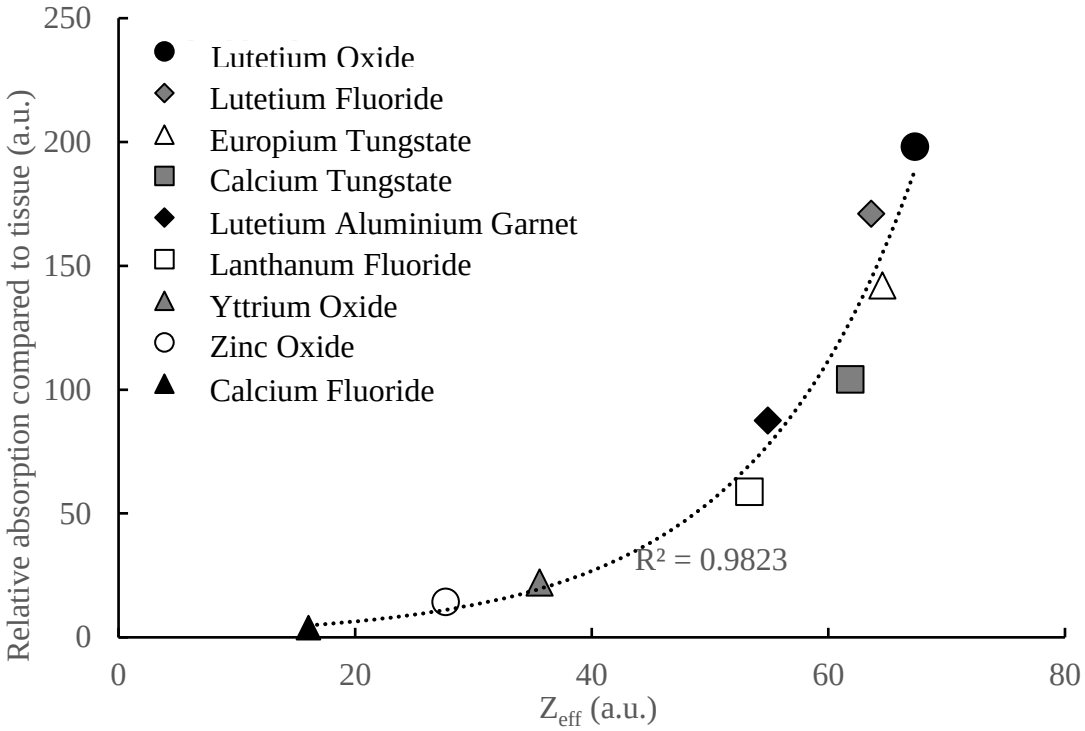

Figure 51 Calculated relative absorption relative to tissue for each material chosen Vs. the calculated effective atomic number (Z_{eff}).

3.1.5. Appropriate sources of ionising radiation

3.1.5.1. Iodine 125(I-125)

The idea of implanting radioactive materials into tumours was first proposed by Pierre Curie in 1901.[173] However, it wasn't until the 1960's that I-125 was introduced in an interstitial cancer therapy for the treatment of lung cancer, lymph nodes and prostate.[174] It has been used in the treatment of brain tumours since 1979[175] and is now the preferred nuclide for the interstitial brachytherapy of brain tumours.[173]

I-125 brachytherapy uses I-125 seeds which are implanted within or near a tumour for a continuous low-dose rate of interstitial irradiation (< 100 cGy/h). However, exclusively low activity seeds (< 20 mCi) are often preferred for a slow proliferating process, which will achieve a dose of 50 - 60 Gy at range of 5 - 20 cGy/h.[173] The continuous low-dose

rate irradiation provides an increased therapeutic ratio as the continual repair of sub-lethal irradiation doses is more efficient in non-neoplastic tissues than in tumours.

I-125 has a very low average photon energy of 28.5 keV. At this energy level, it may prove that LaF_3 and $EuWO_4$, may be the most suitable scintillators for a combinative therapy as they have the highest absorptivity of ionizing radiation at these levels. CaF_2 and ZnO may also prove efficacy at such low energies, particularly ZnO as it may not require conjugation to a photosensitizer, which may in turn increase the efficiency of ROS generation.

3.1.5.2. X-ray tube generators

An X-ray tube has a negative cathode which is heated to emit electrons into an encapsulating vacuum. A potential difference (20 - 200 kV) is applied which accelerates the electrons towards a positive anode, with the kinetic energy (E_k) of the applied voltage, 1 eV being the kinetic energy of a charged particle when accelerated in a potential difference of 1 V. Therefore, if the potential difference is 100 kV, then each electron will have a kinetic energy of 100 keV.

When the electron reaches the anode (usually tungsten), the electron imparts the majority of its energy to the atoms at the anode by instances of ionisation and excitations, with the result that the majority of the energy is transferred into heat energy. However, around one percent of the electrons impacting the target will generate X-rays. This occurs when an electron passes close to or hits an atomic nucleus; it will accelerate in the form of a change in its direction and may lose some energy in the form of a photon. These photons are called bremsstrahlung photons and make up most of the energy spectrum of generated X-rays.

3.1.6. Bremsstrahlung spectrum

Bremsstrahlung X-rays generate a broad distribution of energy, with the majority of the photons generated at lower energies but can range between zero and the whole kinetic energy of the electron. When an electron hits the nucleus directly (**Figure 52**), it loses all of its kinetic energy (E_k) and will create the maximum energy photon (*hv* max), with the same E_k of the impacting electron. This is the lowest probability interaction (about 5% of all interactions) to occur, with further interactions increasing in probability to generate the straight-line spectrum shown in (**Figure 53**).

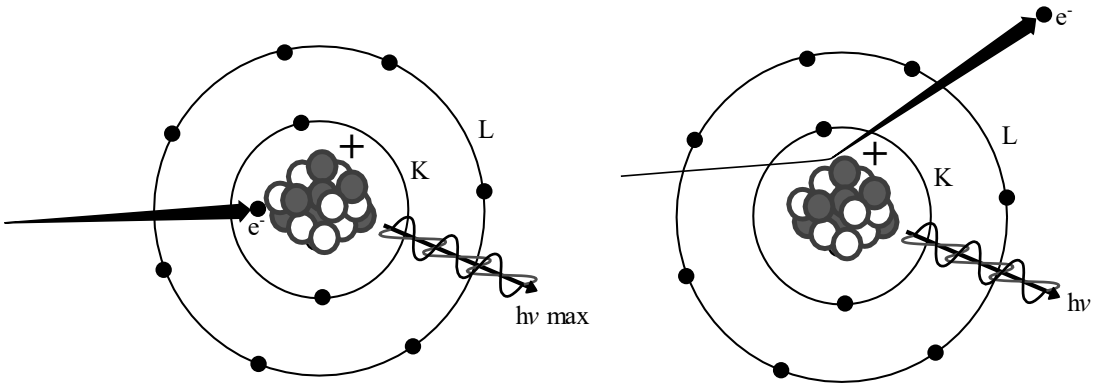

Figure 52 Production of Bremsstrahlung radiation (Left). A direct hit of the atom by the electron leads a loss of all kinetic energy and the maximum energy photon (Right). Near miss leads to a loss of some kinetic energy and lower energy photons.

A theoretical unfiltered spectrum would continue this straight-line distribution. however intrinsic filtration from the anode and additional filters block out the very low energy photons, < 10 keV, as these would have minimal to no tissue penetration and would instead damage the skin of the patient.

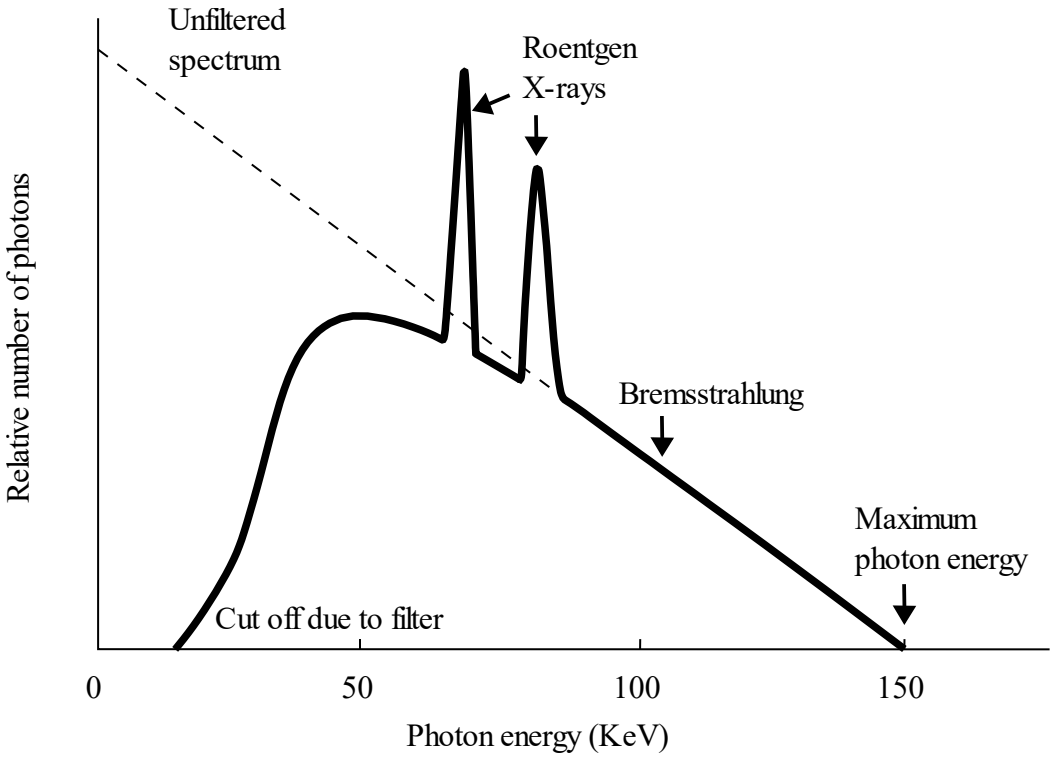

Figure 53 Representation energy spectrum of X-ray tube with tungsten anode using a copper filter.[176]

The sharp peaks shown in the spectrum (**Figure 53**) are the characteristic Roentgen rays (fluorescence radiation) corresponding to the Kα and Kβ photons. An incoming electron with a kinetic energy above the K-shell binding energy collides and ejects (ionises) this K-shell electron creating a vacancy (**Figure 54**).[176] An electron from an outer orbital (L or M) may then fill the vacancy. The difference in the binding energy between the two shells is then radiated as an X-ray photon, which from a tungsten anode gives 59.31 and 67.23 keV, respectively.[177] They can be caused by either ionisations due to the accelerated electrons or the photoelectric absorption of Bremsstrahlung photons with an energy higher than the binding energy of the electrons in the K shell.[164]

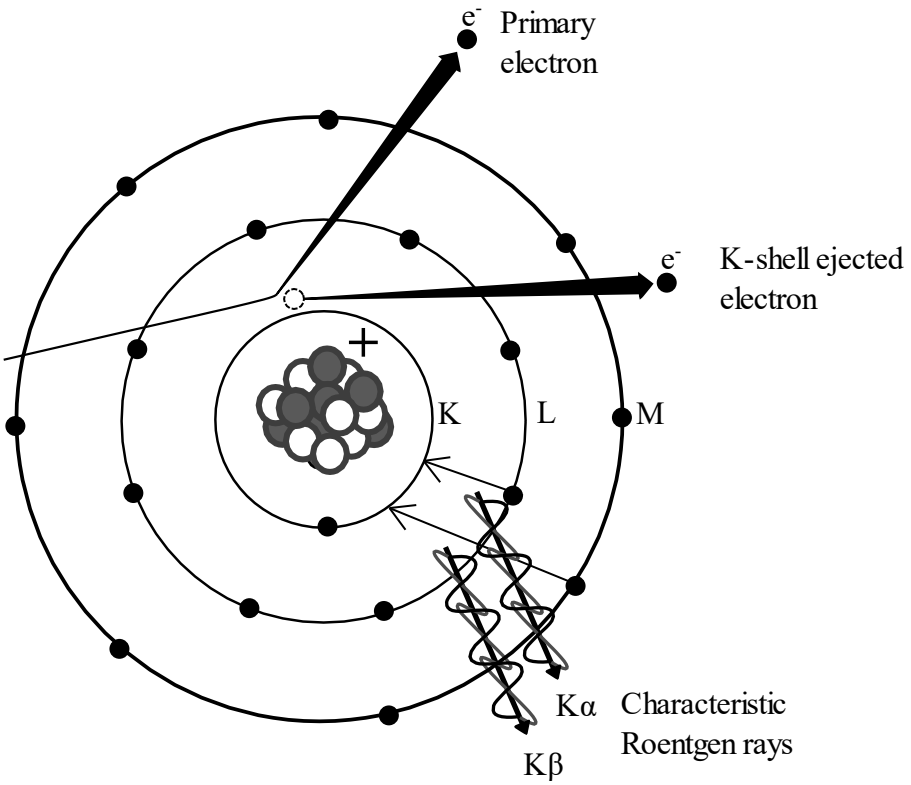

Figure 54 Generation of Roentgen rays. A primary electron with energy above the binding energy of a K-shell electron causes ionisation. An L or M shell electron fills the vacancy generating an X-ray of energy equal to the difference between the binding energies of the two electrons.

3.1.7. Tube potential

The potential applied to the X-ray tube will determine the maximum photon energy, the proportion of higher energy photons or average energy, and whether the Roentgen rays of the anode material are present (**Figure 55**).[177] A rule of thumb states that the effective energy is about 1/3 to 1/2 of the maximum X-ray energy.[176] If the acceleration potential is maintained but the charge through the tube is increased (mAs), the shape of the spectrum will remain the same but the number of photons at each energy level in increases proportionally to the mAs value.[178]

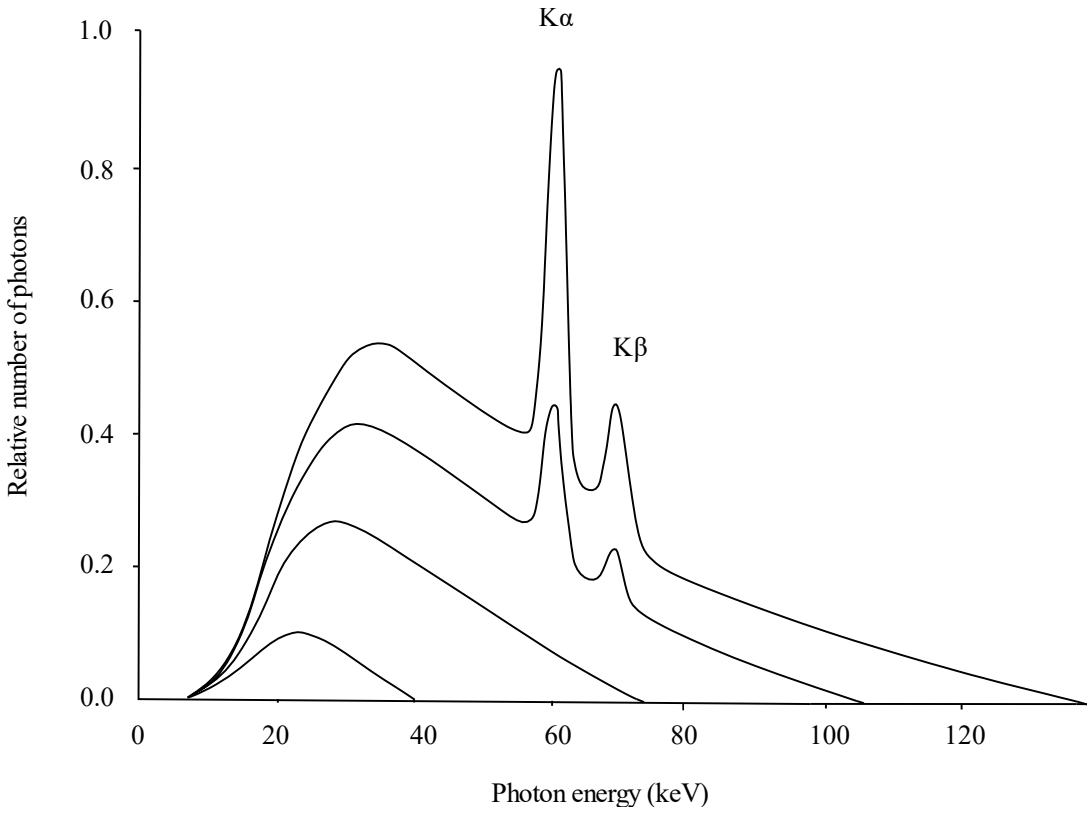

Figure 55 Energy spectrum generated for an X-ray tube with increasing potential difference.[178]

3.2. Research aims and objectives

The aims of this investigation are to synthesise a range of suitable inorganic materials of a high density and Z_{eff}, and to investigate their potential as nanoscale scintillators for the effective energy transfer and stimulation of attached photosensitisers. The successful synthesis and characterisation of each material will be undertaken as well as a test of the materials' ability to fluoresce under the excitation of ionising irradiation.

Upon successful synthesis and characterisation of each material, the nanoparticles will be excited by either an iridium-192 source, with an average energy of 0.370 MeV, or using an X-ray tube from a RadSource-2000 biological irradiator. In each case the luminescence produced by scintillation mechanisms will be measured using a fibre optic cable connected to an Ocean Optics Spectrophotometer, to assess the relative intensity and

wavelength of the light produced, to determine if it is suitable for conjugation to a porphyrin-based photosensitiser.

3.3. Results

3.3.1. Calcium tungstate

$CaWO_4$ is from a family of alkaline earth tungstates with scheelite structure which exhibit thermoluminescence, excitonic luminescence and electro-optical properties.[179,180] It has been used in scintillators for medical devices,[181–184] as well as quantum electronics, laser host materials,[183–186] optical fibre components and even for the detection of dark matter.[187]

$CaWO_4$ also has excellent potential as a scintillator due to its high density (6.06 gcm^{-3}) and high Z-value atoms (Z_{eff} 61.87) as well as having very high light output.[188] $CaWO_4$ exhibits a blue emission luminescence between 420 - 450 nm and a green emission with strong overlap with the blue emission. The blue emission around 420 nm has been shown to be due to self-trapped excitons associated with the WO_4^{2-} species within the lattice and the green emission is due to defect levels present within the optical gap. This very broad emission spectrum has excellent overlap with the strongest absorption band (Soret) in the spectrum of porphyrin based photosensitisers, and even some of the weaker, longer wavelength absorption bands (Q-bands) (**Figure 56**).

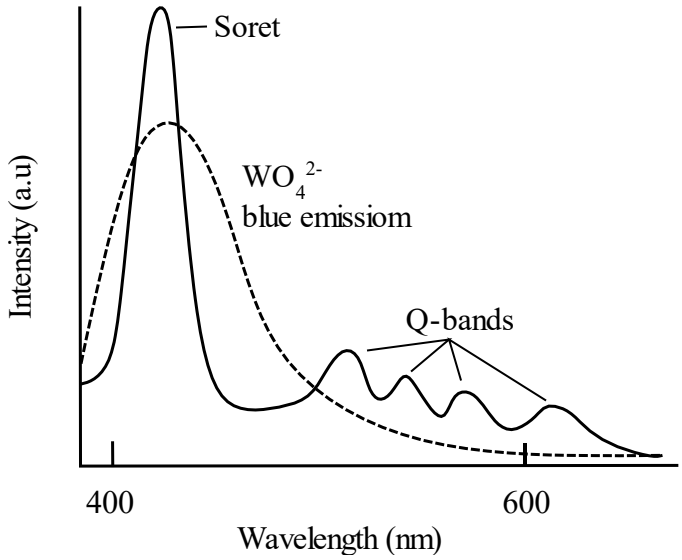

Figure 56 Spectral overlap of porphyrin PSs and $CaWO_4$.

Due to the high absorption K-edge of tungsten (69.5 keV), within $CaWO_4$ (**Figure 57**) this material has a lot of potential in the higher energy range brachytherapies such as Ir-192. It is also considerably less expensive than a large number of the other materials under investigation.

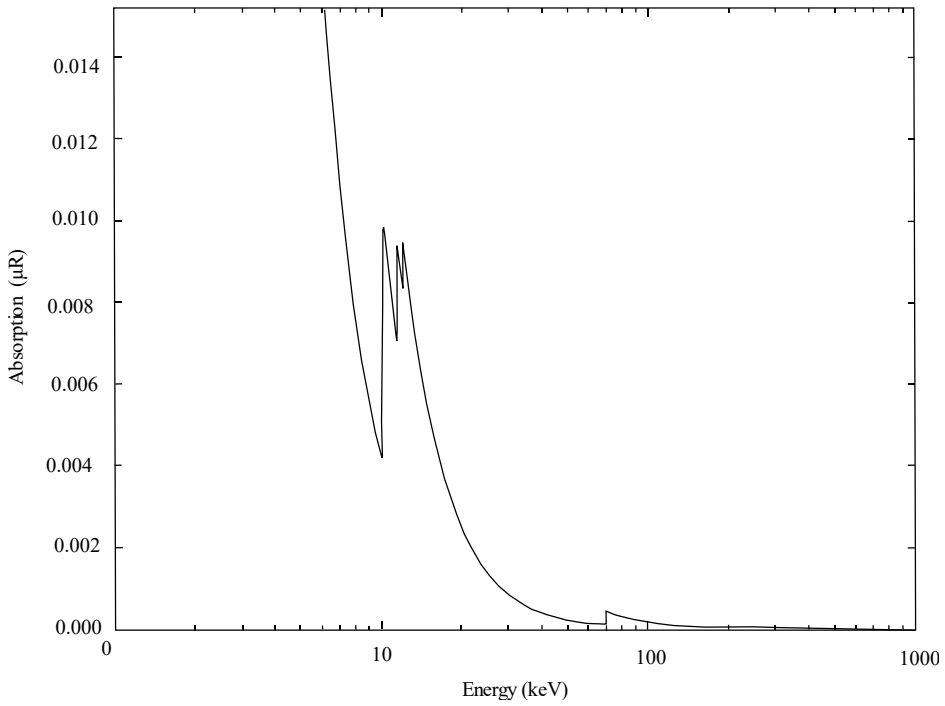

Figure 57 Absorption of $CaWO_4$ to ionising radiation of increasing energy.

3.3.1.1. Synthesis of $CaWO_4$ nanoparticles

Previously reported $CaWO_4$ nanoparticles synthetic methods have included solid state reaction,[189] Pechini method,[190] polymeric precursor method,[191] co-precipitation,[192] solvothermal[185] and combustion methods.[193]

$CaWO_4$ nanoparticles **[10]** were synthesised by a hydrothermal method in which the product was precipitated from a solution of ($Ca(NO_3)_2.4H_2O$ AR) and ($Na_2WO_4{\cdot}2H_2O$ A) solution, acting as the sources of Ca^{2+} and WO_4^{2-} respectively. Analytical grade chemicals were obtained from Sigma Aldrich and used as received. A solution of 500 mg ($Ca(NO_3)_2{\cdot}4H_2O$) in deionised water (DI) (15 ml) was added dropwise to a solution of 750 mg $Na_2WO_4{\cdot}2H_2O$ in DI water (15 ml). Sodium hydroxide was added to adjust the reaction pH to 9 - 9.5. Finally, 5 mL of ethylene glycol (EG) was added and the reaction was heated under reflux at 100 ℃ for three hours. The resulting white precipitate was collected by centrifugation at 15,000 rpm for 10 min, washed several times with water and acetone and dried in a vacuum oven at 50 ℃, overnight.

3.3.1.2. Powder X-ray diffraction of $CaWO_4$ nanoparticles

PXRD analysis was used to determine the purity and the structure of the synthesised $CaWO_4$ nanoparticles (**Figure 58**). The PXRD pattern shows that all diffraction peaks can be attributed to $CaWO_4$ with a tetragonal unit cell. The lattice constants calculated a = 0.5242 and c = 1.1372 nm, are consistent with the standard card (JCPDS no. 07-0210). All peaks were indexed and the product was found to be of a single phase.

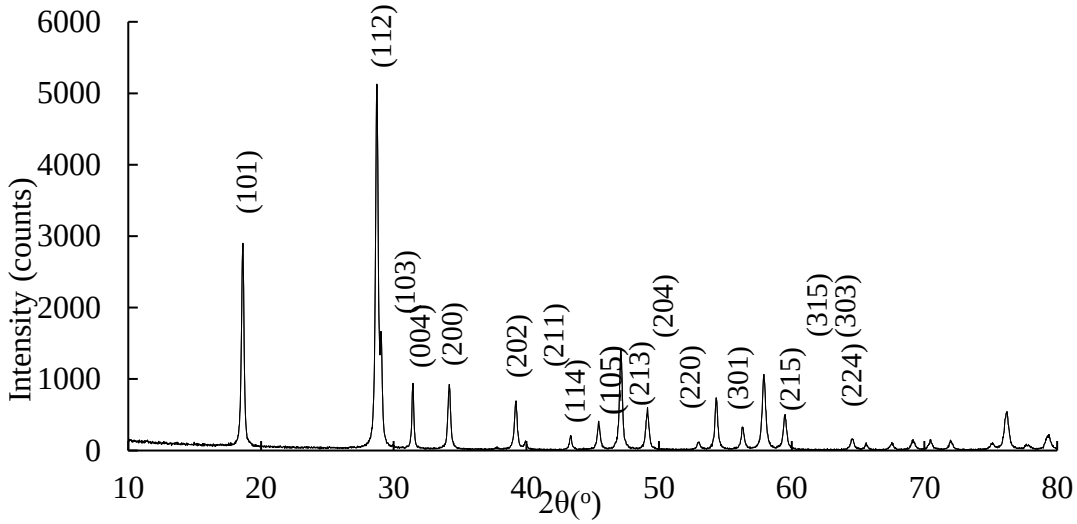

Figure 58 X-ray diffraction pattern of the synthesised $CaWO_4$ nanoparticles **[10]**.

The average diameter of nanoparticles *D* was determined according to the Scherrer equation,[194]

$$D = k\lambda / \beta \cos\theta \quad \textit{Equation 6}$$

where *k* is a constant (about 0.9), λ is the X-ray wavelength (0.15148 nm), β is the full width at half maximum (FWHM) of the diffraction line, and θ is the diffraction angle. Based on the average of all the reflections with an intensity over 500 counts the nanoparticles were determined to be 60.9 nm, which was in good agreement with the scanning electron microscopy (SEM) (**Figure 59**). From SEM the average size was found to be 63.2 ± 5.3 nm.

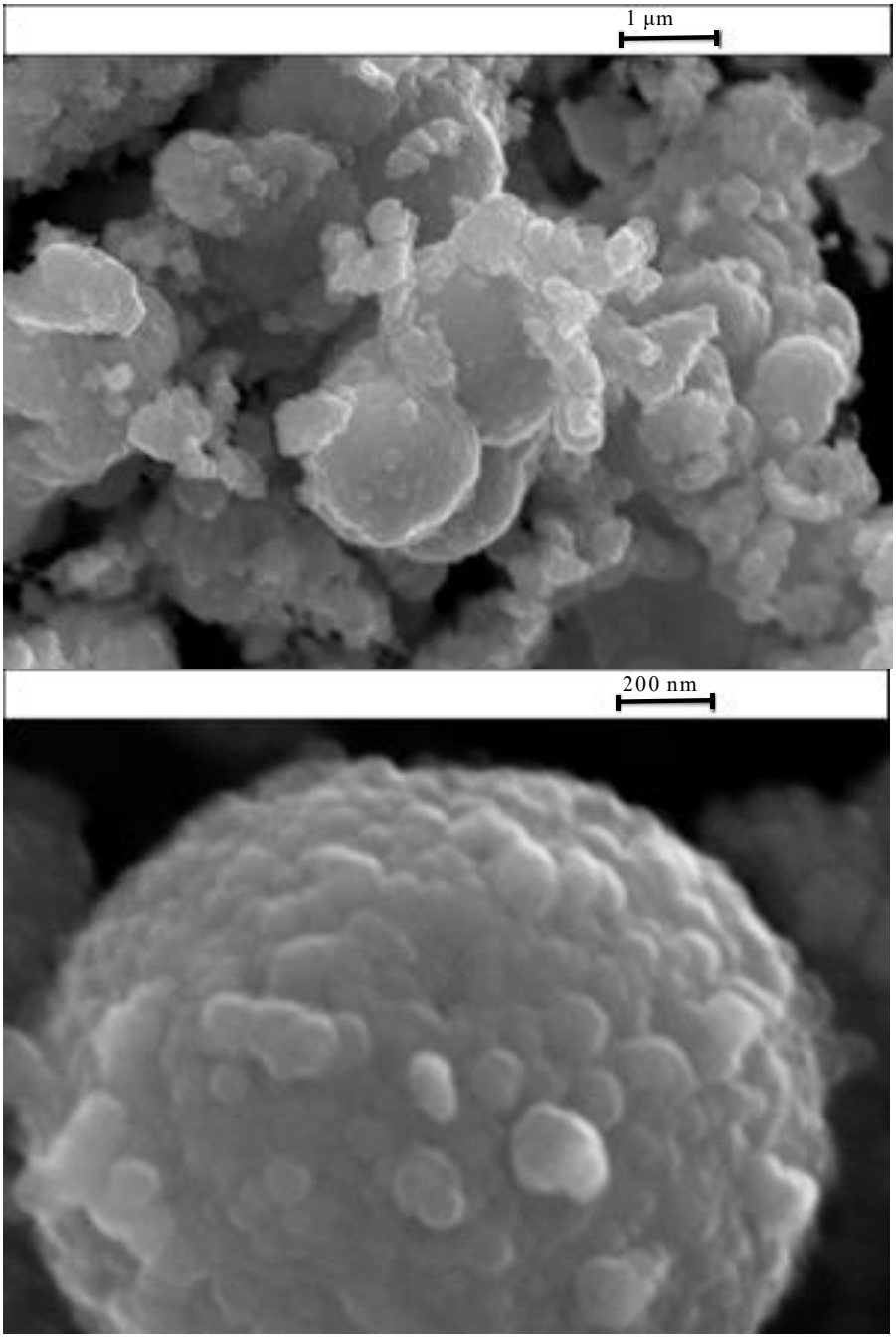

Figure 59 Scanning electron microscope image on $CaWO_4$ **[10]** nanoparticles.

3.3.1.3. X-ray induced luminescence (XRIL) spectra of $CaWO_4$ nanoparticles

There have been no reported accounts of $CaWO_4$ nanoparticles synthesised for X-ray excited optical luminescence to date hence this work constitues the first account of scintillation luminescence recorded for this material on the nanoscale. Despite the high density, cheap and facile synthesis and excellent spectral overlap with many

photosensitisers (PSs), $CaWO_4$ has also not previously been considered as a potential component in scintillating nanoparticle-photosensitiser conjugates.

Figure 60 shows the luminescence of $CaWO_4$ nanoparticles **[10]** irradiated with an Ir-192 source from a brachytherapy suite. Ir-192 decays by beta (β) and gamma (γ) radiation from seven principle energy packets ranging in energy from 200 to 600 keV with an average energy maximum at 330 keV. Irradiation of nanoparticles using Ir-192 as an excitation source has also not previously been reported in the literature. The scintillation luminescence observed for nanoparticle **[10]** was found to have a fairly low intensity, broad band covering the region 400 - 550 nm. However it matched perfectly with the intended PSs, and matches the UV excited luminescence associated with this material.[188]

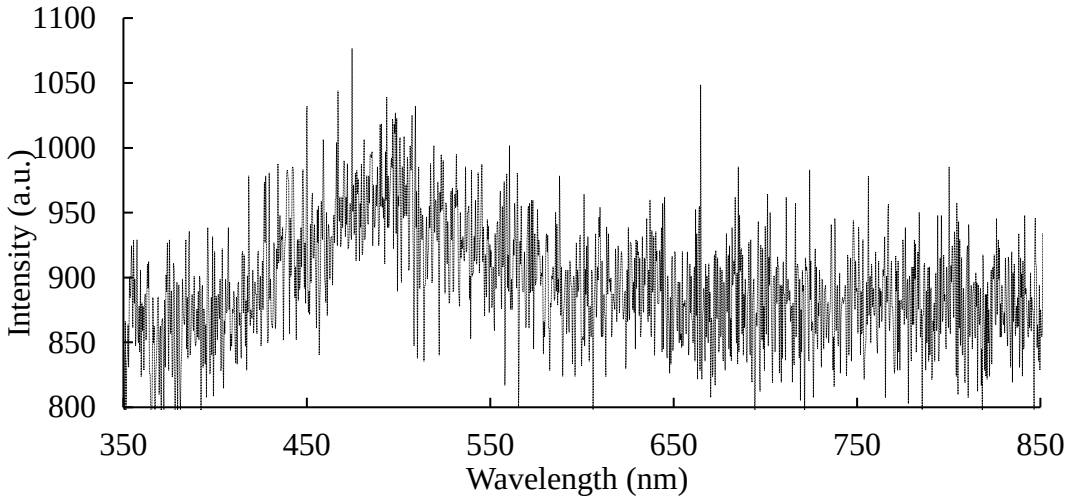

Figure 60 X-ray excited (Ir-192 source) luminescence spectrum of $CaWO_4$ nanoparticles **[10]**.

3.3.1.4. Microwave synthesised $CaWO_4$ nanoparticles

$CaWO_4$ nanoparticles have been synthesised in the literature *via* microwave[195] synthesis previously. The diffusion length of free carriers within $CaWO_4$ is reported to be of the order of 100 nm.[194,196] Therefore larger nanoparticles are likely to attenuate higher energy

X-rays far better than smaller ones. For this reason, we aimed to increase the size of nanoparticles synthesised to 100 nm to improve the scintillation luminescence intensity.

3.3.1.5. Characterisation of microwave synthesised $CaWO_4$ nanoparticles

PXRD (**Figure 61**) shows a pure single phase product with the same reflections observed for the bench synthesised product **[11]**. However, the peaks are more defined, and the Scherrer equation calculates an increase in size to 109.4 nm. This increase in size is corroborated by SEM images which confirm an above 100 nm nanoparticle average of 104.5 ± 2.4 nm as desired. The morphology of the nanoparticle aggregates had fundamentally changed into homogenously sized and spaced spheroids (**Figure 62**). The homogeneity of the size of nanoparticles that form the aggregates was also increased.

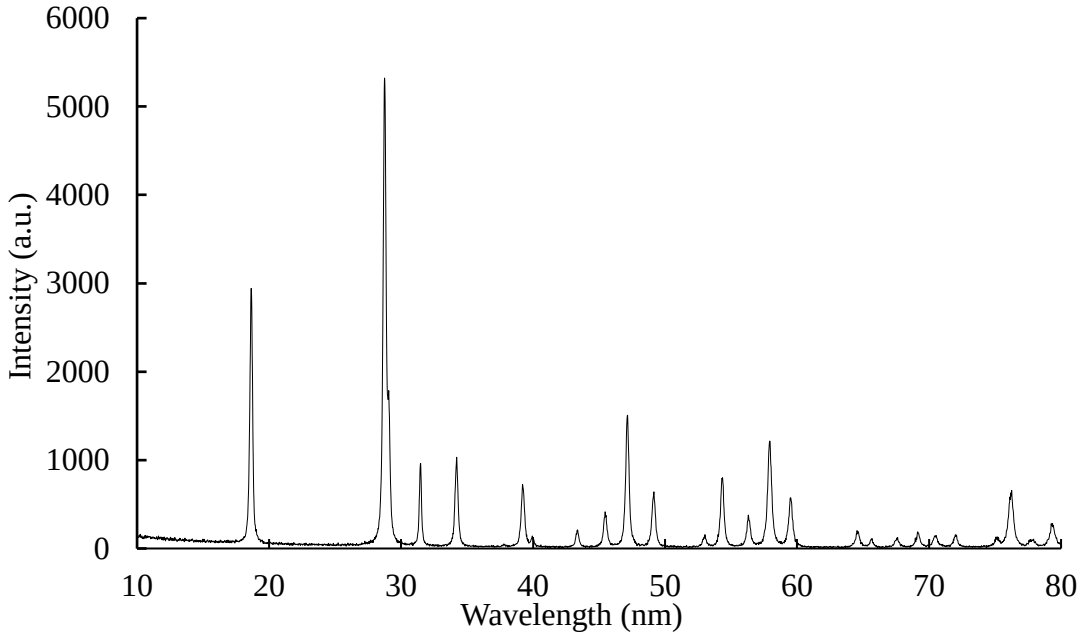

Figure 61 X-ray diffraction pattern of $CaWO_4$ product **[11]**.

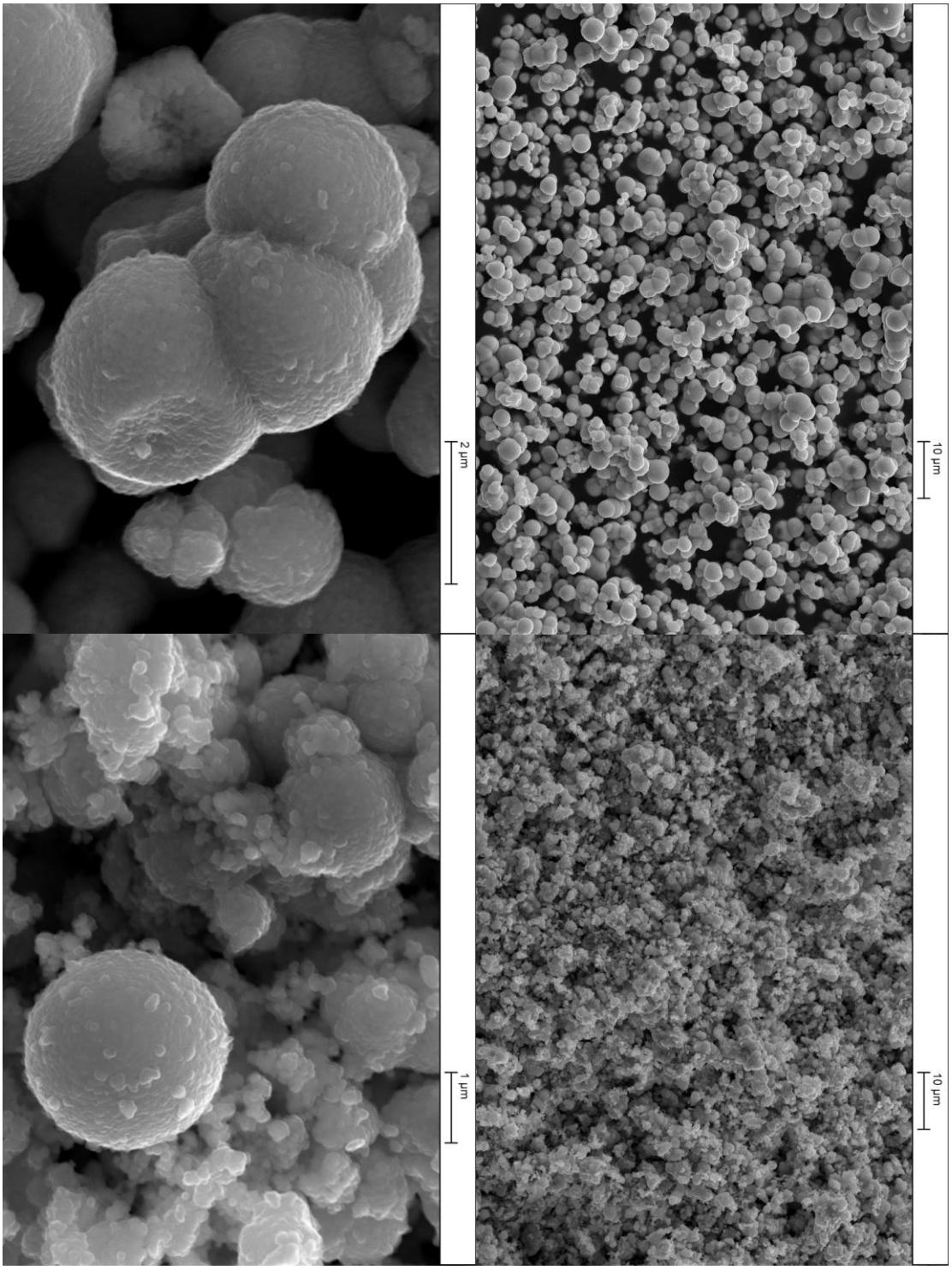

Figure 62 SEM image of $CaWO_4$ **[11]** nanoparticles (top left and right) compared with benchtop prepared **[10]** (bottom left and right).

3.3.1.6. X-ray induced luminescence (XRIL) spectra of $CaWO_4$ nanoparticles

Scintillation luminescence of nanoparticles **[11]** was measured using the Ir-192 source in the same reaction conditions as had been used for nanoparticles **[10]**. A clear increase in

luminescent intensity was observed for the samples prepared *via* microwave-based synthesis (**Figure 63**).

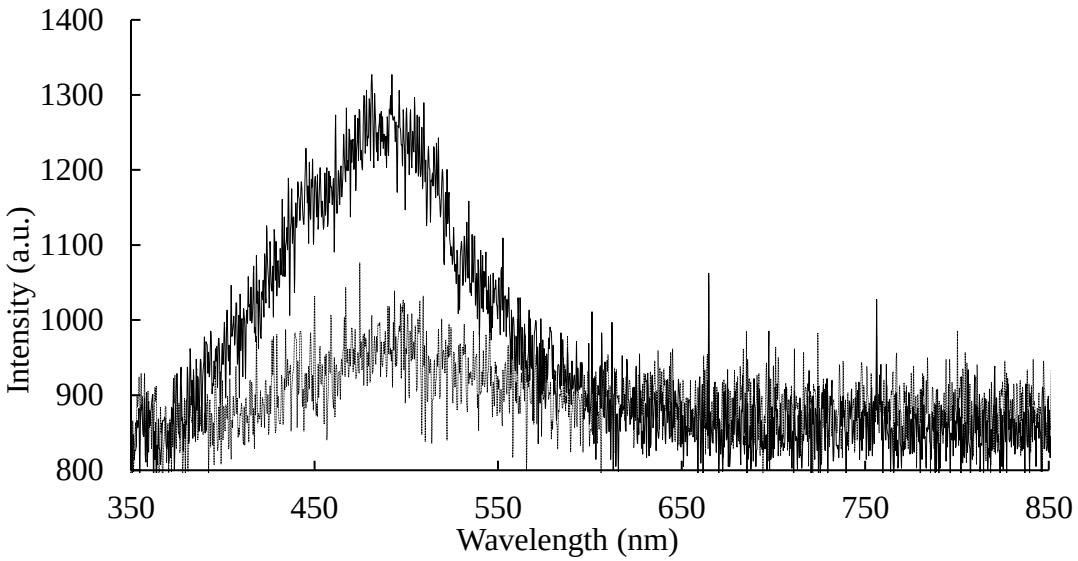

Figure 63 X-ray excited (Ir-192 source) luminescence spectrum of $CaWO_4$ nanoparticles prepared *via* microwave-based synthesis **[10]** (black). $CaWO_4$ nanoparticles prepared *via* hydrothermal method **[11]** shown (grey) for comparison.

3.3.1.7 Microwave anomaly

An interesting effect was observed whilst trialling reaction conditions to identify the optimum set for synthesis *via* microwave heating. Upon increasing the temperature by just 20 °C from previously outlined procedure to 200 °C, a morphological and chemical change occurs. **Figure 64** shows SEM images of this sample, it can be seen that together with nanoparticles there are large sheets and needles which have a transparent appearance, indicating extremely thin depth.

PXRD of this compound indicates that the sample contains single-phase $CaWO_4$. There is no reference to this occurrence in the literature, and without further investigation it is impossible to be sure of the nature of these thin sheets. The luminescence intensity upon

X-ray irradiation is entirely quenched, making this structure useless for the intended application. One hypothesis is that Ca^{2+} layers within the tungstate structure are removed as $Ca(OH)_2$ leaving atomically thin MXene like sheets of WO_3,[197] though this has not been synthesised from $CaWO_4$ previously.

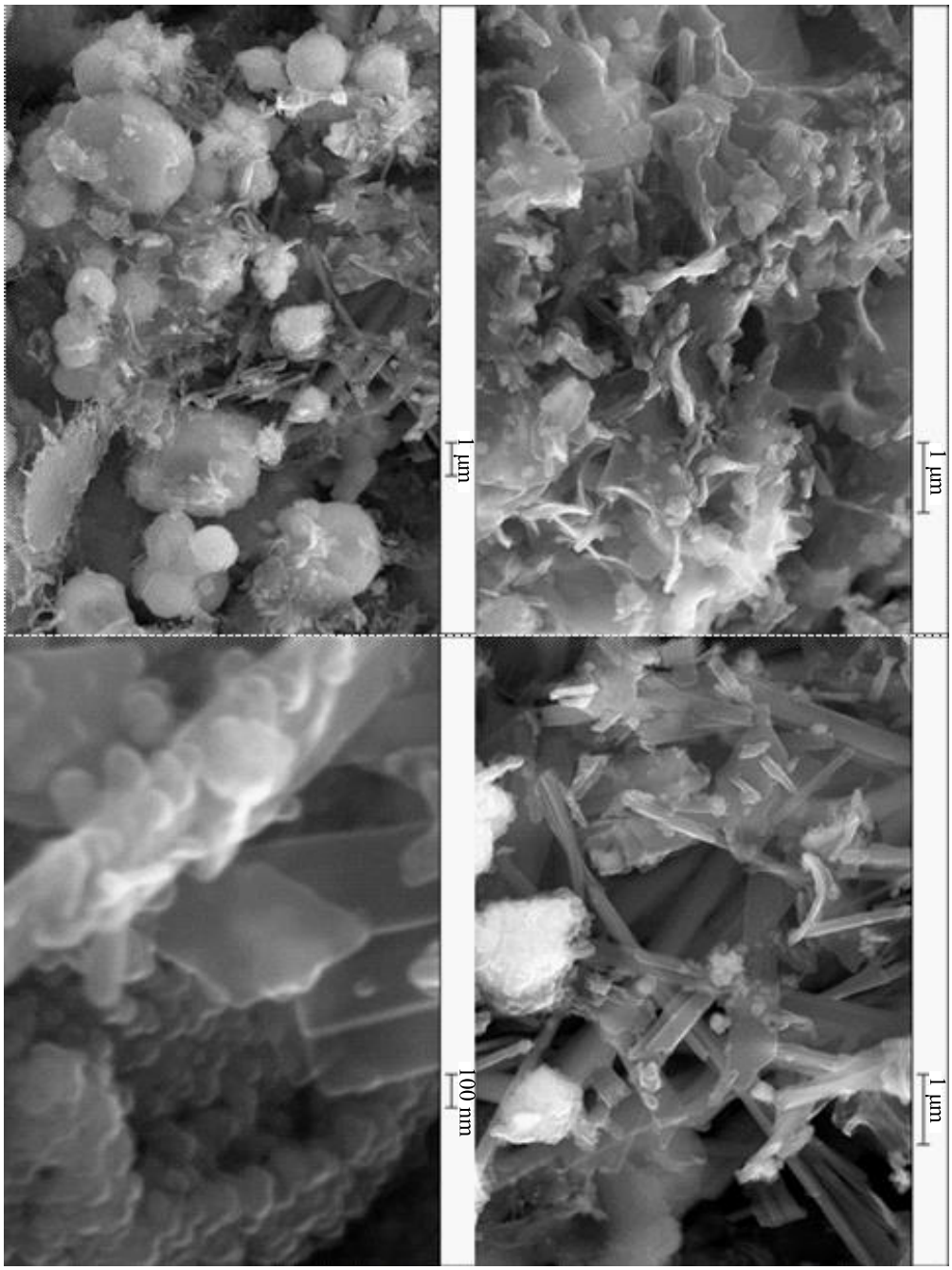

Figure 64 SEM images of anomaly, a mixture of $CaWO_4$ nanoparticles and thin sheets of undetermined origin.

3.3.2. Europium doping of $CaWO_4$ nanoparticles ($Ca_{1-x}Eu_xWO_4$)

As well as the strongly absorbing Soret band within the porphyrin PS absorption spectrum, there are weaker Q-bands at longer wavelengths (**Figure 65**), with increased tissue penetration, which are usually targeted for traditional light delivery methods for PDT. It was reasoned that it may be possible to target the longest wavelength band in order for nanoparticles to activate nearby PSs as well as those directly attached, which could lead to a higher efficiency system. For this reason, $CaWO_4$ was doped with europium to try to achieve spectral overlap with the absorption band of the longest wavelength around 600 nm, as well as the strongly absorbing Soret band at 420 nm. Additionally, non-porphyrin PSs such as chlorins and methylene blue may also be used at this wavelength.

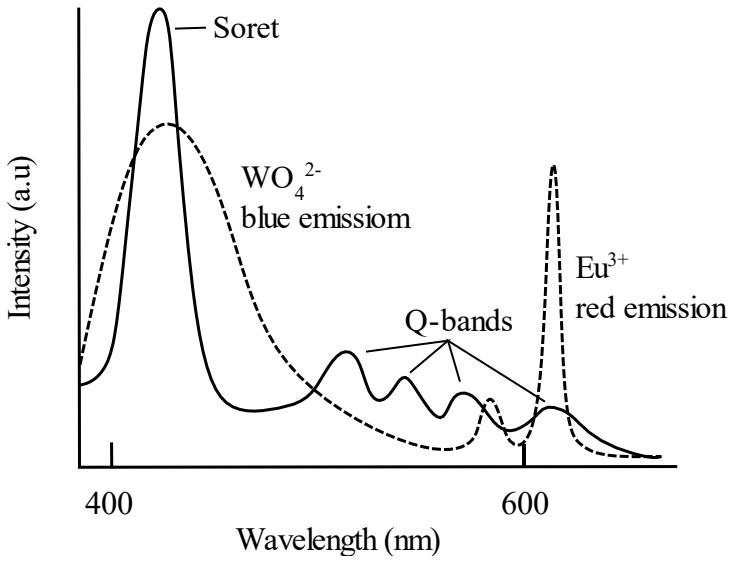

Figure 65 Spectral overlap of a typical porphyrin absorption spectrum with europium doped $CaWO_4$.

As well as tungstates acting as self-activating phosphors, europium doped tungstates have demonstrated an effective transfer of energy to the Eu^{3+} ions to generate a strong red emission.[198] **Figure 66** shows the transition peaks at 592 nm ($^5D_0 \rightarrow {}^7F_1$) and 650 nm

($^5D_0 \rightarrow {}^7F_3$) are due to magnetic dipole transitions and 612 nm ($^5D_0 \rightarrow {}^7F_2$) and 705 nm ($^5D_0 \rightarrow {}^7F_4$) are due to electric dipole transitions.[199] The highly prominent $^5D_0 \rightarrow {}^7F_2$ transition is therefore due to an efficient transfer of energy from tungsten to the Eu^{3+} cation. It also indicates that the Eu^{3+} ions are located at sites without inversion centers.[200]

The tetragonal scheelite structure of $CaWO_4$ has a C_{4h} space group which has a Ca^{2+} ion coordinated by eight oxygen atoms and has an S_4 point symmetry, without an inversion center.[201] The ionic radii for Eu^{3+} (0.107 nm) and Ca^{2+} (0.112 nm); for eight coordination,[202] are close enough that within the host lattice the Eu^{3+} ions will substitute the Ca^{2+} ions. Three Ca^{2+} ions are replaced by two Eu^{3+} ions, $Ca_{1-1.5X}Eu_XWO_4$, in which charge compensation is provided by calcium vancancy.[203]

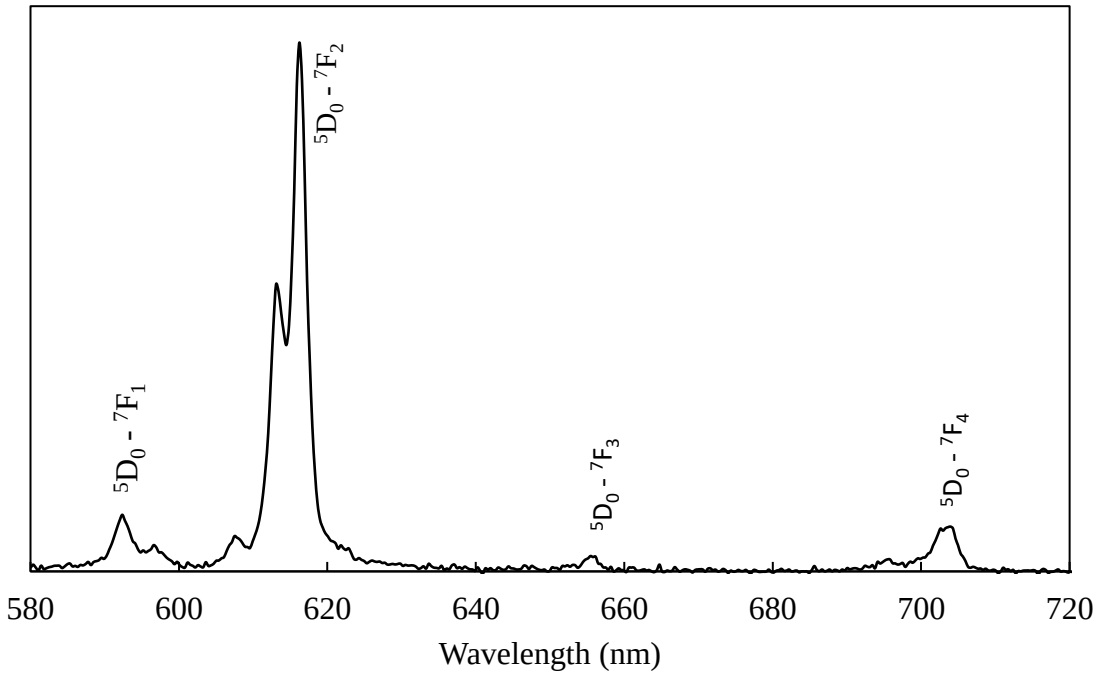

Figure 66 XRIL spectrum of europium doped $CaWO_4$ nanoparticles.

3.3.2.1. Synthesis of europium-doped nanoparticles

Synthesis of nanoparticles used a modified method to what has been previously described for the benchtop synthesis of $CaWO_4$ nanoparticles. Nanoparticles were prepared by substituting a molar percentage of $Eu(NO_3)_3{\cdot}6H_2O$ for that of $Ca(NO_3)_2{\cdot}4H_2O$ to give $Ca_{1-X}Eu_XWO_4$ prepared at 3%, 10% 15% and 20% (**Table 5**).

Table 5 Europium-doped molar percentages prepared, with EDX to confirm Eu uptake and size of particles, determined from SEM

NP sample	Molar percentage prepared (%)	EDX molar percentage (%)	Average size (nm)
[10]	0	0	62 ± 5
[12]	3	2.8	85 ± 11
[13]	10	11.9	70 ± 5
[14]	15	14.0	89 ± 7
[15]	20	20.6	88 ± 8

SEM was used to determine the size of the nanoparticles formed whilst EDX confirmed the molar percentages of Eu^{3+} present.

3.3.2.2. Characterisation of europium-doped nanoparticles

Figure 67 shows the PXRD pattern of prepared samples of 0, 3, 10, 15 and 20% Eu^{3+} doping. XRD patterns agree with the tetragonal system of pure $CaWO_4$ (01-072-1624). Patterns do not exhibit the presence of any other phases or impurities, suggesting that Eu^{3+} has been successfully doped within the lattice sites. The lattice parameters for each of the samples is shown in **Table 6**.

Table 6 Unit cell parameters of samples prepared at 0, 3, 10, 15 and 20% europium-doped CaWO4 NPs.

NP sample	Molar percentage prepared (%)	*a = b (Å)*	*c (Å)*	*V (Å^3)*
[10]	0	5.2400(7)	11.362(2)	311.99
[12]	3	5.2407(7)	11.363(2)	312.09
[13]	10	5.239(2)	11.363(4)	311.84
[14]	15	5.2422(7)	11.372(2)	312.50
[15]	20	5.243(1)	11.366(3)	312.41

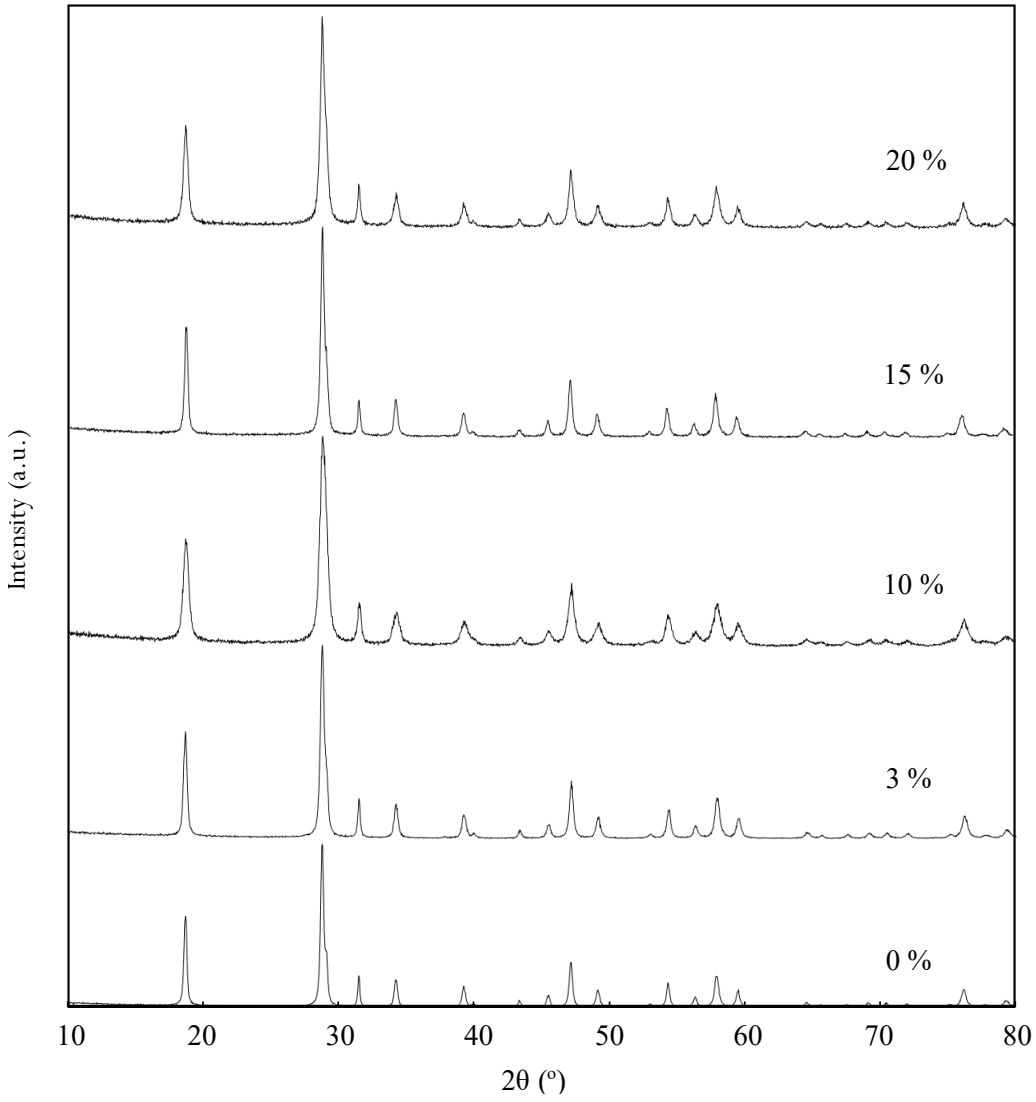

Figure 67 PXRD patterns of samples prepared at 0, 3, 10, 15 and 20% europium-doped $CaWO_4$ NPs.

3.3.2.3. X-ray induced luminescence (XRIL) spectra of europium-doped $CaWO_4$ nanoparticles

The most prominent transition observed from the luminescence of Ir-192 excited nanoparticles was the $^5D_0 \rightarrow {}^7F_2$ transition (614 nm), from an electric dipole transition, arising from transfer of energy from the tungstate group to the Eu^{3+} ion. There is also an increase in intensity of the red luminescence with increasing doping concentration as has been observed in the literature for UV excitation of Eu^{3+} doped $CaWO_4$.[200]

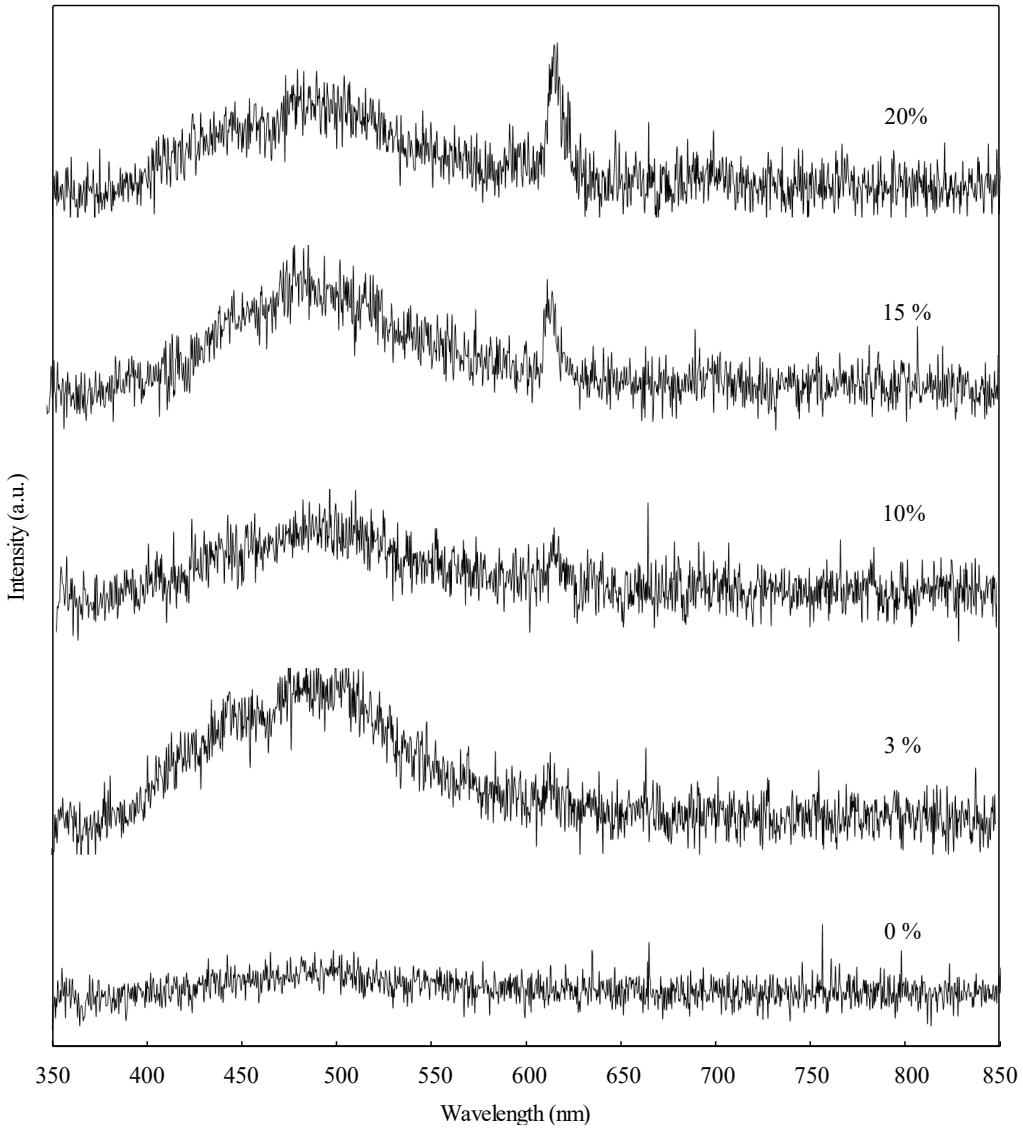

Figure 68 XRIL spectra of europium-doped $CaWO_4$ nanoparticles under Ir-192 irradiation.

3.3.3. Microwave prepared europium-doped $CaWO_4$ nanoparticles

Due to the improved homogeneity of the microwave synthesised product **[11]**. This method was again extended to the europium doped nanoparticles at molar percentages of 10 and 20% for the products **[16]** $Ca_{0.9}Eu_{0.1}WO_4$ and **[17]** $Ca_{0.8}Eu_{0.2}WO_4$.

3.3.3.1. Characterisation of microwave prepared europium-doped nanoparticles

Figure 69 shows the PXRD pattern of prepared samples of 10 and 20% Eu^{3+} doping, giving products **[16]** $Ca_{0.9}Eu_{0.1}WO_4$ and **[17]** $Ca_{0.8}Eu_{0.2}WO_4$. XRD patterns agree with the tetragonal system of pure $CaWO_4$ (01-072-1624). Patterns do not exhibit the presence of any other phases or impurities, suggesting that Eu^{3+} has been successfully doped within the lattice sites. The lattice parameters for each of the samples are shown in **Table 7**.

Table 7 Unit cell parameters of samples prepared at 10 and 20% europium-doped $CaWO_4$ NPs.

NP sample	Molar percentage Eu prepared (%)	*a = b (Å)*	*c (Å)*	*V (Å^3)*
[11]	0	5.241(1)	11.373(4)	312.45
[16]	10	5.242(1)	11.373(3)	312.47
[17]	20	5.242(1)	11.372(3)	312.48

The lattice parameters are strikingly similar at 0, 10 and 20% europium doping. Previously for the non-microwaved synthesised products shown in **Table 6**, there was a great deal of variation, although it did not follow any particular trend. This appears to be another example of the homogeneity in product of microwave prepared samples.

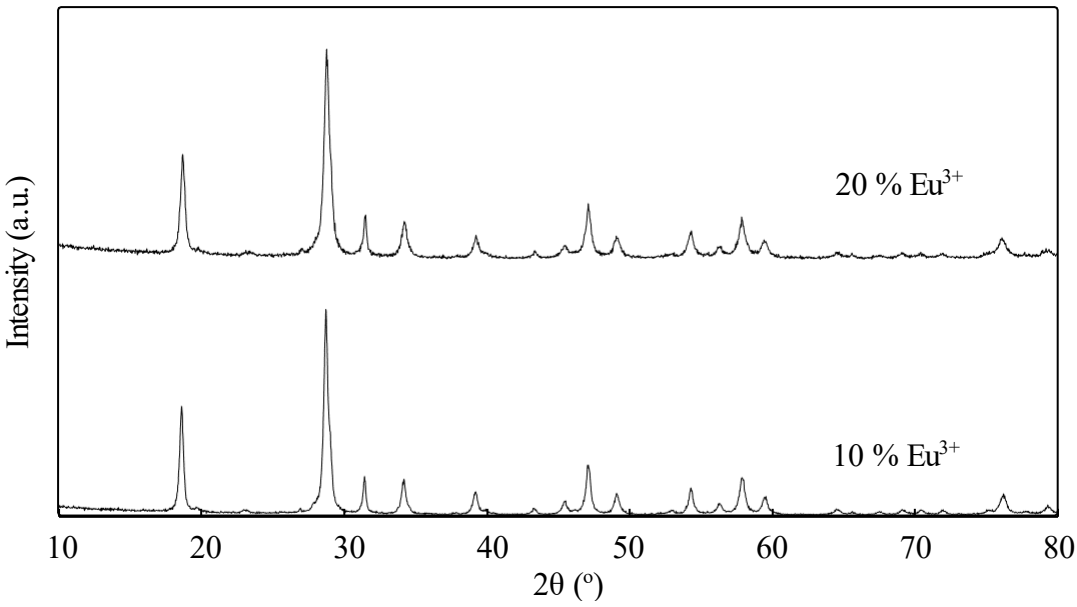

Figure 69 PXRD patterns of microwave prepared samples **[16]** and **[17]** europium doped at 10 and 20% respectively.

Figure 70 shows the SEM of products **[16]** and **[17]** exhibited a change in morphology to the non-microwaved products as well as the microwaved product with no europium present. Under these conditions the morpholgy changes from spheroid particles to short nanorods. Nanoparticle size increased to give a width of 90 nm ± 9 nm and a length of 196 nm ± 20 for NPs **[16]** and a width of 82 nm ± 12 and a length 201 nm ± 16 for NPs **[17]**. Measurements were taken from over 50 nanoparticles using several locations within the sample.

EDX was used to confirm the percentage of europium incorporated which was found to be 12.8% and 22.5% for **[16]** and **[17]** respectively.

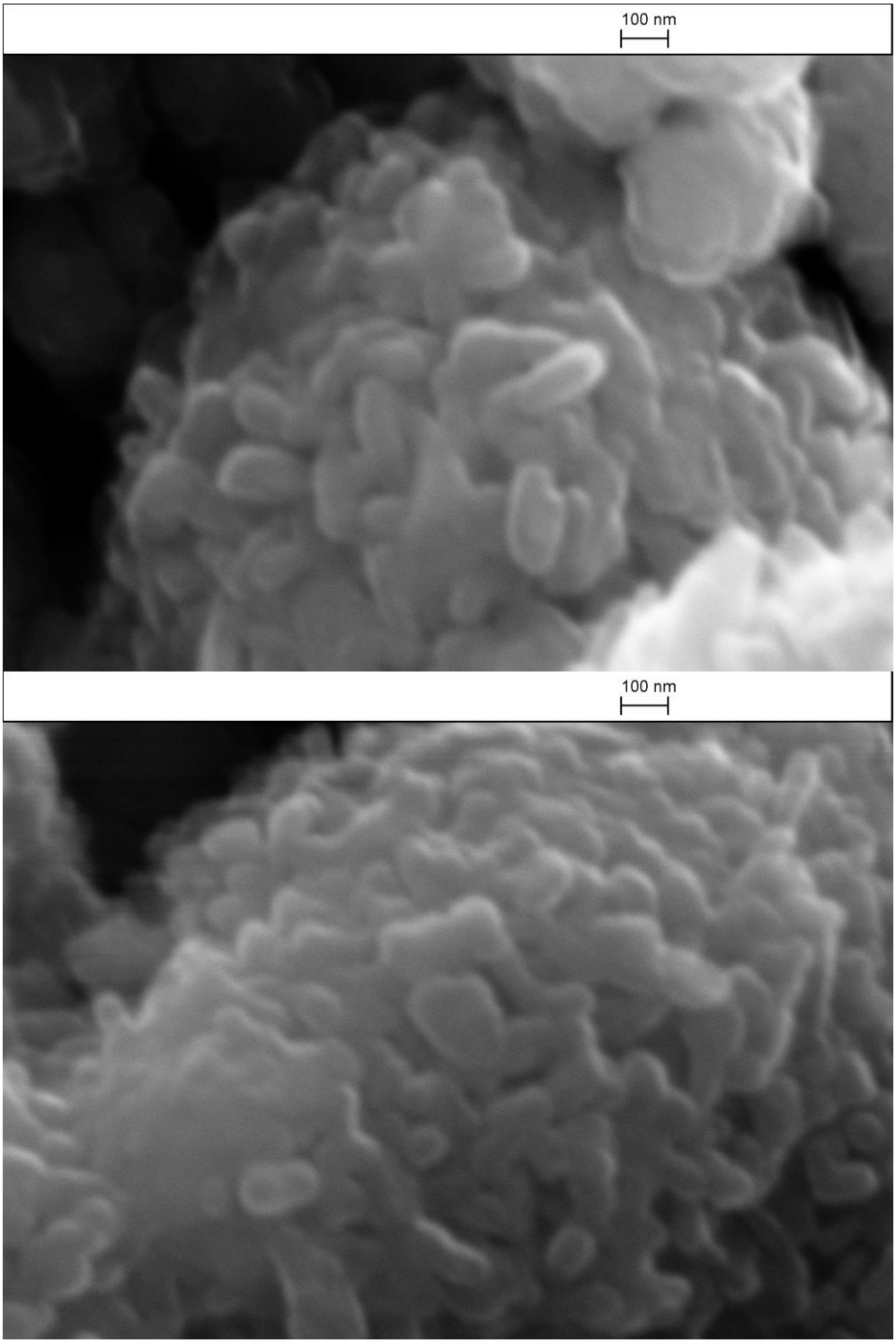

Figure 70 SEM of microwave prepared europium-doped CaWO4 NPs. **[8]** 10% Eu (top), **[9]** 20% Eu (bottom).

3.3.3.2. X-ray induced luminescence (XRIL) spectra of microwave prepared europium-doped $CaWO_4$ nanoparticles

It can be seen from the XRIL spectra of the microwave prepared samples **[11]**, **[16]** and **[17]** that the predominant emission observed for the doped samples is at 614 nm, corresponding to the electric dipole transition $^5D_0 \rightarrow {}^7F_2$. Interestingly the luminescence associated with the WO_4^{2-} ion diminishes as Eu^{3+} content increases, suggesting an efficient transfer of energy from the donor ion to the activator ion.[199] This may indicate that the microwaved samples more efficiently place the Eu^{3+} ions within the Ca^{2+} lattice position.

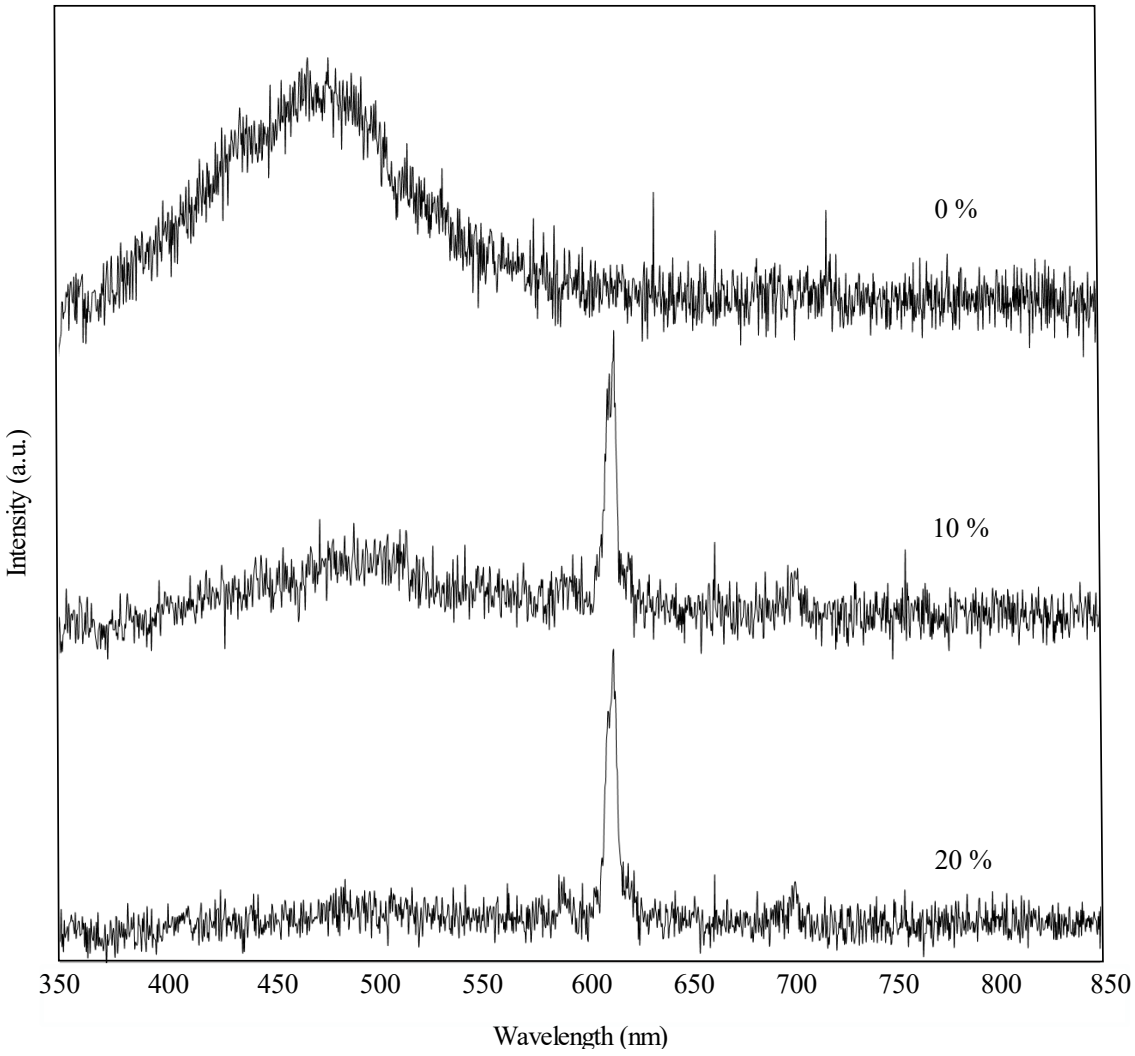

Figure 71 XRIL spectra of microwave prepared europium doped $CaWO_4$ nanoparticles **[11]**, **[16]** and **[17]** under Ir-192 irradiation.

3.3.4. Annealing study of $CaWO_4$ nanoparticles

The effect of annealing nanoparticles at high temperature has previously been shown to increase both the size of nanoparticles, and the luminescence intensity from UV excitation.[188] Previous investigation into the thermoluminescent (TL) effects of annealing $CaWO_4$ and Eu-doped $CaWO_4$ nanoparticles revealed an increase in luminescence under the irradiation of UV excitation.[199] Here, we investigate the effects of annealing at increasing temperatures, first upon $CaWO_4$ NPs and then upon NPs doped with varying molar percentages of Eu.

3.3.4.1. Synthesis of annealed $CaWO_4$ nanoparticles

$CaWO_4$ nanoparticles were prepared using benchtop synthesis previously outlined for the synthesis of **[10]** and then annealed in a box furnace under increasing temperature (**Table 8**). A ramping temperature of 5 ℃ was used to heat the samples which were then held at the desired temperature for 6 hours before cooling under ambient conditions to room temperature before further analysis.

3.3.4.2. Characterisation of annealed nanoparticles

Table 8 $CaWO_4$ nanoparticles annealed at different temperatures, and the corresponding size of nanoparticles measured from the SEM (**Figure 72**).

NP sample	Temperature (℃)	Average nanoparticle size (nm)
[10]	unannealed	63
[18]	500	94
[19]	550	104
[20]	600	115
[21]	650	120
[22]	700	122

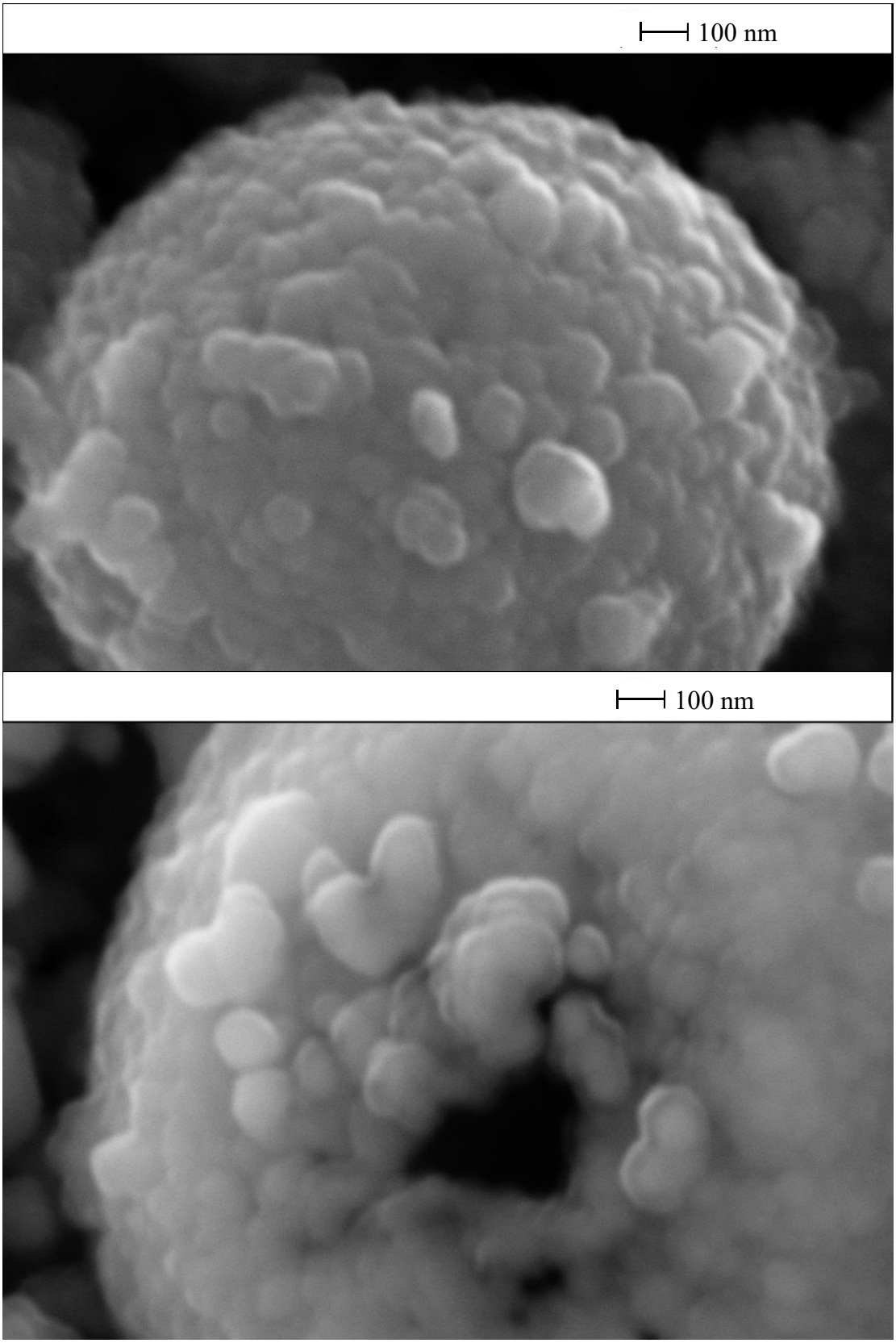

Figure 72 SEM of unannealed sample **[10]** (top), and annealed sample **[22]** (bottom).

Figure 73 shows the PXRD patterns of samples heated to 500, 550, 600, 650, and 700 °C. The pattern fits with tetragonal scheelite crystal structure of $CaWO_4$. A dramatic increase in crystallinity and counts was observed, however the use of Scherrer's equation for estimating the size of particles became unreliable at higher annealing temperatures and all sizes were instead determined from SEM using an average of 50 nanoparticles.

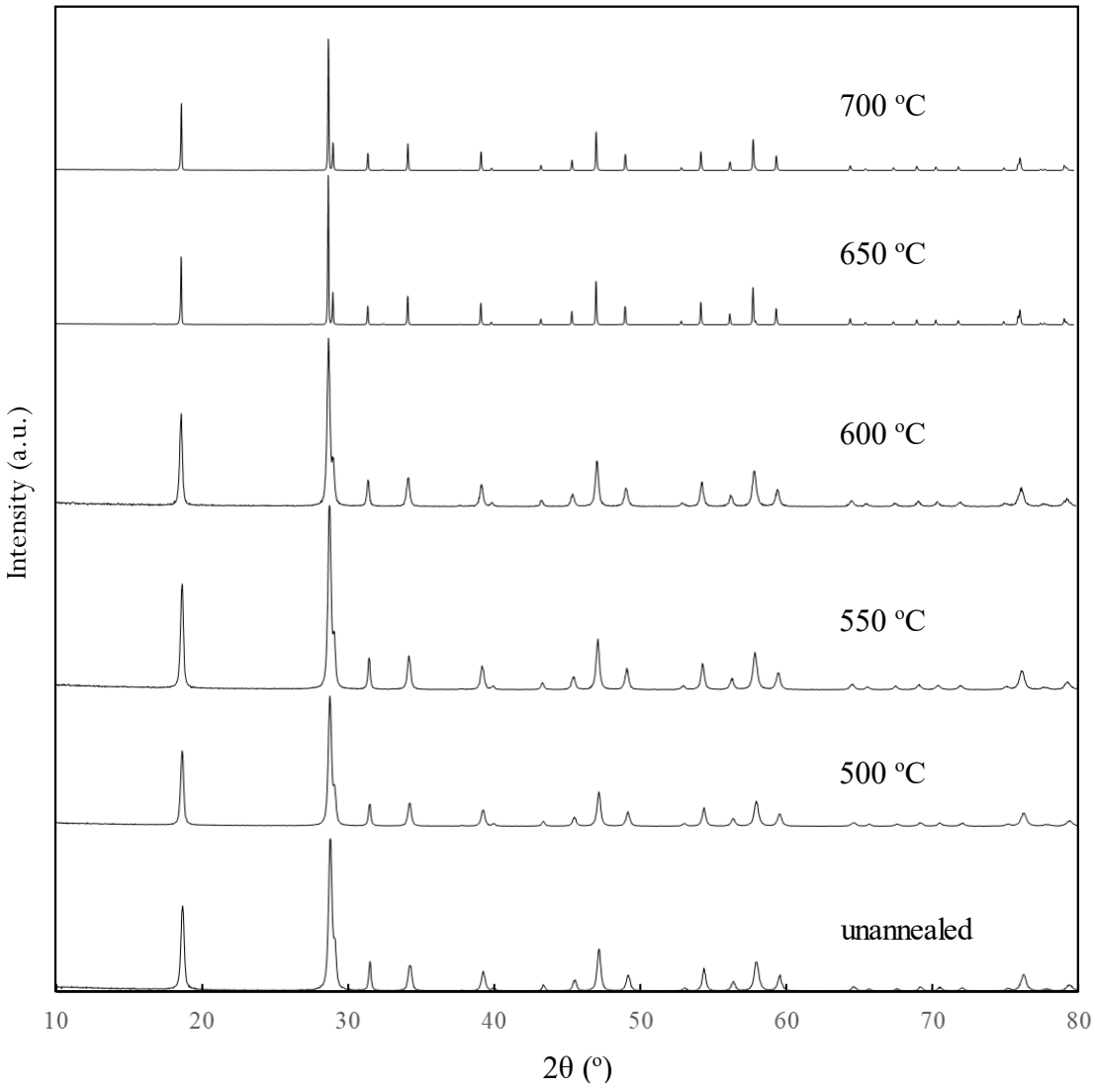

Figure 73 X-ray diffraction pattern of annealed $CaWO_4$ nanoparticles at increasing temperature using box furnace under ambient air conditions.

3.3.4.3. X-ray induced luminescence (XRIL) spectra of annealed $CaWO_4$ nanoparticles

Scintillation of all samples was achieved using an Ir-192 source under identical reaction conditions for all samples with emissions detected using a fibre optic cable and Oceans Optics spectrophotometer.

Figure 74 shows the luminescence spectra of the annealed nanoparticle samples, with ionising radiation from the Ir-192 source. There is a fairly linear (**Figure 75**) increase in luminescence intensity between 500 - 600 ℃ at which point a more dramatic increase in intensity occurs.

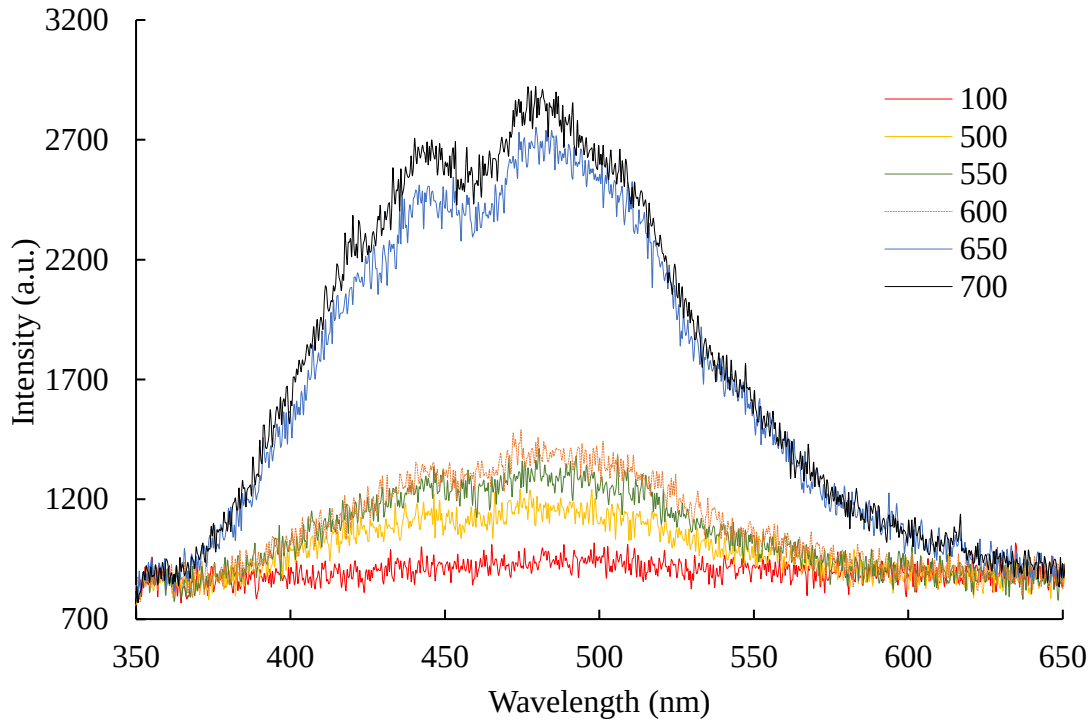

Figure 74 Luminescence spectra of the prepared nanoparticle samples annealed in the furnace at 100 (as prepared), 500, 550, 600, 650 and 700 ℃ with irradiation of the Ir-192 source.

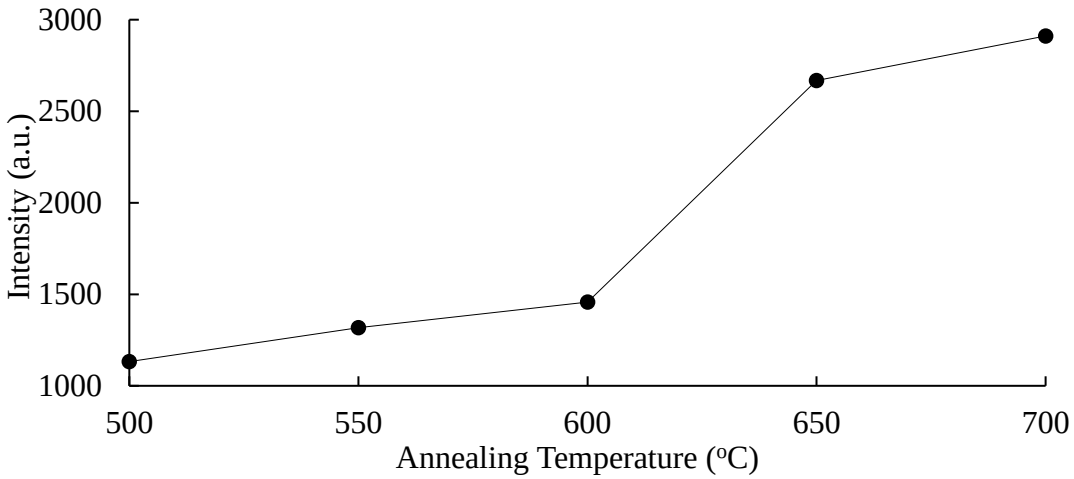

Figure 75 Luminescence maximum of nanoparticles heat treated in the furnace at 100 (as prepared), 500, 550, 600, 650 and 700 °C with irradiation of the Ir-192 source.

Under X-ray irradiation a couple of emission bands can be observed that build up the emission spectra to give a very broad coverage of the visible light spectrum. It is a well described process that gives rise to the blue emission of $CaWO_4$ typically around 418 nm.[199] The excited state of the WO_4^{2-} groups create an exciton from an electron-hole pair, with the hole on the oxygen and the electron of the tungsten, which remain together due to a strong interaction.[204] There is also a green emission band which is extremely strong in the emission spectra of **Figure 74**. It has previously been attributed to WO_3 defect centres associated with oxygen vacancies,[205] as well as intrinsic transitions in the WO_4^{2-} complex. Whatever the origin of this extended luminescence into the visible light spectrum, it is a very welcome effect, for stimulating more of the absorption bands present within the porphyrin absorption spectrum.

3.3.4.4. IR spectra of annealed $CaWO_4$ nanoparticles

It is believed that while an improvement in order and size play a role in the increased optical output,[188] hydroxyls at the surface of the material may also come into play. An

increase in temperature will reduce the content of impurities, such as OH^-, NO_3^- (which may remain from reactants in synthesis) hence increasing the crystallinity of the samples.[199]

Figure 76 shows the IR spectra for $CaWO_4$ before and after annealing at 650 °C and demonstrates the difference in surface groups present. The bands present at 3382 cm^{-1} and 1636 cm^{-1} can be assigned to the O-H stretching vibration and H-O-H vibrations respectively.[199] The band present at 1455 cm^{-1} is attributed to N-O vibration modes, which may be due to remaining NO_3^- from the starting materials. The strong absorption band at 750 - 900 cm^{-1} is attributed to O-W-O stretching of the WO_4 tetrahedron. It can be observed that all but the W-O bond are removed upon annealing, strengthening the explanation of an improved crystallinity due to the removal of impurities.

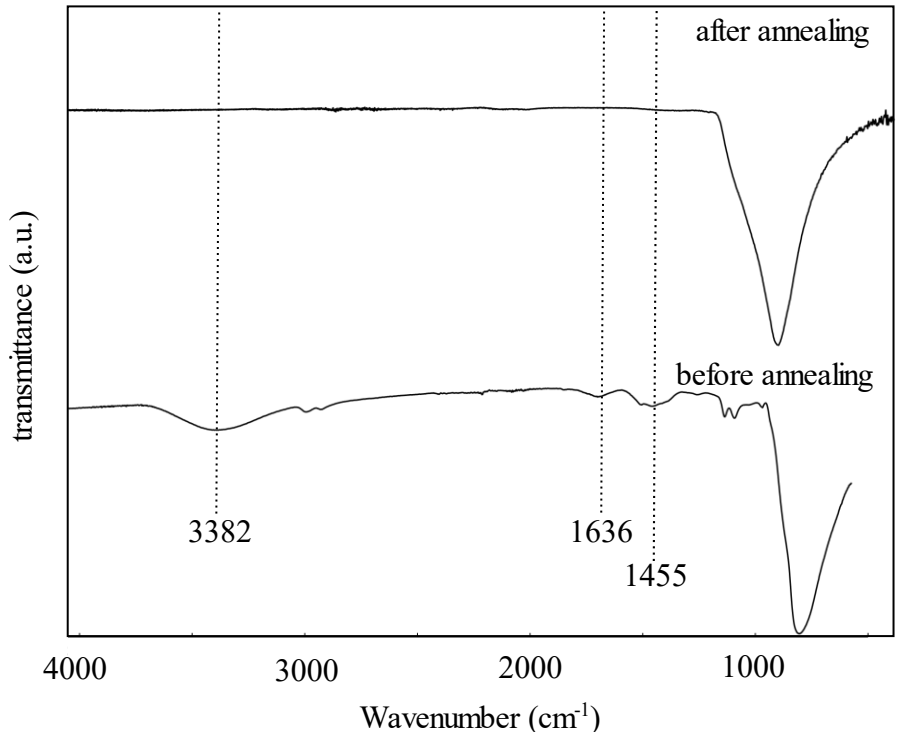

Figure 76 ATR- IR of $CaWO_4$ nanoparticles before and after annealing at 650 °C.

3.3.4.5. Thermogravimetric analysis (TGA) of annealed $CaWO_4$ nanoparticles

Photo-generated holes in the valence band on the surface of $CaWO_4$ nanoparticles become trapped by hydroxyl groups also present at the surface, in a well-known process.[206] This is a competing non-radiative process to the radiative recombination of electron-hole pairs which generate the luminescence of the material. Upon annealing at increasing temperature, more of the OH groups are removed,[188] decreasing the amount of trapping and therefore the competing non radiative processes leading to an increase in luminescence intensity. Thermogravimetric analysis was used to demonstrate this process (**Figure 77**).

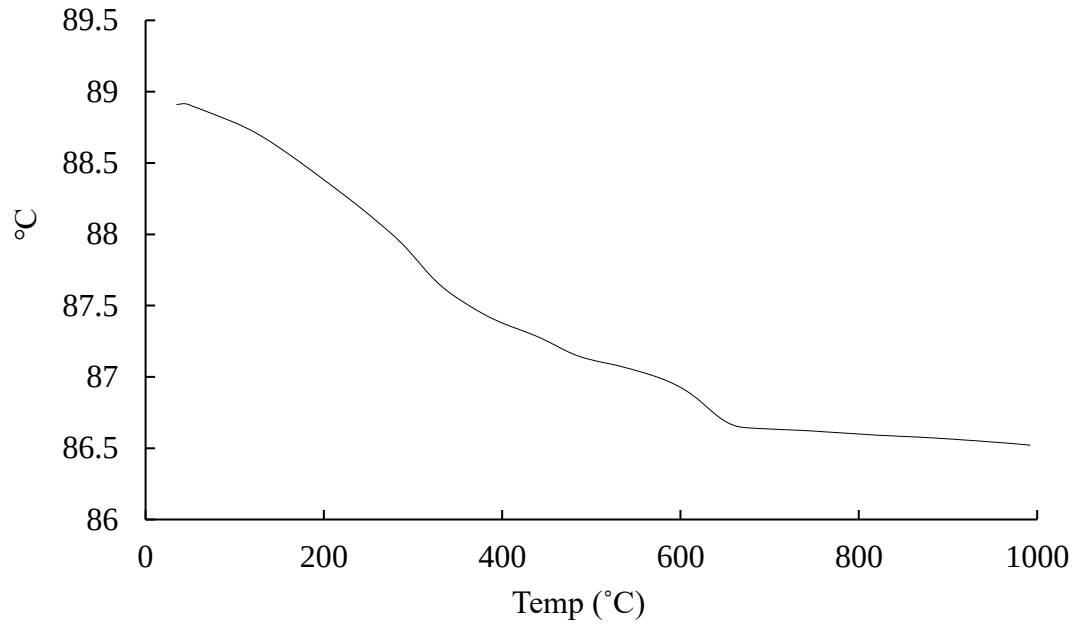

Figure 77 Thermogravimetric analysis showing the change in mass of a sample of $CaWO_4$ nanoparticles with increasing temperature.

An initial drop in mass below 200 ℃ is likely due to the removal of trapped moisture within the nanoparticle aggregates, after which there is a steadier decline in mass before another sudden drop between 600 - 650 ℃. This sudden drop in mass corresponds with

an equally abrupt increase in luminescence intensity. After this point there is a plateau at which there is no further decrease in mass. The loss of hydroxyls at this temperature has previously been reported.[188]

The caveat to this improvement in luminescence intensity is that surface hydroxyls are required for attachment and functionalising nanoparticles to form ScNP-PS conjugates. However, it is indicated that a similar effect may be observed by reacting hydroxyls for functionalisation rather than removing them.[207]

3.3.5. Annealing of europium doped $Ca_{1-x}Eu_xWO_4$ nanoparticles

Europium doped samples all annealed to 650 ℃ were prepared to see if the same increase in luminescence intensity obtained from the blue WO_4^{2-} band, under X-ray irradiation, could also be obtained for the $^5D_0 \rightarrow {}^7F_J$ transitions of the Eu^{3+} ion.

3.3.5.1. Synthesis of annealed $Ca_{1-x}Eu_xWO_4$ nanoparticles

Synthesis of nanoparticles used a modified method to what has been previously described for the benchtop synthesis of $CaWO_4$ nanoparticles **[10]**. Nanoparticles were prepared by substituting a molar percentage of $Eu(NO_3)_3{\cdot}6H_2O$ for that of $Ca(NO_3)_2{\cdot}4H_2O$ to give $Ca_{1-x}Eu_xWO_4$ prepared at 3%, 10% 15% and 20% and 25% (**Table 9**). The samples were then annealed in a box furnace at 650 ℃ with a ramping temperature of 5 ℃ and then held at the desired temperature for 6 hours before cooling under ambient conditions to room temperature before further analysis.

3.3.5.2. Characterisation of annealed $Ca_{1-x}Eu_xWO_4$ nanoparticles

Table 9 shows the different molar percentages used for synthesised nanoparticles corresponding with the luminescence intensity they achieved from X-ray excitation using an Ir-192 source. All samples were annealed at 650 ℃.

Table 9 Europium-doped $CaWO_4$ nanoparticles in molar %s 3, 10, 15, 20, 25 and the corresponding luminescence intensity of the $^5D_0 \rightarrow {}^7F_2$ transition of Eu^{3+}.

NP sample	Molar %	Luminescence intensity (a.u.)
[23]	3	15971
[24]	10	1221
[25]	15	6317
[26]	20	6350
[27]	25	2563

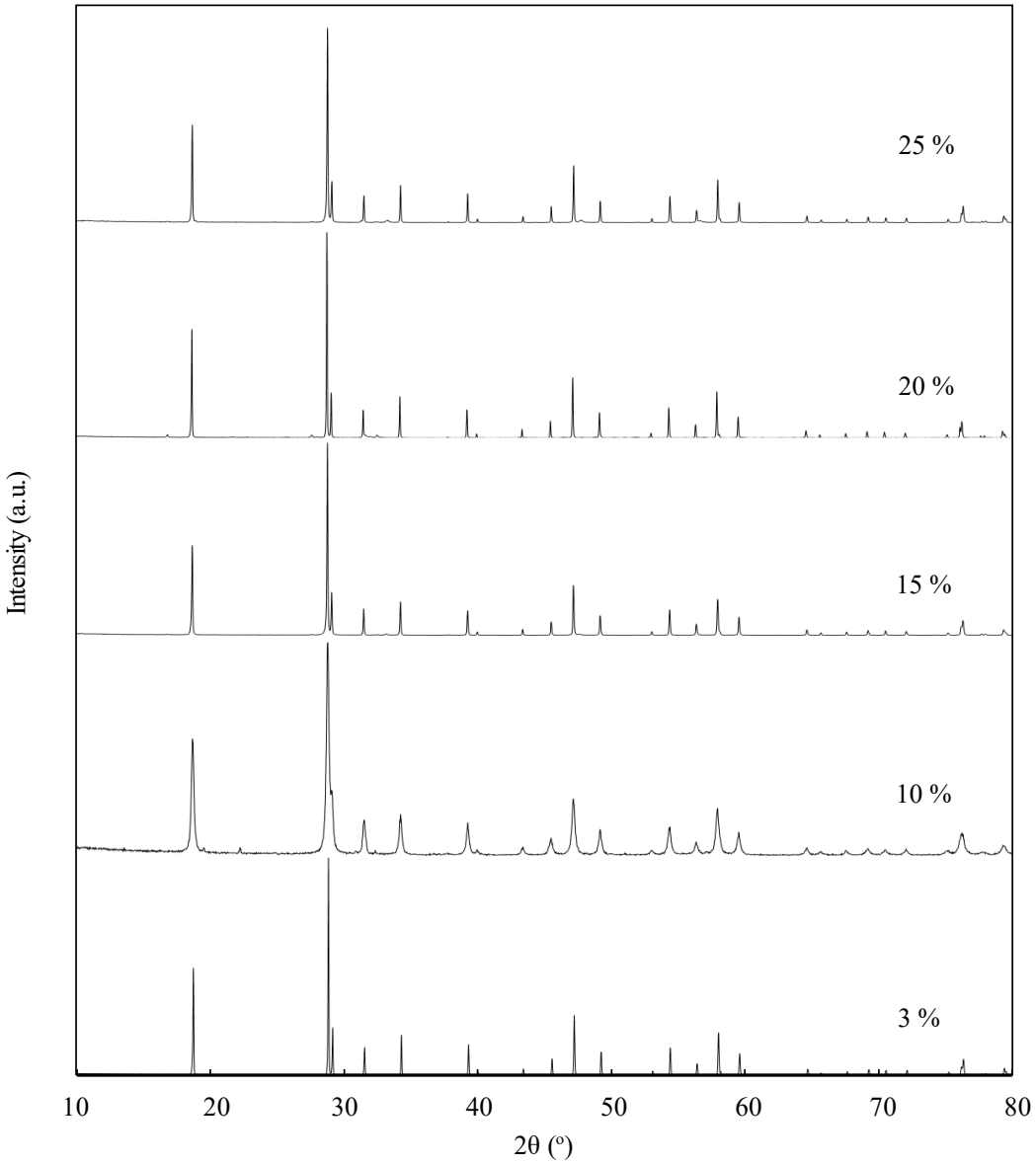

Figure 78 PXRD patterns of annealed $CaWO_4$ nanoparticles with europium doing 3%, 10%, 15%, 20% and 25%.

The emission spectra (**Figure 79**) exhibit identical features, composed of several sharp lines corresponding to the typical 4f emissions of Eu^{3+}. All emissions increase in intensity with the Eu^{3+} doped samples however the $^5D_0 \rightarrow {}^7F_2$ electric dipole transition is highly sensitive to the local environment,[203] and due to the lack of inversion symmetry and break of parity selection rules, this transition is strongest, as previously mentioned.

When compared with the unannealed samples of increasing Eu^{3+} molar %, a different trend emerges (**Figure 79**). Although the intensity increases between 10 and 20% as seen previously the 3% doped annealed NPs have the highest intensity of all samples by large margin. 25% europium doped NPs have a decrease in luminescence intensity due to a known process of concentration quenching. Due to an increase in dipole-dipole interactions, the cross-relaxation amoung Eu^{3+} ions increases when the mean distance between them is below the critical value.[208] The critical value depends the crystal structure of the host material, particle size and type of RE ions.[193]

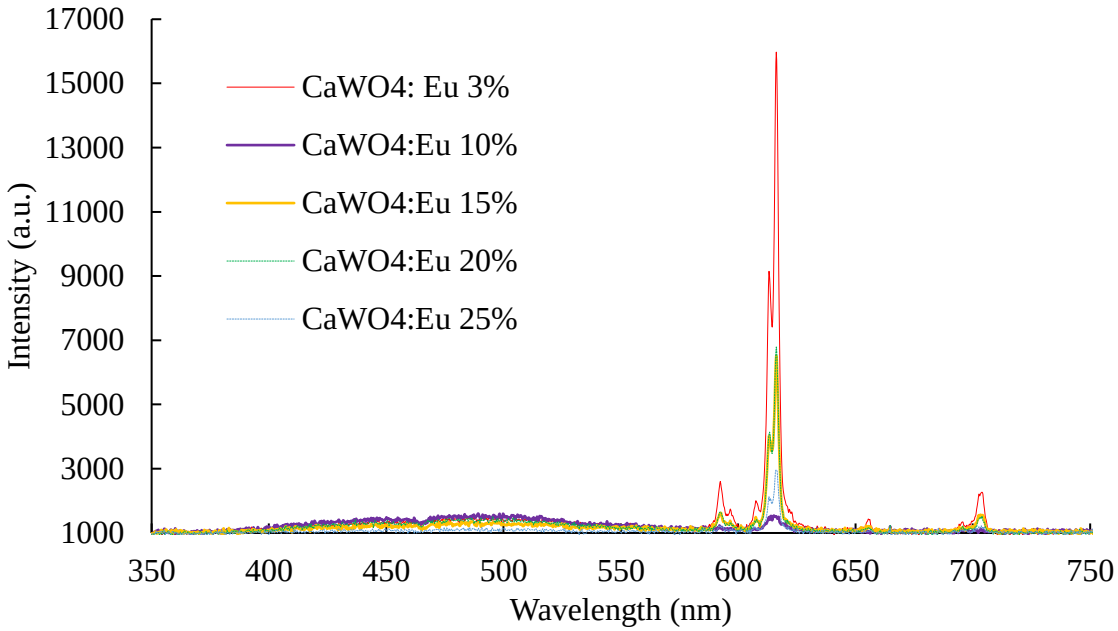

Figure 79 Luminescence spectra of the prepared europium-doped nanoparticles with 3, 10, 15, 20, 25 molar % samples irradiated with an Ir-192 source.

From **Figure 80** it was also observed that the luminescence intensity of the WO_4^{2-} attributed blue band was considerably reduced from the undoped, annealed nanoparticles **[23-27]**. This is the expected result of an efficient transfer of energy from the donor ion to the activator ion.[199]

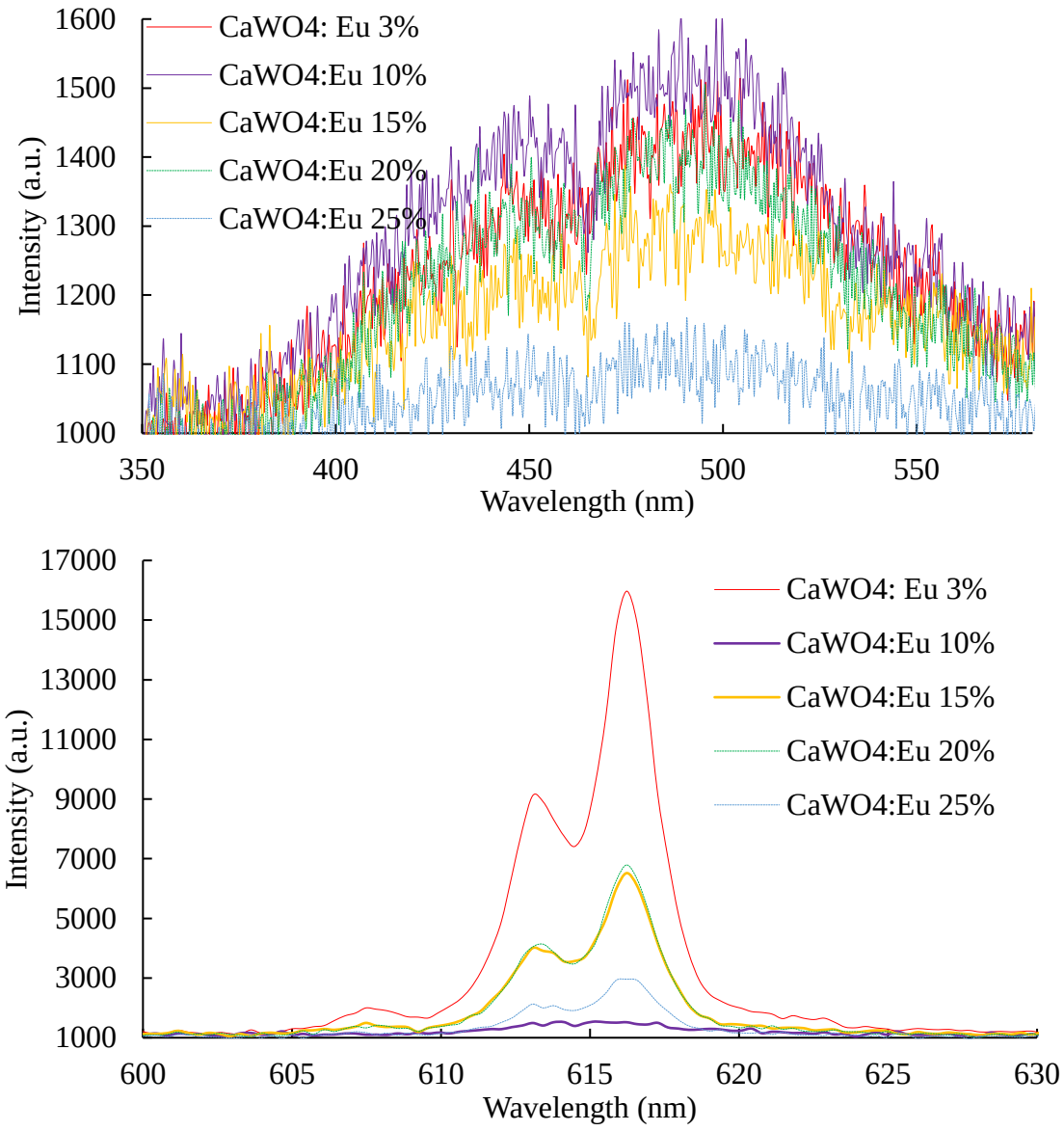

Figure 80 (Above) Zoomed in view of blue (WO_4^{2-}) and (below) Eu^{3+} emissions of XRIL under Ir-192.

3.3.6. Europium tungstate

Having successfully doped $CaWO_4$ with Eu^{3+} at a range of concentrations, it was investigated as to whether 100% doping could be achieved. In other words, whether $EuWO_4$ could be formed from a similar synthetic methodology. It would be expected that the majority of the europium would have to reduce to Eu^{2+} to make this structure, or else it would form the Eu^{3+} wolframite phase $Eu_2(WO_4)_3$.

$EuWO_4$ would be expected to have a very high density (7.56 gcm^{-3}) as well as having the highest energy K-edge from tungsten and another very high K-edge from europium. This would cover the higher energy region of absorption (**Figure 81**).

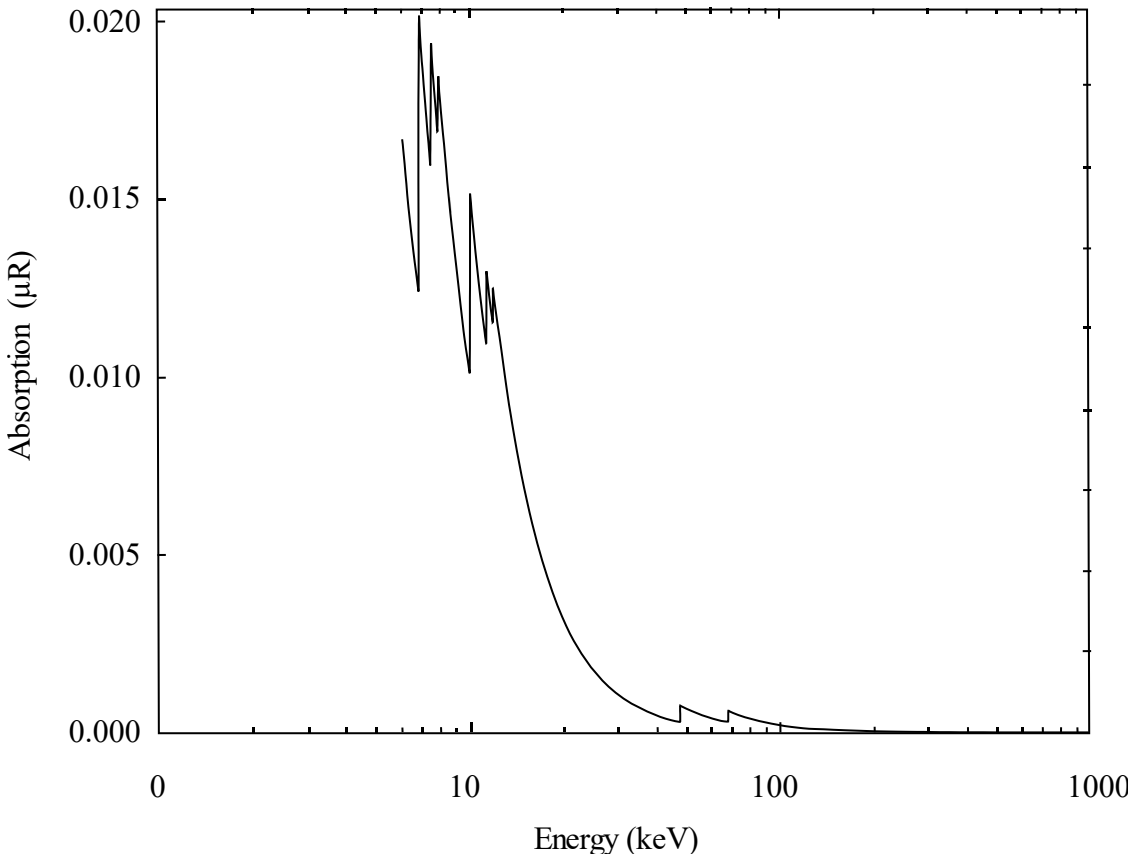

Figure 81 Absorption for $EuWO_4$.

3.3.6.1. Synthesis of europium tungstate

The synthesis of this material was highly sensitive to pH, the use of ethylene glycol and a microwave synthesis. These approaches will be discussed in detail over the following section.

Scheelite $EuWO_4$ has not previously been synthesised in nanoparticle form and so there is no PXRD pattern for comparison.

3.3.6.2. Benchtop synthesis

Benchtop synthesis was attempted using a similar protocol to that employed for the successful synthesis of the $CaWO_4$ nanoparticles. Nanoparticles were synthesised by a hydrothermal method in which the product was precipitated from a solution of ($Eu(NO_3)_6.6H_2O$) and ($Na_2WO_4{\cdot}2H_2O$) solution, acting as the sources of $Eu^{2+/3+}$ and WO^{2-} respectively.

3.3.6.3. Characterisation of $EuWO_4$ nanoparticles

Figure 82 shows the PXD pattern obtained for the synthesis of $EuWO_4$ by a benchtop synthesis. The pattern showed that no crystalline product was obtained.

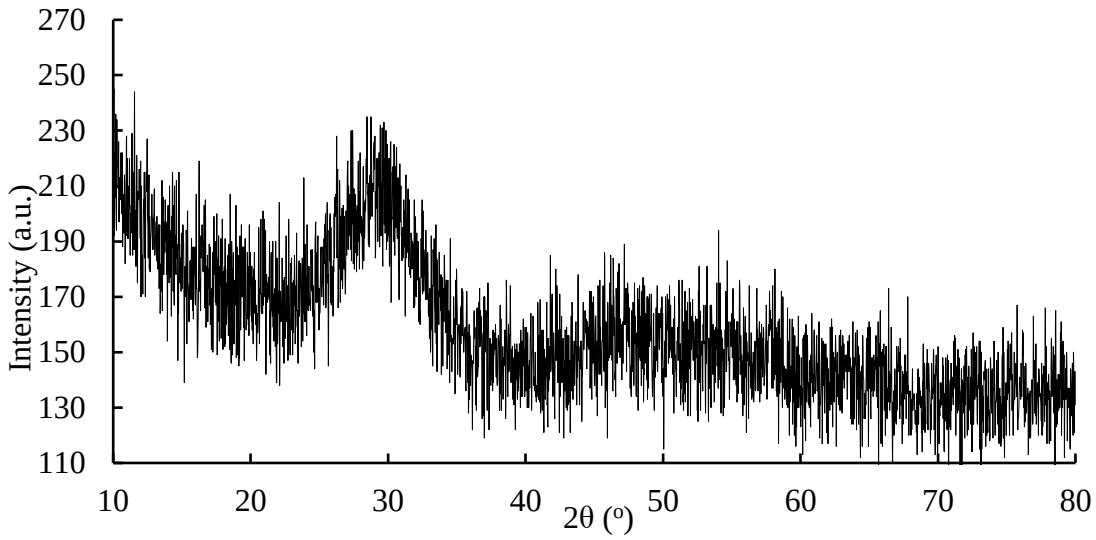

Figure 82 PXRD pattern of **[28]** an attempted benchtop synthesis $EuWO_4$ nanoparticles.

3.3.6.4. Microwave radiation-assisted synthesis

Nanoparticles **[29]** were synthesised by the same procedure as used for the synthesis of **[28]** except *via* microwave heating in a 35 ml vessel at 180 ℃ for 1 hour.

3.3.6.5. Characterisation of $EuWO_4$ nanoparticles by microwave synthesis

Figure 83 shows the PXRD pattern obtained from the microwave synthesised $EuWO_4$ nanoparticles. The phase appears to be scheelite but is not identical to anything that has been previously synthesised, making identification more difficult. Eu tends to form the wolframite structure with tungsten ($Eu_2(WO4)_3$), however, after comparison with PXRD data, it can be concluded that the samples do not contain any ($Eu_2(WO_4)_3$).[209] Another possibility was the incorporation of sodium, present in the synthesis as $Na_2WO_4{\cdot}H_2O$, to give the structure $Na_xEu_yWO_4$ which has been previously been reported in the literature.[210] However, EDX of the compound showed no trace of any sodium present within the compound (**Table 10**) and the comparison of PXRD data dismissed this hypothesis.

Table 10 Weight and atomic percentages of elements in $EuWO_4$ from EDX data.

Element	C	O	Eu	W	Total
Wt%	6.15	23.54	29.70	40.61	100.00
Atomic proportion	0.5125	1.47	0.195	0.22	2.3975
Atomic %	21.37	61.31	8.13	9.17	100

In $EuWO_4$, the Eu:W ratio should be very close to 1. EDX data (**Table 10**) show that it is actually less than 1, indicating the possibility of europium vacancies. These would give the chemical formula $Eu_{0.89}WO_4$. However, this compound does not have a balanced charge if either all of the europium is Eu^{2+} or if all is Eu^{3+} and tungsten is assumed to be entirely in a W^{6+} state. In this case, mixed-valence Eu^{2+}/Eu^{3+} in the ratio ~ 2 : 1 need to be present in order for this species to have a balanced charge. Alternatively, it can be assumed that all europium shows oxidation state +3 and there are cation vacancies on the tungsten site as well. In this case, the compound would have formula $Eu_{0.81}W_{0.926}O_4$, to maintain the ratio 0.89 Eu to W observed by EDX and allow for a charge balance. There is also the possibility of a W5+/W6+ mixed valence, however, in this case, it is not possible to predict a chemical formula.

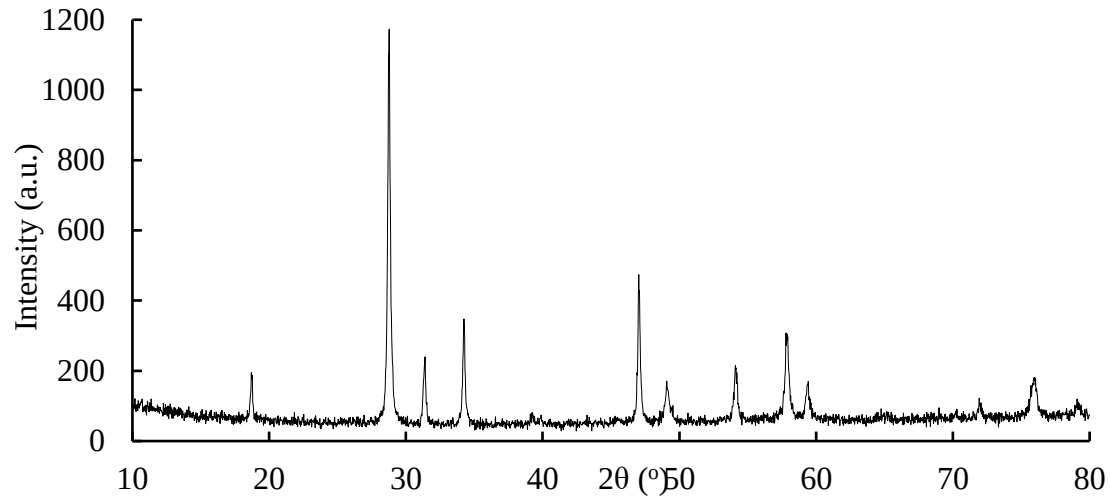

Figure 83 PXRD pattern of **[21]** microwave radiation assisted synthesised nanoparticles.

Data were fitted using a Rietveld refinement method implemented using GSAS-II (**Figure 84**).[211] The refinement performed gave findings that were consistent with EDX that a vacancy on the Eu site of approximately 0.9. A vacancy on the tungsten site did not improve a fit and was fixed for 1.0.

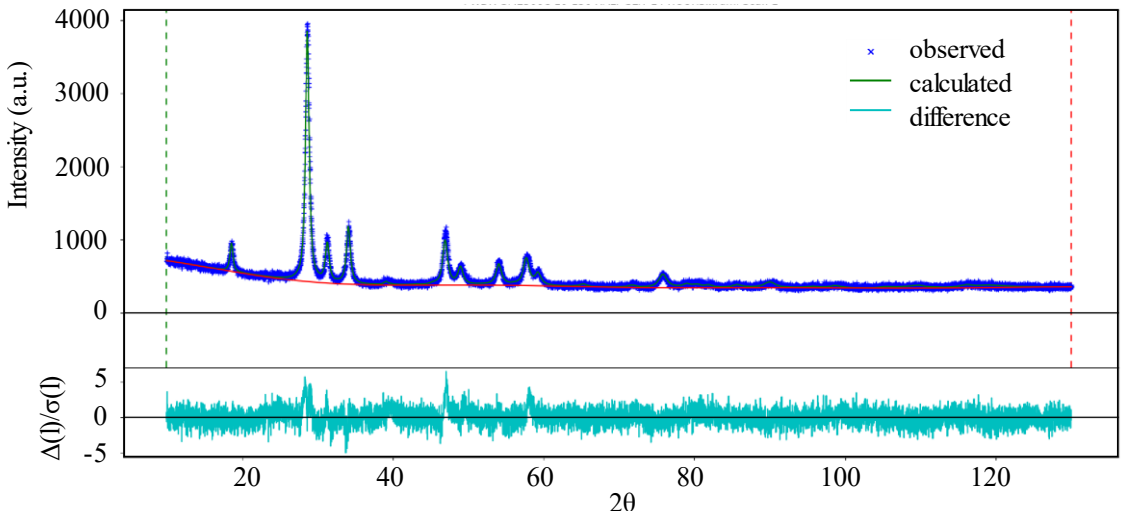

Figure 84 Rietveld refinement of NP sample **[29]**.

Microwave radiation-assisted synthesis is an appealing synthesis for nanoparticles because it can increase yields, dramatically reduce time, as well as enhancing the materials properties such as particle size distribution, phase, and crystallinity.[212–214]

It has also been shown to produce altered lattice ordering, with novel reactions and altered products which cannot be replicated under conventional heating methods. This highlights the result difference between benchtop and microwave synthesis obtained.[214–216] This synthetic approach had never been applied to the preparation of a compound with scheelite structure, where the alkaline-earth cation is fully replaced by Eu. The existence of a "$EuWO_4$" compound is a little controversial from reports in the literature, but it appears it has been achieved in this work, thanks to the microwave-based approach.

3.3.6.6. Investigating the effect of ethylene glycol

It was realised during synthesis that as well as the necessity for microwave radiation-assisted synthesis, without the use of ethylene glycol, the PXRD would again show only an amorphous product. Whether this is due to templating or the EG acting as a mild reducing agent is so far unestablished, however an investigation into how the percentage of EG used in synthesis affects the particles and luminescence was undertaken with percentage ranging from 0 - 100% shown in (**Table 11**).

Table 11 $EuWO_4$ Nanoparticles by Microwave Synthesis with increasing EG content.

NP Sample	Ethylene Glycol %	XRIL Intensity
[29]	5	119
[30]	50	426
[31]	100	260

3.3.6.7. Microwave radiation-assisted synthesis with varying amounts of EG

Synthesis was performed as previously stated using a microwave radiation-assisted synthesis, however the temperature was lowered to 650 ℃ and the volume of EG added to the water was 1, 10 and 20 mL for products **[30]**, **[31]**, **[32]** respectively. A total solvent volume of 20 mL was maintained meaning that the amount of water substituted was also 1, 10 and 20 mL, respectively.

3.3.6.8. Characterisation of microwave radiation-assisted synthesis with varying amounts of EG

Figure 85 shows the PXRD patterns obtained for compounds **[30-32]**. It shows that without the presence of EG the synthesis is unsuccessful. This compound was heated to 950 ℃ and did form a crystalline product but appeared to be a multi-phase sample and it was impossible to determine their nature. It can therefore be concluded that EG is a vital component of the synthesis process. This could be due to its reducing properties and it would support the presence of mixed valencies ($Eu^{2+/3+}$ and/or W^{5+}/W^{6+}) in the compound.

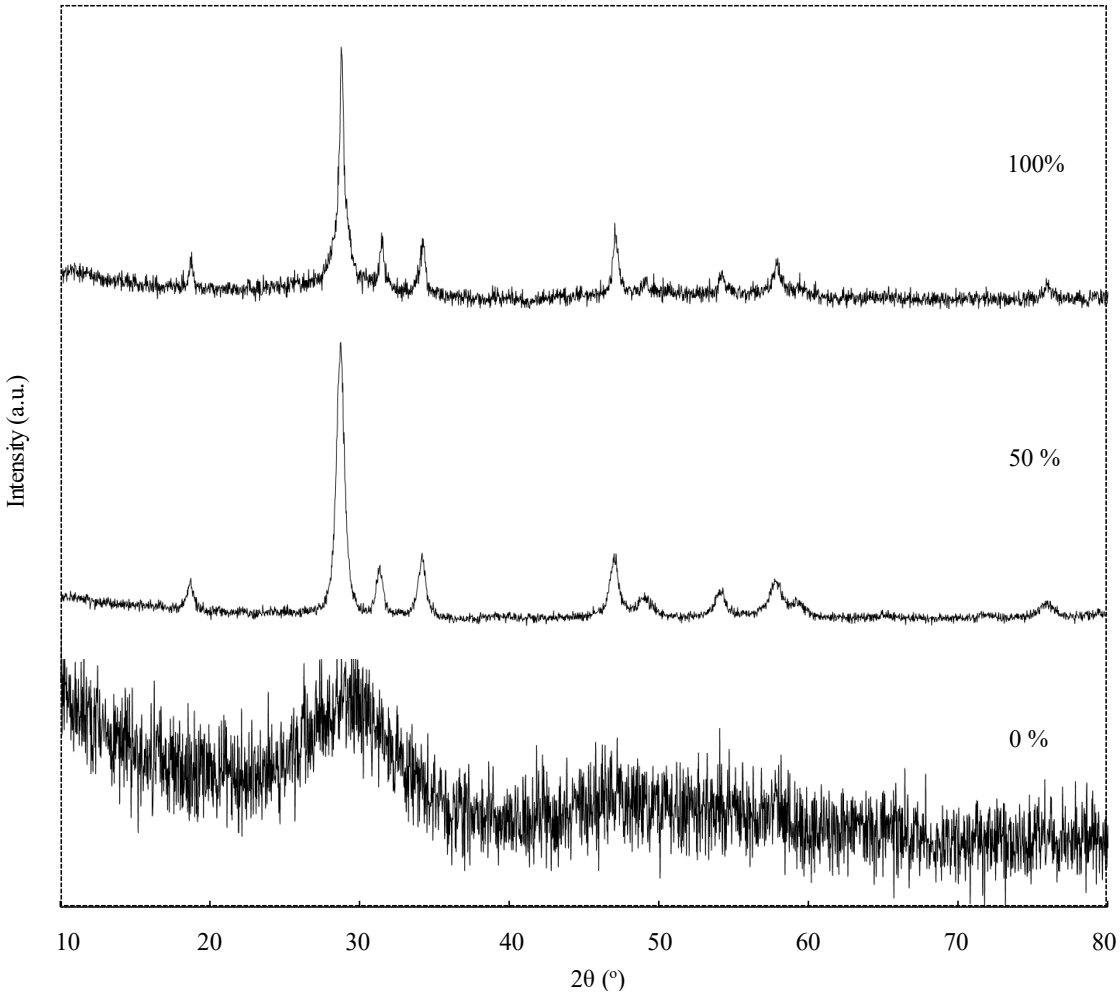

Figure 85 PXRD pattern of microwave radiation-assisted synthesis with varying concentrations of ethylene glycol.

3.3.6.9. X-ray induced luminescence (XRIL) spectra microwave radiation-assisted synthesis with varying amounts of EG

Samples were irradiated using a Radsource-2000 biological irradiator, with an X-ray tube set with a potential of 150 keV and current 25 mAs hitting a tungsten anode and a 0.2 mm copper filter. Luminescence was recorded using a fibre optic cable attached to an Ocean Optics USB2000 CCD array spectrophotometer (**Figure 87**). All samples were recorded under identical conditions for a direct comparison.

For samples **[30-32] Figure 86** shows the XRIL spectra display a prominent peak at 614 nm for the $^5D_0 \rightarrow {}^7F_2$ transition, and perhaps a slight peak 702 nm for the $^5D_0 \rightarrow {}^7F_4$ transition, both transition are the electronic dipole transitions of Eu^{3+}, the magnetic dipole transitions are not observed.[199]

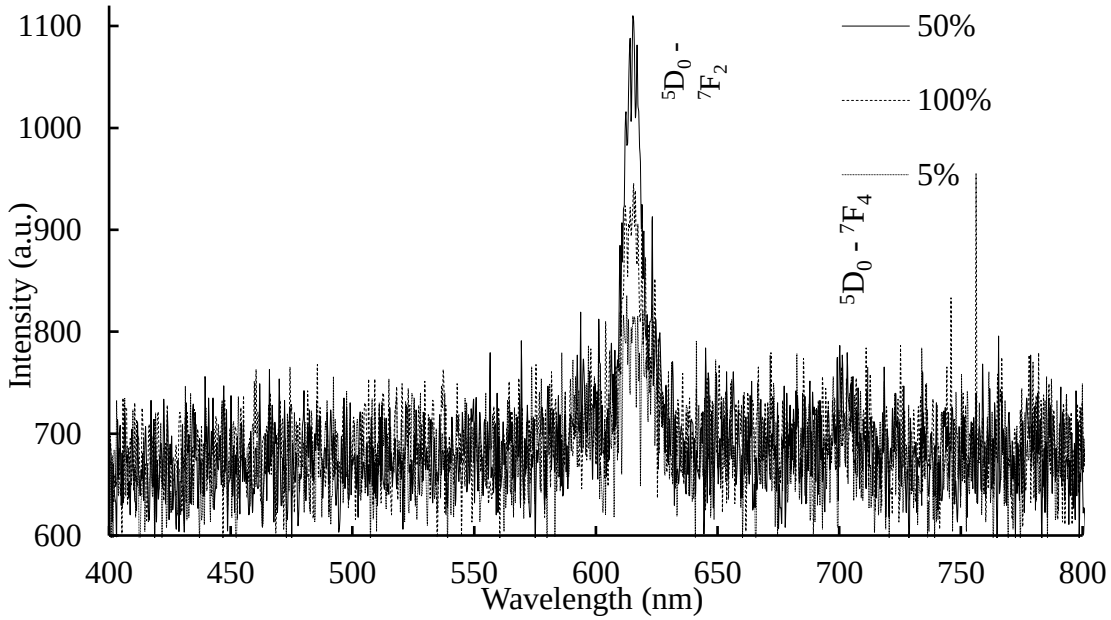

Figure 86 X-ray Irradiated Luminescence Spectra of each sample with increasing percentage of EG used. Irradiated using Radsource-2000 biological irradiator, using an X-ray tube with a potential 150 keV and current 25 mAs with a tungsten anode and a 0.2 mm copper filter.

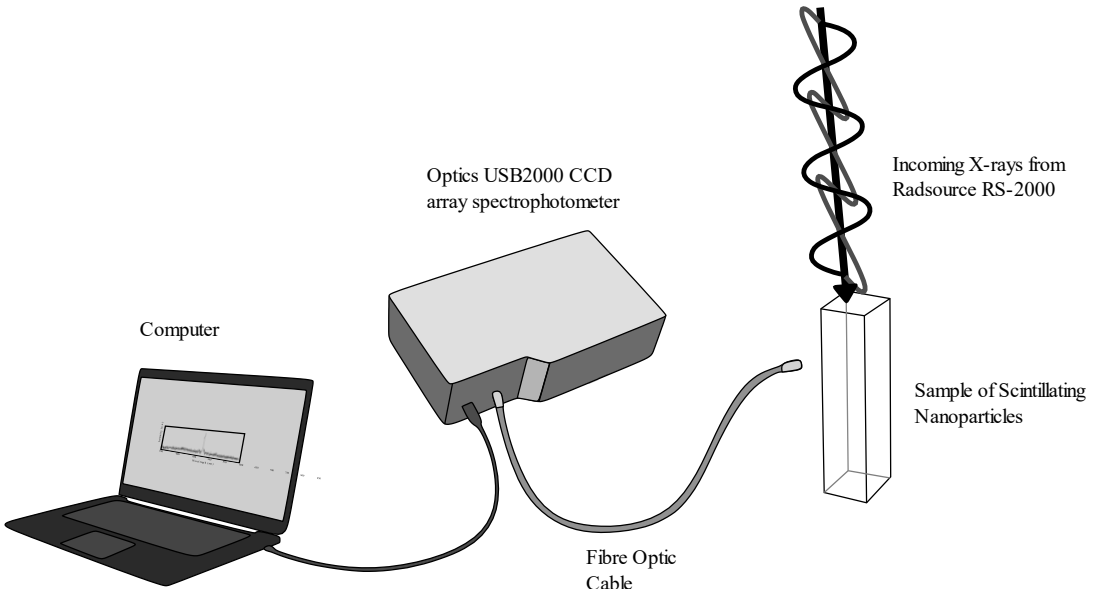

Figure 87 Setup for recording the XRIL spectra of NPs irradiated using the Radsource RS-2000 biological irradiator. Fibre optic cable connects to a portable spectrometer connected to a laptop.

3.3.6.10. Investigating the effect of pH

The effect of pH appeared highly significant. Adapted from earlier used protocols for the synthesis of $CaWO_4$, the synthesis of "$EuWO_4$", utilised NaOH to increase the pH to 9 - 9.5, to improve precipitation of the product. However, it was found that, for "$EuWO_4$", a high pH did not favour the formation of the scheelite phase, but, instead a compound with the apatite structure was formed (**Figure 88**).

Apatites have previously been exhibited using a silicate or phosphate group with a structure such as $Ca_2Ln_8(SiO_4)_6O_2$ (Ln = lanthanide), but have never been shown to exist with a tungstate group.[217] This compound exhibited no luminescence deriving from Eu^{3+}.

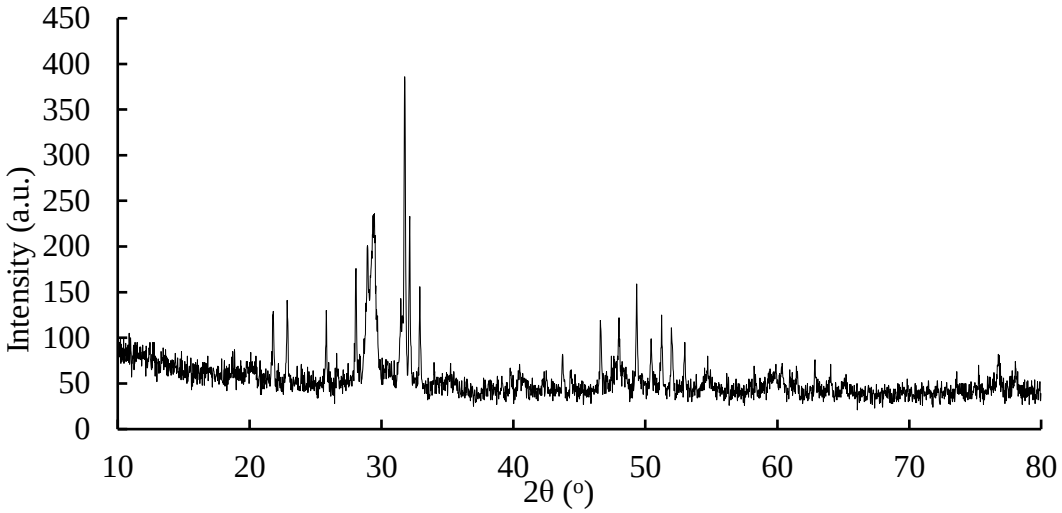

Figure 88 PXRD pattern of apatite phase product formed under high pH conditions.

Whether there is an optimal pH for synthesis, producing the most luminescent particles, or whether it affects the Eu 3+ to 2+ ratio etc, would be an interesting area for further investigation but has not been studied as part of this work.

3.3.7. Zinc oxide (ZnO)

Zinc oxide (ZnO) has a hexagonal wurtzite structure and is a wide band gap (3.36 eV) material (semiconductor) with a large exciton binding energy (~ 60 meV), resulting in efficient excitonic emission at room temperature.[218] Due to a high quantum efficiency and photocatalytic activity ZnO has been examined for use in optics, light-emitting diodes (LEDs), scintillation detectors and as a potential photosensitiser, due to its ability to generate reactive oxygen species (ROS) such as singlet oxygen ($^1O_2$), and hydroxyl radicals ($^{\cdot}OH$) under UV radiation.[219] ZnO nanoparticles are employed in many areas of industry including rubber composites,[220,221] personal care products,[222] textiles[223] and electronics.[224,225] ZnO has been generally recognised as safe by the FDA, and for this

reason there has been a growing interest in biomedical applications, such as antibacterial, anti-cancer and bio imaging.[226]

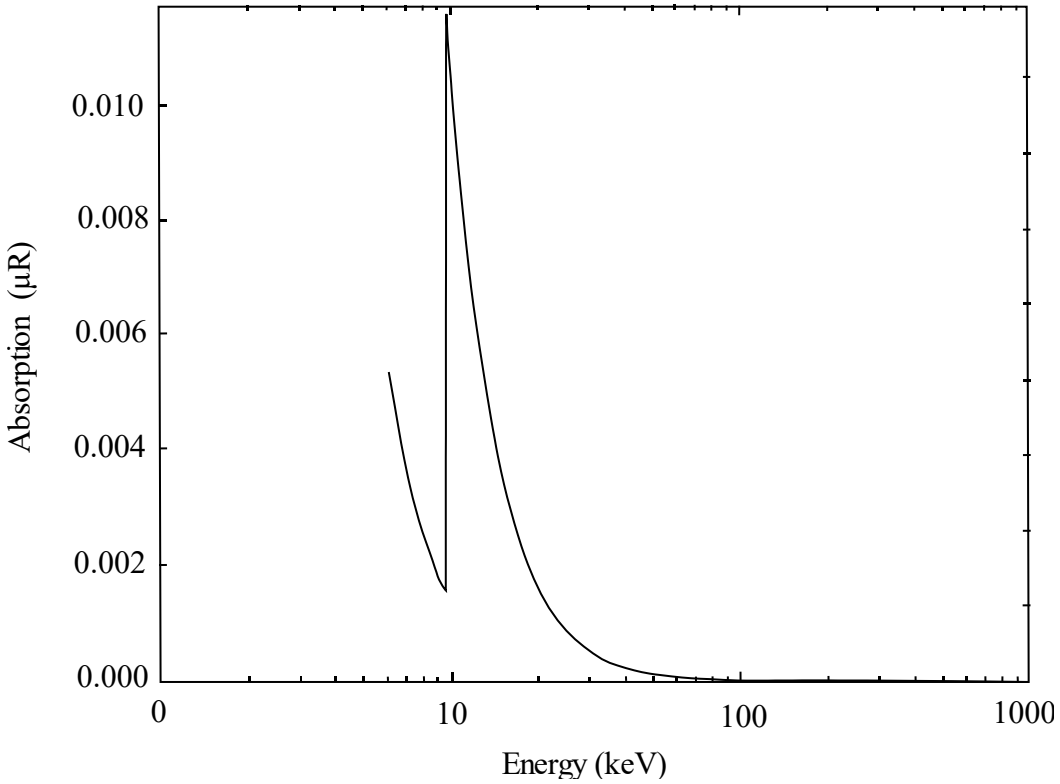

Figure 89 Absorption for ZnO.

ZnO has a unique feature among the materials chosen for study as it is potentially both a scintillator and photosensitiser in one, and has been shown to luminesce under X-ray irradiation[227] suggesting it is highly likely that it can be used to generate ROS under X-ray irradiation. This negates the need for conjugation to a photosensitiser leading to the potential of a highly facile and inexpensive material which could be incorporated into clinical methods with minimal difficulty.

The absorption coefficient for ZnO (**Figure 89**) shows the absorption K-edge at 9.66 keV, before rapidly dropping off in intensity. Irradiating a patient with 10 keV energy would

be unsuitable as it has a poor penetration depth through tissue and would likely burn the skin of the patient. However, irradiating between 30 - 50 keV might still interact with the material in a meaningful way and would extend the penetration depth possible of the material to up to 5 cm.

Currently, when ZnO has been investigated for its potential as a photosensitiser, it has been irradiated within the UV-Vis light spectrum, to achieve a photosensitising effect. This limits the material to a penetration depth of less than 1 mm, making it unsuitable as a PDT agent. For this reason, investigating the potential of producing a PDT response using low energy X-rays, which would be particularly suited to I-125 or Gulmay, is of great interest.

3.3.7.1. Syntheses of ZnO [33-37]

Due to the growing interest in ZnO NPs, there are a vast array of synthetic methods available including precipitation processes,[228,229] sol-gel,[230,231] hydrothermal,[232] emulsion[233] and microwave[234] techniques. For this research, two types of particles were synthesised requiring different synthetic techniques.

The first are the quantum dots, utilising a sol-gel method of Oswald ripening utilising a capping agent for controlling growth size.

The second technique was to create larger nanoparticles, to improve the absorbing potential of X-rays in which a microwave heated technique was developed.

3.3.7.2. Synthesis of ZnO quantum dots

Nanoparticles **[33-37]** were synthesised by a sol-gel synthesis method according to the literature[235] using tetraethyl orthosilicate (TEOS) as a capping agent for particles **[33-35]** to inhibit the growth of the particles and give a functional group on the surface for potential conjugation. It was found by experimentation that a high pH improved both the yield and purity of the product. Upon the addition of an initial source of base, the zinc acetate forms a precipitate in the form of zinc hydroxide, (**Scheme 6**).

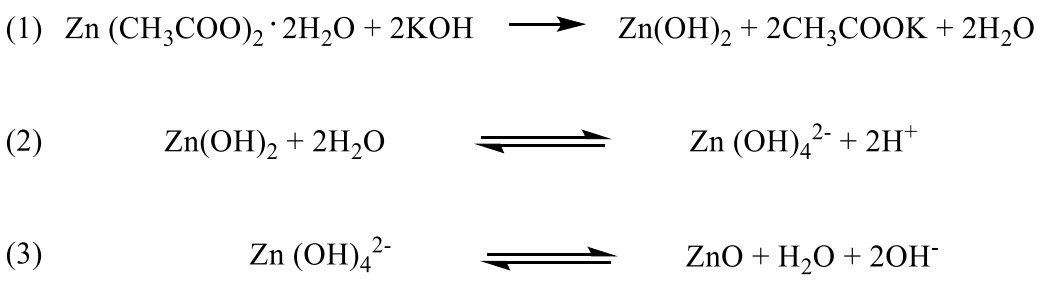

Scheme 6 Synthesis of zinc oxide nanoparticles. (1) KOH is added dropwise until $Zn(OH)_2$ precipitates. (2) upon further addition of KOH $Zn(OH)_4^{2-}$ is formed and goes back into solution. (3) addition of water forms ZnO nanoparticles to precipitate out.

As the pH increases the precipitate resolubilises as it forms zincate ions. In this form the addition of water forms the sol-gel and precipitates ZnO nanoparticles which grow by the process Ostwald ripening. This is a thermodynamically driven process by which larger (lower energy) particles draw material from smaller (high energy) particles. This is because larger particles with high surface to volume ratio are of lower energy due to surface particles being less energetically stable than the well-ordered particles packed in the interior. Due to the mechanism of growth; time becomes a useful way of controlling the size of nanoparticles. Tetraethyl orthosilicate (TEOS) is also added at this step, to cap the growth of the nanoparticles < 5 nm which will be subject to quantum confinement effects.

3.3.7.3. Synthesis of ZnO nanoparticles

The synthesis of the nanoparticles was carried out using a microwave solvothermal synthesis (MSS), adapted from the literature,[236,237] in which only zinc acetate, ethylene glycol (EG) and water are the reacting ingredients, (**Scheme 7**).[236] The EG will act as both solvent and stabilising agent, to promote dispersion in water and suppress agglomeration. It has been demonstrated that synthesising ZnO in boiling polyols such as EG, diethylene glycol (DG) and triethylene glycol (TEG), promotes nucleation and growth.[236] Size control has been achieved previously by increasing the chain length[238] of the polyol used or by increasing the amount of water in the reaction.[236] Water has been shown to have a significant impact on promoting crystal growth in organic solvents.[239]

The following reaction steps are proposed: (1) dissociation, (2) cluster growth, (3) crystallisation, the abridged synthesis equation (4).

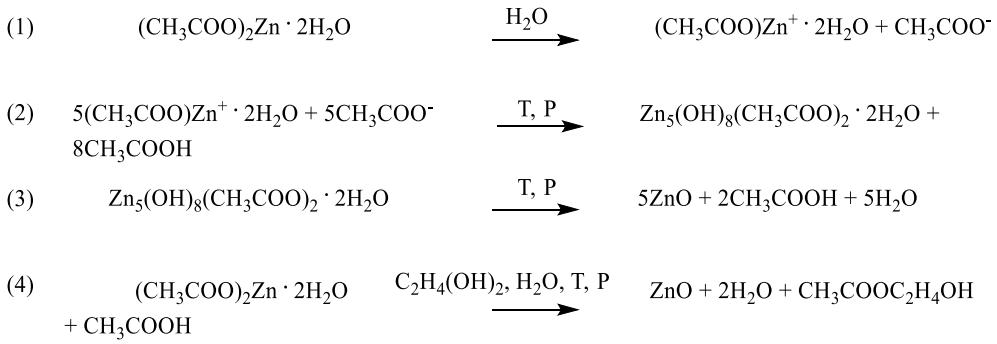

Scheme 7 Proposed mechanism of ZnO NP synthesis.

3.3.7.4. Characterisation of ZnO quantum dots and nanoparticles

Figure 90 shows the XRD patterns of ZnO samples prepared at differing reaction times as well as capped and uncapped and were found to be hexagonal wurtzite phase and of single phase only. Samples were labelled **[33-37]** with reaction time of 5 min, 15 min, 60

min, 15 min and 60 min respectively, where samples **[36]** and **[37]** were also capped with TEOS. No peaks belonging to impurities were observed, indicating high purity ZnO nanoparticles.

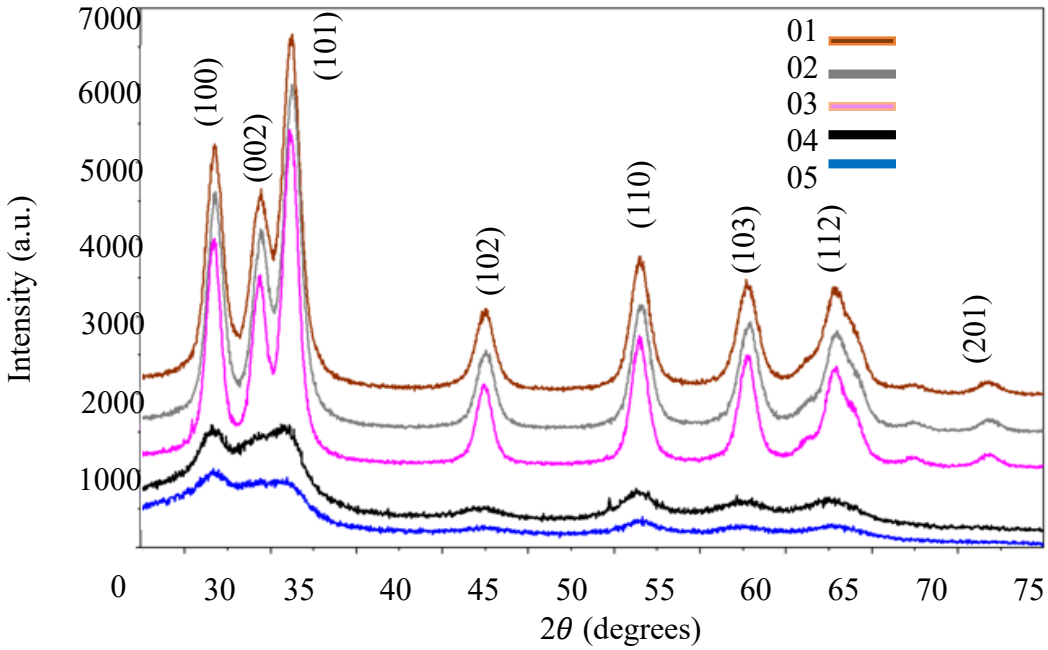

Figure 90 PXRD comparison of ZnO nanoparticles with varying conditions for samples **[33-37]**.

Figure 91 displays the TEM images for samples **[33]**, [**35]** and **[37]**. Good general dispersion was observed, particularly for the capped particles. The size of the particles estimated *via* Scherrer equation are reported in **Table 12**.

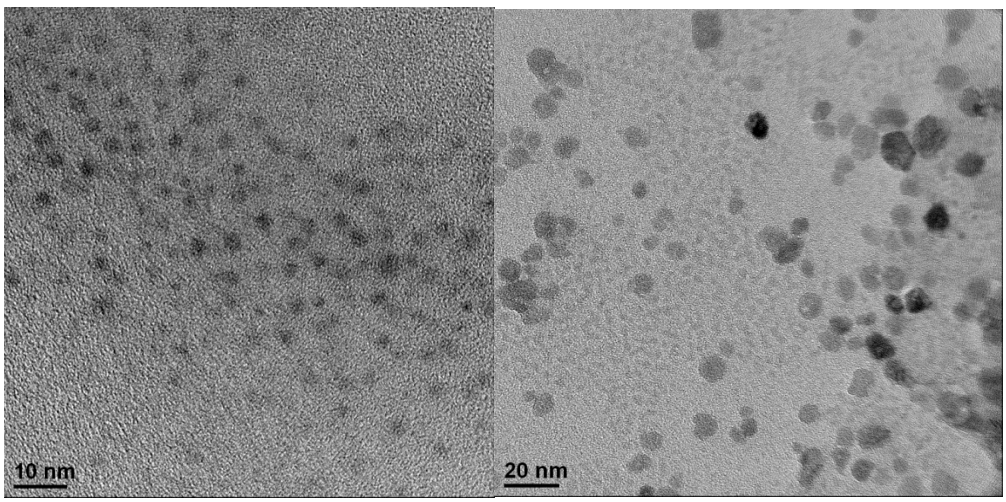

Figure 91 TEM of ZnO nanoparticles. Left sample [**36]**, right sample **[35]**.

Table 12 Effect of reaction time and capping on the size of nanoparticles, estimated by Scherrer's formula and measured by TEM.

Sample	Capped	Reaction time	TEM	Scherrer
[33]	Uncapped	5	7.4 nm ± 0.3	5.4 nm
[34]	Uncapped	15		5.9 nm
[35]	Uncapped	60	8.3 nm ± 1.5	6.6 nm
[36]	Capped	15	2.9 nm ± 0.6	2.4 nm
[37]	Capped	60		2.7 nm

Characterisation shows the phase of the nanoparticles to be hexagonal wurtzite. **Table 12** shows the effect of reaction time and capping on the size of the nanoparticles, estimated by Scherrer's formula and measured by TEM using particle sizing software imageJ.[240]

Interestingly, although increased reaction times did show a slight increase in the size of particles, they also showed a decrease in monodispersity. The best dispersed nanoparticles with consistent particle size can be seen in **Figure 91**, TEM of **[36]**, with an average size of 2.9 nm and an SD of 0.6. TEM of sample **[35]** shows overall larger nanoparticles, with less monodispersity.

Figure 92 shows the PXRD pattern for ZnO nanoparticles synthesised in ethylene glycol under microwave heating conditions. All peaks are well indexed to the hexagonal wurtzite phase on ZnO, with no peaks present from any other phase showing a high purity product. The Scherrer equation was used to estimate the average crystallite size to be 48 nm, far higher than that observed for the other synthesis method employed.

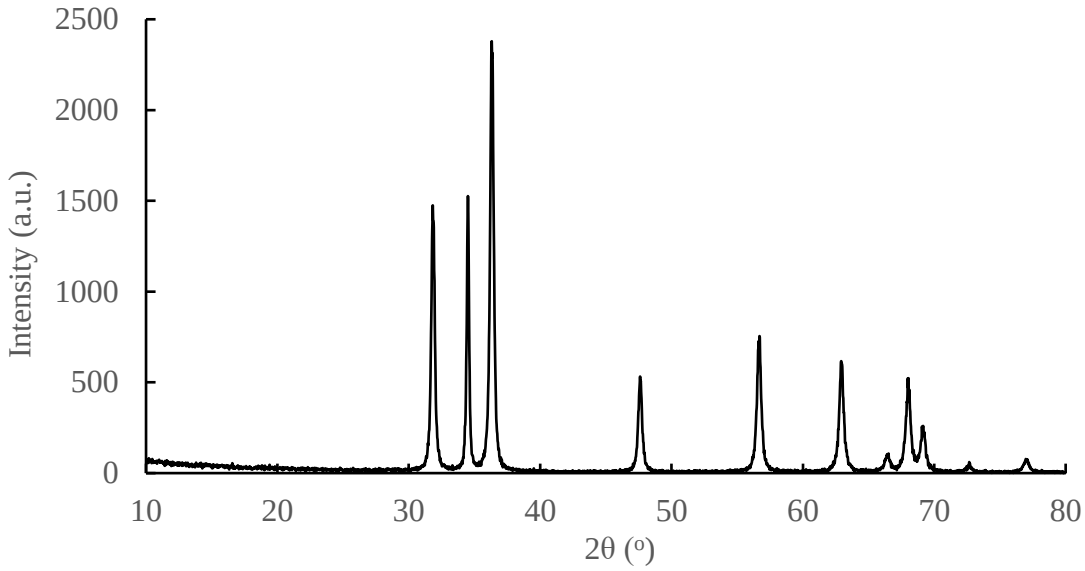

Figure 92 PXRD pattern of ZnO synthesised in ethylene glycol under microwave heating conditions.

3.3.7.5. UV-Vis spectra of ZnO nanoparticles vs. quantum dots

UV absorption spectra of samples **[33-37]**, taken at room temperature are shown in **Figure 93.** The absorption is shown to be substantially blue shifted for the smaller nanoparticles **[33]** and **[34]**, due to strong confinement, and is in keeping with literature.[241,242]

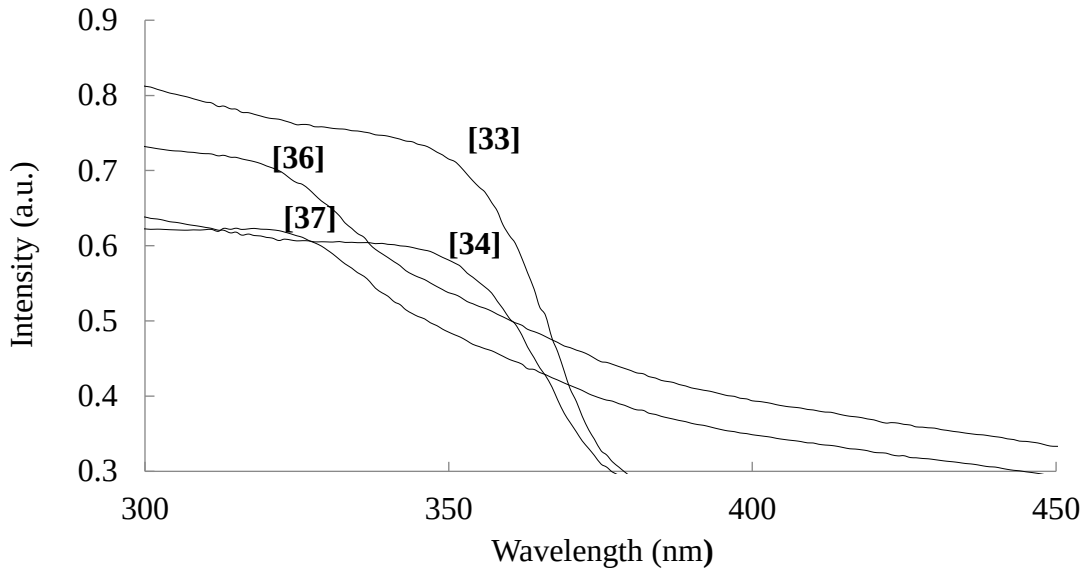

Figure 93 Absorption spectra of samples **[33]**,**[34]**,**[36]** and **[37]** shows evidence of quantum confinement.

Figure 94 shows the UV-Vis absorption spectra of the synthesised ZnO NPs in EG. A clear shift to higher wavelengths has been observed with a strong absorption at 377 nm. It was intended by the synthetic method employed for these NPs to be of a larger particulate size than the previously synthesised QDs. A shift in UV-Vis absorption to higher wavelengths has been shown to correspond to increasing particles size.[238]

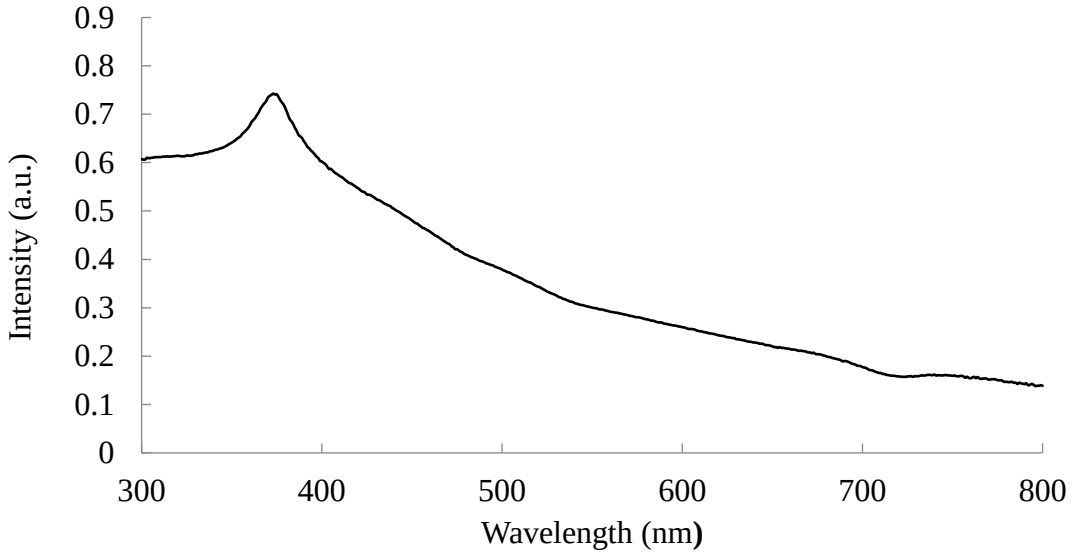

Figure 94 UV-Vis absorption spectrum of ZnO synthesised NP in EG.

It is well understood that semiconductor nanoparticles or quantum dots (QD) have superior optical properties to the bulk material.[218] Guo *et al.*[241] showed a ~ 500x enhancement in third order nonlinear optical response attributed to confinement effects. **Figure 95** shows the excitation spectrum of samples **[33]**, **[34]**, **[36]** and **[37]**. It has been shown that emission intensity of a QD depends on size[242] which is in keeping with the findings presented here, as well as a shift toward higher energy. **Figure 96** shows the fluorescence spectrum of EG prepared ZnO nanoparticles.

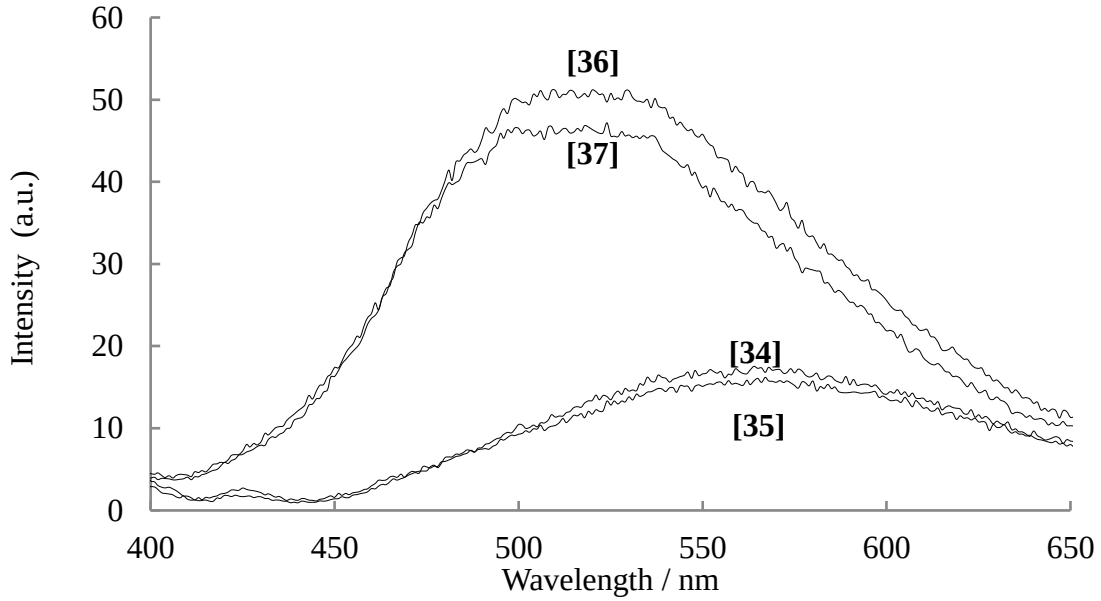

Figure 95 Fluorescence spectra of ZnO samples; the sizes of **[34]** and **[35]** were shown to be < 5 nm, the sizes of **[36]** and **[37]** have been shown to be < 3 nm in diameter.

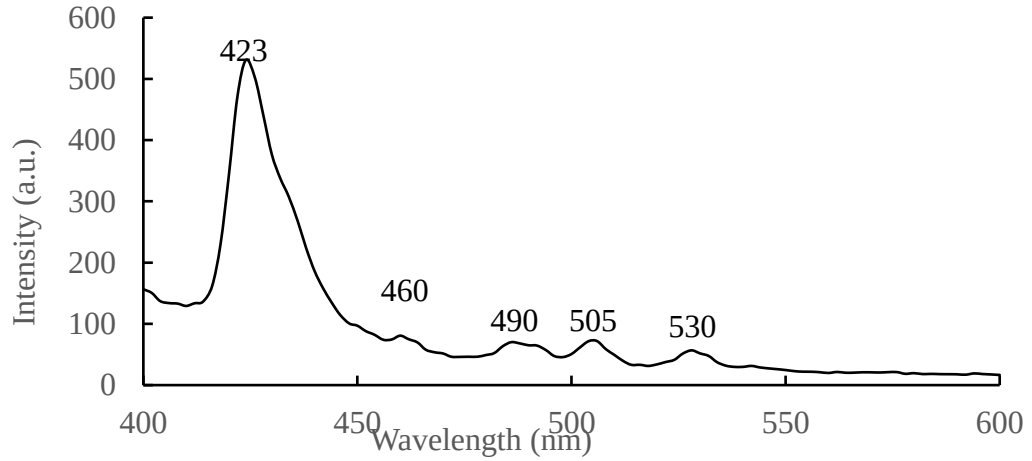

Figure 96 Fluorescence spectrum of ZnO synthesised NP in EG, excitation 370 nm.

3.3.8. Calcium fluoride (CaF_3:Eu)

3.3.8.1. Background

Calcium fluoride offers some potential advantages over oxide host compounds, including a lower phonon energy (~ 450 cm^{-1}) reducing the chances of non-radiative relaxations, minimising the quenching of excited state lanthanides allowing for an efficient luminescence or scintillation. Additionally the ionic radius of calcium cations is close to that of lanthanide dopant ions, enhancing the chances of the lanthanide cation partially replacing the calcium cation reducing the formation of crystal defects and lattice stress.[243]

Europium-doped calcium fluoride is an extrinsic scintillator material, activated by the capture of ionisation holes and electrons by the dopant ions, luminescence is promoted by defect bound exciton emissions.

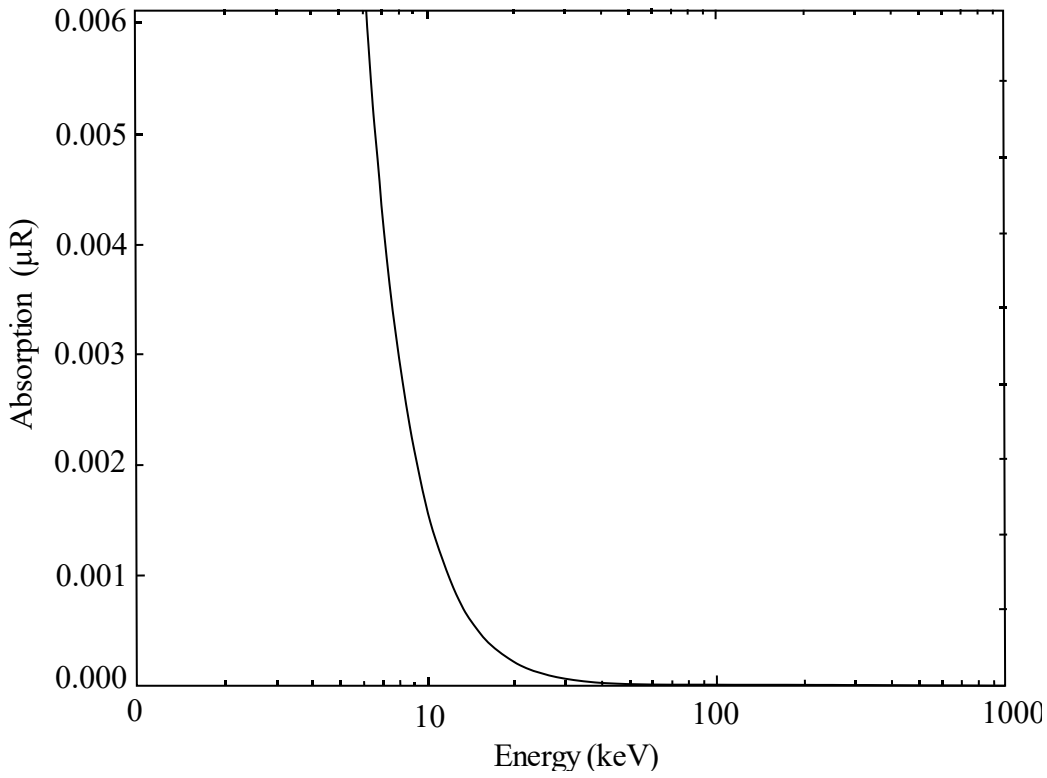

Figure 97 Absorption of CaF_2 under irradiation with ionising radiation.

Europium-doped calcium fluoride nanoparticles offer a cheap and easily synthesised fluoride-based scintillator host material which may prove to be very well suited to lower energy X-ray excitation energies, such as I-125. From the absorption (**Figure 97**) it is observed that a fairly steep decline in absorptivity occurs after ~ 10 keV, however 20 - 30 keV may still be a suitable energy range for this material. Indeed nanoparticulate europium-doped CaF_2 has previously been shown to exhibit scintillation under irradiation using a 40 kV X-ray tube, which would generate a spectrum of energies at a maximum of 40 keV and an average energy between 10 - 30 keV.[244]

3.3.8.2. Synthesis of europium doped calcium fluoride nanoparticles [38]

A number of synthetic methods exist for CaF_2 NPs in the literature.[245–249] The synthesis of 3% molar europium-doped calcium fluoride nanoparticles **[38]** was carried by a reverse strike co-precipitation reaction according with the literature.[244]

The PXRD pattern of the Eu doped CaF_2 NPs is shown in **Figure 98**. All peaks observed were indexed and found to be face centred cubic phase of fluorite structure with a space group *Fm3m* in agreement with the literature.[244] Nanoparticle size was determined to be approximately 20 nm by Scherrer's equation.

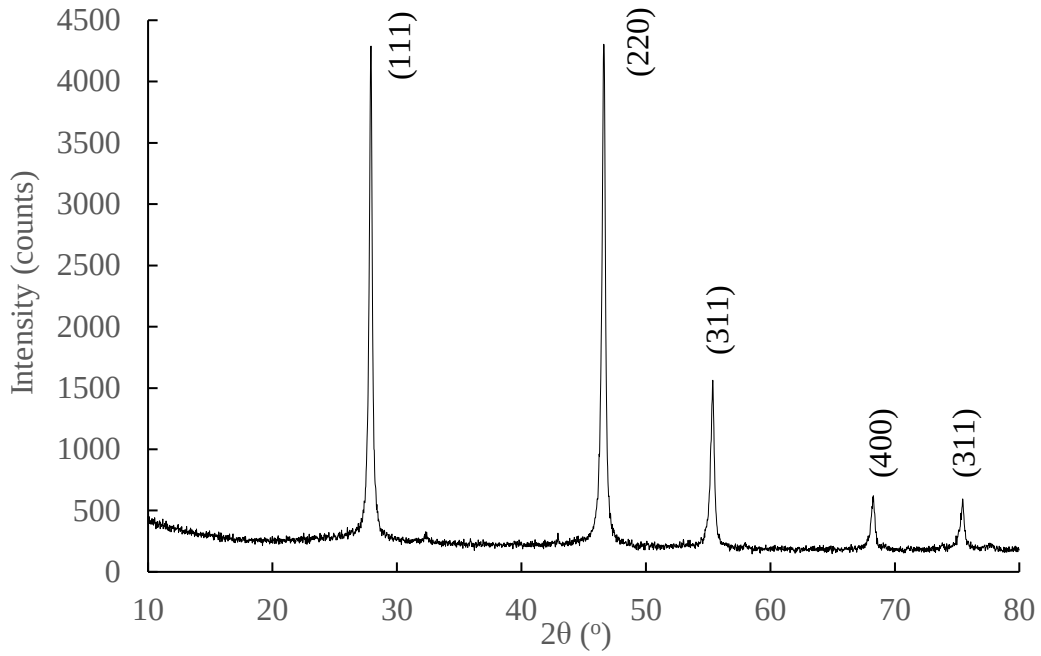

Figure 98 PXRD showing the phase of CaF_2:Eu **[38]** nanoparticles.

3.3.8.3. Irradiation with Radsource RS-2000 and Ir-192

Under irradiation with X-rays, electron-hole pairs are formed and migrate through the scintillator to recombine at the rare earth (RE) ions. It has been previously reported that the diffusion length of electron-hole pairs in alkali halides is around 100 nm (far larger than the size of nanoparticles), making the capture mechanism most likely from lattice defects.[250] It is therefore encouraging to have X-ray excited luminescence shown in **Figure 99** at around 590 nm, corresponding to the luminescence peak generated from a $^5D_0 \rightarrow {}^7F_1$ transition of Eu^{3+}.

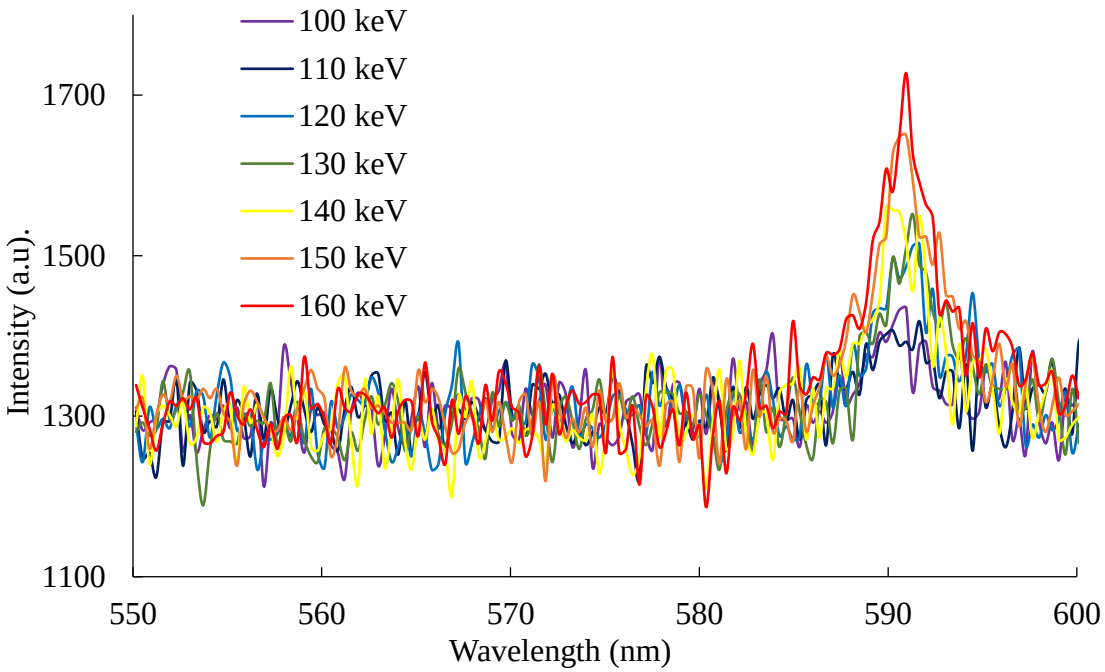

Figure 99 XRIL spectra of CaF_2:Eu **[38]** nanoscintillator.

Figure 99 demonstrates an increase in XRIL intensity with increasing kV which corresponds to energies from 100 - 160 keV for the generated photons. This may at first appear to be contradictory to what was expected from the generated absorption coefficient (**Figure 97**) and the hypothesis that this material is best suited for energies < 50 keV. However, it must be remembered that as a higher potential difference is put through X-ray tube generator, the maximum possible energy of photons increases. The average photon energy does not increase very much but instead increases in intensity, (i.e. the number of photons per second) (**Figure 55**). Indeed, when a higher energy source was used for measuring the XRIL intensity using an Ir-192, which has a much higher average energy of 330 keV, the intensity of the luminescence recorded did drop again (**Figure 100**) as was expected. What this does show however, is that due to the increase in the number of photons generated for the maximum possible voltage; using this maximum voltage is likely preferable for all materials, as it will not dramatically affect the energy spectrum generated, but only the number of photons per second, at each energy.

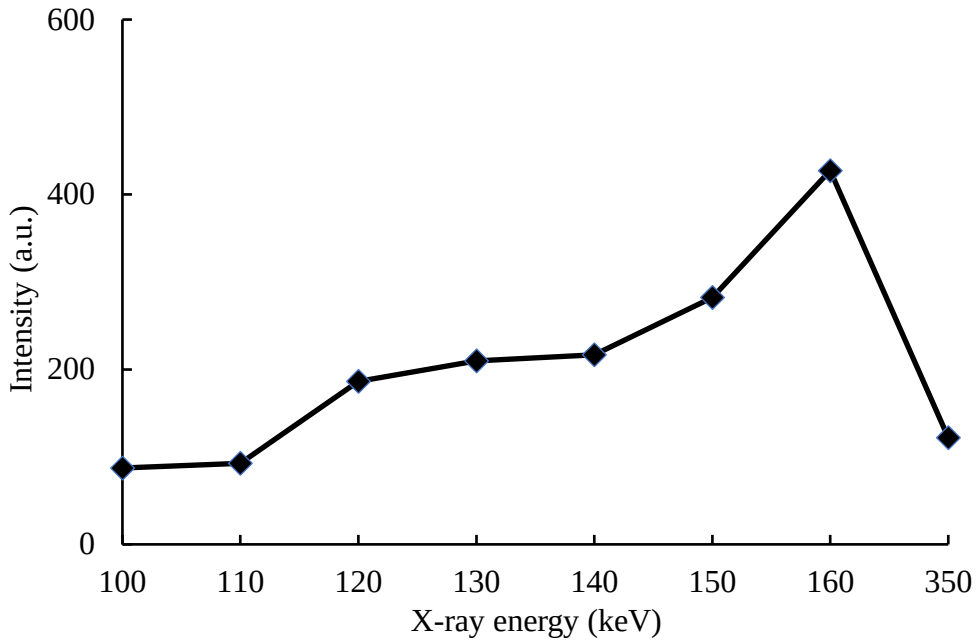

Figure 100 Relative luminescence intensities emitted at 590 nm by **[38]** for X-ray irradiation energies from 100-160 keV and at (average photon energy 330 keV for Ir-192).

3.3.9. Lanthanum fluoride

The LaF_3 host matrix exhibits a high biocompatibility and a good photochemical stability as well a low phonon energy (~ 350 cm^{-1}). Lanthanum fluoride has been investigated as a continuation into the fluoride nanoscintillators. Given the scintillation results from the CaF_2:Eu nanoparticles it was considered that LaF_3 based scintillators, being of greater density and still with luminescence in the desired area of the spectrum, would make the next logical step in finding a better nanoscintillator. The absorption K-edge of lanthanum at 38.9 keV (**Figure 101**), gives LaF_3 the best absorptivity of the 9 materials investigated at 40 keV and the second best at 50 and 60 keV, making this material highly suitable for use with I-125 and Ir-192 brachytherapy sources as well as Gulmay.

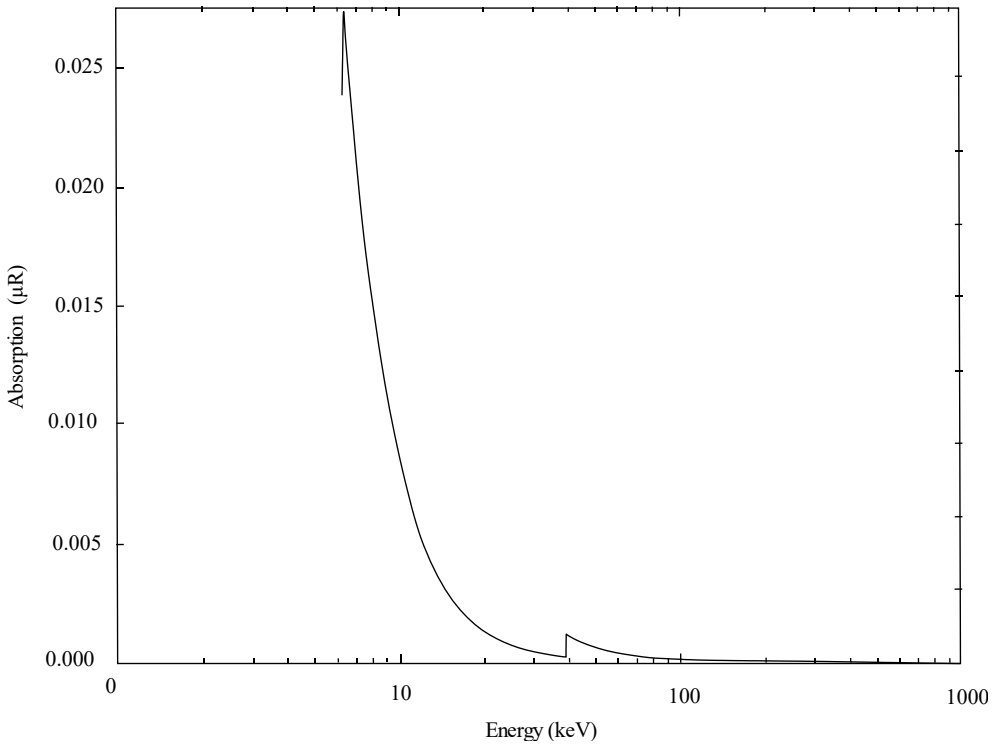

Figure 101 Absorption of LaF_3 at increasing energy of ionising radiation.

3.3.9.1. Synthesis of europium-doped lanthanum fluoride nanoparticles [39]

Rare-earth (RE) doped LaF_3 NPs have been synthesised by a variety of methods previously, including coprecipitation,[251,252] single source precursor,[60] polyol,[253] and hydrothermal[254] methodologies.

Synthesis of 3% molar europium-doped LaF_3 NPs ($La_{0.97}Eu_{0.03}F_3$) was carried out by a reverse strike co-precipitation reaction in accordance with the literature.[244] A precipitation synthesis uses compounds that are soluble in the chosen solvent that will promote chemical reactions of a product which is insoluble. Nitrates, acetates, halides and NH_4^+ compounds are all soluble in water and make suitable reactants. As with the previously synthesised CaF_2 NPs, nitrates and ammonium fluoride was chosen for the precipitation reaction of LaF_3 NPs.

3.3.9.2. Characterisation of $La_{0.97}Eu_{0.03}F_3$ nanoparticles [39]

Figure 102 shows the PXRD pattern of $La_{0.97}Eu_{0.03}F_3$ synthesised under benchtop conditions. The PXRD pattern shows that the sample is single phase LaF_3 with hexagonal structure in agreement with the literature.[244] The nanoparticle size was estimated to be approximately 70 nm by use of Scherrer's formula, in good agreement with the SEM.

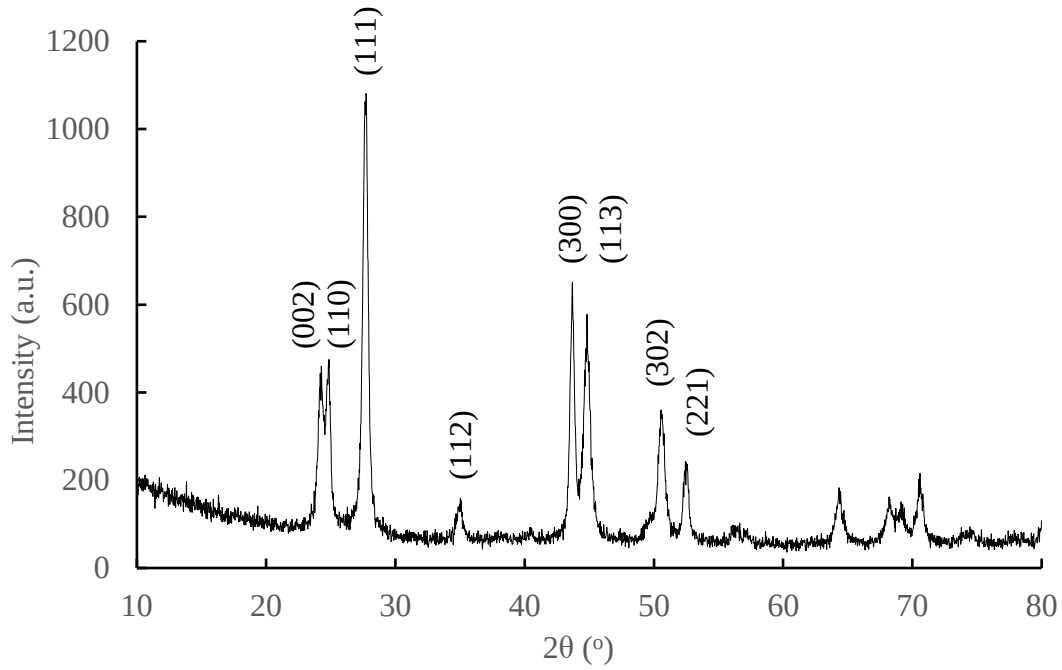

Figure 102 PXRD pattern for compound **[39]** exhibits only single phase LaF_3 hexagonal structure.

Figure 103 shows the PXRD pattern of $La_{0.97}Eu_{0.03}F_3$ synthesised under microwave conditions heating **[40]**. It was noticed from comparing the PXRD patterns of the two methods of synthesis that peaks 002 and 113 have different growth rates under the two conditions. Every peak in the PXRD corresponds to a crystal plane, reflecting that there is a difference in the growth rate of the crystal planes in the formation of the nanocrystal. This has been previously observed for peak 113 in response to an increase in temperature.[254] The other difference observed by PXRD is a higher crystallinity and larger

estimated size of particles by Scherrer's formula. This is not surprising given the increased temperature and reaction times of the microwave synthesis.

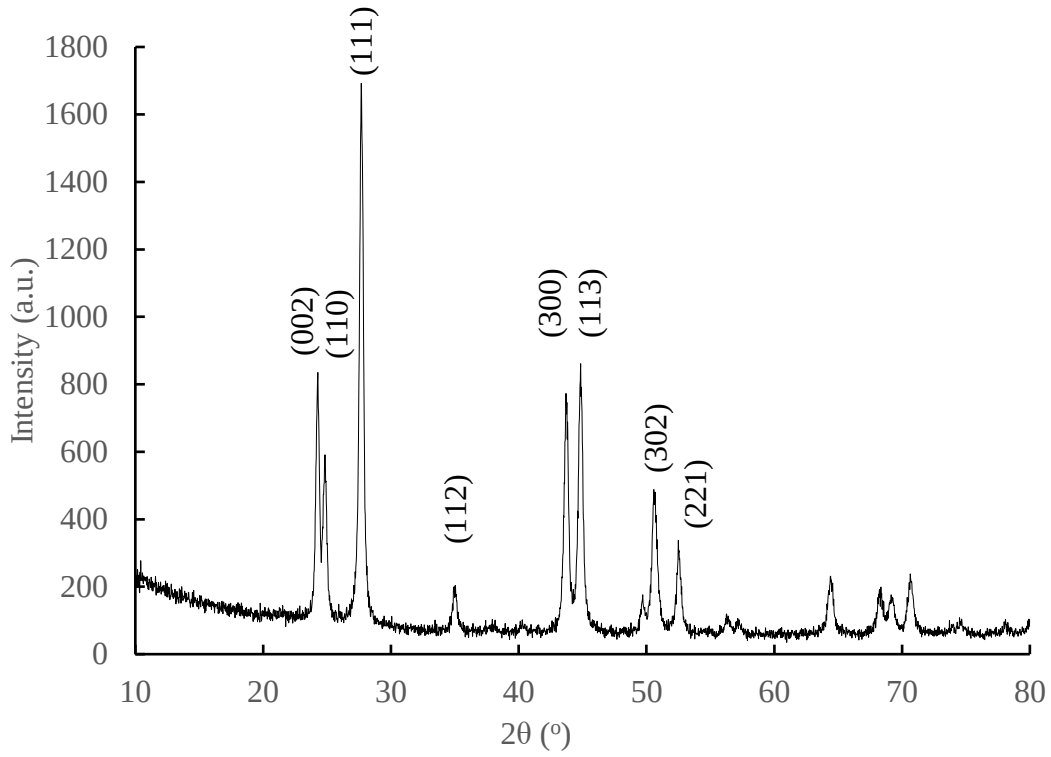

Figure 103 PXRD pattern exhibited by compound **[40]** microwave synthesised LaF_3 nanoparticles.

Figure 104 and **Figure 105** show the SEM of the benchtop and microwave synthesised methods for nanoparticle synthesis. They confirm an increase in size in the microwave synthesised sample as well as a greater degree of homogeneity of size and shape.

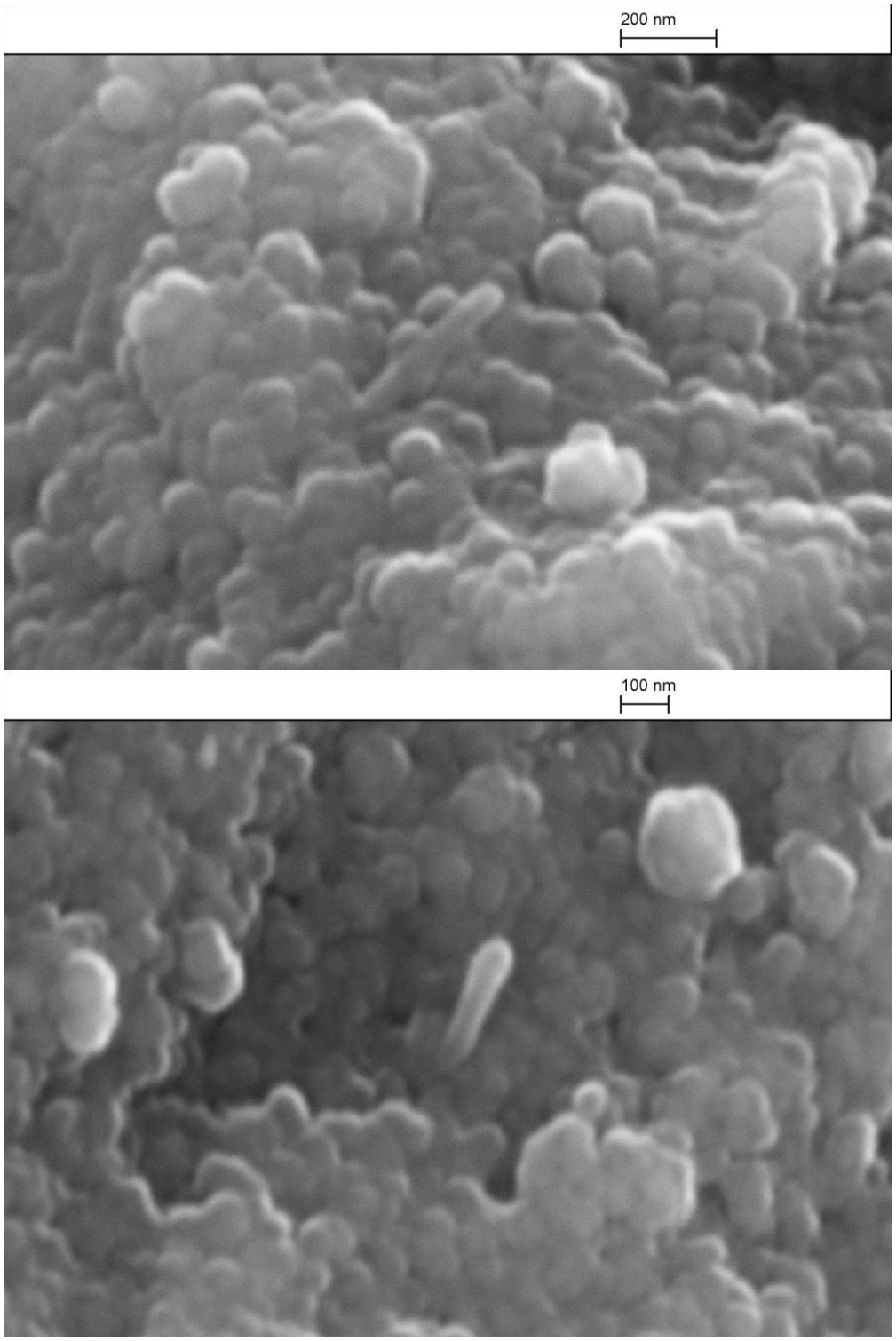

Figure 104 SEM of europium doped LaF_3 synthesised by benchtop methodology **[39]**.

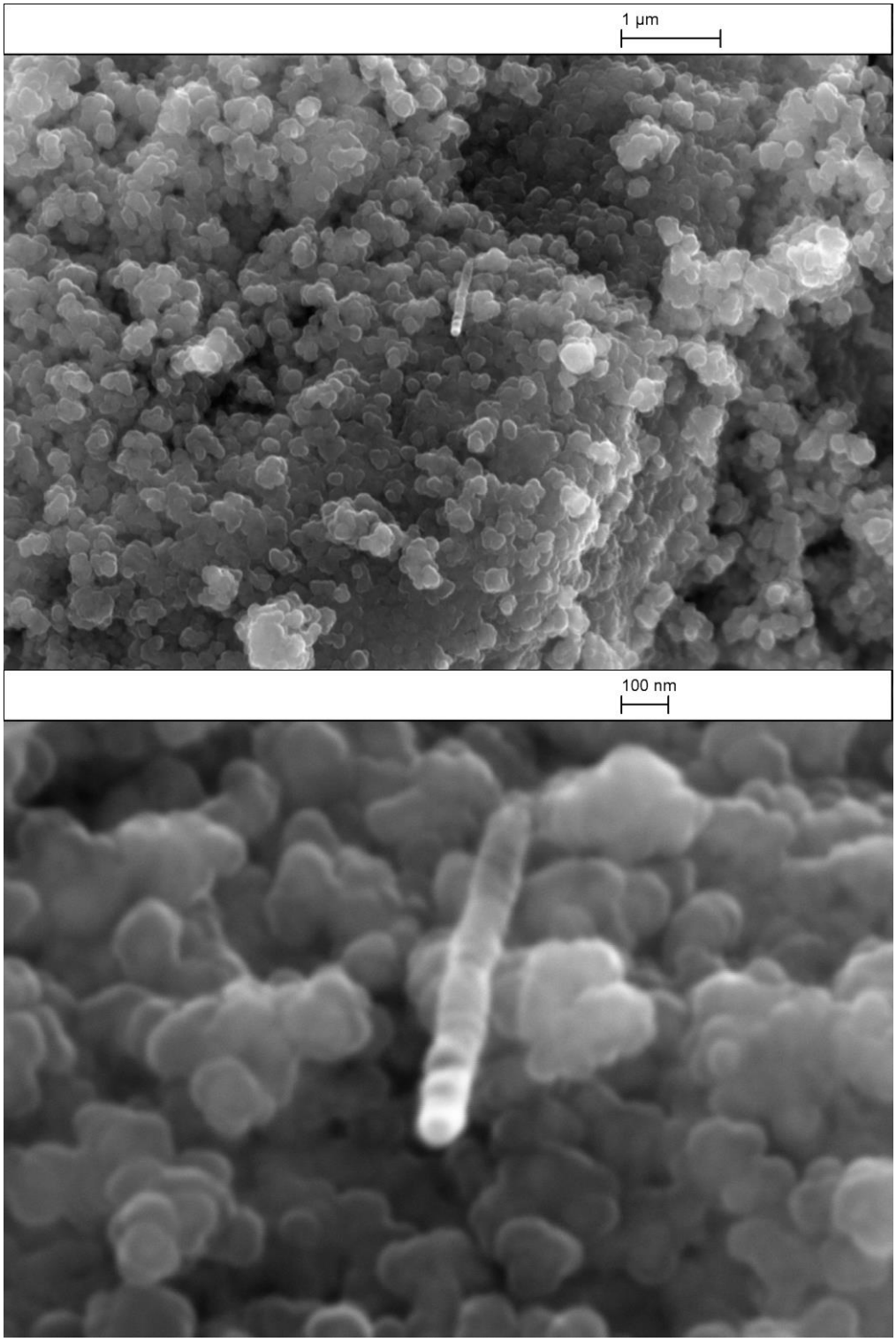

Figure 105 SEM showing microwave synthesised europium-doped LaF_3 nanoparticles **[40]**.

3.3.9.3. X-ray induced luminescence of LaF_3 nanoparticles under irradiation with Ir-192

Figure 106 shows the XRIL spectrum of the microwave synthesised $La_{0.97}Eu_{0.03}F_3$ nanoparticles **[40]** irradiated using an Ir-192 source. Unlike the CaF_2 NPs irradiated under these conditions, LaF_3 exhibited a good luminescent response. The emission spectrum shows two intense bands at 592 and 619 nm, which are associated with the $^5D_0 \rightarrow {}^7F_1$ and $^5D_0 \rightarrow {}^7F_2$ transitions for hexagonal-coordinated Eu^{3+}. The dominant emission at 592 nm corresponding to the $^5D_0 \rightarrow {}^7F_1$ magnetic dipole transition, indicates that the Eu^{3+} is located in a site of inversion symmetry within the LaF_3 matrix.[254]

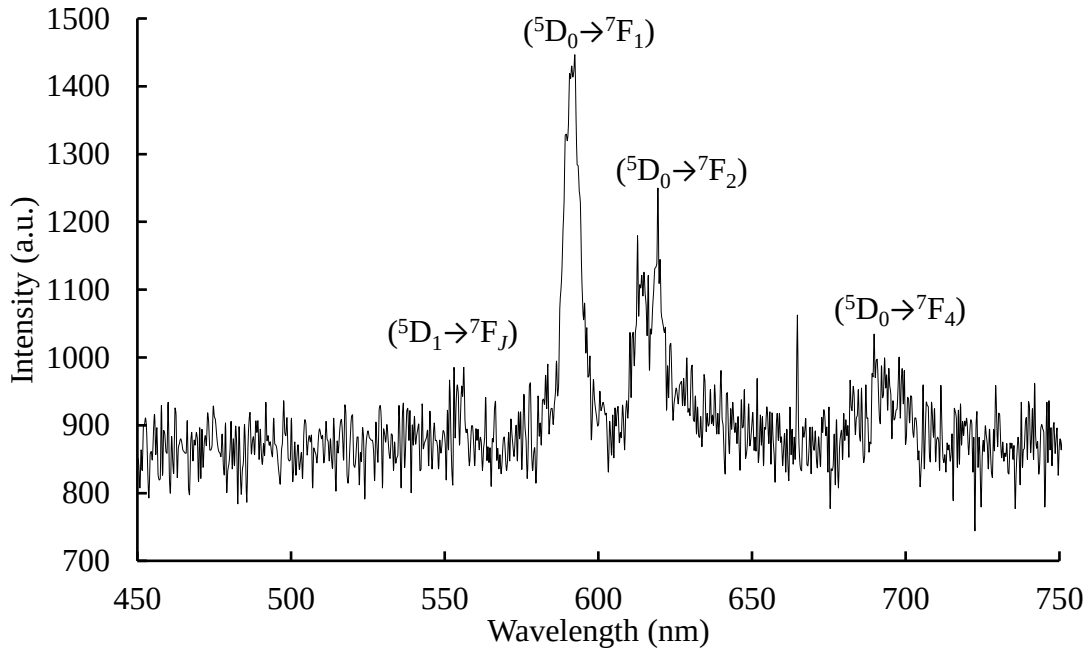

Figure 106 XRIL of LaF_3 nanoparticles **[39]** spectrum under irradiation with Ir-192.

The photoluminesence of LaF_3:Eu nanoparticles has been extensively investigated previously,[255–258] however the XRIL has only been reported once and at much lower energies, using a 40 kV X-ray tube.[244] The X-ray source used here was Ir-192 which has an average energy of 330 keV. The result of a good scintillation here offers an exciting

potential for this material at a range of energies and indicates a real possibility for the use of this material in conjunction with brachytherpay techniques.

3.3.10. Lutetium fluoride (LuF_3) [41]

Lanthanide-doped rare earth fluorides (REF_3) have become a research hot spot due to their potential applications within the areas of optical telecommunications and lasers.[259] RE fluorides exhibit a high chemical stability and have very low vibrational energies compared with oxides which minimizes the quenching of excited-state lanthanides by lattice vibrations and allows for an efficient luminescence or scintillation. This is due to the LnF_3 core exhibiting particularly low phonon energies (300 cm^{-1}).[260]

Although several nanoparticular fluorides have been reported in the literature (YF_3, LaF_3, GdF_3), there are very few reports to be found for the synthesis of LuF_3[259,261–263] and none yet exploring the potential of this nanoparticle as a scintillating material, despite the high effective Z-value (Z_{eff} = ~ 63 at 100 keV) and density of this material (8.29 gcm^{-3}). It is for this reason that the absorptivity of this material is one of the highest of all the materials investigated at every energy range. LuF_3 also has a very high absorption K-edge of 63.3 keV (**Figure 107**), extending its application to higher energy therapies such as Ir-192 brachytherapy.

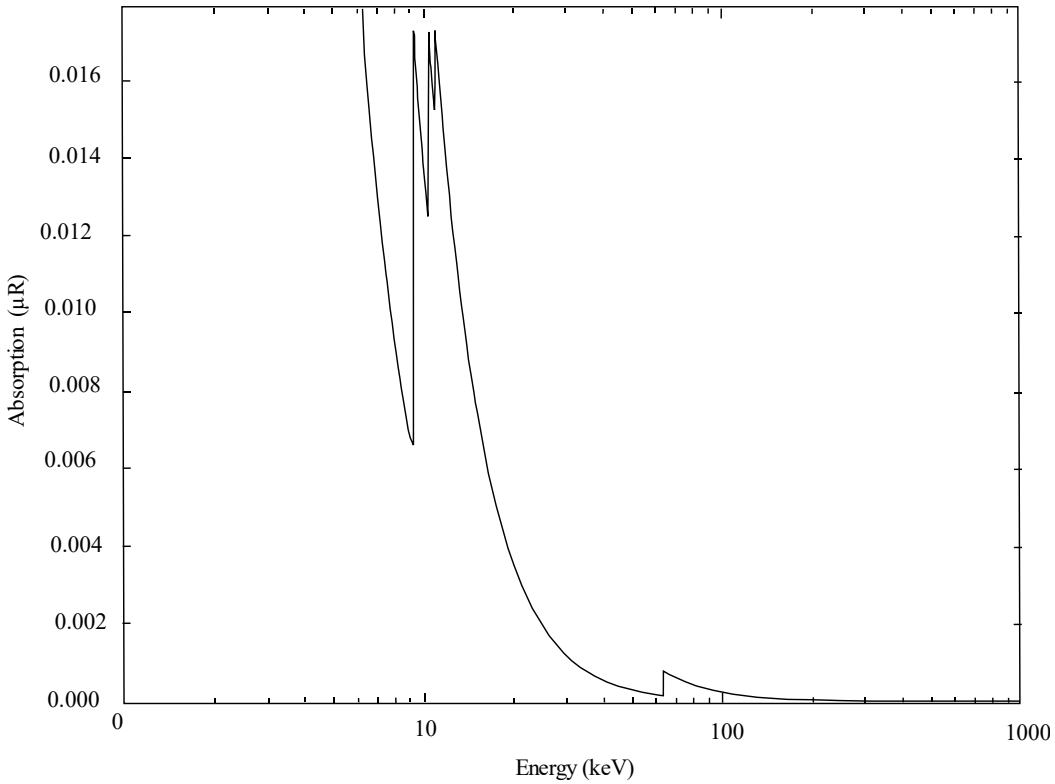

Figure 107 Absorption for LuF_3 at increasing energies of ionising radiation.

3.3.10.1. Synthesis of europium-doped lutetium fluoride nanoparticles

Beccero *et al.* reported a 20% doped sample yielded the highest luminescent intensity from a study of europium incorporation between 0.5 - 30%.[259] For this reason nanoparticles of have been doped at 20% molar $Lu_{0.8}Eu_{0.2}F_3$.

3.3.10.2. Characterisation of $Lu_{0.8}Eu_{0.2}F_3$ nanoparticles

Figure 108 shows the PXRD pattern of the synthesised NPs before annealing. The product is a single phase $NH_4Lu_2F_7$ cubic phase.[264]

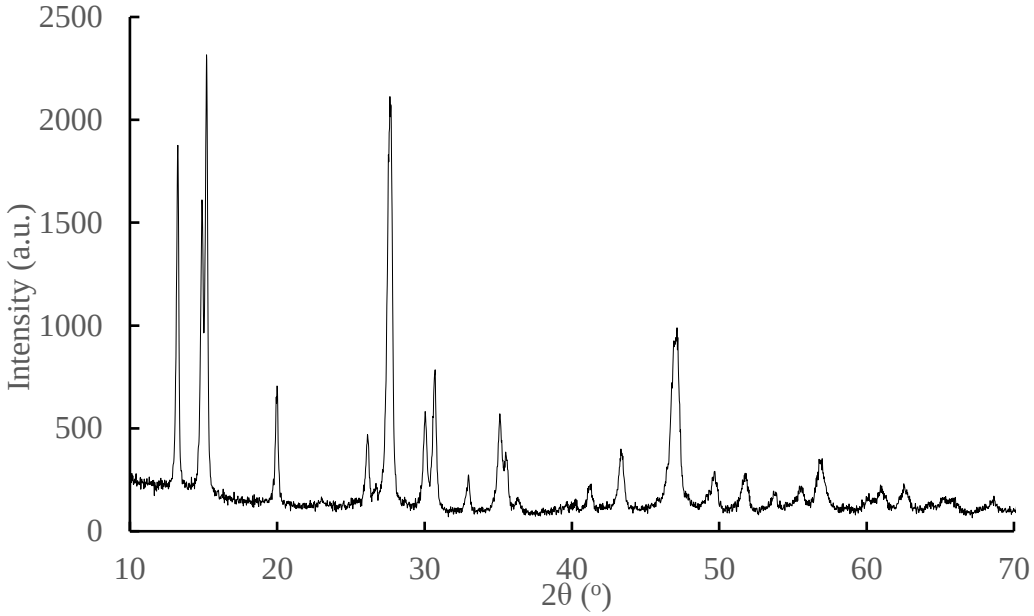

Figure 108 PXRD of LuF_3 NPs before annealing.

After annealing at 400 °C for 5 hours, the product undergoes a phase change, giving a single phase sample of LuF_3 showing orthorhombic crystal phase (space group *Pnma*)[261] (**Figure 109**).

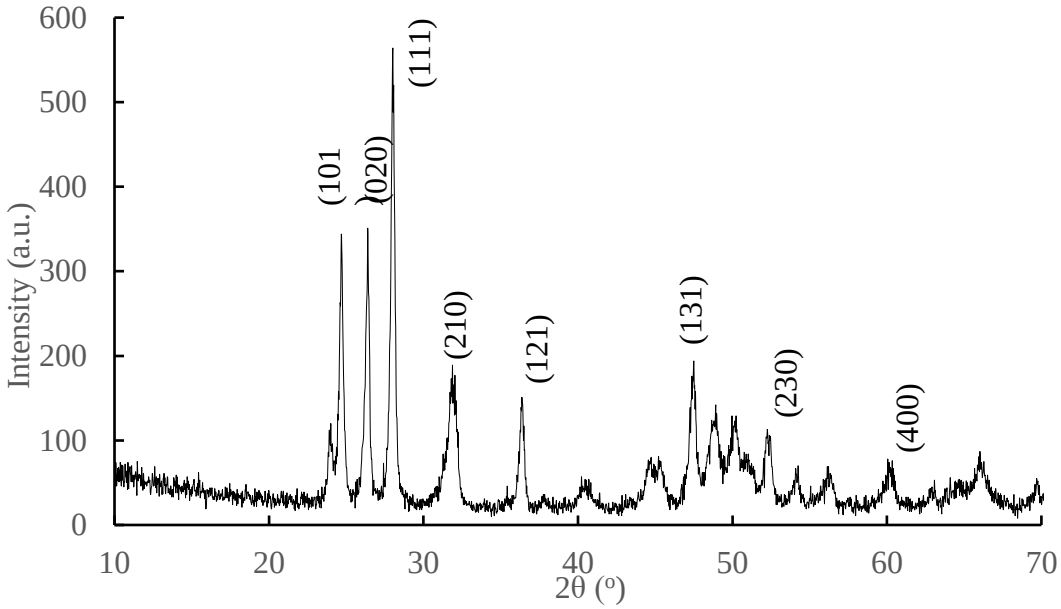

Figure 109 Post annealed PXRD pattern for $Lu_{0.8}Eu_{0.2}F_3$ nanoparticles.

The size of nanoparticles was characterised using SEM (**Figure 110**), with the diameter size ranging from 100 - 120 nm.

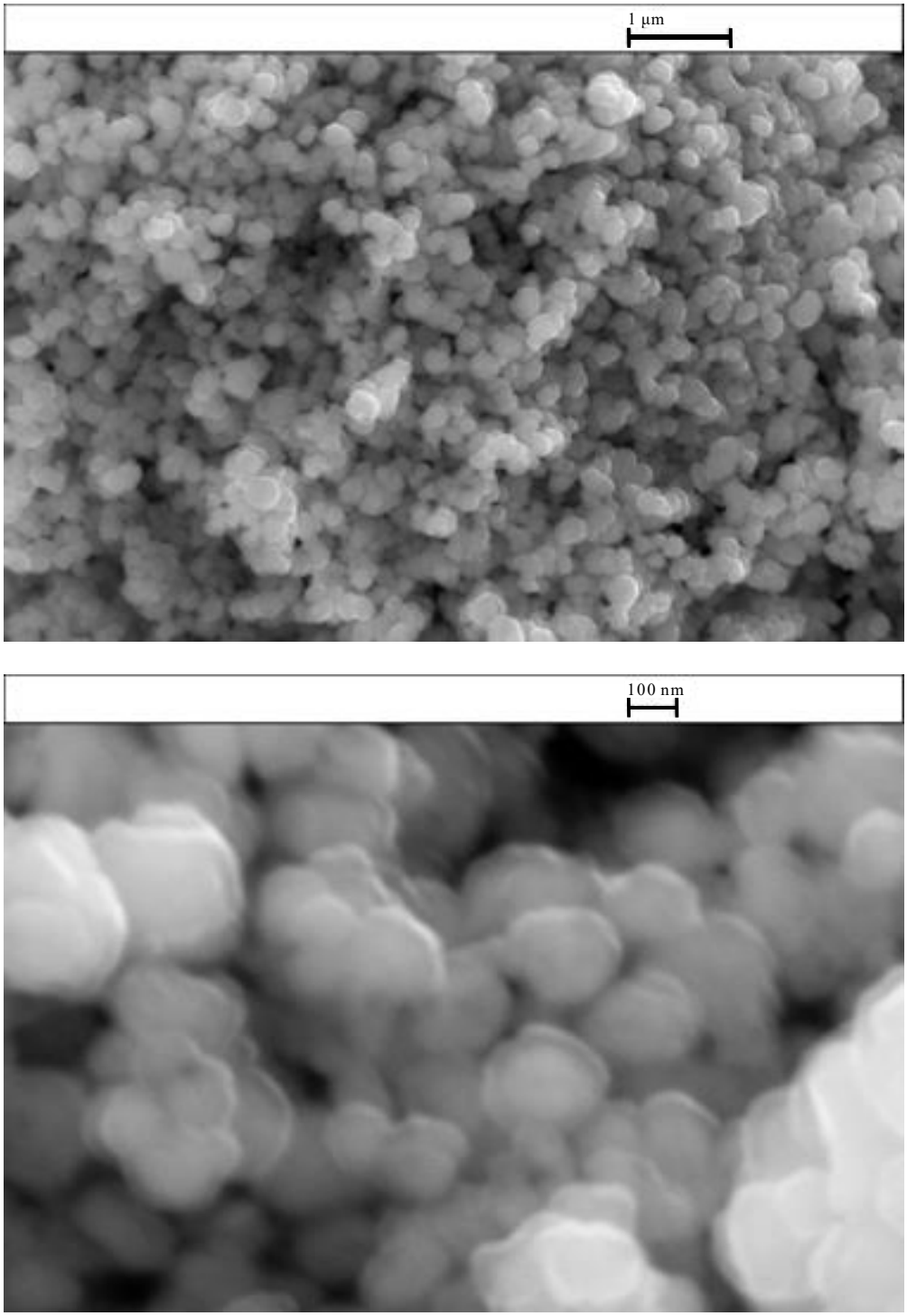

Figure 110 Scanning electron microscopy images of LuF_3 nanoparticles **[41]**.

3.3.10.3. X-ray induced luminescence of europium doped LuF_3 nanoparticles under irradiation

Figure 111 shows the XRIL spectrum of the microwave synthesised $Lu_{0.8}Eu_{0.2}F_3$ nanoparticles **[41]** irradiated using energies from 100 to 160 keV. Like the LaF_3 the emission spectrum shows two intense bands at 592 and 6925 nm, which are associated with the $^5D_0 \rightarrow {}^7F_1$ and $^5D_0 \rightarrow {}^7F_4$ transitions for hexagonal-coordinated Eu^{3+}. The dominant emission at 592 nm corresponding with the $^5D_0 \rightarrow {}^7F_1$ magnetic dipole transition, indicates that the Eu^{3+} is located in a site of inversion symmetry within the LuF_3 matrix.[259]

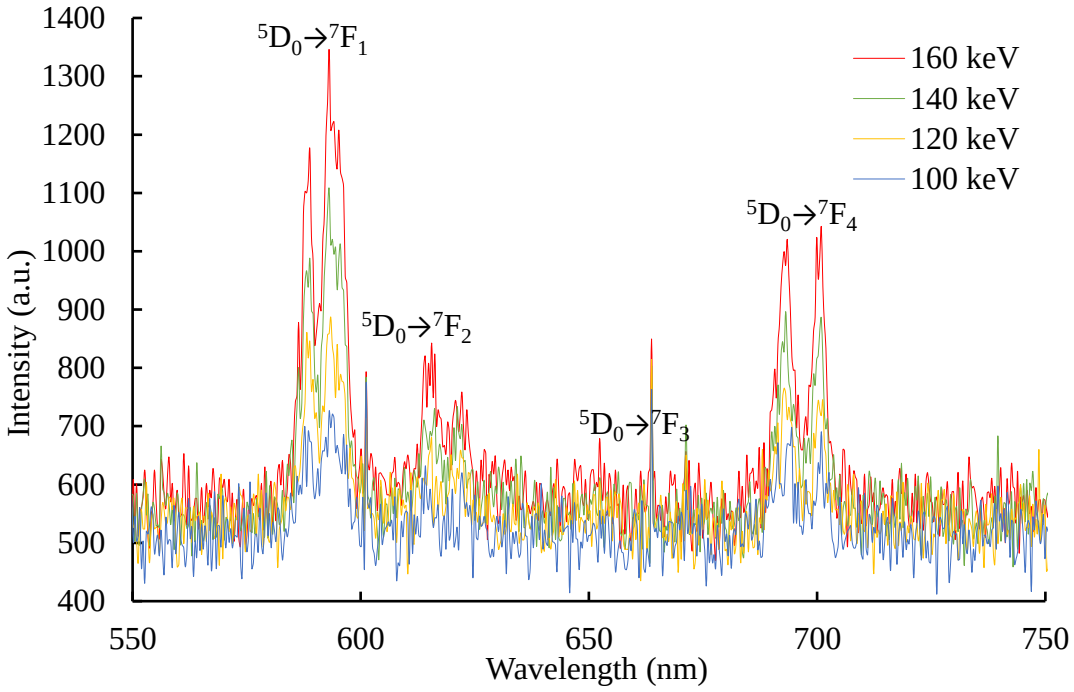

Figure 111 XRIL of europium-doped LuF_3 nanoparticles **[41]** spectrum under irradiation with increasing energies.

3.3.11. Yttrium oxide nanoparticles

Y_2O_3 nanoparticles have been shown to be excellent host materials for RE elements such as samarium, erbium, gadolinium and europium.[265] It has been shown to have a very high refractive index (> 1.9), a large band gap (5.8 eV) and high chemical stability,[266] and has therefore attracted a lot of attention in recent years for applications in optical display technology and medical imaging.[267] $Y_{2-x}Eu_xO_3$ in particular has been studied and found to have high quantum efficiency in the orange-red region.[268]

Figure 112 shows the absorption coefficient for Y_2O_3 with a K-edge of only 17.03, suggesting this material is likely better suited for lower energy irradiations. However, it makes an interesting comparison with Lu_2O_3, which has a much higher density and K-edge.

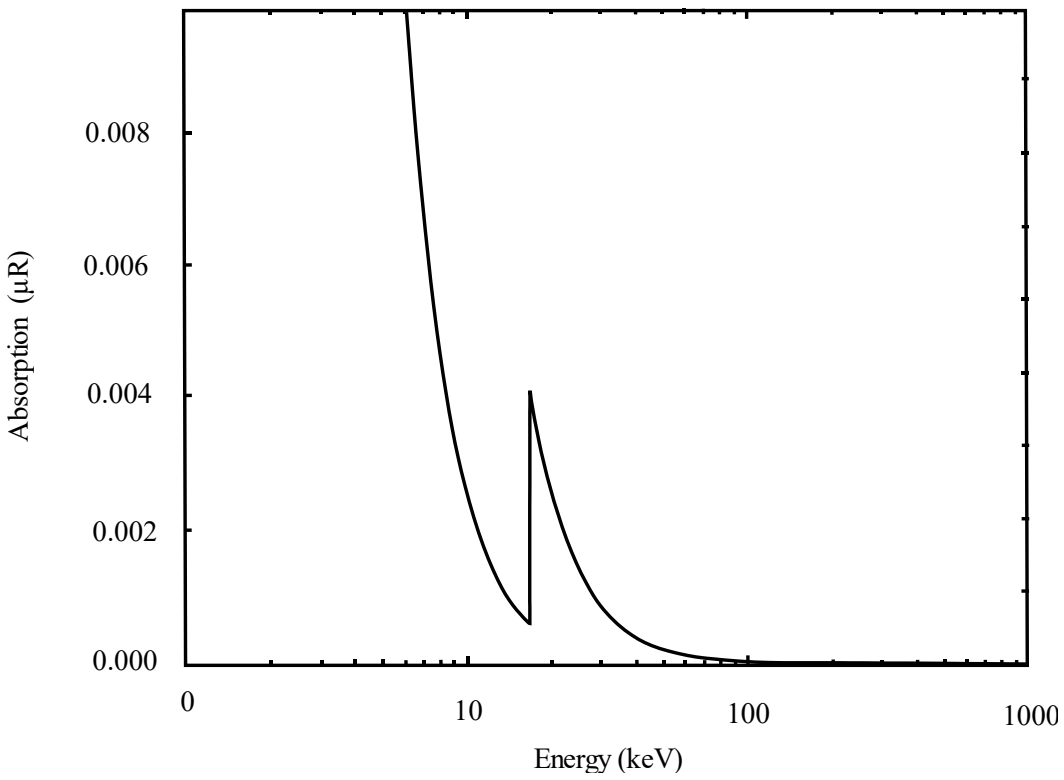

Figure 112 Absorption of Y_2O_3.

3.3.11.1. Synthesis of Y_2O_3 nanoparticles [42]

A number of different syntheses have been employed for the synthesis of Eu-doped Y_2O_3 including hydrothermal, sol-gel, solid state, and wet chemical synthesis.[269–271]

Based on our previous success with microwave radiation assisted syntheses, a new method was developed using a co-precipitation under microwave heating followed by annealing in a box furnace (**Scheme 8**).

(1) $Y(NO_3)_3 \cdot 6H_2O + 3NaOH \longrightarrow 3Na(NO_3) + 6H_2O + Y(OH)_3$

(2) $2Y(OH)_3 \xrightarrow{heat} Y_2O_3 + 3H_2O$

Scheme 8 Mechanism of synthesis of Y_2O_3 NPs. (1) Precipitation reaction forms the hydroxide. (2) Upon annealing hydroxide is oxidised and Y_2O_3 NPs are formed.

3.3.11.2. Characterisation of Y_2O_3 nanoparticles

The PXRD of Y_2O_3 is shown in **Figure 113** and displays a product which is pure, with a single phase and good crystallinity, with a body centred cubic structure.

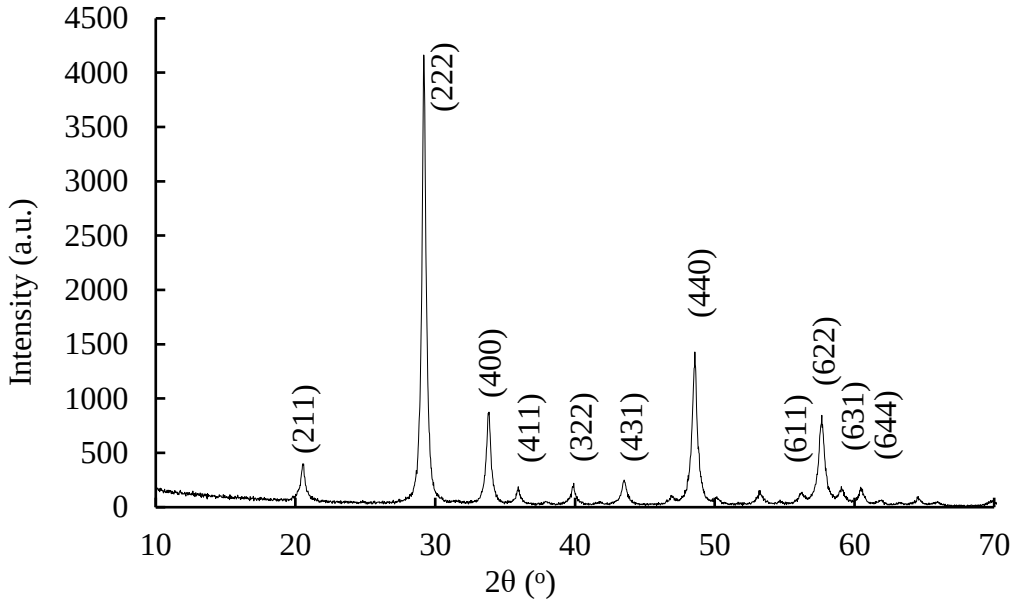

Figure 113 PXRD of Y_2O_3 nanoparticles **[42]**.

3.3.11.3. Synthesis of Y_2-xEu_xO_3 nanoparticles

The syntheses of europium-doped Y_2O_3 nanoparticles with molar percentages of 1, 3 and 5% were undertaken using the previously explained methodology but a percentage of the $Y(NO_3)_3{\cdot}6H_2O$ was substituted for $Eu(NO_3)_3{\cdot}6H_2O$.

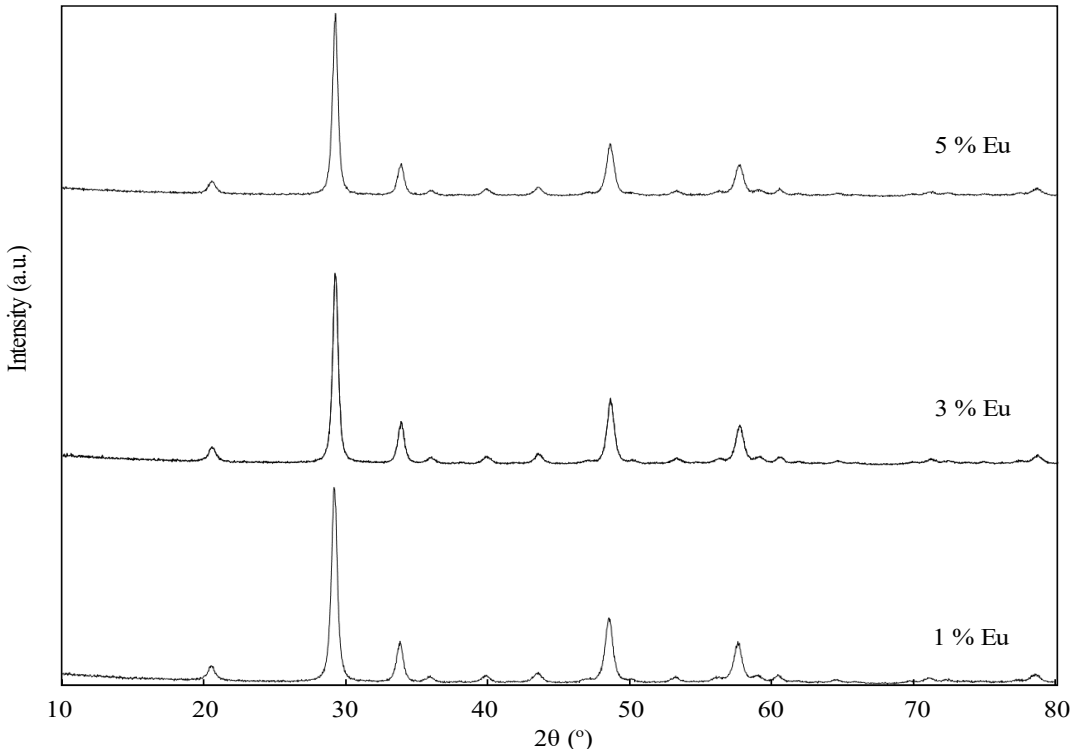

Figure 114 PXRD spectra of europium-doped Y_2O_3 nanoparticles in molar % 1, 3 and 5%.

3.3.12. Lutetium oxide nanoparticles [43]

Lu_2O_3 nanoparticles scintillators are of great interest due to their wide band gap (~ 5.5 eV)[272] high absorption coefficients owing to a high density (9.42 gcm^{-3}) and effective atomic number (67.43) yielding a light output under X-ray irradiation shown to be comparable with CsI:Tl.[273]

There have been numerous detailed studies of Eu^{3+} doped Lu_2O_3[274–277] and the red emission has been shown to possess up to 90% quantum efficiency.[278] These reasons make this material a highly suitable candidate for our purposes and are worth investigation.

3.3.12.1. X-ray induced luminescence of Lu_2O_3 nanoparticles under irradiation with Radsource RS-2000 Biological Irradiator

From the XRIL spectra obtained for the 1, 3 and 5% doped nanoparticles we are able to determine that the 1% doped samples gave the highest intensity luminescence, in keeping with the literature. As Eu^{3+} is highly sensitive to its local environment, directly affecting the luminescence observed, we can infer where the Eu^{3+} ions are likely to be situated within the crystal structure.

Lu_2O_3 has a cubic C-type structure and offers two sites for a Eu^{3+} ion to replace the Lu^{3+} ions. Each has a 6-fold coordination and are C_2, non-centrosymmetric and S_6 centrosymmetric (**Figure 115**).[278] The non-centrosymmetric Eu(C_2) ions have only partially forbidden electric dipole induced transitions, appearing strongly within the spectra at 610 nm ($^5D_0 \rightarrow {}^7F_2$). In asymmetric crystal fields the electric dipole transitions are more probable than the magnetic dipole transitions ($^5D_0 \rightarrow {}^7F_1$). Because the S_6 symmetry site possesses a centre of inversion, only the $^5D_0 \rightarrow {}^7F_1$ transition is allowed.[279]

This strongly suggests that Eu^{3+} is preferentially doping in the C_2 site, as the emission spectra are dominated by the luminescence band at 610 nm and 631 nm ($^5D_0 \rightarrow {}^7F_2$) (**Figure 116**).

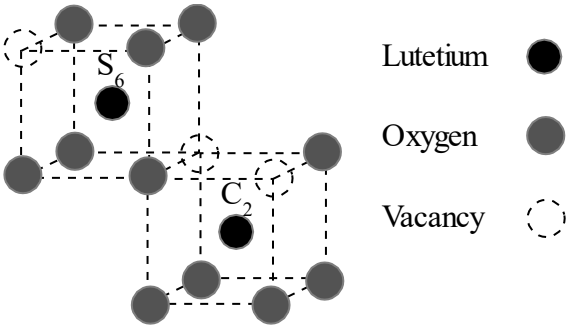

Figure 115 Arrangement of oxygen and vacancies around the C_2 and S_6 symmetry sites of Lu^{3+} within a cubic structure.[280]

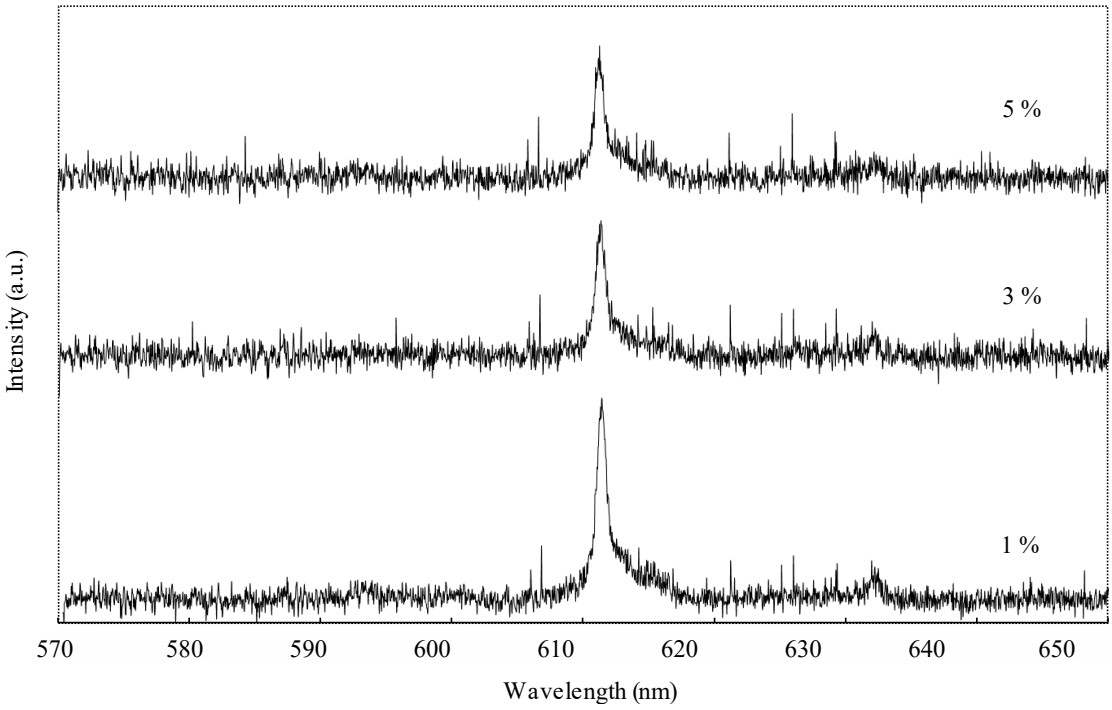

Figure 116 XRIL spectra of europium doped Lu_2O_3 nanoparticles with a molar percentage of 1, 3 and 5% irradiated using the Radsource RS-2000 biological irradiator at 160 keV and 25 mA.

3.4 Conclusions

An approach considering which inorganic materials might be suitable as scintillating nanoparticles at clinically relevant energies of irradiation was undertaken and a range of nanoparticles were synthesised. Nanoparticles were doped with an optimised amount of Eu^{3+} in order to give luminescence in the visible region corresponding with the last absorption Q-band of unmetallated porphyrin photosensitisers. It was found that changes to synthetic parameters improved the luminescence intensity across materials which included annealing temperature, microwave synthesis and doping percentage. $CaWO_4$ was studied in the most detail and this led to the discovery of a scheelite phase $EuWO_4$ nanoparticle which is also a potential scintillator.

Nanoparticles were tested for their potential as scintillators under a range of energies from 100 - 160 keV using an X-ray tube source as well as an Ir-192 source with an average energy of 330 keV.

It was found that materials with a lower density such as CaF_2 would scintillate with a higher intensity as energy increased from 100 keV to 160 keV, likely due to the increased number of photons generated. However, upon using Ir-192, the luminescence intensity decreased for this material as it lacked the necessary stopping power to interact with many of the high energy photons. Other materials such as $CaWO_4$ and LaF_3 however, exhibited a large increase in luminescence intensity when irradiated with Ir-192. Access to this source of irradiation was not consistent, however, and a full comparison could not be made for most compounds, but does highlight the possibilities of tailoring a specific nanoparticle to a certain kind of brachytherapy or even external beam radiation and would make an interesting area of research in the future.

4. Synthesis of porphyrin-nanoparticle conjugates for the generation of singlet oxygen under ionising irradiation

4.1. Conjugation strategies

4.1.1. Scintillating nanoparticle-photosensitiser (ScNP-PS) conjugation strategies

FRET is a radiationless transfer of energy from a donor fluorophore to an acceptor fluorophore and is highly distance dependant. In order to achieve a high energy transfer of Forster Resonance Energy Transfer (FRET) leading to the best possible efficiency of system, conjugation strategies are of paramount consideration. In the published research to date, co-location, porous silica loading, physical loading and covalent conjugation (**Figure 117**) have all been employed as conjugation strategies for scintillating nanoparticle-photosensitiser systems (ScNP-PS) for use in SLPDT. Each strategy has its merits, some are only suitable for proof of principle and others with suitability for *in vivo* application.

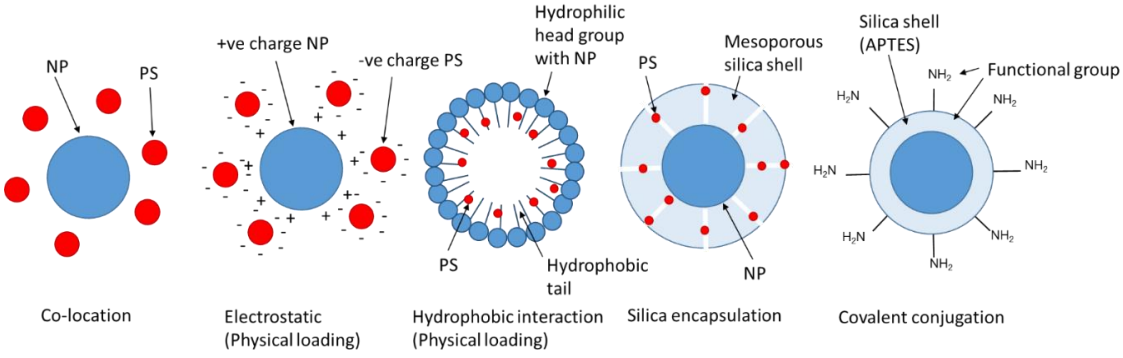

Figure 117 Photosensitiser loading and conjugation strategies.

4.1.2. Co-location strategy

A co-location strategy achieves the activation of PSs by unconjugated ScNPs in proximity alone, for singlet oxygen testing or cell cultures for *in vitro* analysis.[115] Although a

powerful tool for determining the potential of a system's interaction for a preliminary investigation, this strategy clearly suffers from some critical issues.

i) Energy transfer between NPs and PS may be inefficient or undeterminable due to the randomness and uncontrolled distances.

ii) Due to the different bioavailability between PS and NP it would be difficult to co-locate within the same part of a cell for *in vitro* study let alone a complex biological system for *in vivo* application.

4.1.3. Physical loading strategies

Physical loading can be a facile effective method of conjugation employing either electrostatic adherence[129] or hydrophobic interaction[122] to form the ScNP-PS conjugate. Electrostatic adherence can be achieved using charged nanoparticles with ionic PSs. Such systems have shown excellent results *in vitro*[281–283] however, the stability of these systems *in vivo* face huge challenges due to the complexity of the physiological environment.[109]

Generally speaking, the majority of PSs used are hydrophobic in composition, making them unstable in biological systems, requiring complicated synthesis or drug delivery for compatibility. For this reason, hydrophobic interaction serves as a good way for loading PSs for biocompatibility. Nanoparticles are coated in oil solvents with hydrophobic alkane chains, and then wrapped in an aqueous phase of hydrophilic polymers like PEG, chitosan or cyclodextrin. The photosensitiser is then loaded into the hydrophobic layer at the surface of the nanoparticles, and in close proximity, while an outer layer of hydrophilicity gives water solubility and bioavailability. Another take on this strategy was shown by Kaščáková *et al.*[122] by forming micelles from surfactant molecules in which the hydrophilic head is comprised of the positively charged nanoparticle and

anionic molecule, with an alkyl chain forming the hydrophobic interior of a micelle. PSs were then loaded into this hydrophobic core forming the ScNP-PS conjugate.

A problem with these strategies arises due to the potential of photosensitisers to suffer from aggregation within the hydrophobic layer, leading to self-quenching and reduced or no PDT activity.[284] Physical loading strategies have also been widely employed for delivery and controlled release of chemotherapeutic drugs,[109] consequently PSs loaded by this strategy will leak over time during circulation *in vivo* reducing the efficacy of ScNP-PS conjugate over time.

4.1.4. Porous silica strategy

Mesoporous silica nanoparticles (MSNs) have been extensively studied as nanocarriers for drug delivery systems[285] with potential for PS loading as ScNP-PS conjugates[130] due to their intrinsic porous structure and excellent biocompatibility. Due to the negatively charged silica matrix, a cationic, positively charged PS is likely to load most efficiently. Due to the porous nature, MSN coatings showed excellent energy transfer efficiency by Zhang *et al.* when using upconverting nanoparticles (UCNPs) for PDT.[286]

Although there have been developments showing excellent potential for this strategy, several challenges need to be addressed before this delivery system can be considered an ideal loading strategy for PSs into ScNP-PS conjugate systems. There are limited reports on hollow or large surface areas and high pore volumes enabling high drug loading, and those that exist are difficult to achieve on large scale synthesis. Secondly, although intracellular delivery of drugs into animal cells have been achieved, biodistribution, acute toxicities, long term stability and circulation properties are still problematic *in vivo*.[285]

For ScNP-PS particularly, there is still a large chance of PS leakage *in vivo*, that would lead to undesirable phototoxicity.

4.1.5. Covalent conjugation strategies

The physiological microenvironment *in vivo* is orders of magnitude more complicated than *in vitro*, and consequently co-locating or physical loading strategies previously discussed all suffer from inadequate stability for *in vivo* application. For this reason, covalent conjugation has been proposed as a more stable ScNP-PS conjugation strategy with higher selectivity and controllability than other types of loading. Another important aspect of this strategy is the ability to set the distance between NP and PS and consequently design a more energy efficient FRET system. A recent study using UCNPs compared the efficiency of a FRET-based PDT system with NP and PS covalently conjugated with that of the same system using electrostatic interactions. FRET was observed in both cases, however the final PS concentration in the electrostatic adhesion group was an order of magnitude lower than in the covalent conjugation group after washing. For covalent conjugation a chemical linkage requires the PS to be attached to the NP, both requiring complementary functional groups such as carboxylic acids (-COOH) and amines ($-NH_2$) for a peptide coupling reaction for example. This can add complication to the synthesis and preparation of ScNP-PSs compared with some of the other strategies discussed but has the most promise of any system for *in vivo* application.

4.2. Aims

The aims of this chapter were the conjugation of porphyrins to the surface of previously prepared scintillating nanoparticles, to demonstrate the activation of attached

photosensitiser's ability to produce singlet oxygen under irradiation with ionizing radiation.

Conjugation strategies employed included a peptide coupling reaction, click methodology and coordination of a catechol bearing porphyrin (**Table 13**). All of these conjugates were prepared, however due to time constraints, only the peptide coupled and the catechol coordinated conjugations were investigated.

Table 13 Conjugation Strategies for adjoining porphyrin to nanoparticles.

Conjugation Strategy	Nanoparticle functionalization	Conjugation methodology	Photosensitiser
CS1	Silanisation	Peptide coupling	**[47]**
CS2	None	Coordination	**[49]**

4.3. Photosensitiser syntheses

4.3.1. Synthesis of a cationic water-soluble 'N-succinimide' porphyrin [47]

The click reaction has emerged as an efficient alternative to solid phase peptide synthesis with the capacity to promote bioconjugation due to the properties of the triazole linker as a peptide mimetic.[287] It has particular suitability to nanoparticle conjugation as quantitative yields have been reported even when one half of the reacting substituents are not in solution.[288] The suitability of this ligation for forming ScNP-PS conjugates is therefore very apparent; giving selectivity and high yields without side products. However, due to the requirement of a Cu(I) catalyst, the central cavity of porphyrin photosensitisers must be protected from copper chelation. Due to the paramagnetic nature of copper, the photodynamic action of the PS is essentially quenched, and therefore a

diamagnetic metal such as zinc must be inserted before CuAAC ligation can be undertaken. Due to the increase in symmetry and loss of the longer wavelength absorption band (Q-band), this PS loses some of the spectral overlap that initially provides suitability for the Eu^{3+} doped NP targeting this spectral region. Therefore, another water-soluble porphyrin-based photosensitiser was synthesised that can be conjugated via peptide synthesis using the free base porphyrin.

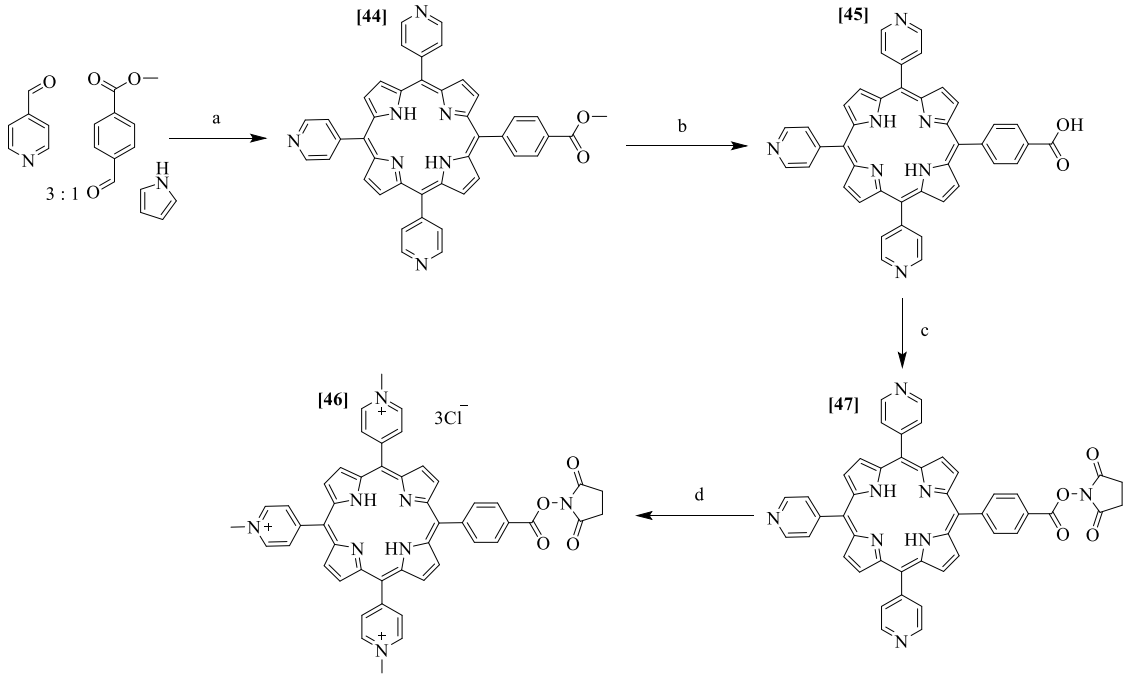

Scheme 9 (a) Pyrrole, 4-pyridinecarboxaldehyde, 4-acetamidobenzaldehyde in propionic acid, 180 °C, 1 h 180 °C 1 h, (b) saponification in DMF with KOH, (c) thionyl chloride and NHS, (d) CH_3I in DMF 40 °C 18 h, counter ion exchange NH_4PF_6 and TBAC.

Synthesis of **[44]** was carried out using a mixed aldehyde condensation reaction in a 3:1 ratio of the aldehydes 4-pyridinecarboxaldehyde and methyl 4-formylbenzoate to form an asymmetrical AB_3 type porphyrin with a 6.9% yield in accordance with the literature.[289] The ester was then saponified using potassium hydroxide in a yield of 84%, with NMR confirming complete saponification after an overnight reaction to give **[45]**.

Synthesis of **[46]** was carried out in a one pot 2-step synthesis, first [**45]** was reacted with thionyl chloride, yielding the acid chloride. The addition of *N*-hydroxysuccinimide the mixture gave the product **[46]** in a 93% yield, comparable to the literature.[220]

Porphyrin **[47]** was obtained by methylation reaction of **[46]**, that was previously described in Chapter 2, to give the cationic pyridiniumyl salt following a literature procedure using methyl iodide in DMF.[76] The yield afforded was 83%, which is slightly lower than for other porphyrins, due in part to a slight solubility toward methanol even after counter ions have been replaced with ammonium hexafluorophosphate, during the work-up procedure. The ^{1}H-NMR clearly showed the presence of CH_3 groups that integrated to 9, indicating that the methylation reaction had gone to completion. The method employed an ammonium hexafluorophosphate/tetrabutylammonium chloride workup as described in the literature.[141] This methodology allows removal of both water-soluble and organic impurities, while also exchanging the iodide counter-anions to chloride ions, improving the water solubility of the porphyrin.

4.3.2. Synthesis of a tetracatechol porphyrin [49]

It has previously been shown that dihydroxybenzenes (catechols) such as dopamine, form a strong bidentate complex with metal oxide nanoparticles,[207,290] with Langmuir isotherms indicating that the desorption from metal oxides is far less favourable than adsorption.[291] Dopamine has also been shown to act as a conductive bridge between metal oxide nanoparticles and biomolecules, allowing the transport of photogenerated holes to the biomolecules which could have important implications for FRET of ScNP-PS conjugates. A particularly facile functionalisation of metal oxides with catechols can be achieved by sonicating for 20 minutes in suspension.

Tetrakis(2,3-dihydroxyphenyl) porphyrin **[49]** was synthesised from tetrakis(dimethoxyphenyl) porphyrin **[48]** which in turn was synthesised as a symmetrical porphyrin using dimethoxybenzaldehyde (**Scheme 10**). Tetrakis(2,3-dimethoxyphenyl) porphyrin **[49]** was prepared by the condensation reaction of dimethoxybenzaldehyde and pyrrole in refluxing propionic acid in accordance with the literature.[292,293] **[48]** was purified by column chromatography (4% MeOH : DCM) with confirmed purity by NMR spectroscopy and MS, in a yield of 22%. The higher yield obtained may be owed in part to the incorporation of a sodium bicarbonate washing step, to remove residual propionic acid and neutralise acidic porphyrins.

In accordance with the literature,[292] demethylation was performed using boron tribromide in dry dichloromethane was added to **[49]** and maintained at 0 ℃ for one hour before being allowed to warm to room temperature. After neutralisation with $NaHCO_3$, the product was passed down a fast silica column using THF to remove some impurities. The product yield was 73%, which is in keeping with the literature, was confirmed by NMR and MS which clearly showed the loss of methyl groups.

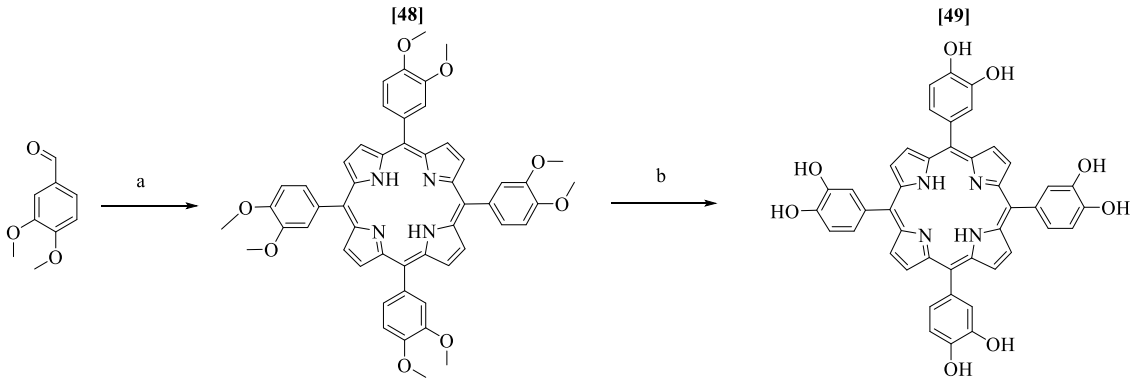

Scheme 10 (a) Condensation 180 ℃ 1 h, (b) Demethylation using BBr_3, (1 M in dry DCM) at 0 ℃ → r.t.

4.4. Silanisation of nanoparticles for amine functionalisation

A modified Stober process was used for the coating of all naked nanoparticles which were treated in the same way to provide a homogenous outer layer of silica with attached amine groups for functionalisation. The procedure first involved the deposition of a silica shell of tetraethoxysilane (TEOS) before the subsequent addition of aminopropyl triethoxysilane (APTES), which contained the functional and terminal amines.

Of the synthesised nanoparticles from chapter 3, the following samples were coated with the silanising agents TEOS and APTES, to give surface amines for further functionalisation.

Table 14 Nanoparticles chosen for silanisation with TEOS and APTES.

Nanoparticle	Sample	APTES functionalised	Sample
$CaWO_4$	**[15]**	$CaWO_4$@$SiONH_2$	**[50]**
$EuWO_4$	**[23]**	$EuWO_4$@$SiONH_2$	**[51]**
LaF_3	**[32]**	LaF_3@$SiONH_2$	**[52]**
LuF_3	**[33]**	LuF_3@$SiONH_2$	**[53]**
Lu_2O_3	**[35]**	Lu_2O_3@$SiONH_2$	**[54]**

The use of silanising agents in coating and functionalising metal oxide nanoparticles is fairly common.[294] Silanising agents were sequentially added to the naked nanoparticles in a suspension of aqueous ethanol and ammonia solution, acting as a catalyst. Silanising agents undergo hydrolysis, losing ethanol in the process and react with hydroxyls on the surface of nanoparticles to undergo a condensation reaction (**Figure 118**) to form a polymer shell around the surface.

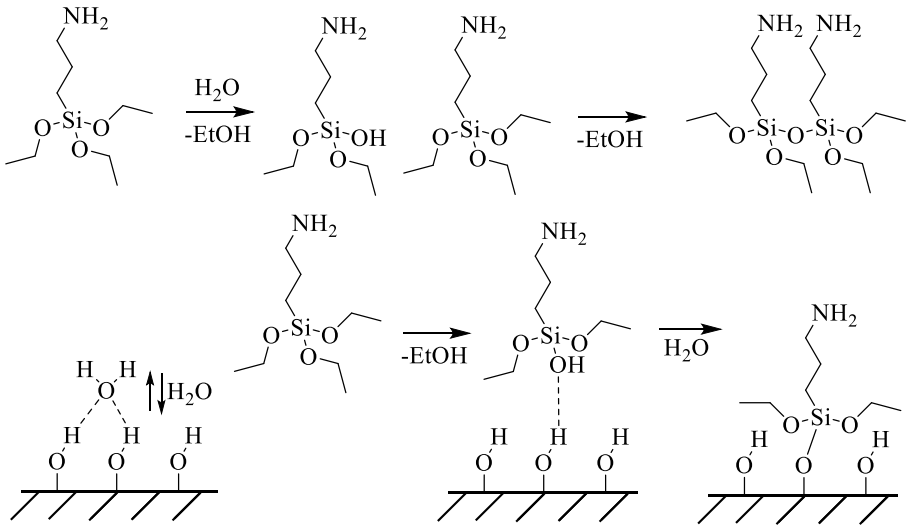

Figure 118 Top shows APTES hydrolysis followed condensation reaction in solution. Bottom shows APTES hydrolysis followed by condensation reaction at nanoparticle surface.

Nanoparticles were well dispersed by sonicating before the addition of silanising agents TEOS and then APTES with ammonia. A thin layer was deposited on the surface of the nanoparticles **[50]** and can be measured using TEM (**Figure 119**). Shell thickness was measured to be approximately 5 nm, EDX was used in the centre and at the surface of nanoparticles to confirm the presence of silica atoms at the surface, shown in **Figure 120**.

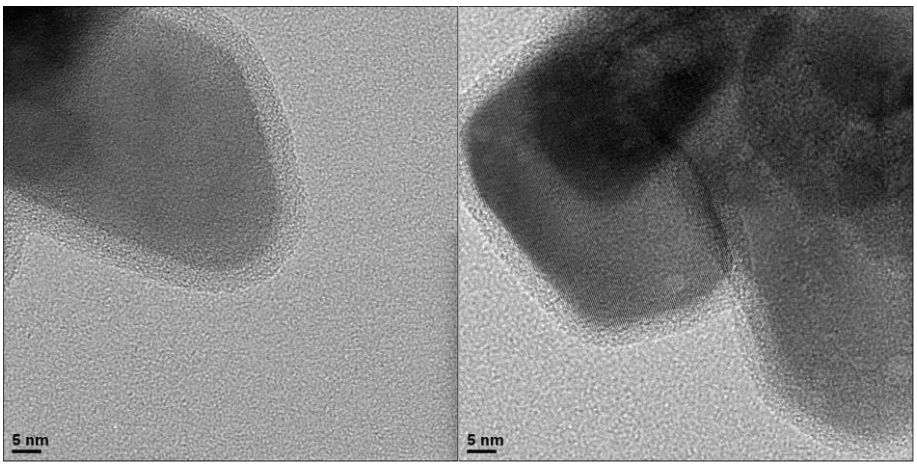

Figure 119 TEM of the silica coating of nanoparticles due to the difference in materials density between core nanoparticles and silica shells **[50]**.

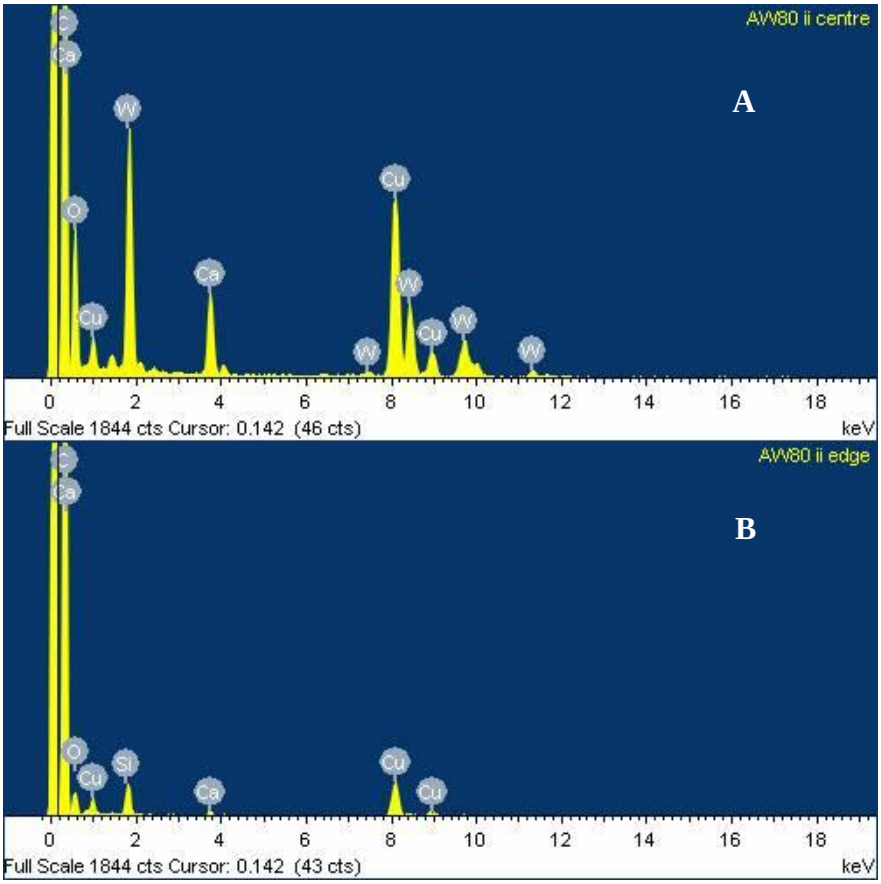

Figure 120 EDX showing the atomic content (A) centred on nanoparticle **[50]**, (B) centred on the surrounding silica shell.

Demonstration of the presence of surface amine groups was also shown by reacting nanoparticles **[50]** with a solution of fluorescamine (4′-phenyl- spiro[2-benzofuran-3,2′-furan]-1,3′-dione) in acetone (1 mg in 5 mL). Nanoparticles were then removed by centrifugation and the solutions were examined under UV lamps (**Figure 121**) to give fluorescence which will only occur when fluorescamine reacts with primary amines. To further demonstrate this, the solutions were excited at 350 nm, giving the emission spectrum shown in **Figure 122**, exhibiting the characteristic spectrum of fluorescamine..

Figure 121. Image taken showing the fluorescence of fluorescamine in the presence of primary amines on the surface of nanoparticles **[50]**.

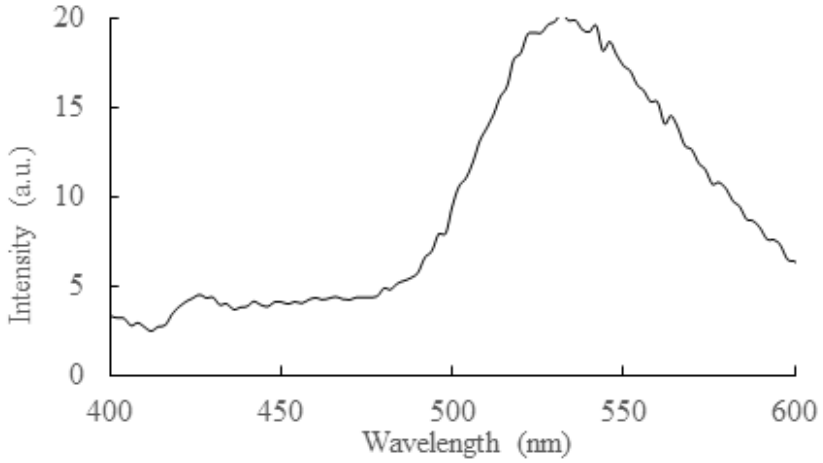

Figure 122 Fluorescence spectrum of fluorescamine (λ_{ex} 254 nm), activated by primary amines on the surface of nanoparticles **[50]** functionalised using APTES.

To further demonstrate the functionalisation of silica coatings to the surface of each group of nanoparticles ATR-IR measurements were taken for naked particles, and silica coated nanoparticles (**Table 14**).

Figure 123 shows the results of ATR, clearly showing the Si-O at 1054 cm^{-1} in samples **[50]**,**[51]** and **[54]**. Due to the position of the La-F and Lu-F stretching the samples **[55]** and **[53]** did not exhibit noticeable differences within the IR, however they had significant mass increases following silanisation.

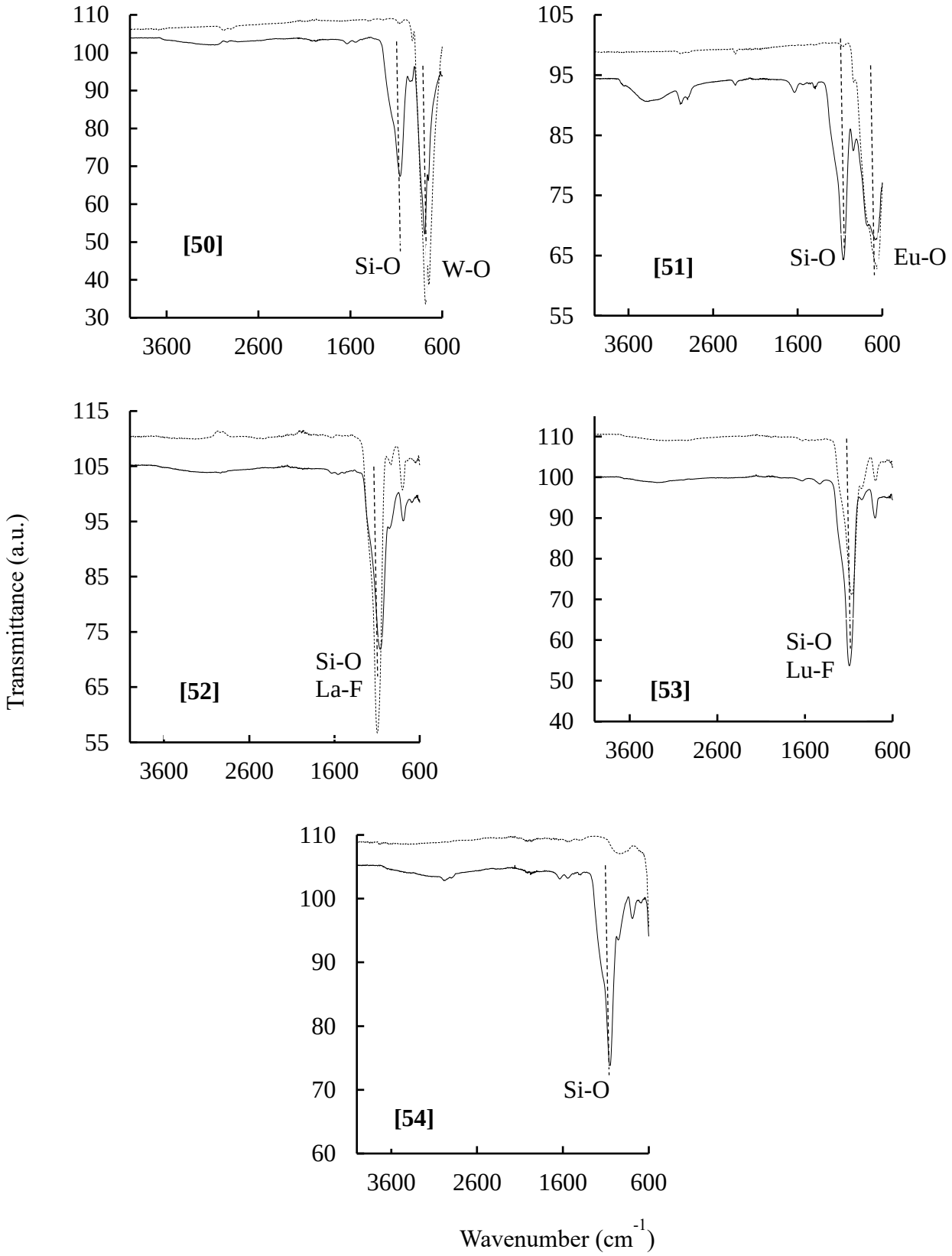

Figure 123 ATR-IR showing naked and silane functionalised samples, **[50]** $CaWO_4$, **[51]** $EuWO_4$, **[52]** LaF_3, **[53]** LuF_3, **[54]** Lu_2O_3.

4.5. Conjugation of photosensitisers to nanoparticles

4.5.1. Peptide coupling conjugation

After the successful amine functionalisation of scintillating nanoparticles **[50-54]**, a water-soluble porphyrin was attached to each to give the corresponding conjugates, shown in **Figure 124**.

A carbodiimide-mediated coupling reacting between the amine terminated nanoparticles **[50-53]** and the *N*-hydroxysuccinimide (NHS) activated porphyrin **[47]** gave the conjugates **[54-68]** (**Table 15**).

Following filtration and washing with water and methanol the coupling efficiency was determined by spectroscopic analysis of the filtrate to determine porphyrin concentration after reaction. The coupling efficiency was therefore determined by subtraction of porphyrin concentration within the filtrate. IR spectroscopy was used to show the presence of porphyrins following the peptide coupling reactions.

Table 15 List of nanoparticle-photosensitiser conjugates synthesised.

APTES functionalised	Sample	ScNP-PS	Sample
$CaWO_4$@$SiONH_2$	**[50]**	$CaWO_4$@$SiONH_2$@PS	**[55]**
$EuWO_4$@$SiONH_2$	**[51]**	$EuWO_4$@$SiONH_2$@PS	**[56]**
LaF_3@$SiONH_2$	**[52]**	LaF_3@$SiONH_2$@PS	**[57]**
LuF_3@$SiONH_2$	**[53]**	LuF_3@$SiONH_2$@PS	**[58]**
Lu_2O_3@$SiONH_2$	**[54]**	Lu_2O_3@$SiONH_2$@PS	**[59]**

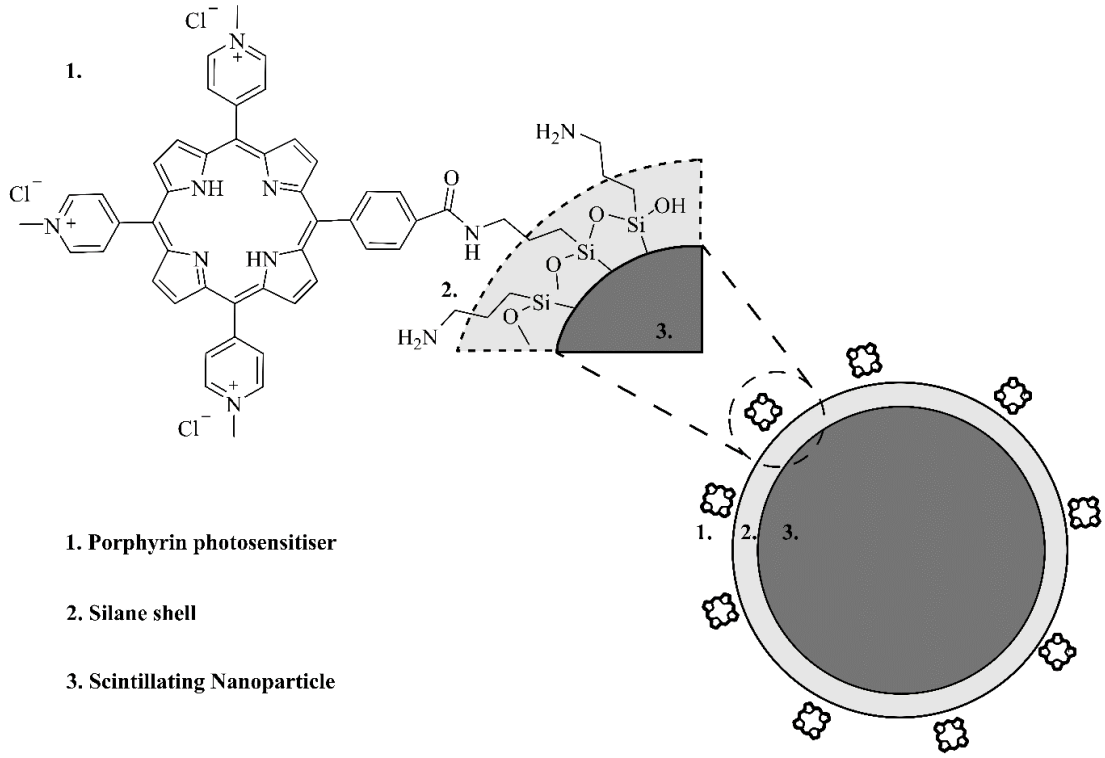

Figure 124 Peptide conjugation *via* a water solubilised succinimide porphyrin and amine bearing silanisation of nanoparticles.

Following conjugation to porphyrin **[47]** the conjugates **[55-59]** were again analysed by ATR-IR shown in **Figure 125**. The introduction of new peaks in the region between 1500 - 1750 cm^{-1} was clearly observed as has previously been shown for porphyrins for ATR analysis, corresponding to the introduction of carbonyls.[295]

After conjugation the filtered solution was centrifuged to remove any unfiltered nanoparticles and analysed by UV-Vis to confirm complete reaction with the nanoparticles due to a lack of signal present from the photosensitiser.

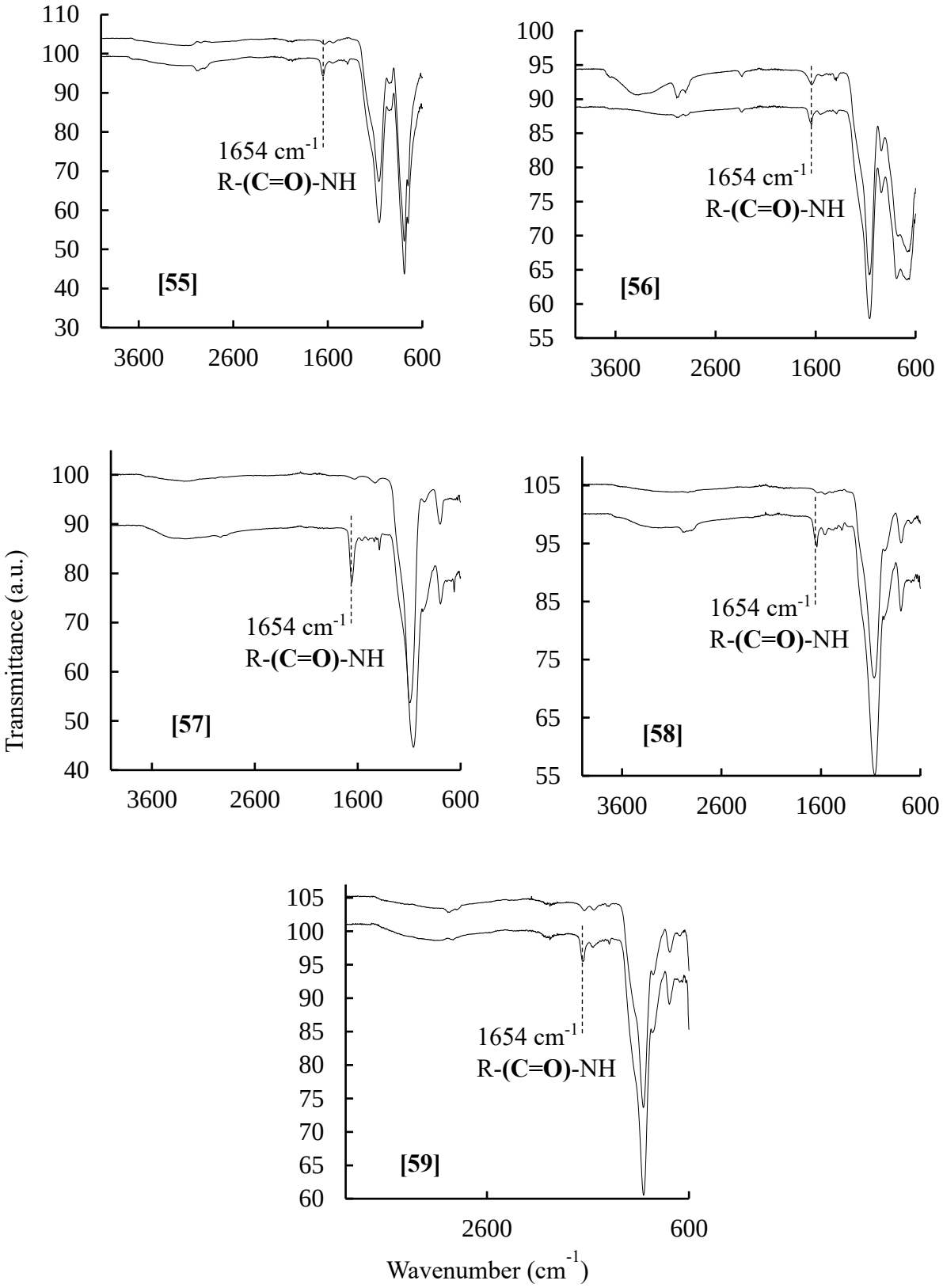

Figure 125 ATR-IR showing silane functionalised samples, **[50]**, **[51]**, **[52]**, **[53]**, **[54]** with the photosensitiser conjugates **[55]** $CaWO_4$, **[56]** $EuWO_4$, **[57]** LaF_3, **[58]** LuF_3, **[59]** Lu_2O_3.

4.5.2. Coordination conjugation [60]

Tetracatechol porphyrin **[49]** was coordinated to the naked europium doped LaF_3 nanoparticles **[32]** in water under sonication with the addition of a small amount of diethyl amine. With 1:1 ratio by mass of photosensitiser to nanoparticle, all of the photosensitiser had attached to the particles. After centrifugation and collection of particles, none of the remaining eluent exhibited any porphyrin by spectrophotometric analysis. Nanoparticles were easily re-dispersed resulting in an extremely water stable solution.

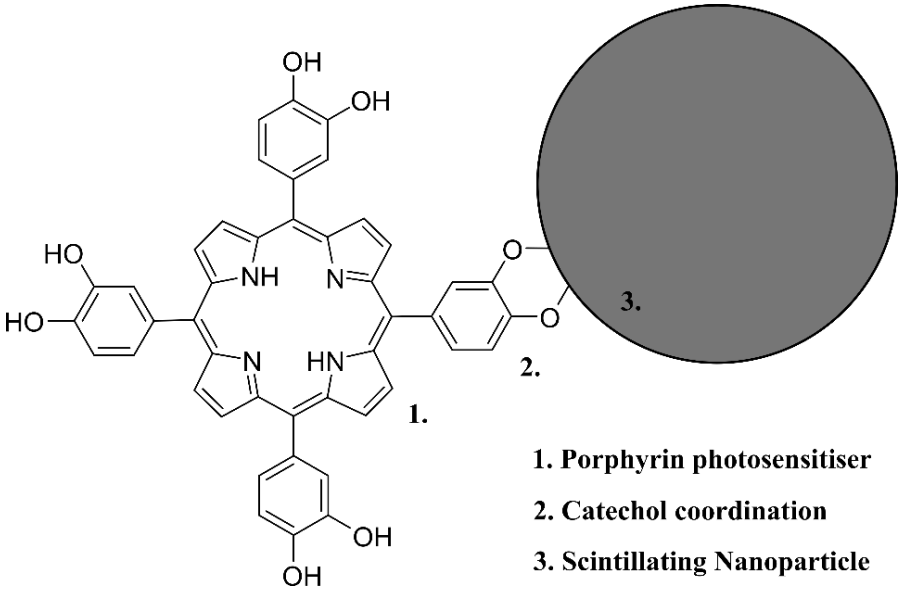

Figure 126 Coordination conjugation *via* a tetra-catechol bearing porphyrin and unfunctionalized nanoparticles.

4.6. Singlet oxygen measurements

Singlet oxygen generation was measured using a singlet oxygen trapping agent 9,10-anthracenediyl-bis(methylene) dimalonic acid (ABDA). In the presence of singlet oxygen ABDA is photobleached through a conversion to the corresponding endoperoxide (**Figure 127**). The subsequent reduction of absorbance bands for ABDA were monitored between 320 and 420 nm spectrophotometrically. A large stock solution of ABDA was prepared for all conjugates tested as well as controls of (ABDA only) and nanoparticles without conjugation to the photosensitiser.

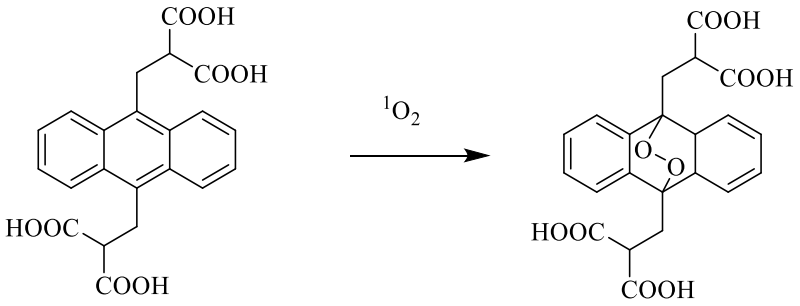

Figure 127 Chemical reaction of ABDA with singlet oxygen.

4.6.1. Singlet oxygen measurements of europium-doped $CaWO_4$ nanoparticles conjugated to a water-soluble porphyrin *via* peptide coupling [55]

Figure 128 shows the UV-Vis absorption spectra of ABDA for the irradiation of samples at an energy of 160 keV for 10 mins, 20 mins, 30 mins and 40 mins. Black and white lines represent irradiation of ABDA only and clearly show that there was a quenching effect from ionising radiation on ABDA alone. This has recently been observed with a number of other singlet oxygen traps.[296] For this reason it was important to show the un-conjugated, naked nanoparticles in the ABDA solution (red lines) which show none or negligible difference to the ABDA only, established baseline. Finally, the nanoparticle-photosensitiser conjugate in the ABDA solution is represented by the blue lines and shows

a clear decrease in absorption compared with the ABDA only, and nanoparticles in ABDA solution, indicating the generation of singlet oxygen.

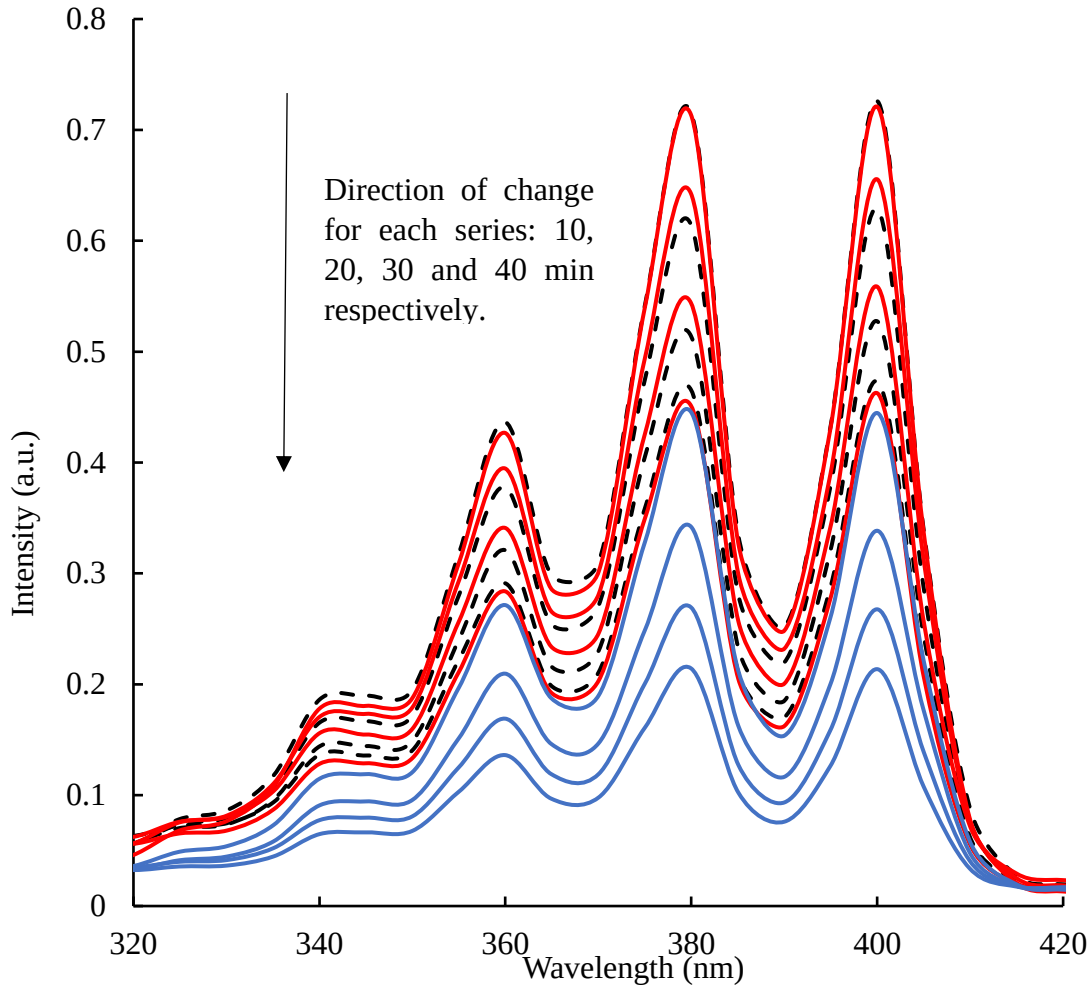

Figure 128 UV-Vis absorption spectra of ABDA upon irradiation with 160 keV ionising radiation at 10, 20, 30 and 40 mins for: (black and white lines) ABDA only, (red lines) nanoparticles only, (blue lines) conjugate **[55]**.

4.6.2. Singlet oxygen measurements of $EuWO_4$ nanoparticles conjugated to a water-soluble porphyrin *via* peptide coupling [56]

Figure 129 shows a slight difference between naked nanoparticles and the baseline, ABDA only data. This may indicate a slight photosensitising effect of this material, though a far more apparent effect was observed for the $EuWO_4$ conjugate.

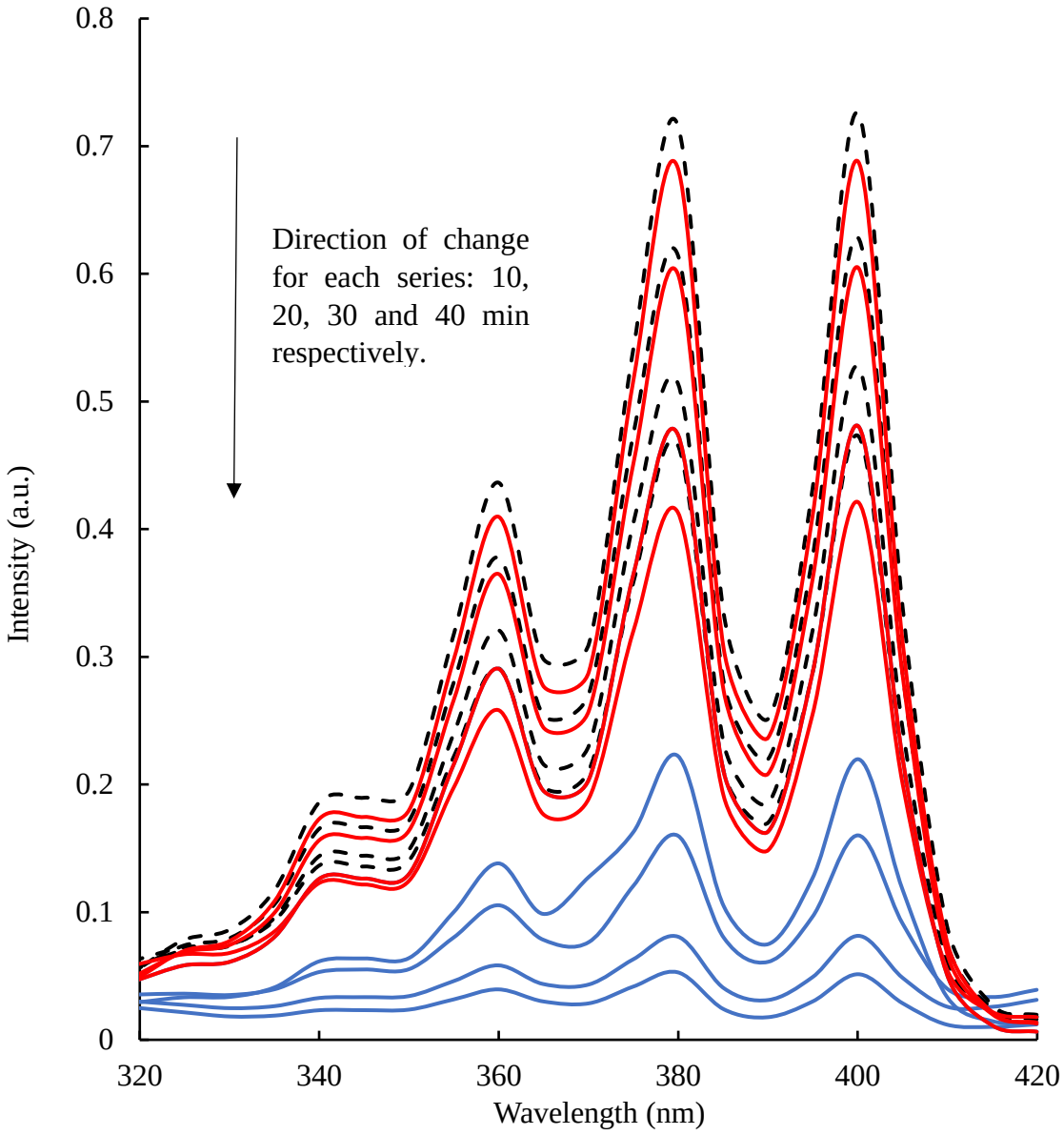

Figure 129 UV-Vis absorption spectra of ABDA upon irradiation with 160 keV ionising radiation at 10, 20, 30 and 40 mins for: (black and white lines) ABDA only, (red lines) nanoparticles only, (blue lines) conjugate **[56]**.

4.6.3. Singlet oxygen measurements of europium doped LaF_3 nanoparticles conjugated to a water-soluble porphyrin *via* peptide coupling [57]

Figure 130 exhibits one of the most effective conjugates tested, showing a complete collapse of ABDA absorption at 20 minutes. The nanoparticles alone showed no difference to the ABDA only controls.

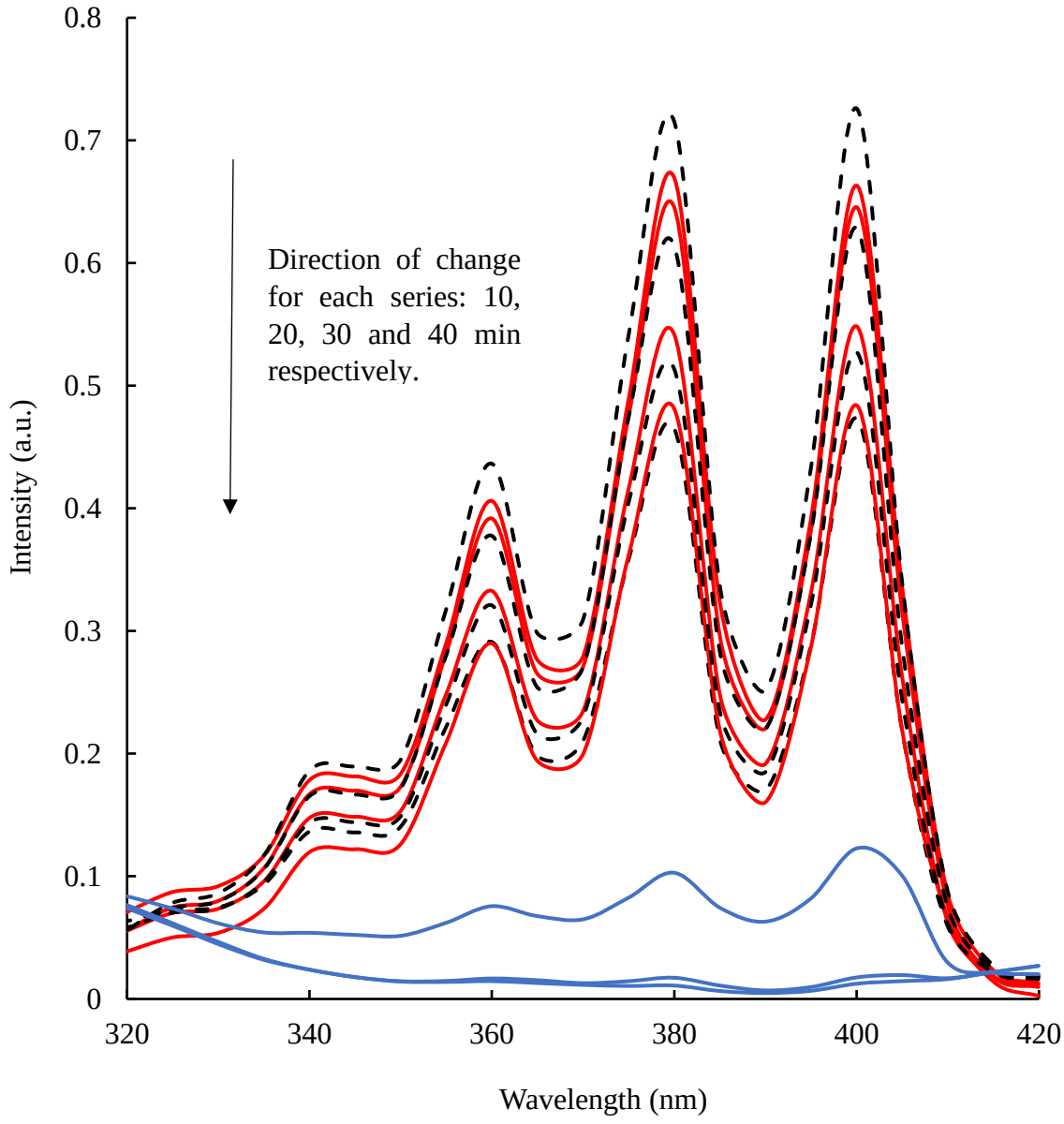

Figure 130 UV-Vis absorption spectra of ABDA upon irradiation with 160 keV ionising radiation at 10, 20, 30 and 40 min for: (black and white lines) ABDA only, (red lines) nanoparticles only, (blue lines) conjugate **[57]**.

4.6.4. Singlet oxygen measurements of europium doped LuF_3 nanoparticles conjugated to a water-soluble porphyrin *via* peptide coupling [58]

Figure 131 exhibits the other of the two most effective conjugates; both being rare earth fluorides. LuF_3 nanoparticles, like the $EuWO_4$ nanoparticles show a slight, potential generation of singlet oxygen before conjugation to the photosensitiser. However again the conjugate displays a far more pronounced difference.

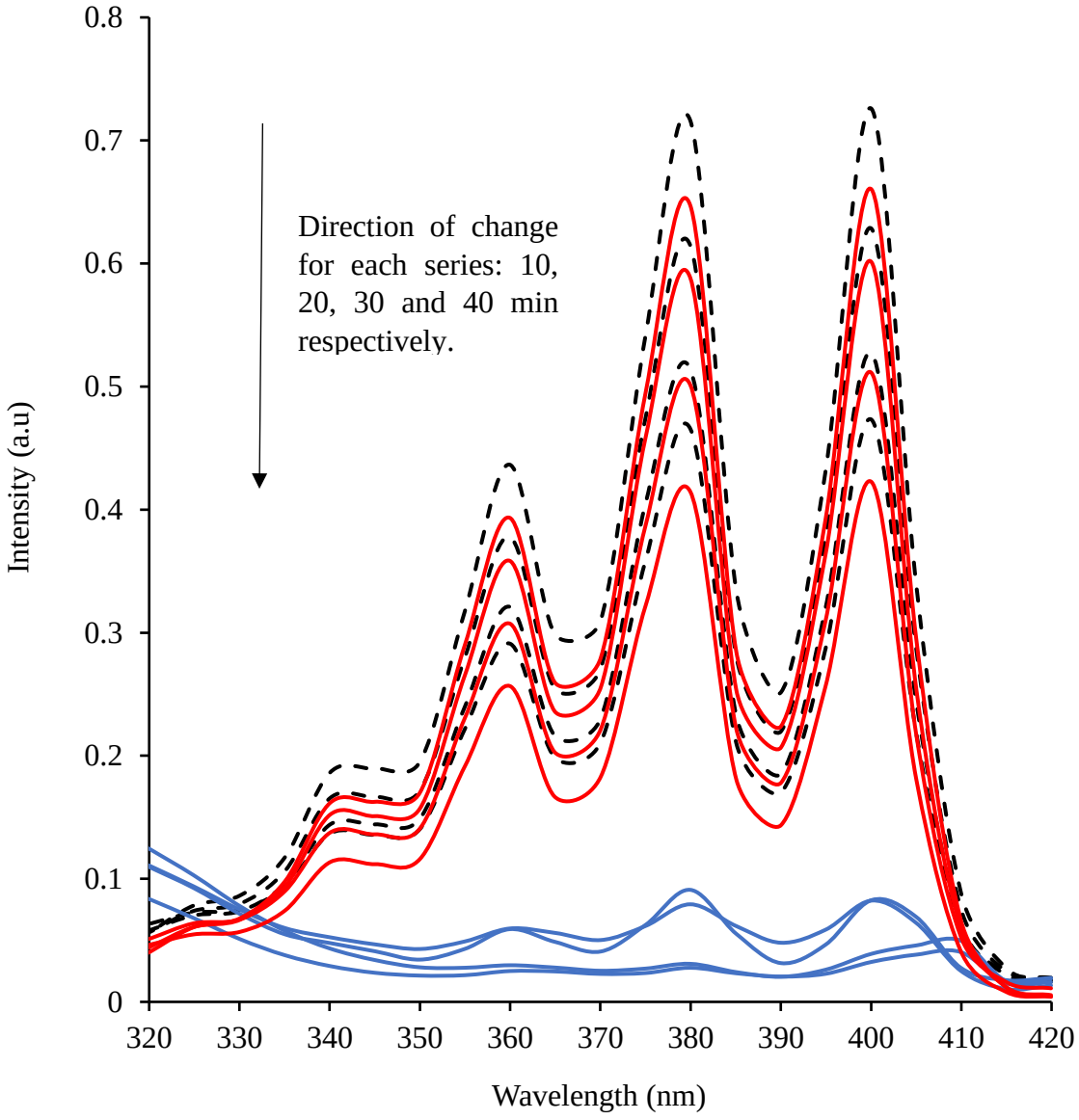

Figure 131 UV-Vis absorption spectra of ABDA upon irradiation with 160 keV ionising radiation at 10, 20, 30 and 40 min for: (black and white lines) ABDA only, (red lines) nanoparticles only, (blue lines) conjugate **[58]**.

4.6.5. Singlet oxygen measurements of europium-doped Lu_2O_3 nanoparticles conjugated to a water-soluble porphyrin *via* peptide coupling [59]

Of all the nanoparticles, Lu_2O_3 exhibited the most convincing data of a possible singlet oxygen generation of nanoparticles only, suggesting a possible photosensitising action attributed to this material. Conjugate results, however, were clearly improved compared to the nanoparticles alone.

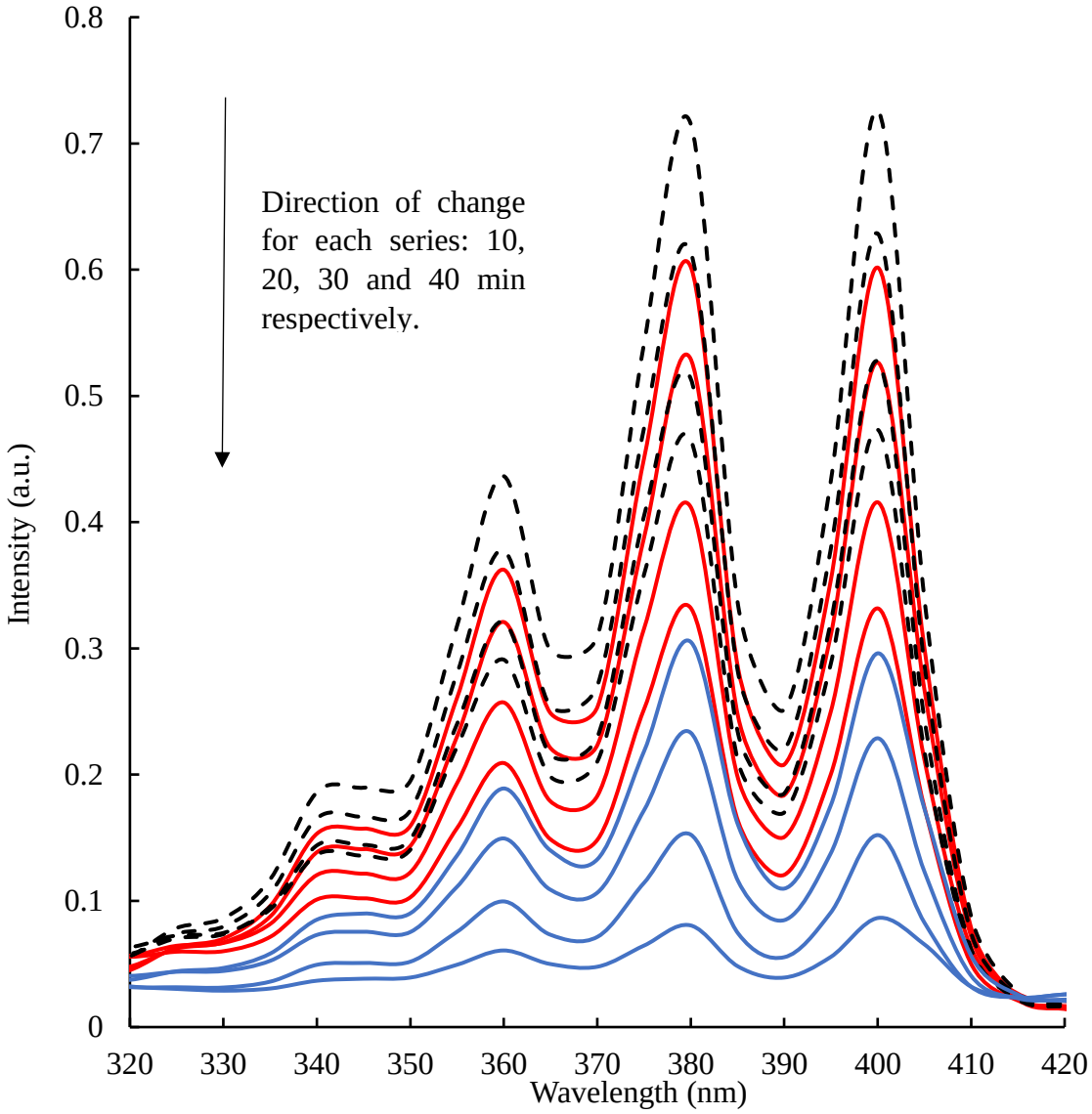

Figure 132 UV-Vis absorption spectra of ABDA upon irradiation with 160 keV ionising radiation at 10, 20, 30 and 40 min for: (black and white lines) ABDA only, (red lines) nanoparticles only, (blue lines) conjugate **[59]**.

4.6.6. Singlet oxygen measurements of europium doped LaF_3 nanoparticles coordinated to a tetra-catechol porphyrin [60]

Figure 133 shows negligible difference to the baseline in all samples and is a good example of the data of a non-working system. It was theorised that the tetracatechol porphyrin may lie flat on the nanoparticles if all four groups coordinate and may account for this negative result. It was for this reason that the cationic, water solubilised catechol porphyrin **[49]** was synthesised to overcome this problem, however time did not permit the testing of this conjugate system.

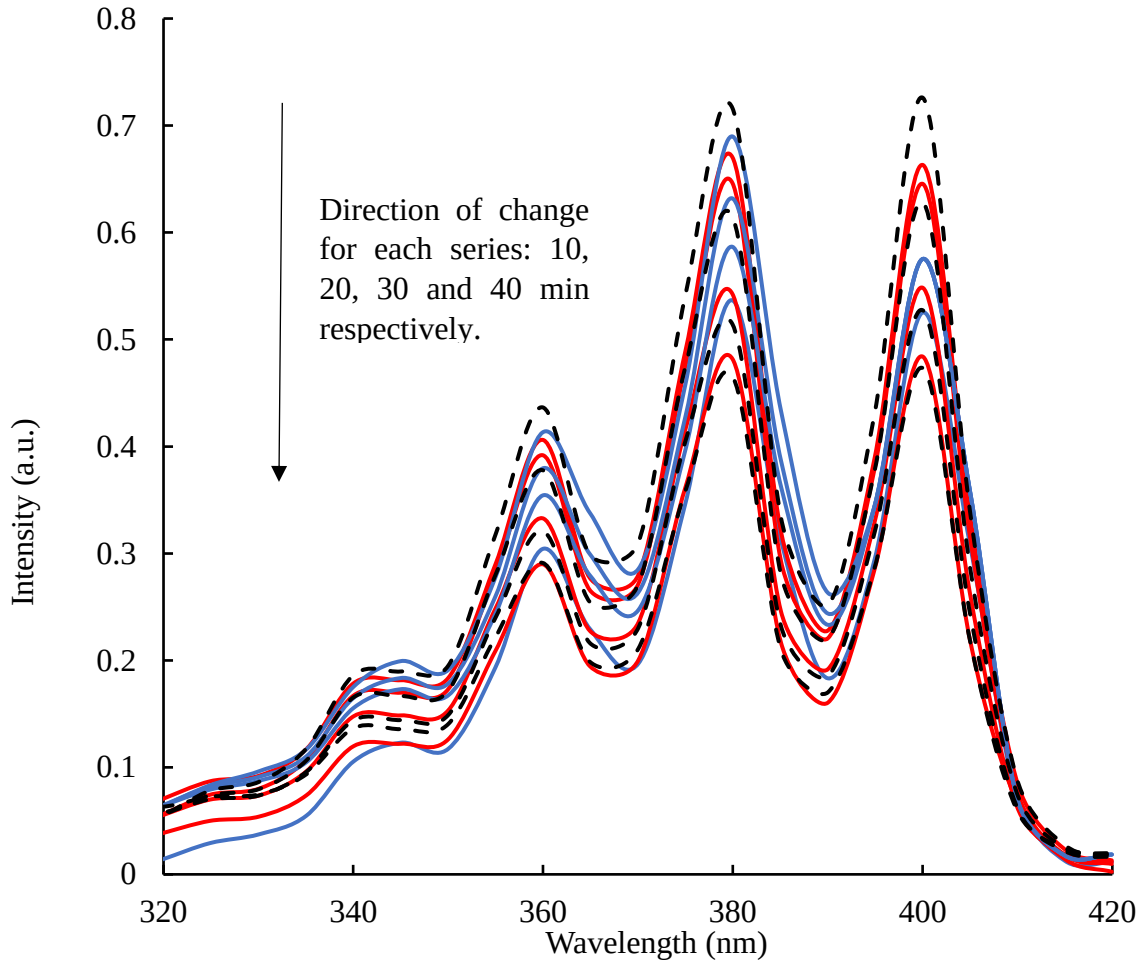

Figure 133 UV-Vis absorption spectra of ABDA upon irradiation with 160 keV ionising radiation at 10, 20, 30 and 40 min for: (black and white lines) ABDA only, (red lines) nanoparticles only, (blue lines) conjugate **[60]**.

Figure 134 shows a comparison of the absorption maximum for all conjugate systems tested.

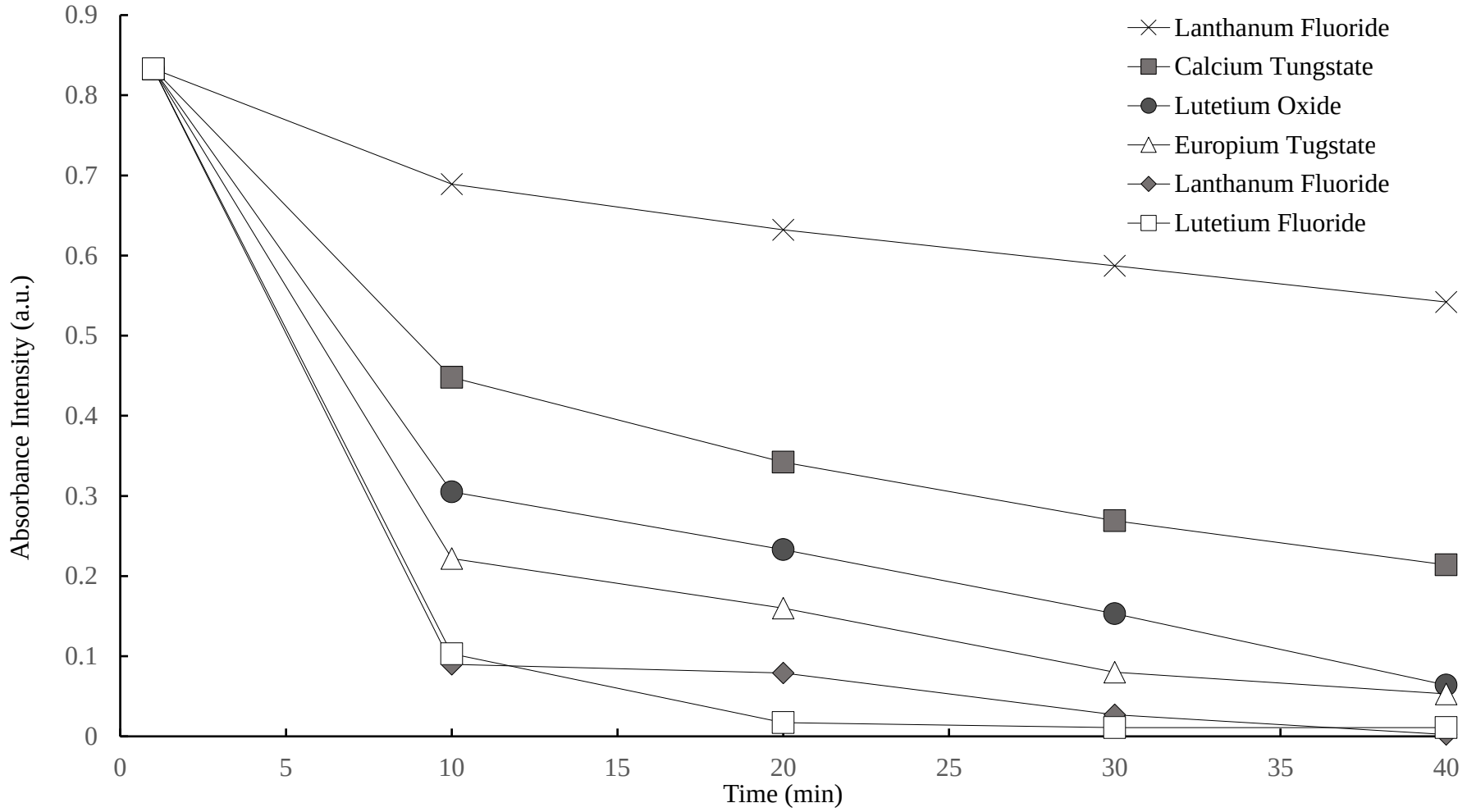

Figure 134 Comparison of absorption maximum (380 nm) for all conjugate systems tested.

4.7. Conclusions

During this work, a range of suitable scintillating nanoparticles that were previously synthesised in Chapter 3, were functionalised by silanisation to give a terminal amine moiety for conjugation with a photosensitiser. Suitable photosensitisers were synthesised to give conjugation options, including peptide coupling and coordination to a tetra catechol porphyrin.

Conjugates were irradiated using a RadSource-2000 biological irradiator at 160 keV and singlet oxygen generation was displayed using ABDA as a sensor, which irreversibly reacted with $^1O_2$ to give a measurable decrease in absorbance, which was measured spectrophotometrically. All the peptide coupled conjugates displayed $^1O_2$ generation, with the rare earth fluorides $La_{1-x}Eu_xF_3$ and $Lu_{1-x}Eu_xF_3$ showing the best results. These were also the samples with the highest loading efficiency of photosensitiser which may account for this observation.

LaF_3 coordinated to a tetracatechol porphyrin was also tested under identical experimental conditions but displayed no evidence of $^1O_2$ generation. This is likely due to coordination of all 4 catechol groups of each photosensitiser to the surface of the nanoparticle which would quench the action of the photosensitiser. Another possibility is that quenching occurred between photosensitisers due to the high loading efficiency of this compound.

5. Conclusions

Two distinct applications of radiation to porphyrin-based photosensitisers have been explored for the purposes of extending the efficacy and tissue penetration of PDT by combination with radiotherapy as well as the combination with a radionuclide for PET to afford a single theranostic agent.

A novel fluorine-18 labelled, single theranostic agent was synthesised and biologically evaluated for potential as both a photocytotoxic compound and a radionuclide for imaging using PET. A cationic water-soluble porphyrin bearing an azide moiety was synthesised and conjugated to a fluorine-18 radiolabelled PEG chain bearing an alkyne moiety *via* a copper-catalysed azide-alkyne cycloaddition (CuAAC). Biological evaluation was undertaken *in vitro*, within the HT-29 human cancer cell line. It was the first time a porphyrin labelled with fluorine-18 had been shown to have retained photocytotoxicity following radiolabelling. *In vivo* evaluation confirmed uptake into neoplastic tissue and demonstrated potential as a radiotracer for PET.

Further work in this area might include using an actively targeting moiety to increase tumour uptake over normal tissue as well as exhibiting PDT *in vivo.*

Investigation into self-lighting photodynamic therapy using ScNP-PS conjugate systems for the generation of $^1O_2$ by the irradiation with hard X-rays at clinically relevant energies was investigated whilst comparing different nanoparticle systems and conjugate strategies that may be suitable. The outcome has indicated that several different ScNP-PS conjugates show potential at an energy that is applicable to clinical medicine, which has often been missing from previous investigations. It was found that under the conditions used, the Eu-doped lanthanum and lutetium fluorides provided the best result, which may be in part to an additional emission peak at approximately 590 nm, providing a better

spectral overlap with the porphyrin used. Interestingly, coordination of a tertracatechol porphyrin directly to europium-doped LaF_3 nanoparticles exhibited no measurable generation of singlet oxygen under irradiation. This method was not tried with the other nanoparticles due to time constraints.

The investigation into the generation of singlet oxygen was largely preliminary in that direct comparisons could not be made as a standard level of loading was not achieved between conjugates; the size of nanoparticles was not the same between compounds and only 160 keV energies were used during irradiation. Different ScNP-PS may be better suited toward different types of brachytherapy or even external beam radiation.

Future investigations could include a range of energies of irradiation to find the most suitable ScNP-PS at different energies that would correspond to different types of radiotherapy such as I-125, Ir-192, Gulmay (X-ray tube) and external beam irradiation. As well no biological evaluation has been exhibited yet as part of this investigation and would make a compelling area of study going forward.

6. Experimental

6.1. Materials and Methods

NMR

All ^{1}H and ^{13}C NMR spectra were recorded using JEOL Eclipse 400 and JEOL Lambda 400 spectrometers. Operating frequency for ^{1}H was 400 MHz, and 100 MHz for ^{13}C. All chemical shifts (δ) are referenced to $CDCl_3$ and DMSO and are in parts per million (ppm). Significant multiplicities are described by a singlet (s), doublet (d) and multiplet (m) with coupling constants (*J*) reported in Hz.

MS

MALDI mass spectra were performed by the EPSRC National Mass Spectrometry Facilities in Swansea, UK.

UV-Vis

Varian Cary spectrophotometer was used to record all UV-Visible spectra.

Ocean Optics USB2000 UV-NIR ES+ miniature spectrometer was used with fibre optic cable for all analysis of scintillation luminescence measurements under irradiation of X-rays using Spectrasuite software.

Chemicals

Chemical reagents and solvents used were purchased from Alfar Aesar and Sigma Aldrich, with any modifications described.

Microwave syntheses

A CEM discover Benchmate microwave reactor using Synergy software was used for all microwave reactions, using an external IR probe to monitor reaction temperatures. For

all reactions, a 10 mL sealed reaction vessel was used with a maximum pressure of 200 bar and a 2 min maximum heating step and maximum stirring.

PXRD

A PANalytical Empyren X-ray diffractometer was used for all PXRD patterns recorded, with an X-ray tube utilising a monochromatic Cu $K\alpha_1$ radiation as the X-ray source with a PIXcel detector. PANalytical Data Collector software was used to acquire the patterns whilst PANalytical HighScore software was used in the data analysis comparing patterns obtained with the International Centre for Diffraction Data (ICDD) database.

SEM

Scanning electron microscopy (SEM) was performed using a Zeiss EVO 60 SEM with beam current = 40 µm and probe current = 101 pA.

Irradiation

A Radsource RS-2000 biological irradiator was used for the irradiation of samples at different energies ranging from 100 - 160 keV with a current always set to 25 mA.

An Ir-192 source was also used for the irradiation of some samples, at the Castle Hill Hospital in Cottingham, U.K.

In vitro

For the irradiation of cells during *in vitro* cytotoxicity evaluations, an Oriel lamp system with a Schott 06515 Long Pass Optical Filter, giving 95 - 98% of light above 515 nm.

Radiochemistry

A 7.5 MeV ABT Biomarker Generator cyclotron from ABT Molecular Imaging Inc, USA was used for the production of all fluorine-18 (^{18}F); from the nuclear reaction $^{18}O(p,n)^{18}F$

from [^{18}O]H_2O > 98% (CMR, Russia). The current reaching the target was ~ 4.2 μA with an average specific activity of the produced ^{18}F of 100 GBq:mol^{-1}, according to the manufacturer.

Analytical HPLC was performed using an Agilent 1200 (Agilent Technologies, USA) using a 254 nm UV detector with effluent radioactivity monitored using a NaI crystal detector with a photomultiplier tube (LabLogic Systems Limited, UK). Semipreparative HPLC was performed using an Agilent 1100 with a 254 nm UV detector with effluent radioactivity monitored using a NaI crystal detector with a photomultiplier tube (LabLogic Systems Limited, UK). An ACE 5 C18 10x250 5A column was used eluting with MeCN : water gradients containing 0.1% TFA at a flow rate of 4.7 mLmin^{-1}.

Incorporation for all reaction was monitored by radio-TLC (silica TLC sheets in 9 : 1 DCM : MeOH solution. Radiochemical yield and radiochemical purity was determined using analytical HPLC (MeCN : water with 0.1% TFA, 25% - 40%, over 30 min). Compound elution times (t_R): **8[^{18}F]** 8.5 min, [**9[^{18}F]** 16:6 min.

9[^{18}F] (3.4 MBq) was partitioned in a mixture of 1 mL of 1-octanol and 1 mL of PBS after being vortexed for 5 min. Following centrifugation at > 1200 *g* for 5 min, the octanol and aqueous phases were sampled and counted. Reported log *P* value is based on the average of three samples.

Fluorine production

The nuclear reaction ^{18}O(p,n)^{18}F on an enriched water target produced the fluoring-18 radionuclide. Oxygen-18 water containing 80 MBq of fluorine-18 was transferred to a 5 mL V-vial a solution of potassium carbonate (0.1 M, 200 μL), and Kryptofix K222 (5 μg) in 300 μL water. Water was removed by azeotropic distillation with acetonitrile whilst under a compressed air stream at 110 ℃.

PET Imaging

Female mice of CD-1 nu/nu (Charles River, UK) bearing subcutaneous xenografts of HT29 or U87 of a volume between 200 - 600 mm^3 were anesthetised with 1 - 2% isoflurane. The tail veins were then catheterised, and the animal placed in the Minerve Small-Animal Imaging Cell (Minerve, France) before transfer to the Super Argus 2R preclinical PET/CT scanner (Sedecal, Spain). At the beginning of PET acquisition, the animals were injected intravenously in the tail vein with ~ 10 MBq of conjugate **[9[^{18}F]]**, before 90 min of data acquisition using the energy window 250 - 700 keV. The data was histogrammed into 3 x 120, 1 x 240, 4 x 600, and 2 x 1200 s bins before reconstruction into a 175 x 175 x 61 (0.3875 × 0.3875 × 0.775 mm) matrix using OSEM2D with 16 subsets and 2 iterations and randoms/scatter/attenuation correction using Sedecal MMWKS software. Image data was normalised, correcting for non-uniformity of response, dead-time count losses and decay of radioactivity to the time of injection. Determination of activity concentrations was achieved by converting count rate data from reconstructed images. Regions of interest were drawn around the liver and the tumour and sections of quadriceps muscle with time-activity curves generated using AMIDE software.[297] Acquisition of CT images was achieved via 360 projections/8 shots with tube voltage 45 kV and a current of 140 μA. Temperature and respiration was monitored throughout *via* SA Instruments 1025 T monitoring system (SA Instruments, CA, USA). All procedures were carried out according to the Animals in Scientific Procedures Act of 1986 and the UKCCR Guidelines of 2010 using approved protocols, following institutional guidelines (Home Office Project License number 60/4549 held by Dr. Cawthorne).

Singlet oxygen probe 9,10-anthracenediyl-bis(methylene)dimalonic acid (ABDA)

Detection of singlet oxygen was determined by the photobleaching of the singlet oxygen chemical probe, 9,10-anthracenediyl-bis(methylene)dimalonic acid (ABDA).

150 μmol L^{-1} of ABDA in PBS solution was made as a stock solution that was used for dissolving all samples for irradiation. ABDA solutions were kept in the dark throughout as much as possible and each sample was treated in an identical manner. After X-ray irradiation was completed for all samples, the ABDA absorbance was recorded within the wavelength range 300 - 550 nm.

6.2. Theranostic syntheses

6.2.1. Synthesis 5-[4-acetamidophenyl]-10,15,20-tri-(4-pyridyl) porphyrin [1]

Porphyrin **[1]** was synthesised from 4-pyridinecarboxaldehyde (4.89 ml, 52.0 mmol) added to a solution of 4-acetamidobenzaldehyde (3.53 g, 21.5 mmol), whilst stirring in propionic acid (500 ml) and heated under reflux. Pyrrole (5 ml, 72 mmol) was slowly added and the mixture was refluxed for a further hour, in the dark. The reaction was allowed to cool to room temperature and the solvent was removed under reduced pressure. Column chromatography was used for purification (5% MeOH:DCM), and the product was recrystallised from methanol over dichloromethane to yield a purple solid (650 mg, 4.4%) UV-Vis ($CDCl_3$): λ_{max}, 418, 512, 549, 588, 644 log (418 nm) = 5.62 $M^{-1}cm^{-1}$. ^{1}H-NMR ($CDCl_3$): δ 2.39 (s, 3H, -CH_3), 7.72 (s, 1H, -NH), 7.95 (d, 2H, 5-m-Ph), 8.15 (m, 8H, βH), 8.85 (m, 6H, 10,15,20-o-Py), 8.94 (d, 2H, 5-o-Ph), 9.04 (m, 6H, 10,15,20-m-Py). ^{13}C-NMR ($CDCl_3$): δ 24.98 (-CH_3), 117.14, 117.53, 118.04, 118.17, 121.15, 129.42 (β-C), 135.11, 137.43, 138.21, 148.42 (β-C), 150.10, 168.84 (C=O). MS: (ESI) m/z 675 (100$[M + H]^+$), HRMS: calcd. for $C_{43}H_{31}N_8O_1$: 675.2615 found 675.2611.

6.2.2. Synthesis of 5-[4-aminophenyl]-10,15,20-tri-(4-pyridyl) porphyrin [2]

Porphyrin **[2]** was synthesised from **[1]** (300 mg, 0.444 mmol) which was dissolved in aqueous HCl (12 M, 100 ml) and stirred under reflux for 3 h. The reaction was cooled to room temperature and concentrated under reduced pressure. The mixture was dissolved in DCM/TEA (9:1, 200 ml) and stirred for 10 minutes. The solution was washed with water (3 x 200 ml) and the organic layer dried (Na_2SO_4). The solvent was removed under reduced pressure and precipitated from methanol over dichloromethane to yield a purple solid (210 mg, 75%). ^{1}H-NMR ($CDCl_3$): δ 7.01 (d, 2H, 5-m-Ph), 7.86 (d, 2H, 5-o-Ph), 8.10 (m, 6H, 10,15,20-o-Py), 8.78 (m, 14H, 10,15,20-m-Py, βH). ^{13}C-NMR δ 116.96, 119.39, 120.05, 126.21, 132.84 (β-C), 139.01, 150.78, 154.05- MS: (ESI) m/z 633 (100$[M + H]^+$), HRMS: calcd. for $C_{41}H_{29}N_8$: 633.2510 found 633.2505.

6.2.3. Synthesis of 5-[4-azidophenyl]-10,15,20-tri-(4-pyridyl) porphyrin [3]

A solution of sodium nitrite (44.0 mg, 0.632 mmol) in water was added to a stirred solution of 5-[4-aminophenyl]-10,15,20-tri-(4-pyridyl) porphyrin (200 mg, 0.315 mmol) in TFA (2 ml) at 0 ℃ and stirred for 15 min. A solution of sodium azide (83 mg, 1.26 mmol) in water was added dropwise and the reaction was stirred at 0 ℃ for 1 h. The mixture was diluted with water and saturated sodium bicarbonate solution was added until the colour changed from green to purple. The aqueous mixture was extracted with dichloromethane, and the organic layer dried (Na_2SO_4) and the solvent was removed under reduced pressure. The product was purified by column chromatography (3% MeOH:DCM) and precipitated from MeOH over DCM to yield a purple solid (201 mg, 97%).^{1}H-NMR ($CDCl_3$): δ 7.46 (d, 2H, 5-m-Ph), 8.18 (m, 8H, βH), 8.85 (m, 6H, 10,15,20-o-Py), 8.91 (d, 2H, 5-0-Ph), 9.06 (m, 6H, 10,15,20-m-Py). ^{13}C-NMR ($CDCl_3$): δ 117.32, 117.64, 117.74, 120.55, 129.45 (β-C), 135.80, 138.26, 140.45, 148.52 (β-C),

149.96, 150.01. MS: (ESI) m/z 660 (100[M + H]$^{+}$), HRMS: calcd. for $C_{41}H_{27}N_{10}$: 659.2415 found 659.2413.

6.2.4. Synthesis of 5-[4-azidophenyl]-10,15,20-tri-(N-methyl-4-pyridinium) porphyrin trichloride [4]

To a solution of Porphyrin **[3]** (100 mg, 0.151 mmol) in dimethylformamide (DMF) (10 mL) was added methyl iodide (2 mL, 32 mmol) via a syringe and mixture was stirred at 40 ℃ overnight. The product was filtered through cotton wool and was dissolved in water. The addition of ammonium hexafluorophosphate precipitated the product which was then filtered. The porphyrin was then dissolved in acetone and the addition of tetrabutylammonium chloride again precipitated the product which was then filtered. The product was precipitated from diethyl ether over MeOH to yield a dark brown solid (148 mg, 90%). UV–Vis (H_2O): max, 424, 520, 562, 590, 648. log (424 nm) = 5.11 M^{-1} cm^{-1}. ^{1}H NMR (DMSO-d_6): δ 4.74 (s, 9H, CH_3),7.65 (d, 2H, 5-m-Ph), 8.28 (d, 2H,5-o-Ph), 9.01 (m, 6H, 10,15,20-o-Py), 9.12 (m, 8H, βH), 9.07 (m, 6H, 10,15,20-m-Py). ^{13}C NMR (DMSO-d_6): δ 40.13 (CH_3), 114.66, 115.42, 117.63, 122.87, 132.11, 132.25 (β-C), 135.53, 143.62 (β-C), 147.88, 148.15, 148.35, 150.19, 158.54. MS: (ESI) *m*/*z* 351 (100 [M – 3Cl]$^{2+}$). HRMS: calcd for $C_{46}H_{33}N_{10}$ 351.1478, found 351.1481.

6.2.5. Synthesis of zinc 5-[4-azidophenyl]-10,15,20-tri-(N-methyl-4-pyridinium) porphyrin trichloride [5]

Zinc (II) acetate (3.00 mg, 0.0133 mmol) was added to a solution of porphyrin **[4]** (10.0 mg 0.0141 mmol) dissolved in water (10 mL). At room temperature for 1 h the mixture was stirred and monitored for completion by TLC. The product was precipitated by the

addition of ammonium hexafluorophosphate and was filtered. The solid was the dissolved in acetone and precipitated again with the addition of tetrabutylammonium chloride, and the mixture was filtered. The product was precipitated from diethyl ether over MeOH (10.4 mg, 95%). UV–Vis (H_2O): max, 436, 564, 612. ^{1}H NMR (DMSO-d_6): δ 4.72 (s, 9H, CH_3),7.61 (d, 2H, 5-m-Ph), 8.21 (d, 2H, 5-o-Ph), 8.9–9.06 (m, 14H, 10,15,20-o-Py, βH), 9.44 (m, 6H, 10,15,20-m-Py). ^{13}C NMR (DMSO-d_6): δ 48.26 (CH_2-N_3), 115.26, 116.03, 118.21, 122.73, 132.13, 132.65 (β-C), 133.70, 136.13, 139.44, 139.87, 144.22 (β-C), 148.75, 148.92, 150.75, 159.10. MS: (ESI) *m*/*z* 400 (100 $[M - 2Cl]^{2+}$). HRMS: calcd for $C_{44}H_{33}Cl_1N_{10}Zn_1$ 400.0929, found 400.0932.

6.2.6. Synthesis of 3,6,9,12-tetraoxapentadec-14-yn-1-ol [6]

Tetraethylene glycol (2.70 g, 13.9 mmol) was added slowly to a solution of NaH (60% in mineral oil, 0.8 g, 20 mmol) in THF (20 mL) at −20 °C. After the reaction had settled (gas production ceased), propargyl bromide (80% in toluene, 1.48 mL, 13.9 mmol) was added, and stirred overnight at room temperature under nitrogen. The mixture was then filtered, and the solvent was removed under reduced pressure. The crude was then purified by column chromatography (4.5% MeOH:DCM) yielding the product as a pale yellow oil (1.82 g, 68%). ^{1}H NMR ($CDCl_3$): δ 2.40 (s, 1H, C≡CH), 2.92 (OH), 3.52–3.66 (m, 16H), 4.13 (d, 2H, CH_2-C). ^{13}C NMR ($CDCl_3$): δ 58.39 (CH_2-C), 61.68 (CH_2-OH), 69.13, 70.37, 70.41, 70.56, 70.58, 70.65, 72.61, 74.65 (C≡CH), 79.66 (C≡CH). MS: (ESI) *m*/*z* 233 (100 $[M + H]^+$). HRMS: calcd for $C_{11}H_{21}O_5$ 233.1384, found 233.1380.

6.2.7. Synthesis of 3,6,9,12-tetraoxapentadec-14-yn-1-yl 4-methylbenzenesulfonate [7]

A solution of PEG chain **[6]** (1.86 g, 8.00 mmol) was prepared in DCM, to which TsCl (1.60 g, 8.39 mmol) and TEA (1.17 mL, 8.39 mmol) were added and stirred at room temperature for 17 h under nitrogen. The solvent was removed under reduced pressure and the product was then purified by column chromatography, yielding the product as a pale-yellow oil (2.47 g, 80%). ^{1}H NMR ($CDCl_3$): δ 2.38 (s, 4H, C≡CH, CH_3), 3.45–3.65 (m, 14H), 4.02–4.14 (m, 4H, CH_2-C, CH_2), 7.26 (d, 2H, J = 7.9 Hz), 7.70 (d, 2H, *J* = 7.1 Hz). ^{13}C NMR ($CDCl_3$): δ 21.57 (CH_3), 58.41 (CH_2-C), 68.75, 69.09, 69.40, 70.35, 70.54, 70.66, 70.73, 74.76 (C≡CH), 79.73 (C≡CH), 127.98, 129.93, 130.37, 132.95 (4-Ar), 144.92 (1-Ar). MS: (ESI) *m*/*z* 404 (100 $[M + NH_4]^+$). HRMS: calcd for $C_{18}H_{30}O_7N_1S_1$ 404.1737, found 404.1726.

6.2.8. Synthesis of 1-fluoro-3,6,9,12-tetraoxapentadec-14-yne [8]

A solution of 1 M TBAF in THF (4.84 mL, 4.84 mmol) was added to a solution of PEG **[7]** (2.47 g, 6.40 mmol) dissolved in 10 mL of anhydrous THF under argon. The solution was then heated to 80 ℃. The product was allowed to cool, and the solvent was removed under reduced pressure and purified by column chromatography using (25% DCM:ethyl acetate) to yield a pale yellow oil (1.35 g, 90%). ^{1}H NMR ($CDCl_3$): δ 2.40 (s, 1H, C-CH), 3.58–3.68 (m, 14H), 4.14 (d, 2H, O-CH_2-C), 4.5, 48 Hz, 4 Hz (dt, 2H, F-CH_2). ^{13}C NMR ($CDCl_3$): δ 21.57 (CH_3), 58.40 (CH_2-C), 70.39, 70.59, 70.69, 70.78, 74.62 (C≡CH), 79.73, 82.38, 84.05, 128.97 *J* = 744 Hz (CH_2-F).^{19}F-NMR ($CDCl_3$): δ 179.50. MS: (ESI) *m*/*z* 252 (100 $[M + NH_4]^+$). HRMS: calcd. for $C_{11}H_{23}F_1O_4N_1$ 252.1606, found 252.1607.

6.2.9. Synthesis of 5- 4 (13-fluoro-2,5,8,11-tetraoxatridecyl)-1-phenyl-1H-1,2,3-triazole) -10,15,20-tri-(N-methyl-4-pyridinium) porphyrinato zinc (II) trichloride [9]

To a 10 mL microwave tube, was added porphyrin **[5]** (10.0 mg 0.0118 mmol) and PEG **[8]** (3.00 mg, 0.013 mmol) in THF:water (1:3, 8 mL). To the mixture was added copper(II) sulfate pentahydrate (5.00 mg, 0.0200 mmol), sodium ascorbate (5.00 mg, 0.0250 mmol), and TBTA (1.00 mg, 1.90 mmol, and the mixture was microwave heated at 45 ℃ (75 W, max pressure 100 bar) for 20 min. The mixture was concentrated under reduced pressure, and ammonium hexafluorophosphate was added to precipitate the product before being filtered. The mixture was then redissolved in acetone before the addition of tetrabutylammonium chloride again precipitated the product before being filtered. The product was finally precipitated from diethyl ether over MeOH to yield the product as a green solid (11.4 mg, 90%). UV–Vis (H_2O): max, 435, 565, 614 log (435 nm) = 5.03 M^{-1} cm^{-1}. ^{1}H NMR (DMSO-d_6): δ 3.65 (m, 14H), 4.53, J = 24 Hz, 4 Hz (dt, 2H, CH_2-F), 4.72 (s, 9H, CH_3), 4.77 (s, 2H, O-CH_2-triazole), 8.34–8.44 (m, 4H, 5-Ph), 8.85–9.06 (m, 14H, 10,15,20-m-Py, m 8H, βH), 9.20 (s, 1H, triazole-H), 9.44 (d, 6H, 10,15,20-o-Py). ^{13}C NMR (DMSO-d_6): δ 40.13, 48.26, 58.05, 64.06, 69.77, 70.44. MS: (ESI) m/z 333 (100 $[M - 3Cl]^{3+}$), HRMS: calcd for $C_{55}H_{52}O_4N_{10}F_1Zn_1$ 333.1144, found 333.1152.

6.3. Radiochemistry

6.3.1. Fluorine production

To a 5 mL V-vial containing Kryptofix K222 (10.2 mg in 1 mL of dry acetonitrile) and potassium hydroxide carbonate solution (0.5 mL, 5 $mgmL^{-1}$) was added ~ 140 μL of oxygen-18 water containing 1.8 GBq of ^{18}F. The water was then removed *via* azeotropic distillation using acetonitrile under a stream of compressed argon at 90 ℃.

6.3.2. Synthesis of [8[^{18}F]] via isotopic substitution

Dried ^{18}F was added **[8]** (5 mg, 0.021 mmol) to dry DMSO (200 μL) in a 5 mL V-vial and was heated to 180 ℃ for 10 min. The mixture was then diluted with methanol (1 mL) and purified using a Sep-Pak Light Alum N cartridge. Radio-TLC was used to determine the radiolabelling yield.

6.3.3. Synthesis of [8[^{18}F]] from [7]

[7] (5 mg, 0.013 mmol) was added to a 5 mL V-vial containing the dried ^{18}F in dry DMSO (200 μL), and was heated to 140 ℃ for 10 min. The mixture then was diluted with methanol (1 mL) and purified using a Sep-Pak Light Alum N cartridge. Radio-TLC was used to determine the radiolabelling yield.

6.3.4. Synthesis of carrier-added [8[^{18}F]]

[7] (5 mg, 0.013 mmol) was added to a 5 mL V-vial containing the dried ^{18}F in dry DMSO (200 μL), and was heated to 140 ℃ for 10 min. Tetrabutylammonium fluoride (5 mg, 0.019 mmol) in dry DMSO (200 μL) was added and the mixture heated to 140 ℃ for 5 min. The mixture then was diluted with methanol (1.5 mL) and purified using a Sep-Pak Light Alum N cartridge. Radio-TLC was used to determine the radiolabelling yield.

6.3.5. General methodology for click reaction [9[^{18}F]]

Porphyrin **[5]** (1 mg, 1 μmol) was added to a 10 mL microwave tube containing **[8[^{18}F]]** in water (0.2 mL). To this a solution of TBTA (174 μg, 0.4 μmol), copper(II) sulfate pentahydrate (50 μg, 0.2 μmol) and sodium ascorbate (80 μg, 0.4 μmol) in water (0.2 mL) was added. Microwave heating of the mixture was performed at 40 ℃ for 20 min (MW,

60 W). The product was diluted with water (20 mL) and purified using a Sep-Pak Light C18 cartridge. The cartridge was washed with water (5 mL) and the product was then eluted in ethanol (0.5 mL).

6.3.6. Synthesis of [8[^{18}F]]

[7] (6.7 mg) in dry acetonitrile (1 mL) was added to a 5 mL V-vial containing dried ^{18}F (1.5 GBq) and the mixture was heated to 90 ℃ for 10 min. The mixture was then purified using a Sep-Pak Light Alum N cartridge with the eluted activity measuring 982 MBq with a 77% radiochemical yield (RCY). Solvent volume was reduced to ~ 0.2 mL at 90 ℃ using a compressed stream of argon before the residue was diluted with 0.5 mL of water. The crude product was purified by semipreparative HPLC (MeCN : water, 20% to 30% in 15 min), and **[8[18F]]** eluted between 10-11 min with activity 726 MBq. The fraction eluted by HPLC was collected and diluted to 40 mL with water and loaded onto a homemade Oasis C18 Sep-Pak cartridge before being washed with 10 mL of water and eluted in methanol (2 mL). The methanol solution containing activity was dried at 60 ℃.

6.3.7. Synthesis of [9[^{18}F]]

A solution containing porphyrin **[5]** (0.2 mg in 100 μL of water, copper(II) sulphate pentahydrate (0.5 mg in 12.5 μL of water), sodium ascorbate (3.75 mg in 50 μL of water), TBTA (0.5 mg in 160 μL of methanol), was added to a champagne HPLC vial (1.7 mL) containing the purified **[8[^{18}F]] (**446 MBq). The reaction was then heated to 60 ℃ for 35 min before purification using semipreparative HPLC (MeCN : water 20% to 40% in 30 min). **[9[^{18}F]]** eluted at 15 – 16 min with activity 72.6 MBq and radiochemical yield 16.2%. This fraction was collected and diluted with water before being purified by Oasis Sep-Pak cartridge, eluted with ethanol (0.5 mL) with a 0.22 μm filter. The solution was

dried under a stream of compressed argon at 60 ℃ and dissolved in 0.2 μL of heparin-water (33.6 MBq).

6.4. Nanoparticle syntheses

6.4.1. Synthesis of $CaWO_4$ nanoparticles [10]

$CaWO_4$ nanoparticles **[10]** were synthesised by a hydrothermal method in which the product was precipitated from a solution of ($Ca(NO_3)_2.4H_2O$) and ($Na_2WO_4{\cdot}2H_2O$) solution, acting as the sources of Ca^{2+} and WO_4^{2-} respectively. Analytical grade chemicals were obtained from Sigma Aldrich and used as received. A solution of 500 mg ($Ca(NO_3)_2{\cdot}4H_2O$) in deionised water (DI) (15 mL) was added dropwise to a solution of 750 mg $Na_2WO_4{\cdot}2H_2O$ in DI water (15 mL). Sodium hydroxide was added to adjust the reaction pH to 9 - 9.5. Finally, 5 mL of ethylene glycol (EG) was added and the reaction was heated under reflux at 100 ℃ for three h. The resulting white precipitate was collected by centrifugation at 15,000 rpm for 10 min, washed several times with water and acetone and dried in a vacuum oven at 50 ℃, overnight.

6.4.2. Synthesis of microwave prepared $CaWO_4$ nanoparticles [11]

Nanoparticles **[11]** were synthesised by the same procedure as used for the synthesis of **[10]** except *via* microwave heating in a 35 ml vessel at 180 ℃ for 1 h. $CaWO_4$ nanoparticles **[11]** were synthesised by a hydrothermal method in which the product was precipitated from a solution of ($Ca(NO_3)_2.4H_2O$ AR) and ($Na_2WO_4{\cdot}2H_2O$ A) solution, acting as the sources of Ca^{2+} and WO_4^{2-} respectively. A solution of 500 mg ($Ca(NO_3)_2{\cdot}4H_2O$) in DI water (15 mL) was added dropwise to a solution of 750 mg $Na_2WO_4{\cdot}2H_2O$ in DI water (15 mL). Sodium hydroxide was added to adjust the reaction pH to 9 - 9.5. Finally, 5 mL of EG was added and the reaction was heated under

microwave irradiation at 180 ℃ (300 W, max pressure 17.0 bar) for 1 h. The resulting white precipitate was collected by centrifugation at 15,000 rpm for 10 min, washed several times with water and acetone and dried in a vacuum oven at 50 ℃, overnight.

6.4.3. Synthesis of europium-doped nanoparticles [12], [13], [14] and [15]

Nanoparticles were prepared by substituting a molar percentage of $Eu(NO_3)_3{\cdot}6H_2O$ for that of $Ca(NO_3)_2{\cdot}4H_2O$ to give $Ca_{1-X}Eu_XWO_4$ prepared at 3%, 10% 15% and 20% of Eu.

$CaWO_4$ nanoparticles **[12-15]** were synthesised by a hydrothermal method in which the product was precipitated from a solution of ($Ca(NO_3)_2.4H_2O$), ($Eu(NO_3)3{\cdot}6H_2O$ and ($Na_2WO_4{\cdot}2H_2O$) solution, acting as the sources of Ca^{2+} and WO^{2-} respectively. A solution of 500 mg ($Ca(NO_3)_2{\cdot}4H_2O$) in deionised water (DI) (15 mL) was added dropwise to a solution of 750 mg $Na_2WO_4{\cdot}2H_2O$ in DI water (15 mL). Sodium hydroxide was added to adjust the reaction pH to 9 - 9.5. Finally, 5 mL of ethylene glycol (EG) was added and the reaction was heated under reflux at 100 ℃ for three h. The resulting white precipitate was collected by centrifugation at 15,000 rpm for 10 min, washed several times with water and acetone and dried in a vacuum oven at 50 ℃, overnight.

6.4.4. Microwave prepared europium-doped $CaWO_4$ nanoparticles [16–17]

Nanoparticles were prepared by substituting a molar percentage of $Eu(NO_3)_3{\cdot}6H_2O$ for that of $Ca(NO_3)_2{\cdot}4H_2O$ to give $Ca_{1-X}Eu_XWO_4$ prepared at 10% and 20% of Eu.

$CaWO_4$ nanoparticles **[16-17]** were synthesised by a hydrothermal method in which the product was precipitated from a solution of ($Ca(NO_3)_2{\cdot}4H_2O$), ($Eu(NO_3)3{\cdot}6H_2O$ and ($Na_2WO_4{\cdot}2H_2O$) solution, acting as the sources of Ca^{2+} and WO^{2-} respectively. A solution of 500 mg ($Ca(NO_3)_2{\cdot}4H_2O$) in DI water (15 mL) was added dropwise to a solution of

750 mg $Na_2WO_4{\cdot}2H_2O$ in DI water (15 mL). Sodium hydroxide was added to adjust the reaction pH to 9 - 9.5. Finally, 5 mL of EG was added and the reaction was heated under microwave irradiation at 180 ℃ (300 W, max pressure 17.0 bar) for 1 h. The resulting white precipitate was collected by centrifugation at 15,000 rpm for 10 min, washed several times with water and acetone and dried in a vacuum oven at 50 ℃, overnight.

6.4.5. Synthesis of annealed $CaWO_4$ nanoparticles [18-22]

$CaWO_4$ nanoparticles **[18-22]** were synthesised by a hydrothermal method in which the product was precipitated from a solution of ($Ca(NO_3)_2.4H_2O$ AR) and ($Na_2WO_4{\cdot}2H_2O$ A) solution, acting as the sources of Ca^{2+} and WO_4^{2-} respectively. A solution of 500 mg ($Ca(NO_3)_2{\cdot}4H_2O$) in deionised water (DI) (15 ml) was added dropwise to a solution of 750 mg $Na_2WO_4{\cdot}2H_2O$ in DI water (15 ml). Sodium hydroxide was added to adjust the reaction pH to 9 - 9.5. Finally, 5 mL of ethylene glycol (EG) was added and the reaction was heated under reflux at 100 ℃ for three hours. The resulting white precipitate was collected by centrifugation at 15,000 rpm for 10 min, washed several times with water and acetone and dried in a vacuum oven at 50 ℃, overnight.

$CaWO_4$ nanoparticles were then then annealed in a box furnace under increasing temperature, a ramping temperature of 5 ℃ was used to heat the samples which were then held at the desired temperature for 6 h before cooling under ambient conditions to rt before further analysis.

Table 16 $CaWO_4$ nanoparticles **[18-22]** annealed at increasing temperature.

NP sample	Temperature (℃)
[18]	500
[19]	550
[20]	600
[21]	650
[22]	700

6.4.6. Synthesis of annealed $Ca_{1-x}Eu_xWO_4$ nanoparticles [23-27]

Nanoparticles were prepared by substituting a molar percentage of $Eu(NO_3)_3{\cdot}6H_2O$ for that of $Ca(NO_3)_2{\cdot}4H_2O$ to give $Ca_{1-x}Eu_xWO_4$ prepared at 3, 10, 15, 20 and 25%. $CaWO_4$ nanoparticles **[23-27]** were synthesised by a hydrothermal method in which the product was precipitated from a solution of ($Ca(NO_3)_2{\cdot}4H_2O$), ($Eu(NO_3)_3{\cdot}6H_2O$) and ($Na_2WO_4{\cdot}2H_2O$) solution, acting as the sources of Ca^{2+} and WO_4^{2-} respectively. A solution of 500 mg ($Ca(NO_3)_2{\cdot}4H_2O$) in DI water (15 ml) was added dropwise to a solution of 750 mg $Na_2WO_4{\cdot}2H_2O$ in DI water (15 ml). Sodium hydroxide was added to adjust the reaction pH to 9 - 9.5. Finally, 5 mL of EG was added and the reaction was heated under microwave irradiation at 180 ℃ (300 W, max pressure 17.0 bar) for 1 h. The resulting white precipitate was collected by centrifugation at 15,000 rpm for 10 min, washed several times with water and acetone and dried in a vacuum oven at 50 ℃, overnight.

The samples were then annealed in a box furnace at 650 ℃ with a ramping temperature of 5 ℃ and then held at the desired temperature for 6 h before cooling under ambient conditions to room temperature before further analysis.

Table 17 Europium doped $CaWO_4$ nanoparticles **[23-27]** with an increasing molar percentage of Eu^{3+}.

NP sample	Molar %
[23]	3
[24]	10
[25]	15
[26]	20
[27]	25

6.4.7. Synthesis of europium tungstate by benchtop synthesis [28]

A solution of 500 mg ($Eu(NO_3)_3 \cdot 6H_2O$), (1.12 x 10^{-3} mol) in DI water (15 ml) was added dropwise to a solution of 750 mg $Na_2WO_4 \cdot 2H_2O$ (1.35 x 10^{-3} mol) in DI water (15 ml). Sodium hydroxide was added to adjust the reaction pH to 9 - 9.5. Finally, 5 mL of EG was added and the reaction was heated under reflux at 100 ℃ for 3 h. The resulting white precipitate was collected by centrifugation at 15,000 rpm for 10 min, washed several times with water and acetone and dried in a vacuum oven at 50 ℃, overnight. The product was then annealed in a box furnace at 950 ℃, with a ramping temperature of 5 ℃/min and held at temperature for 6 h before being cooled.

6.4.8. Microwave radiation-assisted synthesis of europium tungstate [29]

A solution of 500 mg ($Eu(NO_3)_3 \cdot 6H_2O$), (1.12 x 10^{-3} mol) in DI water (15 ml) was added dropwise to a solution of 750 mg $Na_2WO_4 \cdot 2H_2O$ (1.35 x 10^{-3} mol) in DI water (15 ml). Sodium hydroxide was added to adjust the reaction pH to 9 – 9.5. Finally, 5 mL of EG was added and the reaction was heated under microwave irradiation at 180 ℃ (300 W, max pressure 17.0 bar) for 1 h. The resulting white precipitate was collected by

centrifugation at 15,000 rpm for 10 min, washed several times with water and acetone and dried in a vacuum oven at 50 ℃, overnight. The product was then annealed in a box furnace at 950 ℃, with a ramping temperature of 5 ℃/min and held at temperature for 6 hours before being allowed to cool.

6.4.9. Microwave radiation-assisted synthesis of europium tungstate with varying amounts of EG [30-32]

Synthesis was performed as previously stated using a microwave radiation-assisted synthesis, however the temperature was lowered to 650 ℃ and the volume of EG added to the water was 1, 10 and 20 mL for products **[30]**, **[31]**, **[32]** respectively. A total solvent volume of 20 mL was maintained meaning that the amount of water substituted was also 1, 10 and 20 mL respectively.

6.4.10. Synthesis of ZnO nanoparticles [33-37]

Zinc acetate was dissolved in EG (0.273 $moldm^{-3}$) under MW irradiation at 70 ℃ for 10 min until complete dissolution was achieved. To this 1.5 mL of deionised water was added and the reaction was heated to 180 ℃ for one h.

6.4.11. Synthesis of CaF_2 nanoparticles [38]

The dropwise addition of a 25 mL (8.9 $x10^{-2}$ $moldm^{-3}$) of calcium nitrate and (2.7 $x10^{-3}$ $moldm^{-3}$) europium nitrate solution to ammonium fluoride solution was performed under stirring at a temperature of 75 ℃ for 15 min before being allowed to cool down. NPs were washed with methanol and deionised water and collected by centrifugation.

6.4.12. Synthesis of europium-doped lanthanum fluoride nanoparticles [39]

Ammonium fluoride was dissolved in water with heating to 75 ℃. A solution of $La(NO_3)_3 \cdot 5H_2O$ and 3 mol % $Eu(NO_3)_3 \cdot 6H_2O$, in water was added dropwise. The pH was monitored during addition to maintain a neutral pH. The solution was left stirring at temperature for 2 h before cooling. The resulting nanoparticles were centrifuged and washed several times with water before drying overnight in a vacuum oven at 50 ℃.

6.4.13. Synthesis of europium-doped lanthanum fluoride nanoparticles by microwave [40]

The dropwise addition of a 10 mL mixed nitrate solution, $La(NO_3)_3 \cdot 5H_2O$ and $Eu(NO_3)_3 \cdot 6H_2O$ was performed at room temperature under stirring into a 10 mL fluoride solution NH_4F at room temperature. The suspension was then heated under MW irradiation at 180 ℃ for one h.

6.4.14. Synthesis of europium-doped lutetium fluoride nanoparticles [41]

$Lu_{0.8}E_{0.2}F_3$ were prepared using a co-precipitation hydrothermal method. A solution of ammonium fluoride (0.33 g, 9 $x10^{-3}$ mol) in water 15 mL was added dropwise to a solution of $Lu(NO_3)_3 \cdot 6H_2O$ (0.3 g, 8. $3x10^{-4}$ mol) and 20 mol % $Eu(NO_3)_3 \cdot 6H_2O$ (70 mg, 1.66 $x10^{-4}$) dissolved in a minimum of water. The powder obtained was kept at 100 ℃ for 1 h then dried and annealed at 400 ℃ for 5 h.

6.4.15. Synthesis of europium-doped yttrium oxide nanoparticles [42]

To a solution of $Y(NO_3)_3 \cdot 6H_2O$ (1 g, 3 mmol) in 8 mL of DI water, was added a solution of NaOH (192 mg, in 16 mL (0.3 M)), dropwise with stirring at ambient conditions. The mixture was heated in a CEM benchtop microwave at 180 ℃ for 1 h. The white precipitate was filtered, washed repeatedly with water and acetone before being dried in a vacuum oven at 50 ℃ overnight. The sample was annealed at 1100 ℃ in a box furnace for 6 h (ramping temperature 5 ℃ min^{-1}).

6.4.16. Synthesis of europium-doped lutetium oxide nanoparticles [43]

To a solution of $Lu(NO_3)_3 \cdot 6H_2O$ (1 g, 3 mmol) in 8 mL of DI water, was added a solution of NaOH (192 mg, in 16 mL (0.3 M)), dropwise with stirring at ambient conditions. The mixture was heated in a CEM benchtop microwave at 180 ℃ for 1 h. The white precipitate was filtered washed repeatedly with water and acetone before being dried in a vacuum oven at 50 ℃ overnight. The sample was annealed at 1100 ℃ in a box furnace for 6 h (ramping temperature 5 ℃ min^{-1}).

6.5. Conjugate syntheses

6.5.1. Synthesis of 5-(4-methoxycarboxyphenyl)-10,15,20-tris-(4-pyridyl) porphyrin [44]

Porphyrin **[44]** was synthesised from methyl-4-formylbenzoate (2.79 g, 17 mmol) added to a solution of pyridine-4-carboxaldehyde (4.75 ml, 68 mmol), whilst stirring in propionic acid (500 ml) and heated under reflux. Pyrrole (4.75 ml, 68 mmol) was slowly added and the mixture was refluxed for an hour, in the dark. The reaction was allowed to cool to room temperature and the solvent was removed under reduced pressure, with any

excess acid neutralised by a saturated solution of sodium bicarbonate. Column chromatography was used to purify the crude product (2% MeOH:DCM) and the product was precipitated from MeOH over DCM to yield a purple solid. (600 mg, 5.33%), ^{1}H-NMR ($CDCl_3$): δ 4.14 (s, 3H, C=OOC$\underline{H}_3$), 8.14 (m, 6H, 10,15,20-o-Py), 8.29 (d, 2H, J=7.96 Hz, 5-m-Ph), 8.44 (d, 2H, J=8.16 Hz, 5-o-Ph), 8.86 (m, 8H, βH), 9.03 (m, 6H, 10,15,20-m-Py). ^{13}C-NMR ($CDCl_3$): δ 52.47 (CH3), 117.59, 128.02, 129.91 (β-C), 134.47, 146.18, 148.34 (β-C), 167.09 (C=O). MS: (ESI) m/z 675 (100[M]+), HRMS: calcd. for $C_{43}H_{29}N_7O_2$: 675.2377 found 675.2356.

6.5.2. Synthesis of 5-[4-carboxyphenyl]-10,15,20-tri-(4-pyridyl) porphyrin [45]

Porphyrin **[45]** was synthesised from porphyrin **[44]** 5-(4-methoxycarboxyphenyl)-10,15,20-tris-(4-pyridyl) porphyrin. To a stirred solution of **[44]** (400 mg, 0.592 mmol) in DMF (40 ml) a solution of potassium hydroxide (1.60 g, 28.6 mmol) in water (10 ml) was added and left to stir at room temperature overnight. The solvent was removed under reduced pressure, with any residue neutralised by 1 M HCl aqueous solution. The mixture was cleaned up by running down a pre-column and precipitated from MeOH over DCM to yield a purple solid 321 mg (83%).^{1}H-NMR δ 8.13 (m, 6H, 10,15,20-o-Py), 8.31 (d, 4H, J=8.3 Hz, 5-m-Ph), 8.88-8.95 (m, 14H, 6H, 10,15,20-m-Py, βH). ^{13}C-NMR ($CDCl_3$): δ 116.80, 117.20, 117.74, 120.84, 129.68 (β-C), 132.83, 134.23, 147.78 (β-C), 150.71. MS: (ESI) m/z 662 (100[M+-H]$^{+}$), HRMS: calcd. for $C_{42}H_{26}O_2N_7$: 662.2299 found 662.2294.

6.5.3. Synthesis of 5-[4-(succinimide-N-oxycarbonyl)phenyl]-10,15,20-tri-(4-pyridyl) porphyrin [46]

Porphyrin **[46]** was synthesised from porphyrin **[45]** 5-[4-Carboxyphenyl]-10,15,20-tri-(4-pyridyl) porphyrin. To a stirred solution of **[45]** (100 mg, 0.151 mmol) in dry pyridine (10 ml) was added thionyl chloride (0.20 ml, 2.72 mmol), dropwise. The reaction was heated to 50 ℃, under nitrogen and protected from light, for a period of 30 min. *N*-hydroxysuccinimide (400 mg, 3.47 mmol) was added and left for 3 h. Pyridine was removed by filtration and the residue was dissolved in DCM before being washed with a saturated aqueous solution of sodium carbonate and water. The organic layer was then dried with $MgSO_4$ and the solvent was removed under reduced pressure. The residue was precipitated from hexane over chloroform to yield a red solid. (101 mg, 88%). ^{1}H-NMR ($CDCl_3$): δ 3.03 (br s, 4H, CH_2),8.22 (m, 6H, 10,15,20-o-Py), 8.37 (d, 2H, 5-m-Ph), 8.57 (d, 2H, 5-o-Ph), 8.85 (m, 8H, βH), 9.07 (m, 6H, 10,15,20-m-Py). ^{13}C-NMR ($CDCl_3$): δ 25.75, 117.47, 119.45, 125.03, 127.54, 129.21, 129.63 (β-C), 134.89, 148.01 (β-C), 150.5, 169.49 (C=O), 172.60(C=O). MS: (ESI) m/z 759 (100$[M + H]^+$), HRMS: calcd. for $C_{46}H_{31}N_8O_4$: 759.2463 found 759.2460.

6.5.4. Synthesis of 5-[4-(succinimide-N-oxycarbonyl)phenyl]-10,15,20-tri-(4-pyridinumyl) porphyrin trichloride [47]

To a solution of porphyrin **[46]** (100 mg, 0.132 mmol) in DMF (10 mL) was added methyl iodide (2 mL, 32 mmol) via a syringe and the mixture was stirred at 40 ℃ overnight. The product was filtered through cotton wool and was dissolved in water. The addition of ammonium hexafluorophosphate precipitated the product which was then filtered. The porphyrin was then dissolved in acetone and the addition of TBACl again precipitated the product which was then filtered. The product was precipitated from diethyl ether over

MeOH to yield a dark mauve solid (108 mg, 90%). UV-Vis ($CDCl_3$): λmax, 425, 516, 554, 592, 650 log (425 nm) = 5.11 $M^{-1}cm^{-1}$ H-NMR (DMSO-d_6): δ 3.01 (s, 4H, CH_2) 4.78 (d, 9H) 8.51(d, 2H), 8.60 (d, 2H), 9.11 (m, 14H, βH), 9.56 (d, 6H). ^{13}C NMR (100 MHz, DMSO- d_6): δ 26.18, 38.36, 115.60, 116.11, 121.23, 125.14, 129.46, 132.66, 135.69, 144.88, 147.90, 156.97, 162.56, 171.10. MS: (ESI) m/z 267 ($[M-3Cl]^{3+}$), HRMS: calcd. for $C_{49}H_{39}N_8O_4$: 267.7659 found 267.7656.

6.5.5. Synthesis of 5,10, 15, 20-tetrakis-(3,4 dimethoxyphenyl) porphyrin [48]

Porphyrin **[48]** was synthesised from 3,4-dimethoxybenzaldehyde (6 g, 40 mmol) whilst stirring in propionic acid (375 ml) and heated under reflux. Pyrrole (2.8 ml, 40 mmol) was slowly added and the mixture was refluxed for an hour, in the dark. The reaction was allowed to cool to room temperature and the solvent was removed under reduced pressure. The product was purified by precolumn (4% MeOH:DCM) and precipitated from methanol over DCM to yield a solid (1.75 g, ~20%). ^1H-NMR ($CDCl_3$): δ 2.76 (s, 2H), 3.98 (3H, s), 4.15 (s, 3H), 7.27 (d, 4H, J = 4.5 Hz), 7.75 (d, 4H, J =4.5 Hz), 7.79 (s, 4H,) 8.90 (s, 8H).

6.5.6. Synthesis 5,10, 15, 20-Tetrakis – (3,4 dihydroxyphenyl) porphyrin [49]

To a stirred solution of **[48]** (1 g, 1.17 mmol) in dry pyridine (10 ml) cooled to 0 ℃ was added boron tribromide (25 ml, 1 M in DCM). The reaction was allowed to reach rt and stirred for 48 h. The reaction mixture was then cooled again to 0 ℃ and methanol (10 mL) was slowly added and allowed to stir for 30 min. The precipitate was collected by filtration and washed with methanol and water. Column chromatography was used to purify the crude product (THF) to yield a purple powder (608 mg, 70% yield). ^1H-NMR

(d_6-acetone): δ -2.76 (s, 2H), 7.56 (d, 4H), 7.59 (dd, 4H), 8.35 (s, 8H), 9.01 (bs, 8H) MS: (ESI) m/z 746 (100$[M + H]^+$), HRMS: calcd. for $C_{44}H_{31}N_4O_8$: 746.1363 found 746.1360.

6.5.7. Synthesis of APTES functionalised nanoparticles [53-57]

Nanoparticles (0.7 g) were added in 25 mL solution of ethanol: water, 1:1 (*v*/*v*) and sonicated for 10 min to get uniform dispersion. APTES solution (2.8 mL) was injected into the mixture under N_2 atmosphere, while maintaining the temperature of the water bath at 40 ℃. The reaction was followed for 2 h at 40 ℃ with stirring. The resulting particles were finally precipitated by centrifugation and washed with absolute ethanol and deionised water and oven dried at 50 ℃ overnight.

Table 18 APTES functionalisation of nanoparticles yielding product **[50-54]**.

APTES functionalised	Sample
$CaWO_4$@$SiONH_2$	**[50]**
$EuWO_4$@$SiONH_2$	**[51]**
LaF_3@$SiONH_2$	**[52]**
LuF_3@$SiONH_2$	**[53]**
Lu_2O_3@$SiONH_2$	**[54]**

6.5.8. Synthesis of porphyrin-nanoparticle conjugates [55-59]

50 mg of APTES functionalised nanoparticles **[50-54]** were dispersed into dry DMF and sonicated for a period of 30 min to minimise aggregation. (20 mg, 2.64 $x10^{-5}$ mol) of **[47]** was added to each sample followed by EDC·HCl (5 mg, 3.17 $x10^{-5}$ mol) and HOBt (4.5 mg, 3.17 $x10^{-5}$ mol). Finally, DIPEA (0.2 mL) was added and the reaction temperature was raised to 50 ℃ and stirred overnight. Mixtures were filtered and washed with MeOH and water.

Table 19 ScNP-PS conjugates **[55 -59]**.

ScNP-PS	Sample
$CaWO_4$@$SiONH_2$@PS	**[55]**
$EuWO_4$@$SiONH_2$@PS	**[56]**
LaF_3@$SiONH_2$@PS	**[57]**
LuF_3@$SiONH_2$@PS	**[58]**
Lu_2O_3@$SiONH_2$@PS	**[59]**

6.5.9. Synthesis of porphyrin-nanoparticle conjugate [60]

20 mg of europium-doped LaF_3 nanoparticles **[40]** were suspended in 10 mL of DI Water and sonicated for 10 mins. Whilst maintaining under conditions of sonication a solution of **[49]** (10 mg) in 2.5 mL of methanol was added dropwise. 2 ml of triethylamine was added and the suspension was left to sonicate for a further 10 min. The suspension was then filtered and washed with MeOH and water.

7. References

1 E. D. Sternberg, D. Dolphin and C. Bruckner, *Tetrahedron*, 1998, **54**, 4151–4202.

2 C. Brückner, E. D. Sternberg and D. Dolphin, *Tetrahedron*, 1998, **54**, 4151–4202.

3 S. B. Brown, E. A. Brown and I. Walker, *Lancet Oncol*. 2004, **5**, 497–508.

4 C. Foote, *Photochem. Photobiol.*, 1991, **54**, 659.

5 A. P. Castano, T. N. Demidova and M. R. Hamblin, *Photodiagnosis Photodyn. Ther.*, 2004, **1**, 279–293.

6 K. R. Weishaupt, C. J. Gomer and T. J. Dougherty, *Cancer Res.*, 1976, **36**, 2326–2329.

7 R. Bonnett, *Chem. Soc. Rev.*, 1995, **24**, 19–33.

8 P. W. Helman and A. B. Ross, *J. Phys. Chem. Ref. Data*, 1993, **22**, 113–262.

9 L. B. Josefsen and R. W. Boyle, *Met. Based. Drugs*, 2008, **2008**, 27–40.

10 W. M. Sharman, C. M. Allen and J. E. van Lier, *Drug Discov. Today*, 1999, **4**, 507–517.

11 J. F. Kerr and A. H. Wyllie, *Br. J. Cancer*, 1972, **26**, 239–257.

12 M. L. Agarwal, M. E. Clay, E. J. Harvey, H. H. Evans, A. R. Antunez and N. L. Oleinick, *Cancer Res.*, 1991, **51**, 5993–5996.

13 D. L. Vaux and A. Strasser, *Proc. Natl. Acad. Sci.* 1996, **93**, 2239–2244.

14 T. J. Dougherty, C. J. Gomer, B. W. Henderson, G. Jori, D. Kessel, M. Korbelik, J. Moan and Q. Peng, *J. Natl. Cancer Inst.*, 1998, **90**, 889–905.

15 L. B. Josefsen and R. W. Boyle, *Met. Based. Drugs*, 2008, **2008**, 1–23.

16 S. L. Fink and B. T. Cookson, *Infect. Immun.*, 2005, **73**, 1907–1916.

17 P. Agostinis, K. Berg, K. a Cengel, T. H. Foster, A. W. Girotti, S. O. Gollnick, S. M. Hahn, M. R. Hamblin, A. Juzeniene, D. Kessel, M. Korbelik, J. Moan, P.

Mroz, D. Nowiz, J. Piette, B. C. Willson and J. Golab, *Am. Cancer Soc.*, 2011, **61**, 250–281.

18 R. Bonnett and G. Martõ, *Tetrahedron*, 2001, **57**, 9513–9547.

19 I. J. Macdonald and T. J. Dougherty, *J. Porphyrins Phthalocyanines*, 2001, **5**, 105–129.

20 L. B. Josefsen and R. W. Boyle, *Br. J. Pharmacol.*, 2008, **154**, 1–3.

21 L. B. Josefsen and R. W. Boyle, *Theranostics*, 2012, **2**, 916–66.

22 E. S. Nyman and P. H. Hynninen, *J. Photochem. Photobiol. B.*, 2004, **73**, 1–28.

23 Z. Luksiene, P. Juzenas and J. Moan, *Cancer Lett.*, 2006, **235**, 40–47.

24 Q. Peng, J. Moan and L. S. Cheng, *Cancer Lett.*, 1991, **58**, 29–35.

25 H. Von Tappeiner and A. Jesionek, *Muench, Med. Wochenschr.*, 1903, **47**, 2042–2044.

26 H. Von Tappeiner and A. Jodlbauer, *Arch. Klin. Med.*, 1904, **80**, 427–487.

27 O. Raab, *Z. Biol.*, 1900, **39**, 524–546.

28 J. Moan and Q. Peng, in *Photodynamic Therapy*, ed. T. Patrice, 2003, pp. 15–31.

29 W. Hausmann, *Biochem. Z.*, 1913, **30**, 276–316.

30 H. Pfeifer, in *Handbuch der Biochemischen, Arbeitsmethoden*, ed. E. Abderhaldan, Berlin, Germany, 1911, pp. 563–571.

31 F. Meyer-Betz, *Dtsch. Arch. Klin. Med.*, 1913, **112**, 476–550.

32 A. Policard, *Soc. Biol.*, 1924, **91**, 1423–1428.

33 H. Auler and G. Banzer, *Z. Krebsforsch*, 1942, **53**, 65–68.

34 S. K. Schwartz, K. Absolon and H. Vermund, *Univ. Minn. Med. Bull*, 1955, **27**, 7–8.

35 R. L. Lipson, E. J. Baldes and A. M. Olsen, *J. Natl. Cancer Inst.*, 1961, **26**, 1–11.

36 T. J. Dougherty, *Photochem. Photobiol.*, 1987, **45**, 879–889.

37 A. E. O'Connor, W. M. Gallagher and A. T. Byrne, *Photochem. Photobiol.*,

2009, **85**, 1053–1074.

38 J. Celli, N. Solban, A. Liang, S. Pereira and T. Hasan, *Lasers Surg Med.*, 2012, **43**, 565–574.

39 B. Javaid, P. Watt and N. Krasner, *Lasers Med. Sci.*, 2002, **17**, 51–6.

40 R. Sinha, G. J. Kim, S. Nie and D. M. Shin, *Mol. Cancer Ther.*, 2006, **5**, 1909–17.

41 T. G. St. Denis, K. Aziz, A. A. Waheed, Y. Y. Huang, S. K. Sharma, P. Mroz and M. R. Hamblin, *Photochem. Photobiol. Sci.*, 2011, **10**, 792–801.

42 H. S. Hwang, H. Shin, J. Han and K. Na, *J. Pharm. Investig.*, 2018, **48**, 143–151.

43 J. W. Kleinovink, P. B. Van Driel, T. J. Snoeks, N. Prokopi, M. F. Fransen, L. J. Cruz, L. Mezzanotte, A. Chan, C. W. Löwik and F. Ossendorp, *Clin. Cancer Res.*, 2016, **22**, 1459–1468.

44 N. M. Candido, M. T. De Melo, L. P. Franchi, F. L. Primo, A. C. Tedesco, P. Rahal and M. F. Calmon, *J. Biomed. Nanotechnol.*, 2018, **14**, 994–1008.

45 L. Freitag, A. Ernst, M. Thomas, R. Prenzel, B. Wahlers and H. N. Macha, *Thorax*, 2004, **59**, 790–793.

46 A. Colasanti, A. Kisslinger, M. Quarto and P. Riccio, *Acta Biochim. Pol.*, 2004, **51**, 1039–1046.

47 P. Mroz, J. T. Hashmi, Y. Y. Huang, N. Lange and M. R. Hamblin, *Expert Rev. Clin. Immunol.*, 2011, **7**, 75–91.

48 A. D. Garg, D. Nowis, J. Golab, P. Vandenabeele, D. V. Krysko and P. Agostinis, *Biochim. Biophys. Acta - Rev. Cancer*, 2010, **1805**, 53–71.

49 S. O. Gollnick, L. Vaughan and B. W. Henderson, *Cancer Res.*, 2002, **62**, 1604–8.

50 H. Zhang, W. Ma and Y. Li, *Lasers Med. Sci.*, 2009, **24**, 549–552.

51 M. Korbelik and J. Sun, *Cancer Immunol. Immunother.*, 2006, **55**, 900–909.

52 A. D. Garg, D. Nowis, J. Golab and P. Agostinis, *Apoptosis*, 2010, **15**, 1050–1071.

53 M. Korbelik, J. Sun, I. Cecic and K. Serrano, *Photochem. Photobiol. Sci.*, 2004, **3**, 812–816.

54 M. A. Stanley, *Clin. Exp. Dermatol.*, 2002, **27**, 571–577.

55 P. L. Martin-Hirsch, C. Whitehurst, C. H. Buckley, J. V. Moore and H. C. Kitchener, *Lancet*, 1998, **351**, 1403.

56 H. W. Herr, D. M. Schwalb, Z. F. Zhang, P. C. Sogani, W. F. Whitmore and H. F. Oettgen, *Class. Pap. Curr. Comments Highlights Genitourin. Cancer Res.*, 1998, **13**, 1404–1408.

57 H. Lee, J. Han, H. Shin, H. Han, K. Na and H. Kim, *J. Control. Release*, 2018, **283**, 190–199.

58 N. P. Brodin, C. Guha and W. A. Tomé, *Technol. Cancer Res. Treat.*, 2015, **14**, 355–368.

59 K. K. Y. Cheung, J. Y. W. Chan and K. P. Fung, *Drug Chem. Toxicol.*, 2013, **36**, 474–483.

60 X. Q. Wei, H. Q. Ma, A.-H. Liu and Y. Z. Zhang, *Asian Pac. J. Cancer Prev.*, 2013, **14**, 3023–8.

61 J. C. Ahn, R. Biswas, A. Mondal, Y. K. Lee and P.-S. Chung, *Gen. Physiol. Biophys.*, 2014, **33**, 53–62.

62 K. Berg, P. K. Selbo, A. Weyergang, A. Dietze, L. Prasmickaite, A. Bonsted, B. O. Engesaeter, E. Angell-Petersen, T. Warloe, N. Frandsen and A. Hogset, *J. Microsc.*, 2005, **218**, 133–147.

63 V. X. D. Yang, P. J. Muller, P. Herman and B. C. Wilson, *Lasers Surg. Med.*, 2003, **32**, 224–232.

64 C. Fritsch, B. Homey, W. Stahl, P. Lehmann, T. Ruzicka and H. Sies, *Photochem. Photobiol.*, 1998, **68**, 218–221.

65 D. Kessel, *Cancer Lett.*, 1986, **33**, 183–188.

66 J. F. Lovell, T. W. B. Liu, J. Chen and G. Zheng, *Chem. Rev.*, 2010, **110**, 2839–2857.

67 P. A. Waghorn, *J. Labelled Comp. Radiopharm.*, 2013, **57**, 1–10.

68 J. Shi, T. W. B. Liu, J. Chen, D. Green, D. Jaffray, B. C. Wilson, F. Wang and G. Zheng, *Theranostics*, 2011, **1**, 363–70.

69 E. R. Ranyuk, N. Cauchon, H. Ali, R. Lecomte, B. Guérin and J. E. van Lier, *Bioorg. Med. Chem. Lett.*, 2011, **21**, 7470–3.

70 H. Mukai, Y. Wada and Y. Watanabe, *Ann. Nucl. Med.*, 2013, **27**, 625–39.

71 F. Zoller, P. J. Riss, F.-P. Montforts, D. K. Kelleher, E. Eppard and F. Rösch, *Nucl. Med. Biol.*, 2013, **40**, 280–8.

72 B. B. Azad, C. Cho, J. D. Lewis and L. G. Luyt, *Appl. Radiat. Isot.*, 2012, **70**, 505–11.

73 N. Vahidfar, A. R. Jalilian, Y. Fazaeli, A. Bahrami-Samani, D. Beiki and A. Khalaj, *J. Radioanal. Nucl. Chem.*, 2012, **295**, 979–986.

74 M. Ethirajan, Y. Chen, P. Joshi and R. K. Pandey, *Chem. Soc. Rev.*, 2011, **40**, 340–362.

75 Boyle R.W., Clarke O., Sutton J. M., Greenman J., US 2003/0203888 A1, 2003, 1, 20.

76 J. M. Sutton, O. J. Clarke, N. Fernandez and R. W. Boyle, *Bioconjug. Chem.*, 2002, **13**, 249–63.

77 S. S. Kelkar and T. M. Reineke, *Bioconjug. Chem.*, 2011, **22**, 1879–903.

78 J. V Frangioni, *Curr Opin Chem Biol*, 2003, **7**, 626–634.

79 T. W. Liu, E. Huynh, T. D. MacDonald and G. Zheng, *Porphyrins for Imaging, Photodynamic Therapy, and Photothermal Therapy*, Elsevier, 2014.

80 R. L. Lipson, J. . Pratt and E. . Baldes, *Obs. Gynecol.*, 1964, **24**, 78.

81 R. L. Lipson, E. J. Baldes and M. J. Gray, *Cancer*, 1967, **20**, 2255–2257.

82 Y. Fradet, H. B. Grossman, L. Gomella, S. Lerner, M. Cookson, D. Albala and M. J. Droller, *J. Urol.*, 2007, **178**, 68–73.

83 M. A. Brown and R. C. Semelka, in *MRI Basic Principles and Applications*, John

Wiley & Sons, Chapel Hill, 3rd edn., 2003, pp. 1–5.

84 M. Ethirajan, Y. Chen, P. Joshi and R. K. Pandey, *Chem. Soc. Rev.*, 2011, **40**, 340–362.

85 P. A. M. Dirac, *Proc. R. Soc. A.*, 1928, **117**, 610–624.

86 P. A. M. Dirac, *Proc. Suc. Exp. Biol. Med*, 1929, **43**, 491–494.

87 C. D. Anderson, *Phys. Rev.*, 1933, **238**, 491–494.

88 P. A. M. Dirac, *Proc. R. Soc. A Math. Phys. Eng. Sci.*, 1931, **133**, 60–72.

89 K. Herholz and W. D. Heiss, in *Molecular Imaging and Biology*, 2004, vol. 6, pp. 239–269.

90 D. L. Bailey, D. W. Townsend, P. E. Valk and M. N. Maisey, in *Positron Emission Tomography Basic Sciences*, eds. P. E. Valk and M. N. Maisey, Springer-Verlag, 2005, pp. 1–13.

91 N. Ramakrishnan, M. E. Clay, L. R. Friedman, A. R. Antunez and N. L. Oleinick, *Photochem. Photobiol.*, 1990, **52**, 555–559.

92 G. Delaney, S. Jacob, C. Featherstone and M. Barton, *Cancer*, 2005, **104**, 1129–1137.

93 A. S. Bhide and C. M. Nutting, *BMC Med.*, 2010, **8**, 25–30.

94 A. Barrett, J. Dobbs, S. Morris and T. Roques, in *Practical Radiothreapy Planning*, ed. G. Jamieson, Hodder Arnold, London, 4th edn., 2009, pp. 9–15.

95 J. L. Meyer, L. Verhey, P. Pia and J. Wong, in *IMRT, IGRT, SBRT - Advances in the Treatment Planning and Delivery of Radiotherapy*, ed. L. Meyer, John, Karger, San Francisco, 1st edn., 2007, pp. 6–17.

96 A. Boyer, P. Biggs, J. Galvin, E. Klein, T. LoSasso, D. Low, K. Mah and C. Yu, *Basic applications of multileaf collimators, AAPM REPORT NO. 72 BASIC*, Madison, 2001.

97 I. Madani, W. Duthoy, C. Derie, W. De Gersem, T. Boterberg, M. Saerens, F. Jacobs, V. Grégoire, M. Lonneux, L. Vakaet, B. Vanderstraeten, W. Bauters, K. Bonte, H. Thierens and W. De Neve, *Int. J. Radiat. Oncol. Biol. Phys.*, 2007, **68**,

126–135.

98 S. S. Lo, B. S. Teh, J. J. Lu and T. E. Schefter, in *Stereotactic Body Radiation Therapy*, eds. L. W. Brady, H.-P. Heilmann, M. Molls and C. Nieder, Springer, New York, 1st edn., 2002, pp. 1–8.

99 F. Alongi, S. Arcangeli, A. R. Filippi, U. Ricardi and M. Scorsetti, *Radiat. Oncol.*, 2012, **17**, 1100–1107.

100 Y. Norihisa, Y. Nagata and K. et al. Takayama, *Int J Radiat Oncol Biol Phys*, 2008, **72**, 398–403.

101 R. Onimaru and S. Shirato, *Int J Radiat Oncol Biol Phys*, 2003, **56**, 126–135.

102 Z. Fuks and R. Kolesnick, *Cancer Cell*, 2005, **8**, 89–91.

103 A. Juzeniene, K. P. Nielsen and J. Moan, *J. Environ. Pathol. Toxicol. Oncol.*, 2006, **25**, 7–28.

104 W. Chen and J. Zhang, *J Nanosci Nanotechnol.*, 2006, **6**, 1159–66.

105 G. Blasse and B. C. Grabmaier, in *Luminescent Materials*, eds. G. Blasse and B. Grabmaier, Springer-Verlag, London, 1st edn., 1994, pp. 118–119.

106 M. J. Weber, *J. Lumin.*, 2002, **100**, 35–45.

107 P. Lecoq, A. Annenkov, A. Gektin, M. Korzhik and C. Pedrini, in *Inorganic scintillators for detector systems*, eds. P. Lecoq, A. Annenkov, A. Gektin, M. Korzhik and C. Pedrini, Springer, New York, 1st edn., 2006, pp. 1–5.

108 M. J. Weber, *Nucl. Instruments Methods Phys. Res. Sect.*, 2004, **527**, 9–14.

109 J. Hu, Y. Tang, A. H. Elmenoufy, H. Xu, Z. Cheng and X. Yang, *Small*, 2015, **11**, 5860–5887.

110 A. Kamkaew, F. Chen, Y. Zhan, R. L. Majewski and W. Cai, *ACS Nano*, 2016, **10**, 3918–3935.

111 S. S. Lucky, K. C. Soo and Y. Zhang, *Chem. Rev.*, 2015, **115**, 1990–2042.

112 Y. Liu, W. Chen, S. Wang and A. G. Joly, *Appl. Phys. Lett.*, 2008, **92**, 1–4.

113 J. P. Scaffidi, M. K. Gregas, B. Lauly, Y. Zhang and T. Vo-Dinh, *ACS Nano*,

2011, **5**, 4679–4687.

114 I. N. Ogorodnikov, A. V Kruzhalov and V. Y. Ivanov, *Delft Prog. Rep*. 1996, 216–219.

115 E. Abliz, J. E. Collins, J. S. Friedberg, A. Kumar, R. W. Waynant and D. B. Tata, *J. X-Ray Sci. Technol.*, 2010, **7565**, 1–13.

116 A. L. Bulin, C. Truillet, R. Chouikrat, F. Lux, C. Frochot, D. Amans, G. Ledoux, O. Tillement, P. Perriat, M. Barberi-Heyob and C. Dujardin, *J. Phys. Chem. C*, 2013, **117**, 21583–21589.

117 X. Zou, M. Yao, L. Ma, M. Hossu, X. Han, P. Juzenas and W. Chen, *Nanomedicine*, 2014, **9**, 2339–2351.

118 M. Yao, Y. Li, M. Hossu, A. G. Joly, Z. Liu, Z. Liu and W. Chen, *J. Phys. Chem. B*, 2011, **115**, 9352–9359.

119 Y. Tang, J. Hu, A. H. Elmenoufy and X. Yang, *ACS Appl. Mater. Interfaces*, 2015, **7**, 12261–12269.

120 A. H. Elmenoufy, Y. Tang, J. Hu, H. Xu and X. Yang, *Chem. Commun.*, 2015, **51**, 12247–12250.

121 Z. Li and Y. Zhang, *Angew. Chemie Int. Ed.*, 2006, **45**, 7732–7735.

122 S. Kaščáková, A. Giuliani, S. Lacerda, A. Pallier, P. Mercère, É. Tóth and M. Réfrégiers, *Nano Res.*, 2015, **8**, 2373–2379.

123 K. M. Wagstaff and D. A. Jans, *Eur. J. Pharmacol.*, 2009, **625**, 174–180.

124 H. Chen, G. D. Wang, Y. J. Chuang, Z. Zhen, X. Chen, P. Biddinger, Z. Hao, F. Liu, B. Shen, Z. Pan and J. Xie, *Nano Lett.*, 2015, **15**, 2249–2256.

125 C. Zhang, K. Zhao, W. Bu, D. Ni, Y. Liu, J. Feng and J. Shi, *Angew. Chemie Int. Ed.*, 2015, **54**, 1770–1774.

126 J. Fuchs and J. Thiele, *Free Radic. Biol. Med.*, 1998, **24**, 835–847.

127 Y. Li, W. Zhang, J. Niu and Y. Chen, *ACS Nano*, 2012, **6**, 5164–5173.

128 A. Y. Satoh, J. E. Trosko and S. J. Masten, *Environ. Sci. Technol.*, 2007, **41**, 2881–2887.

129 S. Clement, W. Deng, E. Camilleri, B. C. Wilson and E. M. Goldys, *Sci. Rep.*, 2016, **6**, 19954.

130 H. Chen, G. D. Wang, Y.-J. Chuang, Z. Zhen, X. Chen, P. Biddinger, Z. Hao, F. Liu, B. Shen, Z. Pan and J. Xie, *Nano Lett.*, 2015, **15**, 2249–2256.

131 C. Zhang, K. Zhao, W. Bu, D. Ni, Y. Liu, J. Feng and J. Shi, *Angew. Chem.*, 2015, **54**, 1–6.

132 G. M. Entract, F. Bryden, J. Domarkas, H. Savoie, L. Allott, S. J. Archibald, C. Cawthorne and R. W. Boyle, *Mol. Pharm.*, 2015, **12**, 4414–4423.

133 J. Funkhouser, *Curr. Drug Discov.*, 2002, 17–19.

134 H. Zheng, *Technol Cancer Res Treat.*, 2005, **4**, 283–293.

135 R. Brookfield, H. Ellul and A. Harriman, *J. Chem. Soc.*, 1985, **81**, 1837–1848.

136 P. W. Miller, N. J. Long, R. Vilar and A. D. Gee, *Angew. Chem. Int. Ed.*, 2008, **47**, 8998–9033.

137 R. Kavali, B. C. Lee, B. S. Moon, S. D. Yang, K. S. Chun, C. W. Choi, C. H. Lee and D. Y. Chi, *J. Label. Compd. Radiopharm.*, 2005, **48**, 749–758.

138 E. Ranyuk, H. Ali, B. Guerin and J. E. van Lier, *J. Porphyrins Phthalocyanines*, 2013, **17**, 850–856.

139 F. Bryden and R. W. Boyle, *Synlett*, 2013, **24**, 1978–1982.

140 F. Giuntini, F. Bryden, R. Daly, E. M. Scanlan and R. W. Boyle, *Org. Biomol. Chem.*, 2014, **12**, 1203–6.

141 F. Giuntini, F. Dumoulin, R. Daly, V. Ahsen, E. M. Scanlan, A. S. P. Lavado, J. W. Aylott, G. Rosser, A. Beeby and R. W. Boyle, *Nanoscale*, 2012, **4**, 2034–45.

142 P. Rothemund, *J. Am. Chem. Soc.*, 1935, **57**, 2010–2011.

143 P. Rothemund and A. R. Menotti, *J. Am. Chem. Soc.*, 1941, **63**, 267–270.

144 J. S. Lindsey, I. C. Schreiman, H. C. Hsu, P. C. Kearney and A. M. Marguerettaz, *J. Org. Chem.*, 1987, **52**, 827–836.

145 A. D. Adler, F. R. Longo, J. D. Finarelli, J. Goldmacher, J. Assour and L.

Korsakoff, *J. Org. Chem.*, 1967, **32**, 467.

146 J. S. Lindsey, in *The Porphyrin Handbook; Synthesis and organic chemistry*, eds. K. M. Kadish, K. M. Smith and R. Guilard, Elsevier, 1st edn., 2000, pp. 53–55.

147 S. W. Staley, B. Eliasson, P. C. Kearney, I. C. Schreiman and J. S. Lindsey, eds. F. L. Carter, R. E. Siatowski and H. Wohltjen, Elsevier (North Holland), 3rd edn., 1988, p. 543.

148 V. D. Bock, H. Hiemstra and J. H. van Maarseveen, *Eur. J. Org. Chem.*, 2006, **2006**, 51–68.

149 V. V Rostovtsev, L. G. Green, V. V Fokin and K. B. Sharpless, *Angew. Chem. Int. Ed. Engl.*, 2002, **41**, 2596–9.

150 C. W. Tornøe, C. Christensen and M. Meldal, *J. Org. Chem.*, 2002, **67**, 3057–64.

151 L. Zhang, X. Chen, P. Xue, H. H. Y. Sun, I. D. Williams, K. B. Sharpless, V. V Fokin and G. Jia, *J. Am. Chem. Soc.*, 2005, **127**, 15998–9.

152 C. O. Kappe and E. Van Der Eycken, *Chem. Soc. Rev.*, 2010, **39**, 1280–1290.

153 A. P. Belanger, M. K. Pandey and T. M. DeGrado, *Nucl Med Biol.*, 2011, **38**, 435–441.

154 J. L. Sesslar, A. Gebauer and E. Vogel, in *The Porphyrin Handbook; Heteroporphyrins, expanded porphyrins and related macrocycles*, eds. K. M. Kadish, K. M. Smith and R. Guilard, Academic Press, 2000, p. 40.

155 J. W. Winkelman and G. H. Collins, *Photochem. Photobiol.*, 1987, **46**, 801–807.

156 F. Giuntini, F. Bryden, R. Daly, E. M. Scanlan and R. W. Boyle, *Org. Biomol. Chem.*, 2014, **12**, 1203–6.

157 E. B. Fleischer and A. M. Shachter, *Inorg. Chem.*, 1991, **30**, 3763–3769.

158 L. N. Goswami, Z. H. Houston, S. J. Sarma, S. S. Jalisatgi and M. F. Hawthorne, *Org. Biomol. Chem.*, 2013, **11**, 1116–26.

159 J. M. Harris, E. C. Struck, M. G. Case, S. Paley and M. Yalpani, *J. Polym. Sci.*, 1984, **22**, 341–352.

160 G. Schwach, P. Thamyongkit, L. M. Reith, B. Svejda, G. Knör, R. Pfragner and

W. Schoefberger, *Bioorg. Chem.*, 2012, **40**, 108–113.

161 U. Prabhakar, H. Maeda, R. K. Jain, E. M. Sevick-Muraca, W. Zamboni, O. C. Farokhzad, S. T. Barry, a. Gabizon, P. Grodzinski and D. C. Blakey, *Cancer Res.*, 2013, **73**, 2412–2417.

162 S. Huang, K. Shao, Y. Liu, Y. Kuang, J. Li, S. An, Y. Guo, H. Ma and C. Jiang, *ACS Nano*, 2013, **7**, 2860–2871.

163 C. P. Hollis, H. L. Weiss, M. Leggas, B. M. Evers, R. A. Gemeinhart and T. Li, *J. Control. Release*, 2013, **172**, 12–21.

164 C. Baker, in *Walter & Miller's Textbook of Radiotherapy : Radiation Physics, Therapy and Oncology*, eds. P. Symonds, C. Deehan and J. Mills, Elsevier Churchill Livingstone, 7th edn., 2012, pp. 15–32.

165 K. Thayalan, in *The Physics of Radiology and Imaging*, Jaypee Brothers Medical Publishers (P) Ltd, New Delhi, 1st edn., 2014, pp. 24–50.

166 N. Y. Morgan, G. Kramer-Marek, P. D. Smith, K. Camphausen and C. Jacek, *Radiat. Res*, 2009, **171**, 236–244.

167 T. Yanagida, *Proc. Jpn. Acad. Ser. B*, 2018, **94**, 75–97.

168 P. Avci, A. Gupta, M. Sadasivam, D. Vecchio and M. Hamblin, *Semin. Cutan. Med. Surg.*, 2013, **32**, 41–52.

169 J. H. Hubbell and S. M. Seltzer, *Tables of X-Ray Mass Attenuation Coefficients and Mass Energy-Absorption Coefficients from 1 keV to 20 MeV for Elements Z = 1 to 92 and 48 Additional Substances of Dosimetric Interest*, 1995.

170 R. B. Von Dreele, M. R. Suchomel and B. H. Toby, *U.S. Dep. Energy*, 2013.

171 R. C. Murty, *Nature*, 1965, **205**, 398–399.

172 K. Thayalan, in *The Physics of Radiology and Imaging*, Jaypee Brothers Medical Publishers (P) Ltd, New Delhi, 1st edn., 2014, pp. 1–24.

173 S. B. Schwarz, N. Thon, K. Nikolajek, M. Niyazi, J. C. Tonn, C. Belka and F. W. Kreth, *Radiat. Oncol.*, 2012, **7**, 30.

174 J. H. Kim and B. Hilaris, *Am. J. Roentgenol.*, 1975, **132**, 163–169.

175 M. Bernstein and P. H. Gutin, *Neurosurgery*, 1981, **9**, 741–750.

176 K. Thayalan, in *The Physics of Radiology and Imaging*, Jaypee Brothers Medical Publishers (P) Ltd, New Delhi, 1st edn., 2014, pp. 50–80.

177 E. L. Nickoloff and H. L. Berman, *Radiographics*, 1993, **13**, 1337–1348.

178 C. A. Carlsson and G. A. Carlsson, *Basic physics of X-ray imaging*, Linkoping University, Sweden, Linkoping, 2nd edn., 1996.

179 D. Mishra, S. Anand, R. K. Panda and R. P. Das, *Mater. Lett*, 2000, **12**, 38–45.

180 G. Zhang, R. Jia and Q. Wu, *Mater. Sci. Eng. B*, 2006, **128**, 254–259.

181 L. Sun, M. Cao, Y. Wang, G. Sun and C. Hu, *J. Cryst. Growth*, 2006, **289**, 231–235.

182 T. Thongtem, S. Kungwankunakorn, B. Kuntalue, A. Phuruangrat and S. Thongtem, *J. Alloys Compd.*, 2010, **506**, 475–481.

183 Y. Wang, J. Ma, J. Tao, X. Zhu, J. Zhou, Z. Zhao, L. Xie and H. Tian, *Mater. Lett.*, 2006, **60**, 291–293.

184 Y. Tian, Y. Liu, R. Hua, L. Na and B. Chen, *Mater. Res. Bull.*, 2012, **47**, 59–62.

185 S. J. Chen, J. Li, X. T. Chen, J. M. Hong, Z. Xue and X. Z. You, *J. Cryst. Growth*, 2003, **253**, 361–365.

186 P. Parhi, T. N. Karthik and V. Manivannan, *J. Alloys Compd.*, 2008, **465**, 380–386.

187 F. Petricca, G. Angloher, C. Cozzini, T. Frank, D. Hauff, J. Ninković, F. Pröbst, W. Seidel and S. Uchaikin, *Nucl. Instruments Methods Phys. Res. Sect. A Accel. Spectrometers, Detect. Assoc. Equip.*, 2004, **520**, 193–196.

188 S. Basu, B. Sanyasi Naidu, B. Viswanadh, V. Sudarsan, S. N. Jha, D. Bhattacharyya and R. K. Vatsa, *RSC Adv.*, 2014, **4**, 15606–15612.

189 M. V. Nazarov, D. Y. Jeon, J. H. Kang, E. J. Popovici, L. E. Muresan, M. V. Zamoryanskaya and B. S. Tsukerblat, *Solid State Commun.*, 2004, **131**, 307–311.

190 C. A. Kodaira, H. F. Brito and M. C. F. C. Felinto, *J. Solid State Chem.*, 2003, **171**, 401–407.

191 E. Orhan, M. Anicete-Santos, M. A. M. A. Maurera, F. M. Pontes, A. G. Souza, J. Andrès, A. Beltràn, J. A. Varela, P. S. Pizani, C. A. Taft and E. Longo, *J. Solid State Chem.*, 2005, **178**, 1284–1291.

192 E. F. Paski and M. W. Blades, *Anal. Chem.*, 1988, **60**, 1224–1230.

193 M. L. Pang, *J. Phys. Condens. Matter*, 2003, **15**, 5157–5169.

194 Q. Xiao, Q. Zhou and M. Li, *J. Lumin.*, 2010, **130**, 1092–1094.

195 Q. Li, Y. Shen and T. Li, *Asian J. Chem*, 2013, **2013**, 1–5.

196 V. B. Mikhailik, H. Kraus, G. Miller, M. S. Mykhaylyk and D. Wahl, *J. Appl. Phys.*, 2005, **97**, 1–8.

197 K. Kalantar-Zadeh, A. Vijayaraghavan, M. H. Ham, H. Zheng, M. Breedon and M. S. Strano, *Chem. Mater.*, 2010, **22**, 5660–5666.

198 Q. Dai, H. Song, G. Pan, X. Bai, H. Zhang, R. Qin, L. Hu, H. Zhao, S. Lu and X. Ren, *J. Appl. Phys.*, 2007, **102**, 1–8.

199 K. Gayatri Sharma, N. Shanta Singh, Y. Rangeela Devi, N. Rajmuhon Singh and S. Dorendrajit Singh, *J. Alloys Compd.*, 2013, **556**, 94–101.

200 K. G. Sharma and N. R. Singh, *J. Rare Earths*, 2012, **30**, 310–314.

201 A. G. Page, S. V. Godbole and M. D. Mastry, *J. Phys. Chem. Solids*, 1989, **50**, 571–575.

202 R. D. Shannon, *Acta Cryst.*, 1976, **32**, 751–767.

203 S. Shi, J. Gao and J. Zhou, *Opt. Mater.*, 2008, **30**, 1616–1620.

204 L. F. Johnson, G. D. Boyd, K. Nassau and R. R. Soden, *Phys. Rev.*, 1962, **126**, 1406–1410.

205 A. B. Campos, A. Z. Simões, E. Longo, J. A. Varela, V. M. Longo, A. T. De Figueiredo, F. S. De Vicente and A. C. Hernandes, *Appl. Phys. Lett.*, 2007, **91**, 2005–2008.

206 C. Ribeiro, E. J. H. Lee, T. R. Giraldi, E. Longo, J. A. Varela and E. R. Leite, *J. Phys. Chem. B*, 2004, **108**, 15612–15617.

207 E. A. Rozhkova, I. Ulasov, B. Lai, N. M. Dimitrijevic, M. S. Lesniak and T. Rajh, *Nano Lett.*, 2009, **9**, 3337–3342.

208 K. Riwotzki and M. Haase, *J. Phys. Chem. B*, 2002, **102**, 10129–10135.

209 M. Rahimi-Nasrabadi, S. M. Pourmortazavi, M. R. Ganjali, A. Reza Banan and F. Ahmadi, *J. Mol. Struct.*, 2014, **1074**, 85–91.

210 A. K. Munirathnappa, V. C. Petwal, J. Dwivedi and N. G. Sundaram, *New J. Chem.*, 2018, **42**, 2726–2732.

211 B. H. Toby and R. B. Von Dreele, *J. Appl. Crystallogr.*, 2013, **40**, 544–549.

212 A. De La Hoz, Á. Díaz-Ortiz and A. Moreno, *Chem. Soc. Rev.*, 2005, **34**, 164–178.

213 M. Baghbanzadeh, L. Carbone, P. D. Cozzoli and C. O. Kappe, *Angew. Chemie Int. Ed.*, 2011, **50**, 11312–11359.

214 S. K. Jha, X. L. Phuah, J. Luo, C. P. Grigoropoulos, H. Wang, E. García and B. Reeja-Jayan, *J. Am. Ceram. Soc.*, 2019, **102**, 5–31.

215 G. B. Dudley, R. Richert and A. E. Stiegman, *Chem. Sci.*, 2015, **6**, 2144–2152.

216 M. Gharibeh, G. Tompsett, F. Lu, S. M. Auerbach, K. S. Yngvesson and W. C. Conner, *J. Phys. Chem. B*, 2009, **113**, 12506–12520.

217 N. Massoni, R. Hegron and L. Campayo, *Acta Crystallogr. Sect. E Crystallogr. Commun.*, 2018, **74**, 955–959.

218 V. A. Fonoberov and A. A. Balandin, *Appl. Phys. Lett.*, 2004, **85**, 5971–5973.

219 W. He, H. Jia, J. Cai, X. Han, Z. Zheng, W. G. Wamer and J. J. Yin, *J. Phys. Chem. C*, 2016, **120**, 3187–3195.

220 R. Schneider, F. Schmitt, C. Frochot, Y. Fort, N. Lourette, F. Guillemin, J.-F. Müller and M. Barberi-Heyob, *Bioorg. Med. Chem.*, 2005, **13**, 2799–808.

221 S. Sahoo, M. Maiti, A. Ganguly, J. George and A. Bhowmick, *J. Appl. Polym. Sci.*, 2007, **105**, 2407–2145.

222 M. D. Newman, M. Stotland and J. I. Ellis, *J. Am. Acad. Dermatol.*, 2009, **61**, 685–692.

223 A. Hatamie, A. Khan, M. Golabi, A. P. F. Turner, V. Beni, W. C. Mak, A. Sadollahkhani, H. Alnoor, B. Zargar, S. Bano, O. Nur and M. Willander, *Langmuir*, 2015, **31**, 10913–10921.

224 A. Kołodziejczak-Radzimska and T. Jesionowski, *Materials*, 2014, **7**, 2833–2881.

225 F. X. Xiao, S. F. Hung, H. B. Tao, J. Miao, H. Bin Yang and B. Liu, *Nanoscale*, 2014, **6**, 14950–14961.

226 J. Jiang, J. Pi and J. Cai, *Bioinorg. Chem. Appl.*, 2018, **2018**, 1–18.

227 J. Ji, A. M. Colosimo, W. Anwand, L. A. Boatner, A. Wagner, P. S. Stepanov, T. T. Trinh, M. O. Liedke, R. Krause-Rehberg, T. E. Cowan and F. A. Selim, *Sci. Rep.*, 2016, **6**, 1–9.

228 W. Jia, S. Dang, H. Liu, Z. Zhang, C. Yu, X. Liu and B. Xu, *Mater. Lett.*, 2012, **82**, 99–101.

229 K. Mohan Kumar, B. K. Mandal, E. Appala Naidu, M. Sinha, K. Siva Kumar and P. Sreedhara Reddy, *Spectrochim. Acta A*, 2013, **104**, 171–174.

230 T. H. Mahato, G. K. Prasad, B. Singh, J. Acharya, A. R. Srivastava and R. Vijayaraghavan, *J. Hazard. Mater.*, 2009, **165**, 928–932.

231 S. Yue, Z. Yan, Y. Shi and G. Ran, *Mater. Lett.*, 2013, **98**, 246–249.

232 D. Chen, X. Jiao and G. Cheng, *Solid State Commun.*, 2002, **113**, 363–366.

233 C. H. Lu and C. H. Yeh, *Mater. Lett.*, 1997, **33**, 129–132.

234 J. J. Schneider, R. C. Hoffmann, J. Engstler, A. Klyszcz, E. Erdem, P. Jakes, R. A. Eichel, L. Pitta-Bauermann and J. Bill, *Chem. Mater.*, 2010, **22**, 2203–2212.

235 M. K. Patra, M. Manoth, V. K. Singh, G. Siddaramana Gowd, V. S. Choudhry, S. R. Vadera and N. Kumar, *J. Lumin.*, 2009, **129**, 320–324.

236 J. Wojnarowicz, A. Opalinska, T. Chudoba, S. Gierlotka, R. Mukhovskyi, E. Pietrzykowska, K. Sobczak and W. Lojkowski, *J. Nanomater.*, 2016, **2016**.

237 W. Lojkowski, C. Leonelli, T. Chudoba, J. Wojnarowicz, A. Majcher and A. Mazurkiewicz, *Inorganics*, 2014, **2**, 606–619.

238 B. W. Chieng and Y. Y. Loo, *Mater. Lett.*, 2012, **73**, 78–82.

239 J. Wang, C. Loose, J. Baxter, D. Cai, Y. Wang, J. Tom and J. Lepore, *J. Cryst. Growth*, 2005, **283**, 469–478.

240 B. D. Cullity, ed. M. Cohen, Addison-Wesley, London, 2nd edn., 1978, pp. 450–452.

241 L. Guo, S. Yang, C. Yang, P. Yu, J. Wang, W. Ge and G. K. L. Wong, *Appl. Phys. Lett.*, 2000, **76**, 2901.

242 Z. Chen, X. X. Li, G. Du, N. Chen and A. Y. M. Suen, *J. Lumin.*, 2011, **131**, 2072–2077.

243 B. Ritter, T. Krahl, K. Rurack and E. Kemnitz, *J. Mater. Chem. C*, 2014, **2**, 8607–8613.

244 L. G. Jacobsohn, K. B. Sprinkle, S. Roberts, C. J. Kucera, T. L. James, E. G. Yukihara, T. DeVol and J. Ballato, *J. Nanomater.*, 2010, **2011**, 1–6.

245 L. Song, J. Gao and R. Song, *J. Lumin.*, 2010, **130**, 1179–1182.

246 X. Sun, M. Gu, S. Huang, X. Jin, X. Liu, B. Liu and C. Ni, *J. Lumin.*, 2009, **129**, 773–777.

247 C. Feldmann, M. Roming and K. Trampert, *Small*, 2006, **2**, 1248–1250.

248 J. Wang, W. Miao, Y. Li, H. Yao and Z. Li, *Mater. Lett.*, 2009, **63**, 1794–1796.

249 S. Sasidharan, A. Jayasree, S. Fazal, M. Koyakutty, S. V. Nair and D. Menon, *Biomater. Sci.*, 2013, **1**, 294–305.

250 K. Schwartz, in *Quantum Mechanics*, ed. W. Beiglbock, Springer, Berlin, Germany, 1997, p. 357.

251 F. Wang, Y. Zhang, X. Fan and M. Wang, *Nanotechnology*, 2006, **17**, 1527–1532.

252 S. Sivakumar, F. C. J. M. Van Veggel and M. Raudsepp, *J. Am. Chem. Soc.*, 2005, **127**, 12464–12465.

253 Y. Wei, F. Lu, X. Zhang and D. Chen, *Mater. Lett.*, 2007, **61**, 1337–1340.

254 J. Meng, M. Zhang, Y. Liu and S. Man, *Spectrochim. Acta A*, 2007, **66**, 81–85.

255 V. Sudarsan, F. C. J. M. Van Veggel, R. A. Herring and M. Raudsepp, *J. Mater. Chem.*, 2005, **15**, 1332–1342.

256 Z. Wang, M. Li, C. Wang, J. Chang, H. Shi and J. Lin, *J. Rare Earths*, 2009, **27**, 33–37.

257 J. W. Stouwdam and F. C. J. M. Van Veggel, *Langmuir*, 2004, **20**, 11763–11771.

258 Z. L. Wang, H. L. W. Chan, H. L. Li and J. H. Hao, *Appl. Phys. Lett.*, 2008, **93**, 1–4.

259 A. I. Becerro, D. Gonzalez-Mancebo and M. Ocaña, *J. Nanoparticle Res.*, 2015, **17**.

260 P. R. Diamente, M. Raudsepp and F. C. J. M. Van Veggel, *Adv. Funct. Mater.*, 2007, **17**, 363–368.

261 P. Qiu, N. Zhou, Y. Wang, C. Zhang, Q. Wang, R. Sun, G. Gao and D. Cui, *CrystEngComm*, 2014, **16**, 1859–1863.

262 S. Xiao, X. Yang, J. W. Ding and X. H. Yan, *J. Phys. Chem. C*, 2007, **111**, 8161–8165.

263 J. Lin, J. Huo, Y. Cai and Q. Wang, *J. Lumin.*, 2013, **144**, 1–5.

264 L. Guo, Y. Wang, L. Han, Q. Qiang, W. Zeng, Z. Zou, B. Wang and X. Guo, *J. Mater. Chem. C*, 2013, **1**, 7952–7962.

265 R. Srinivasan, N. R. Yogamalar, J. Elanchezhiyan, R. J. Joseyphus and A. C. Bose, *J. Alloys Compd.*, 2010, **496**, 472–477.

266 J. R. Jayaramaiah, B. N. Lakshminarasappa and B. M. Nagabhushana, *Sensors Actuators, B Chem.*, 2012, **173**, 234–238.

267 N. Rakov, W. Lozano B, G. S. Maciel and C. B. de Araújo, *Chem. Phys. Lett.*, 2006, **428**, 134–137.

268 R. P. Singh, K. Gupta, A. Pandey and A. Pandey, *WJNSE*, 2012, **2**, 13–18.

269 M. Aghazadeh, T. Yousefi and M. Ghaemi, *J. Rare Earths*, 2012, **30**, 236–240.

270 E. T. Goldburt, B. Kulkarni, R. N. Bhargava, J. Taylor and M. Libera, *J. Lumin.*, 1997, **72**–**74**, 190–192.

271 E. J. Popovici, L. Muresan, H. Amalia, E. Indrea and M. Vasilescu, *J. Alloys Compd.*, 2007, **434**–**435**, 809–812.

272 W. Xie, M. Ivanov, R. Yavetskiy, N. Jiang, Y. Shi, H. Chen, H. Kou, J. Wang and J. Li, *Opt. Mater.*, 2018, **86**, 550–561.

273 W. Xie, J. Wang, M. Cao, Z. Hu, Y. Feng, X. Chen, N. Jiang, J. Dai, Y. Shi, V. Babin, E. Mihóková, M. Nikl and J. Li, *Opt. Mater.*, 2018, **80**, 22–29.

274 E. Zych, M. Wawrzyniak, A. Kossek, J. Trojan-Piegza and L. Kepiński, *J. Alloys Compd.*, 2008, **451**, 591–594.

275 E. Zych, D. Hreniak and W. Strek, *J. Phys. Chem. B*, 2002, **106**, 3805–3812.

276 Z. Wang, W. Zhang, B. You and M. Yin, *Spectrochim. Acta - Part A Mol. Biomol. Spectrosc.*, 2008, **70**, 835–839.

277 A. Lempicki, C. Brecher, P. Szupryczynski, H. Lingertat, V. V. Nagarkar, S. V. Tipnis and S. R. Miller, *Nucl. Instruments Methods Phys. Res. Sect. A Accel. Spectrometers, Detect. Assoc. Equip.*, 2002, **488**, 579–590.

278 G. Concas, G. Spano, E. Zyen and J. Trojan-Piegza, *J. Phys. Condens. Matter*, 2005, **17**, 2597–2604.

279 H. Forest and G. Ban, *J. Electrochem. Soc.*, 1969, **116**, 474–478.

280 J. Trojan-Piegza and E. Zych, *J. Phys. Chem. C*, 2010, **114**, 4215–4220.

281 C. Xing, Q. Xu, H. Tang, L. Liu and S. Wang, *J. Am. Chem. Soc.*, 2009, **131**, 13117–13124.

282 W. S. Kuo, C. N. Chang, Y. T. Chang, M. H. Yang, Y. H. Chien, S. J. Chen and C. S. Yeh, *Angew. Chemie Int. Ed.*, 2010, **49**, 2711–2715.

283 L. Shi, B. Hernandez and M. Selke, *J. Am. Chem. Soc.*, 2006, **128**, 6278–6279.

284 N. A. Kuznetsova, N. S. Gretsova, V. M. Derkacheva, O. L. Kaliya and E. A. Lukyanets, *J. Porphyrins Phthalocyanines*, 2003, **07**, 147–154.

285 P. Yang, S. Gai and J. Lin, *Chem. Soc. Rev.*, 2012, **41**, 3679.

286 N. M. Idris, M. K. Gnanasammandhan, J. Zhang, P. C. Ho, R. Mahendran and Y. Zhang, *Nat. Med.*, 2012, **18**, 1580–1585.

287 J. Lahann, in *Click chemistry for biotechnology and materials science*, ed. J. Lahann, Wiley, 1st edn., 2009, p. 2.

288 V. Castro, H. Rodriguez and F. Albericio, *ACS Comb. Sci.*, 2016, **18**, 1–14.

289 Y. Ishikawa, A. Yamashita and T. Uno, *Chem. Pharm. Bull. (Tokyo).*, 2001, **49**, 287–93.

290 C. Xu, K. Xu, H. Gu, R. Zheng, H. Liu, X. Zhang, Z. Guo and B. Xu, *J. Am. Chem. Soc.*, 2004, **126**, 9938–9939.

291 T. Rajh, L. X. Chen, K. Lukas, T. Liu, M. C. Thurnauer and D. M. Tiede, *J. Phys. Chem. B*, 2002, **106**, 10543–10552.

292 S. Osati, N. Safari, M. K. Bojdi and S. S. H. Davarani, *J. Electroanal. Chem.*, 2011, **655**, 120–127.

293 M. Adineh, P. Tahay, M. Ameri, N. Safari and E. Mohajerani, *RSC Adv.*, 2016, **6**, 14512–14521.

294 F. Hosseini, M. Seyedsadjadi and N. Farhadyar, *Orient. J. Chem.*, 2014, **30**, 1609–1618.

295 S. Belali, A. R. Karimi and M. Hadizadeh, *Int. J. Biol. Macromol.*, 2018, **110**, 437–448.

296 H. Liu, P. J. H. Carter, A. C. Laan, R. Eelkema and A. G. Denkova, *Sci. Rep.*, 2019, **9**, 1–8.

297 A. M. Loening and S. S. Gambhir, *Mol. Imaging*, 2003, 2, 131–137.